High Baryon Densities Achievable in the Fragmentation Regions of High Energy Heavy-Ion Collisions

A THESIS

SUBMITTED TO THE FACULTY OF THE GRADUATE SCHOOL

OF THE UNIVERSITY OF MINNESOTA

BY

Ming Li

IN PARTIAL FULFILLMENT OF THE REQUIREMENTS

FOR THE DEGREE OF

Doctor of Philosophy

Joseph Kapusta, Advisor

August, 2018

Acknowledgements

First of all, I would like to thank my advisor, Joseph Kapusta, for all the guidance, encouragement and support during the course of my graduate studies at the University of Minnesota. I especially benefited from his emphasis on physics intuition in the training, his optimism on progress of projects, his connections in the field that give me the opportunity to interact with many people, and the freedom and independence of pursuing interesting physics problems. I would also like to thank my collaborator Chun Shen, from whom I learned hydrodynamic modeling and computations. I am grateful to Michael Albright, a former member of our group, for sharing his codes of the crossover Equation of State. I also want to acknowledge discussions with Rainer Fries, Guangyao Chen, Raju Venugopalan, Sangyong Jeon, Laszlo Csernai, Larry McLerran and Chris Plumberg. Finally, I would like to thank my friends and fellow graduate students for making my stay at Minnesota an enjoyable experience.

Dedication

To my parents and my sister.

Abstract

In high energy heavy-ion collisions, the two colliding nuclei pass through each other leaving behind an almost baryon-free central region. Most of the baryon charges are carried away by the receding nuclear remnants. During the collisions, a large amount of kinetic energy is deposited in the central region where a new form of matter called quark-gluon plasma is formed. At the same time, the colliding nuclei are highly compressed, resulting in very high baryon densities in the nuclear remnants. In this thesis, we will explore the high baryon density achievable in the nuclear remnants and study the hydrodynamic evolution of the high baryon density matter. To reach this goal, the central region is modeled as classical gluon fields at the initial stage of the collision within the framework of color glass condensate. We first compute the energy-momentum tensor of classical gluon fields by solving classical Yang-Mills equations semi-analytically using the method of power series expansion in proper time. With the help of the energy-momentum tensor, we further obtain the momentum space rapidity losses and the thermal excitation energies of the receding nuclei by imposing energy momentum conservation on the system of gluon fields and receding nuclei. Nuclear compression in high energy heavy-ion collisions is then related to the changes of momentum space rapidity. The baryon densities in the nuclear remnants are found to be more than ten times larger than the normal nuclear density for collision energies attainable at BNL Relativistic Heavy-Ion Collider and CERN Large Hadron Collider. Given

the high baryon density and also the large energy density, we further assume partonic systems in the nuclear remnants are thermalized baryon-rich quark-gluon plasma and their space-time evolution follows hydrodynamic principles, just like what happens in the central region. Using a realistic equation of state, we solve the 1+1D relativistic hydrodynamic equations with baryon diffusion. We found that baryon charges diffuse from the fragmentation regions to the central region due to fugacity gradients. Possible temperatures and chemical potentials of the high baryon density matter are found to be in regions of the phase diagram of Quantum Chromodynamics (QCD) where a phase transition might happen. This may provide an alternative approach to the ongoing Beam Energy Scan program at RHIC in studying the phase transition and searching for a critical point of the strongly interacting matter.

Contents

List of Tables

List of Figures

Chapter 1

Introduction

1.1 Phases of Quantum Chromodynamics

Quantum Chromodynamics (QCD) is the fundamental theory of strong interactions. Strong interactions are responsible for the binding of protons and neutrons to form nucleus and for the gluing of quarks to form hadrons (*i.e.* protons, neutrons, pions etc.). Quarks and gluons are fundamental degrees of freedom of QCD. They are point like particles with quarks carrying fractional electric charges ($\pm 1/3$ or $\pm 2/3$) and gluons carrying zero electric charges. Importantly, both quarks and gluons carry a new quantum charge called color. It is this color charge that is the origin of the strong interaction and explains why the interaction is called "chromo" dynamics. There are three color states for the quarks; they are red, blue and green. There are eight color states for the gluons; they are the color octet built out of the three red, blue and green states. The transformations of three color states constitute a three-dimensional matrix space which is a representation of the $SU(3)$ group. QCD is formulated as an $SU(3)$ non-Abelian gauge

field theory, which means the Lagrangian of the theory is required to be invariant under $SU(3)$ transformations at every space-time point. The Lagrangian of QCD is [1]

$$\mathcal{L} = -\frac{1}{4}F^a_{\mu\nu}F^{\mu\nu,a} + \bar{\psi}^C_i(i\gamma^\mu\partial_\mu\delta_{CD} - g\gamma^\mu T^a_{CD}A^a_\mu - m_i\delta_{CD})\psi^D_i. \qquad (1.1)$$

Here $F^a_{\mu\nu}(x) = \partial_\mu A^a_\nu(x) - \partial_\nu A^a_\mu(x) + gf^{abc}A^b_\mu(x)A^c_\nu(x)$ is the field strength tensor with $A^a_\mu(x)$ being the gluon fields whose quanta represent gluon particles. The upper index $a = 1, 2, \ldots, 8$ indicates the eight different color states of gluons. The totally antisymmetric tensor f^{abd} is the structure constant of the $SU(3)$ group. The coupling constant g measures the strength of strong interactions. The spinor fields ψ^C_i represent quarks with the color index $C = 1, 2, 3$ indicating the three color states of quarks. The subscript "i" indicates different types of quarks. There are six types of quarks. They are the six flavor states: up, down, charm, strange, top and bottom. Summation over all the quark flavors is understood in the Lagrangian. The γ^μ are Dirac γ-matrices and T^a_{CD} are the eight 3×3 matrices representing the generators of the $SU(3)$ group. Finally, each quark flavor has its own mass m_i.

There are two main properties of QCD. One is called "asymptotic freedom" [2, 3] which says that strong interactions between quarks and gluons become weaker and weaker as the interaction energy increases. Equivalently speaking, the strong coupling constant $g \equiv g(Q^2)$ is a monotonically decreasing function of the energy scale Q. The asymptotic freedom has been proved theoretically by perturbative QCD calculations and been verified by experimental data. Another property of QCD is called "quark confinement" which describes the fact that we have never been able to directly detect an individual colored quark or gluon.

Instead, what we detect are confined states of quarks that are color neutral and carry integer units of electric charges. These are the mesons (made of quark and antiquark pairs) and baryons (made of three quarks). There is no theoretical proof of quark confinement yet.

These two properties have deep and rich consequences. On the quark confinement side, considering a system of weakly interacting hadrons (mesons and baryons), when the number of particles are large and the system is close to equilibrium, it is reasonable to describe the system thermodynamically, thus the term hadronic matter. A crucial property of hadronic matter [4] is that as the energy of the system increases, the temperature reaches a limiting value called the Hagedorn temperature which has a value of about 160 MeV. Above the Hagedorn temperature, the hadronic matter becomes unstable and the description in terms of a system of hadrons becomes invalid. Shortly after the idea of asymptotic freedom was introduced, two independent groups [5, 6] realized that it is possible to form deconfined states of quarks and gluons at very high temperature or very large density. This new state of matter at high temperature is now known as Quark-Gluon Plasma (QGP) while on the high density extreme it is called quark matter. What are the properties of these phases? What are the phase boundaries among different phases and what are the order of phase transitions? These are the main themes in the fields of QCD at high temperature and high density and the heavy-ion collision physics. A conjectured schematic picture showing possible phases of QCD and phase transitions is given in Fig. 1.1. (see also [7, 8])

For $\mu_B = 0$, it has been found by lattice QCD calculation [9] that the transition from the quark-gluon plasma phase to the hadronic phase is a smooth, rapid
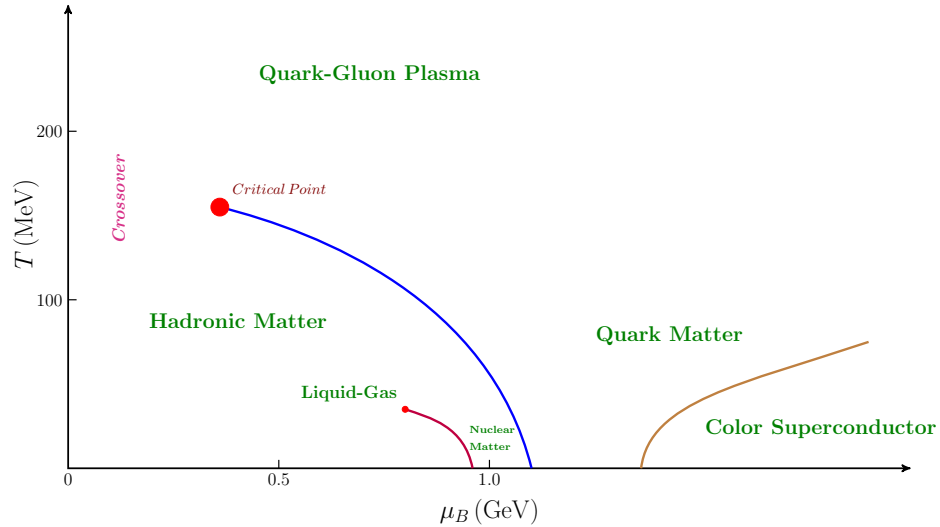
Figure 1.1: Conjectured phase diagram of QCD.

crossover and happens around temperature $T_c \sim 160 \, \text{MeV}$. The lattice QCD approach, which numerically solves the QCD thermodynamics on discrete Euclidean space-time grids, has its intrinsic problem, known as sign problem, in extending the baryon chemical potential μ_B to non-zero values. Therefore, a definite conclusion about phase transitions at finite values of baryon chemical potential has not been obtained by the lattice QCD approach up to now (see the review in [10]). On the other hand, at very low temperature T but large values of baryon chemical potential μ_B, several theoretical studies indicate that the phase transition is first order [7, 8]. It is therefore expected that the first order phase transition line ends somewhere on the phase diagram at a critical point. However, the existence and location of the critical point has not been verified by experimental data, nor has the first order phase transition line.

Apart from its own interest in exploring strongly interacting matter at extreme conditions, the phase diagram of QCD is also relevant to the evolution of our

Universe and to revealing the inner structure of astrophysical objects like neutron stars. It is believed that after several microseconds after the big bang, the Universe was in a state similar to the quark-gluon plasma state with a tiny amount of net baryon charge and a transition to the hadronic phase happens as the Universe cools. Inside the inner core of neutron star, it is conjectured that quark matter may exist.

1.2 Heavy-Ion Collisions and Quark Gluon Plasma

1.2.1 Discovery of Quark Gluon Plasma at RHIC

The Possibility of creating deconfined states of quarks and gluons in a laboratory setting by smashing heavy ions was suggested in the 1970s [11, 12, 13, 14]. The basic idea is to deposit a fraction of the kinetic energy as well as baryon charge from the colliding nuclei into a limited volume. When the energy density deposited is high enough a thermalized state with large numbers of deconfined quarks and gluons may be produced. In particular, Bjorken [15] argued theoretically that in ultra-relativistic heavy-ion collisions, quark-gluon plasma with almost zero baryon charge can be formed in the central region (around the collision point) and he studied the subsequent space-time evolution of the matter using hydrodynamics. Over the years, heavy-ion accelerators with increasing collision energies have been built, from the Bevalac at LBNL with the center-of-mass energy per nucleon pair $\sqrt{s_{NN}} \approx 1\,\text{GeV}$, to the AGS at BNL with $\sqrt{s_{NN}} = 5\,\text{GeV}$, the SPS at CERN with $\sqrt{s_{NN}} = 17\,\text{GeV}$, the RHIC at BNL with $\sqrt{s_{NN}} \leq 200\,\text{GeV}$ and the LHC at CERN with $\sqrt{s_{NN}} \leq 5.02\,\text{TeV}$. In 2005, the four experiments at RHIC reported

strong evidence for the formation of quark-gluon plasma in the collision of Au-Au at $\sqrt{s_{NN}} = 200\,\text{GeV}$ [16, 17, 18, 19].

The central experimental observable in heavy-ion collisions is the particle momentum spectrum $\frac{dN_i}{dy\,p_T\,dp_T\,d\phi}$ for particle species i with transverse momentum p_T, azimuthal angle ϕ and momentum-space rapidity $y = \frac{1}{2}\ln\frac{E+p_z}{E-p_z}$. The p_z is the longitudinal (along the beam direction) momentum of the particle and $E = \sqrt{p_z^2 + p_T^2 + m_i^2}$ is the corresponding energy for a particle with mass m_i. The azimuthal angle is defined relative to the reaction plane which is the plane spanned by the beam axis and the impact parameter vector between the two colliding nuclei. In realistic experimental detectors, especially for large values of rapidity y, it is difficult to identify the particle species as these particles are traveling in directions close to the beam direction. As a consequence, the information on m_i is difficult to extract for large rapidity y. Instead, experimentalists measure the pseudorapidity distribution $\frac{dN_i}{d\eta\,p_T\,dp_T\,d\phi}$ with $\eta = -\ln\left[\tan\left(\theta/2\right)\right] = \frac{1}{2}\ln\frac{|\mathbf{p}|+p_z}{|\mathbf{p}|-p_z}$. The magnitude of the three-momentum is $|\mathbf{p}| = \sqrt{p_T^2 + p_z^2}$ and the angle θ measures the relative angle to the beam direction.

Depending on the value of the transverse momentum, the particles observed can be classified as "soft" (low-p_T, typically $p_T \leq 2.0\,\text{GeV}$) and "hard" (high-p_T, typically $p_T > 2.0\,\text{GeV}$). Most of the particles observed are low-p_T particles [20]. The first evidence in favor of the creation of quark-gluon plasma is the charged particle pseudorapidity distribution $dN_{\text{ch}}/d\eta$, see Fig. 1.2 taken from the PHOBOS collaboration of RHIC. The 0-6% centrality bin represents the most central collisions with an impact parameter close to zero while larger values mean larger impact parameters. The quantity $dN_{\text{ch}}/d\eta$ is a measure of the entropy

density at the freeze-out (the moment when the particles cease interaction and fly to the detector). It can be used to estimate a lower limit on the initial energy density. With the help of Bjorken's space-time picture of high energy collisions [15], the estimated lower limit of the initial energy density is $\varepsilon \approx 5\,\mathrm{GeV/fm}^3$ [16, 17] which is about five times larger than the predicted critical energy density for QGP formation from lattice QCD calculations. The fact that a large number of particles are produced hints a new state of matter with very high energy density has been created.
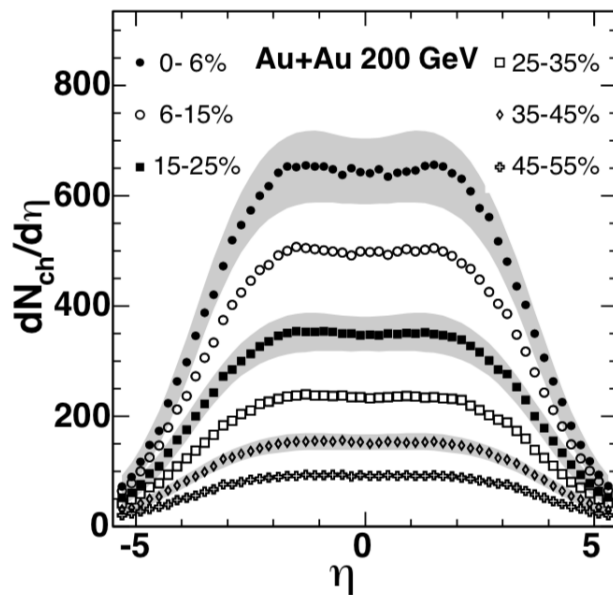
Figure 1.2: Charged particle pseudorapidity distribution of different centralities for Au-Au at $\sqrt{s_{NN}} = 200\,\mathrm{GeV}$. Figure is adapted from [17].

The second piece of evidence is the observed hadron yields and hadron yield ratios, see Fig. 1.3. The hadron yields and hadron yield ratios can be successfully described by a thermal statistical model which assumes the system is in thermal

and chemical equilibrium before the chemical freeze-out (the moment when inelastic collisions of particles cease). In the grand-canonical ensemble, only three parameters, the temperature T, the baryon chemical potential μ_B and the volume of the system V are needed. Fitting the experimental data gives the chemical freeze-out temperature $T_{\mathrm{ch}} = 162\,\mathrm{MeV}$ and the baryon chemical potential $\mu_B = 24\,\mathrm{MeV}$. The explanation of the hadron yields and hadron yield ratios suggests that a thermally and chemically equilibrated state has been formed.
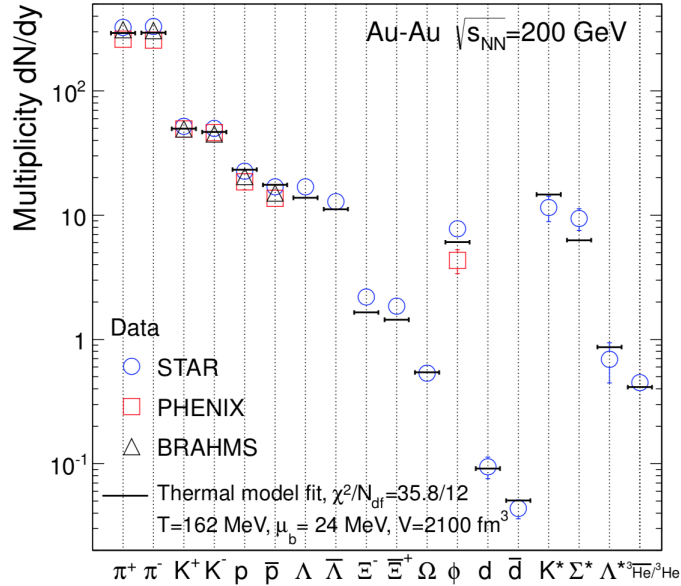
Figure 1.3: The observed hadron yields of different species and the thermal statistical model fitting for Au-Au at $\sqrt{s_{NN}} = 200\,\mathrm{GeV}$. Figure is adapted from [22].

The third piece of evidence is the anisotropic collective flow. The azimuthally angular distribution in the particle momentum spectrum can be decomposed as a

series of Fourier components

$$\frac{dN}{dy\,p_T dp_T d\phi} = \frac{1}{2\pi}\frac{dN}{dy\,p_T dp_T}\left(1 + 2\sum_{n=2} v_n \cos n\phi\right). \qquad (1.2)$$

Here reflection symmetry with respect to the reaction plane is assumed so that sine functions of the azimuthal angle do not contribute. For central collisions (impact parameter $b = 0$) all $v_n = 0$ in the absence of fluctuations. For non-central collisions (impact parameter $b \neq 0$), the flow coefficients appear, in particular the elliptic flow term whose strength is characterized by the coefficient v_2. The momentum space anisotropy characterized by v_2 carries information about the early time coordinate space anisotropy of the fireball. For non-central collisions, the reaction zone is almost like in shape so that the pressure gradient in the reaction plane is larger than the pressure gradient perpendicular to the reaction plane. The different flow strengths reveal themselves in particle correlations. Figure 1.4 shows the elliptic flow coefficient v_2 as an increasing function of the transverse momentum p_T for identified hadrons. The value of v_2 is found to be inversely related to the mass of the hadron in the low-p_T region. Hydrodynamic modeling of the high energy density matter provides a very successful explanation of the experimental data of the elliptic flow [26, 27]. The applicability and success of the hydrodynamics indicates that a locally equilibrated thermal state was formed. The partonic nature of this thermalized state is further revealed by Fig. 1.5. In this figure, the elliptic flow is scaled by the number of valence quarks inside the hadrons and it is ploted as a function of the transverse kinetic energy $KE_T = \sqrt{p_T^2 + m^2}$.

The fourth piece of evidence is related to the high-p_T part of the hadron spectrum, specifically the high-p_T hadron suppression phenomena in high energy
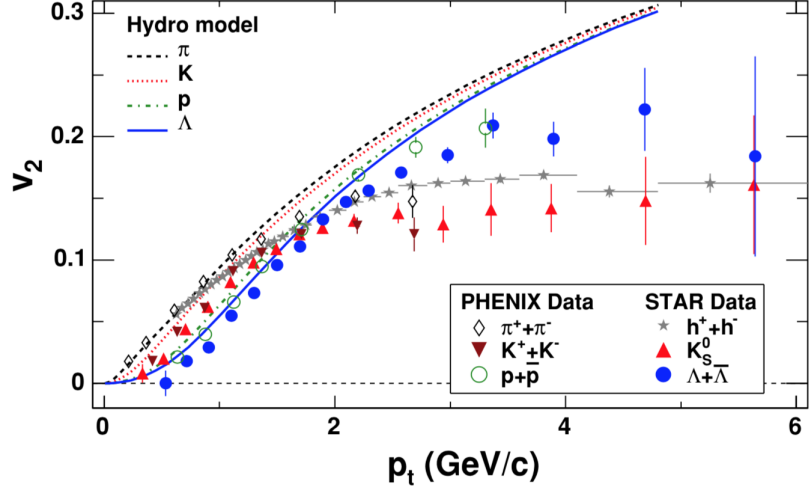
Figure 1.4: The elliptic flow coefficient v_2 as a function of the transverse momentum p_T for identified hadron species. The figure is adapted from [24].
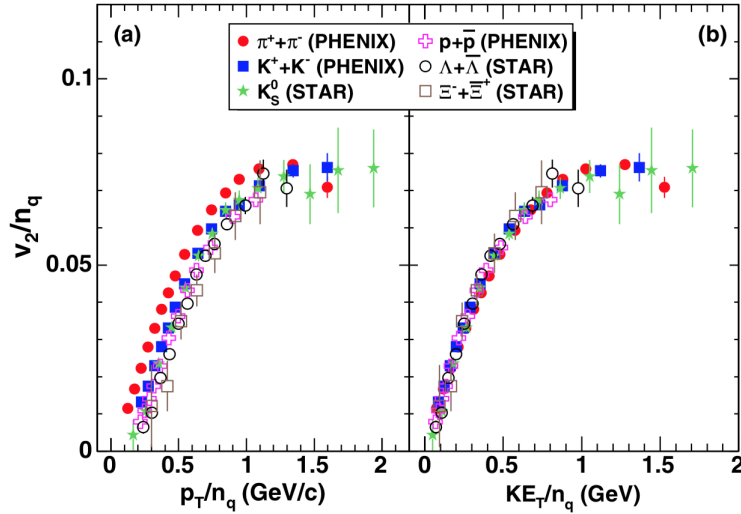
Figure 1.5: The scaled elliptic flow coefficient v_2 as a function of the transverse kinetic energy KE_T for identified hadron species. The scale factor is the number of valence quarks inside the hadrons n_q. The figure is adapted from [25].

heavy-ion collisions. The high-p_T part of the observed hadron production is suppressed by the existence of medium effects. The experimentally measured quantity is the nuclear modification factor R_{AA}

$$R_{AA}(p_T, y) = \frac{d^2 N^{AA}/dp_T^2 dy}{\langle N_{\text{bin}} \rangle d^2 N^{pp}/dp_T^2 dy}.$$ (1.3)

The nuclear modification factor R_{AA} represents the suppression effect of particle production in a nucleus-nucleus collision as compared to the scaled particle production from a proton-proton collision. Here the normalization factor $\langle N_{\text{bin}} \rangle$ characterizes the number of binary nucleon-nucleon collisions in a given nucleus-nucleus collision. If there are no medium effects, the nucleus-nucleus collision is simply a collection of incoherent nucleon-nucleon collisions and the nuclear modification factor is $R_{AA} = 1$. If there is a medium present, the high-p_T particles would lose energy as they traverse through it resulting in less particles at that momentum. Figure 1.6 shows the nuclear modification factors for direct γ, π^0 and η. Photons do not carry color charge and therefore experience no suppression effects as they propagate through the colored medium. On the other hand, hadrons like π^0 and η originating from high-p_T colored partons experience large suppression as they traverse the medium. The solid line is from theoretical fitting using the GLV parton energy loss mechanism [29]. The experimental results of R_{AA} indicate the formation of a dense medium that is opaque to high-p_T partons.

The combined experimental data of the bulk particle production, hadron yields at chemical freeze-out, anisotropic collective flows and jet quenching provide strong evidence for the creation of quark-gluon plasma in high energy heavy-ion collisions at RHIC. These experimental observations are further corroborated at even higher collision energies at the LHC (Pb+Pb at $\sqrt{s_{NN}} = 2.76\,\text{TeV}$ and
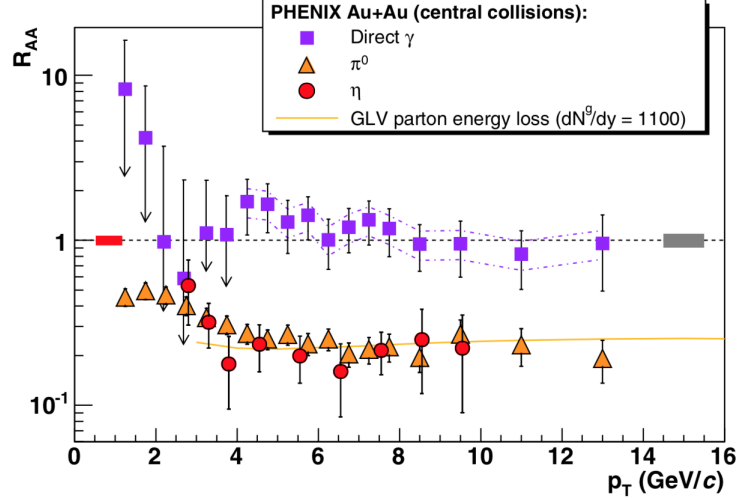
Figure 1.6: The nuclear modification factor R_{AA} as a function of transverse momentum for direct γ, π^0 and η in Au-Au central collisions at $\sqrt{s_{NN}} = 200\,\text{GeV}$. The figure is adapted from [28].

$\sqrt{s_{NN}} = 5.02\,\text{TeV}$). The successful agreement between the elliptic flow data and predictions from hydrodynamic modeling leads people to believe that the quark-gluon plasma created at RHIC is actually strongly coupled quark-gluon plasma (sQGP) with a very small value of viscosity to entropy density ratio [32, 33], making it among the most perfect fluids in nature. This is different from what people have anticipated, a weakly coupled quark-gluon plasma at very high temperature when QCD is in the perturbative regime.

1.2.2 Search for Critical Point and Beam Energy Scan

Quark-gluon plasma created in the midrapidity region ($\eta \sim 0$) in Au+Au collision at the top RHIC collision energy $\sqrt{s_{NN}} = 200\,\text{GeV}$ contains very small net baryon charge. The estimated baryon chemical potential at chemical freeze-out is $\mu_B \approx$

20 MeV. Most of the baryon charges are carried away by the receding nuclei after the collision. At very small baryon chemical potential, the change from quark-gluon plasma to hadronic matter turns out to be a rapid and smooth crossover [9]. To explore the conjected first order phase transition and the possible critical point of the QCD phase diagram, quark-gluon plasma with large values of baryon chemical potential have to be created. The Beam Energy Scan (BES) program at RHIC, which performs a series of low energy Au+Au collisions, pursues this goal. The BES Phase-I has collided Au+Au nuclei at center-of-mass collision energies from 7.7 GeV to 200 GeV with the estimated baryon chemical potential ranging from 20 MeV to 420 MeV as detailed in Table 1.1 [34]. These baryon chemical potentials are estimated by fitting the hadron yields at chemical freeze-out using the thermal statistical model discussed before. By scanning through the collision energy, the BES experiment aims to locate the threshold collision energy below which the established experimental signals for quark-gluon plasma formation (elliptic flow, jet quenching, et al) are turned off. In search for the first order phase transition, when thermodynamic quantities have discontinuities, signatures related to the softening of the equation of state like a minimum in the radial flow rapidity derivative dv_1/dy at midrapidity when varying the collision energy was proposed [35, 36] and measured by the STAR collaboration of RHIC [37]. Finally, measurements on locating the critical point are focused on the large fluctuations of conserved charges like net electric charge, net baryon charge and net strangeness near the critical point [38, 39, 40, 41].

The BES Phase-I has found encouraging evidence for the onset of QGP, the first order phase transition and the critical point by varying the collision energy

$\sqrt{s_{NN}}$ (GeV)	μ_B (MeV)
7.7	420
11.5	315
14.5	260
19.6	205
27	155
39	115
62.4	70
200	20

Table 1.1: Collision energies at the center-of-mass frame $\sqrt{s_{NN}}$ and the correspondingly estimated baryon chemical potential μ_B.

[37, 41, 42]. However, the data suffers large uncertainties, and higher statistics are needed to give definite answers. The second stage of the BES program, aiming to increase data statistics, will be running in 2018 and 2019 focusing on the low collision energy region $7.7\,\text{GeV} \leq \sqrt{s_{\text{NN}}} \leq 19.6\,\text{GeV}$. If, unfortunately, the critical point is beyond $\mu_B = 420\,\text{MeV}$, the BES will switch to the fixed-target mode by injecting stationary gold targets into the beam pipe. This way, even lower center-of-mass collision energies can be achieved $\sqrt{s_{NN}} = 3.0, 3.2, 3.5, 3.9$ and $4.5\,\text{GeV}$. The largest possible baryon chemical potential in the fixed-target mode is around $\mu_B = 720\,\text{MeV}$. Finally, there are other ongoing experiments in parallel to the RHIC BES program that are also aiming to search for the first order phase transition and the critical point. They are the NA61/SHINE fixed-target experiment at CERN SPS [43], the HADES/SIS18 [44] in the collider mode at GSI Helmholtz Center for Heavy Ion Research in Darmstadt, Germany. In addition, the CBM experiment [45] at FAIR in Darmstadt, Germany, the BM@N experiment at NICA [46] in Dubna, Russia and the J-PARC-HI project [47] in Japan are under planning and construction. These experiments are all performed

in the regime of low center-of-momentum collision energy.

1.3 Nuclear Compression in High Energy Heavy-Ion Collisions

1.3.1 Baryon Stopping

The experimental finding that at very high collision energy, QGP formed in the midrapdity region has very small baryon charges while at low collision energy, QGP formed in the midrapidity region has large baryon charges reveals one important difference between heavy-ion collisions at high collision energy and at low collision energy. This observation is supported by different baryon chemical potentials at the chemical freeze-out extracted from the thermal statistical model in fitting hadron yields and hadron yield ratios. On the other hand, direct evidence from measuring the baryon stopping power, the net baryon rapidity distribution dN_B/dy as a function of collision energy, also confirms this observation. Figure 1.7 shows the net proton rapidity distributions measured at three different collision energies. Baryon number is a conserved quantity in heavy-ion collisions. The total number of baryon charges equals the total number of nucleons inside the two colliding nuclei before the collision. The net proton rapidity distribution is what can be directly measured experimentally since neutral particles that carry baryon charge like neutrons are difficult to measure. From Fig. 1.7, we see net protons are piled up around the central rapidity region $y \sim 0$ at low collision energy. As the collision energy increases, net protons are gradually piled up around the forward/backward rapidity region leaving smaller and smaller number of net

protons in the central rapidity region. Before the collision, all the protons have initial rapidity y_p. If the final rapidities of net protons after the collision are close to $y = 0$, then net protons are fully stopped during the collision. If, on the other hand, the final rapidities of net protons after the collision are close to $y = y_p$, then net protons are transparent during the collision. Schematic figures of nuclear stopping and nuclear transparency are shown in Fig. 1.8 and Fig. 1.9.
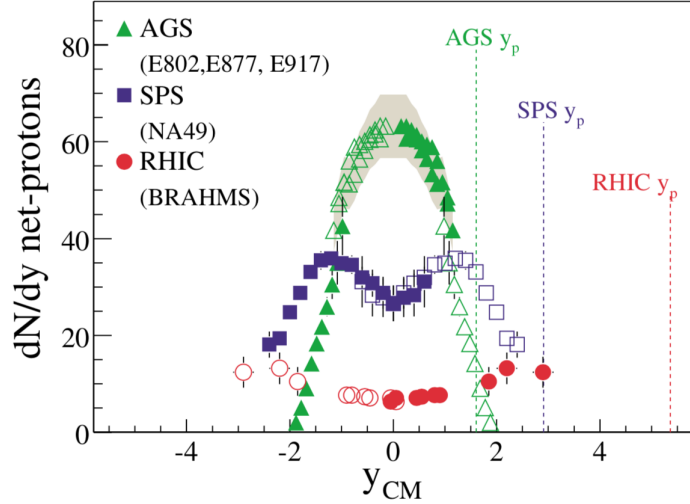
Figure 1.7: Net-proton rapidity distribution from AGS (Au+Au at $\sqrt{s_{NN}} = 5\,\text{GeV}$), SPS (Pb+Pb at $\sqrt{s_{NN}} = 17\,\text{GeV}$) and RHIC (Au+Au at $\sqrt{s_{NN}} = 200\,\text{GeV}$). The initial beam rapidity y_p are shown by the dashed vertical lines. Here y_{CM} is the rapidity measured in the center-of-momentum frame. Figure is adapted from [48].

Nuclear stopping measurements tells us two different phase space regions where baryons are located depending on the collision energy. At low collision energy, most of the baryons are located around the central region while at high collision energy, most of the baryons are located around the fragmentation regions. Here

$$v_i \rightarrow \qquad v_i \leftarrow \qquad v_f \approx 0$$

Before Collision   *After Collision*
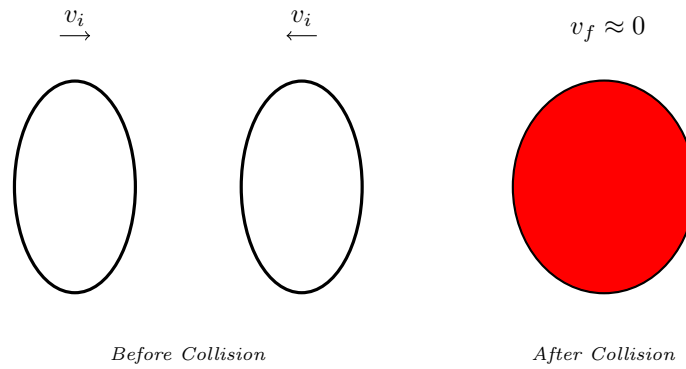
Figure 1.8: Schematic illustration of *baryon stopping* in low energy heavy-ion collisions. Colliding nuclei are moderately Lorentz contracted before collision and come to a stop, merging together after collision. QGP is formed in the overlapped region.

$$v_i \rightarrow \qquad v_i \leftarrow \qquad v_f \leftarrow \quad v_f \rightarrow$$

Before Collision   *After Collision*
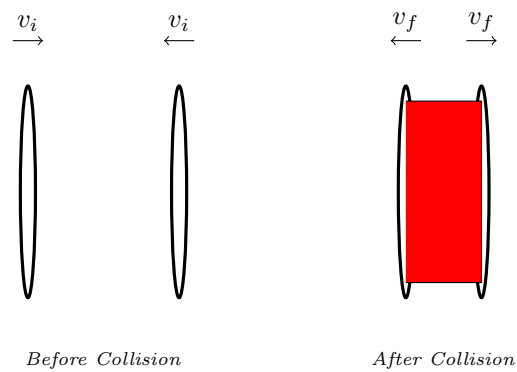
Figure 1.9: Schematic illustration of *baryon transparency* in high energy heavy-ion collisions. Colliding nuclei are highly Lorentz contracted before collision and pass through each other after collision. QGP is formed in the central region.

the central region means rapidities are close to zero in the center-of-momentum frame while the fragmentation regions mean rapidities are close to the original beam rapidity. Both regions are in momentum space rather than coordinate space. As a consequence, if one would like to probe the QCD phase diagram at finite baryon density using heavy-ion collisions, one can either collide heavy ions at low collision energy and focus on observables at the central region or collide heavy ions at high collisional energy and focus on observables at the fragmentation regions. The former idea is extensively exploited by the Beam Energy Scan at RHIC and other ongoing experiments. The latter idea however has been overlooked. There are two main reasons for this. First, early theoretical estimations on the energy density achievable in the fragmentation regions of high energy heavy-ion collisions ($\sqrt{s_{NN}} \sim 30\,\text{GeV}$) give relatively smaller values [50, 51, 52, 53] while energy density in the central region of high energy collisions is estimated to be much larger [15]. Second, in the collider mode, measuring particle production from the central region is easier while particles produced from the fragmentation regions are difficult to identify because they are traveling in directions close to the beam directions.

Nowadays, high energy heavy-ion collisions are common, from the top RHIC collision energy $\sqrt{s_{NN}} = 200\,\text{GeV}$ to the LHC operational energies $\sqrt{s_{NN}} = 2.76\,\text{TeV}$ and $\sqrt{s_{NN}} = 5.02\,\text{TeV}$. Energy densities achievable in the fragmentation regions should be much larger than early estimates. In addition, our theoretical understanding of the initial stage of high energy heavy-ion collisions has been very much advanced, focusing more and more on partonic degrees of freedom in contrast to nucleonic degrees of freedom. We therefore would like to put the study of

the fragmentation regions of high energy heavy-ion collision in a modern context and ask the question of what baryon density and energy density could be achieved in the fragmentation regions. This will be the theme of the thesis. These questions might also be interesting to astrophysics, particularly neutron star physics, as compressed nuclear matter is involved.

1.3.2   Nuclear Compression at High Collision Energy

In high energy heavy-ion collisions, there exist two paradigms concerning the space-time picture of the collisions. One is Bjorken's paradigm [15] that describes the collision in the Center-of-Momentum Frame (CMF). A schematic picture is shown in Fig. 1.9. Before the collision, the colliding nuclei are highly Lorentz contracted so that they look like pancakes for observers in the CMF. The two pancakes pass through each other and deposit energy in the central region due to strong interactions. The deposited energy comes from kinetic energy losses of the colliding nuclei. When the energy density in the central region is larger than the critical energy density, quark-gluon plasma can be formed. Bjorken's paradigm concerns the central region where the quark-gluon plasma created has very small baryon charge while ignoring the fragmentation regions where most of the baryon charges are carried by the receding nuclei. This paradigm has become the standard space-time picture of high enery heavy-ion collisions at high collision energies attainable at RHIC and LHC.

The other paradigm is due to Anishetty, Koehler and McLerran (AKM) [50] that describes the collision process in the Target Rest Frame (TRF). A schematic picture is shown in Fig. 1.10. In the target nucleus's rest frame, the projectile

nucleus is highly Lorentz contracted due to its high collision energy. The projectile nucleus travels at a speed close to the speed of light, sweeps through the target nucleus, imparts energy and momentum into the target nucleus and compresses the target nucleus. If the collision energy is high enough, the projectile nucleus will be separated from the target nucleus after the collision. During the collision, part of the kinetic energy loss of the projectile nucleus is deposited in the target nucleus. Enhanced by the nuclear compression, the energy density deposited in the target nucleus could be large enough that quark-gluon plasma may be formed in the target nucleus, which is called the target fireball. Similarly, projectile fireball is also formed at the same time when considering the collision in the projectile rest frame. Quark-gluon plasma in the fireball has very large baryon density in contrast to the quark-gluon plasma formed in the central region from Bjorken's paradigm. Furthermore, fireballs have momentum space rapidity close to the initial rapidities of the target nucleus and projectile nucleus, respectively. Therefore, the baryon-rich fireballs are said to be formed in the fragmentation regions. It is worth noting that the central region is also shown as the region between the projectile fireball and the target fireball after the collision in the space-time picture of AKM's paradigm illustrated by Fig. 1.10.

Nuclear compression in AKM's paradigm is estimated as follows [50, 51]. Considering the target nucleus as a system of nucleons, as the the projectile nucleus sweeps through the target nucleus, it gives each target nucleon a kick. The first nucleon encountered by the projectile receives an average velocity v_F and moves along the same direction as the projectile nucleus inside the target nucleus. Before the projectile nucleus kicks the second nucleon along its way, the first nucleon
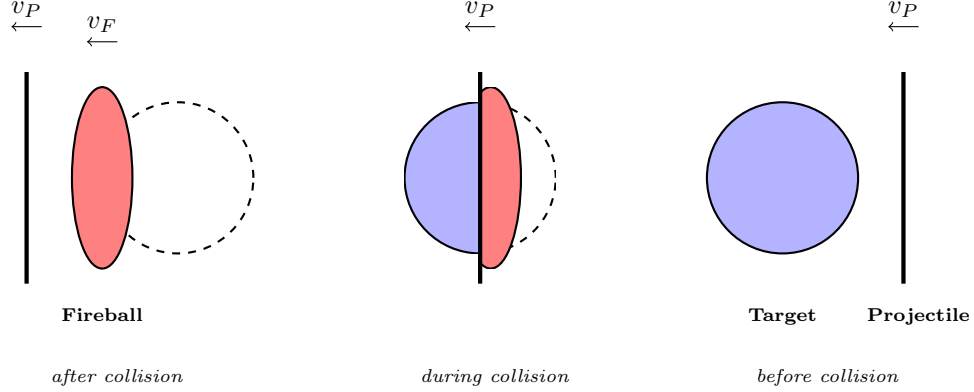
Figure 1.10: Schematic space-time picture of nuclear compression in high energy heavy-ion collisions viewed in the target rest frame.

moves towards the second nucleon a distance $v_F(\Delta x/v_P)$. Here Δx is the original distance between the two nucleons considered; v_P is the velocity of the projectile and v_F is the average velocity each nucleon in the target nucleus received after being struck by the projectile nucleus. As a consequence, the distance between the two nucleons is reduced to $\Delta x(1 - v_F/v_P)$. This is the reduction of inter-nucleon distance viewed in the TRF; the reduction viewed in the local rest frame of the target fireball is compensated by a Lorentz factor $\gamma_F = 1/\sqrt{1 - v_F^2}$. Finally, the inter-nucleon distance inside the target fireball as viewed in the local rest frame of the fireball is

$$\Delta x' = \Delta x \, \frac{1 - v_F/v_P}{\sqrt{1 - v_F^2}} \simeq \Delta x \sqrt{\frac{1 - v_F}{1 + v_F}}. \tag{1.4}$$

In the second equality, we used the fact that at high collisional energy, the velocity of the projectile nucleus is very close to the speed of light $v_P \simeq 1$. In terms of momentum space rapidity y_F which is defined as $v_F = \tanh y_F$, also considering that the initial velocity of the target nucleus is zero, the nuclear compression effect

can be expressed as a Lorentz invariant scalar

$$\frac{\Delta x'}{\Delta x} = e^{-y_F} \equiv e^{-\Delta y}. \tag{1.5}$$

Here Δy is the increase of rapidity for the target nucleus after the projectile sweeps through it. It has the value y_F when viewed in the TRF. The nuclear compression formula Eq. (1.5) had also been confirmed in [53] by modeling the target nucleus as a fluid and the interaction between the projectile and the target as color flux tube. Equation (1.5) relates the nuclear compression effect to baryon stopping in high energy heavy ion collisions. It is therefore fair to say that baryon stopping implies nuclear compression in high energy heavy-ion collisions. Furthermore, Eq. (1.5) is invariant under Lorentz boosts along the beam direction; calculations of the rapidity change Δy can be done in the CMF as well as the TRF. With the nuclear compression, one can further estimate the baryon density in the fireball after collision by

$$n(\mathbf{r}_\perp, z) = e^{\Delta y} \rho_A(\mathbf{r}_\perp, z\, e^{\Delta y}) \tag{1.6}$$

The expression is understood in the local rest frame of the fireball. Here ρ_A is the nuclear density distribution of the atomic nucleus usually parameterized by the Woods-Saxon distribution [54]. The z is the longitudinal coordinate and $\mathbf{r}_\perp = (x, y)$ are the tranverse coordinates. They are all defined relative to the center of the fireball. The exponential of rapidity change $e^{\Delta y}$ determines both the enhancement of the baryon density and the compression of the nuclear profile.

In AKM's paradigm, excitation energy inside the fireball is estimated by considering secondary particles produced in inelastic nucleon-nucleon collisions as the projectile sweeps through the target. This excitation energy, together with the nuclear compression effect, gives the energy density inside the fireball. It is worth

pointing out that Eq. (1.5) represents a kinematic compression. The target nucleus also got excited along with the compression as the projectile sweeps through it. Nuclear compression changes inter-nucleon distances which result in changes of the potential energy between nucleons. In the body of the thesis, we will estimate the rapidity change in the center-of-momentum frame instead of the target rest frame. We model the central region using the Color Glass Condensate (CGC) framework and consider the interaction of the central region and the fragmentation regions. In this analysis, the CGC framework not only provides the rapidity change in high energy heavy-ion collisions, but also gives excitation energy as the amount of energy interchanged between the central region and the fragmentation regions. If the energy density is large enough it is possible that baryon-rich quark-gluon plasma may be formed in the fragmentation regions. Therefore, exploring the baryon-rich QGP in the fragmentation regions of high energy heavy-ion collisions may provide an alternative to studying the QCD phase diagram as compared to the baryon-rich QGP at the central region of low energy heavy-ion collisions.

1.4   Outline

In this thesis, we estimate the baryon density and the energy density in the fragmentation regions of high energy heavy-ion collisions. When the energy density and baryon density are large enough, we assume baryon-rich quark-gluon plasma are formed in the fragmentation regions. The subsequent space-time evolution of the baryon-rich quark-gluon plasma in the fragmentation regions in combination with the almost baryon-free quark-gluon plasma in the central region are studied using fluid dynamics. The outline of this thesis is as follows:

- To obtain the rapidity change in the center-of-mass frame, in Chapter 2, we focus on the central region. In high energy heavy-ion collisions, the initial stage in the central region is effectively described by classical gluon fields in the framework of Color Glass Condensate (CGC). The time evolution of the nonequilibrium system at the central region is thus governed by the classical Yang-Mills equations with initial (boundary) conditions. After a short review of the CGC framework, the classical Yang-Mills equations are solved by assuming the solutions having the form of a power series expansion in proper time. The Energy-momentum tensor of the classical gluon fields is then calculated under the leading Q^2 approximation, and its features are discussed.

- In Chapter 3 , we compute the rapidity change in the center-of-momentum frame for Au+Au collision at $\sqrt{s_{NN}} = 200\,\mathrm{GeV}$. The classical gluon fields in the central region and the receding nuclei at the fragmentation regions are treated as one single system. Energy and momentum conservation are imposed on this system, requiring the energy and momentum losses of the receding nuclei equal to the corresponding energy and momentum increases of the classical gluon fields. We are able to obtain the rapidity changes as well as the excitation energy of the fireballs. We then estimate the baryon density and energy density achieved in the fragmentation regions of Au+Au collision at $\sqrt{s_{NN}} = 200\,\mathrm{GeV}$. We further study asymmetric collisions like Au+Cu and collisions between deformed nucleus like Uranium nuclei. The collision energy and collision centrality are also varied to explore different collision configurations.

- The baryon density in central Au+Au collision at $\sqrt{s_{NN}} = 200\,\mathrm{GeV}$ is found to be more than ten times larger than normal nuclear density and the energy density is found to be much larger than the critical density for the formation of quark-gluon plasma. In Chapter 4 , assuming thermalization is reached both in the central region and the fragmentation region, we perform 1+1D global hydrodynamic simulation for the space-time evolution of the baryon-rich QGP. Baryons are found to diffuse from the fragmentation regions to the central region. The relevance to the QCD phase diagram of studying the fragmentation regions at high collision energy is discussed.

Chapter 2

Energy-Momentum Tensor of Glasma

2.1 Introduction

In high energy heavy-ion collisions as viewed in the center-of-momentum frame, the two colliding nuclei are highly Lorentz contracted and propagate at speeds close to the speed of light. The pancake-like nuclei collide, pass through each other and recede away. At very short time ($\tau \lesssim 1.0\,\text{fm/c}$) after the collision, quark-gluon plasma is formed in the space-time region between the two receding nuclei, the so-called central region. As the system expands and cools, the quark-gluon plasma evolves in space and time until its temperature and density become low enough that deconfined quarks and gluons recombine into confined objects, the hadrons. The hadronic matter further expands and cools until individual hadron ceases interacting with each other. These final stable hadrons travel towards the

detectors and are registered as experimental signals. The above evolution is the standard space-time picture of high energy heavy-ion collisions in the collider mode such as RHIC and LHC.

In this chapter, we focus on the early time dynamics of high energy heavy-ion collisions, the time period after the collision but before the formation of quark-gluon plasma. In particular, we are interested in properties of the system in the central region and its space-time evolution. This very early stage at high collision energy can be effectively described within the Color Glass Condensate (CGC) framework [56, 57]. In this framework, the system in the central region is characterized as an overoccupied and strongly correlated soft gluon system whose effective description is by classical gluon fields. The space-time evolution of the system in the central region thus is governed by the classical Yang-Mills equations. As the system expands, the overpopulated soft gluon system eventually become dilute and decohered so that gluons are liberated as on-shell particles. This nonequlibrium gluon system (a mixture of fields and particles) before the formation of quark-gluon plasma is called Glasma (glass+plasma) [55]. To understand the property of the Glasma, the central issue then becomes solving the classical Yang-Mills equations with appropriate initial conditions. Once we have the solutions to the classical Yang-Mills equations, properties of the Glasma like the energy-momentum tensor can be readily computed. We will discuss a semi-analytic approach in solving the classical Yang-Mills equations in this chapter and also discuss the property of the energy-momentum tensor obtained using this approach.

The outline of this chapter is as follows. In Sec. 2.2, we briefly explain the Color

Glass Condensate framework, particularly the McLerran-Venugopalan model that will be used. Applications of the CGC framework to high energy heavy-ion collisions are discussed in Sec. 2.3 and the semi-analytic approach to solving the classical Yang-Mills equations is explained. In Sec. 2.4, the energy-momentum tensor of the Glasma is computed under the leading Q^2 approximation in this semi-analytic approach. Properties of the energy density and pressures of the central region are presented.

2.2   Color Glass Condensate

The Color Glass Condensate framework is an effective field theory used to describe the high energy limit of hadronic and nuclear wavefunctions [56, 57]. In the high energy limit, as viewed in the infinite momentum frame, the partonic contents of a hadron can be classified according to their fraction of the hadron's longitudinal momentum. Those carrying relatively large fractional longitudinal momentum are called fast partons (such as the valence quarks) and those carrying very small fractional longitudinal momentum are called wee partons (or small-x partons to be explained in the following). Fast partons, acting as color sources, radiate small-x partons through the bremsstrahlung process. As the longitudinal momentum of the hadron becomes larger and larger (high energy limit), the density of the small-x partons produced inside of the hadron becomes larger and larger and finally saturates to form a condensate. On the other hand, the fast partons look like static color sources due to the large time dilation from the view of the small-x partons. This resembles the behavior of a glass which is disordered and behaves like a solid in the short time and like a liquid in the long time. These considerations

are behind the terminology Color Glass Condensate.

2.2.1 Small-x Physics and Gluon Saturation

The internal structure of a hadron as a system of partons is probed in momentum space by two variables: Q, the transverse momentum scale, characterizes the transverse size of partons that it can distinguish; $x = p^+_{\text{parton}}/p^+_{\text{hadron}}$ represents the longitudinal momentum of the parton as a fraction of the hadron's longitudinal momentum. The light cone momentum is defined as $p^+ = (E + p^z)/\sqrt{2}$. See Appendix A for more on the light cone language. Experimentally, the parton distribution function $f(x, Q^2)$ inside a hadron is measured by deep inelastic scattering processes [1]. Fig. 2.1 shows the parton distribution functions of the proton measured at two different transverse momentum scales $Q^2 = 10\,\text{GeV}^2$ and $Q^2 = 10^4\,\text{GeV}^2$. Note the different symbol μ^2 in the figure used to represent the transverse momentum scale. There are two important features of the parton distribution function. First, gluons dominate the distribution at small x (note the gluon distribution is scaled down by a factor of ten in Fig. 2.1). Second, given a specific value of the transverse momentum scale Q^2, the distribution function increases very quickly with a decrease of x. However, the number of small-x gluons cannot increase forever as it will violate the Froissart bound [58] for the total cross section required by unitarity of the scattering matrix. In deep inelastic scattering, the x variable is also identified as the Bjorken variable $x_B = Q^2/2p \cdot q$ with the momentum transfer q^μ satisfying $q^2 = -Q^2$ and the four momentum of proton being p^μ. The Bjorken variable x_B is related to the center-of-momentum collision energy $\sqrt{s}$ by $x_B \sim Q^2/s$. Therefore, the small x regime corresponds to large

center-of-momentum collision energy. With increasing collision energy, the Frois-sart bound requires the total cross section to scale at most $\ln^2 \sqrt{s}$. However, the experimental data shows the gluon distribution function increases as a power law down to $x \sim 10^{-3}$. This power law behavior must be tamed at a certain energy scale. That's where the phenomena of gluon saturation [59, 60] emerges.
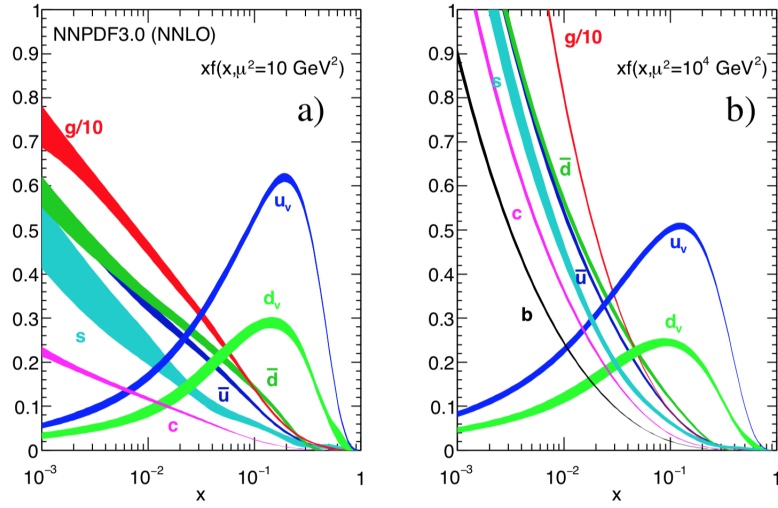
Figure 2.1: Parton distribution function of the proton for valence quarks, sea quarks and gluons. The magnitude of the gluon distribution is scaled down by a factor of ten. The two figures are for two different transverse momentum scales $Q^2 = 10 \, \mathrm{GeV}^2$ and $Q^2 = 10^4 \, \mathrm{GeV}^2$, respectively. Figure is adapted from [1].

Gluon saturation happens when the nonlinear effects of gluon fusion $g + g \rightarrow g$ start to balance the linear increase of gluon number from bremsstrahlung processes $g \rightarrow g + g$ and $q \rightarrow q + g$. Here g represents gluon and q represents quark. To be specific, as the number of gluons $xG(x, Q^2)$ increases, gluon fusion begins to play an important role at the moment when $\rho \, \sigma_{gg \rightarrow g} \sim 1$. The $\rho \sim xG(x, Q^2)/\pi R^2$ is the gluon number per unit area and $\sigma_{gg \rightarrow g} \sim \alpha_s(Q^2)/Q^2$ approximates the gluon fusion cross section. These relations determine a critical transverse momentum

scale Q_s, the saturation scale.

$$Q_s^2 \sim \frac{1}{\pi R^2}\, xG(x, Q_s^2). \tag{2.1}$$

The dynamically generated saturation scale Q_s is determined by the number of gluons per unit transverse area. It depends on the collision energy (the variable x) as well as the nuclear atomic number A for a nucleus. If the saturation scale is much larger than the Λ_{QCD} scale $Q_s^2(x, A) \gg \Lambda_{QCD}^2$, the coupling constant $\alpha(Q_s^2)$ becomes small and perturbative QCD methods can be used. We are therefore in the weakly coupling regime of QCD.
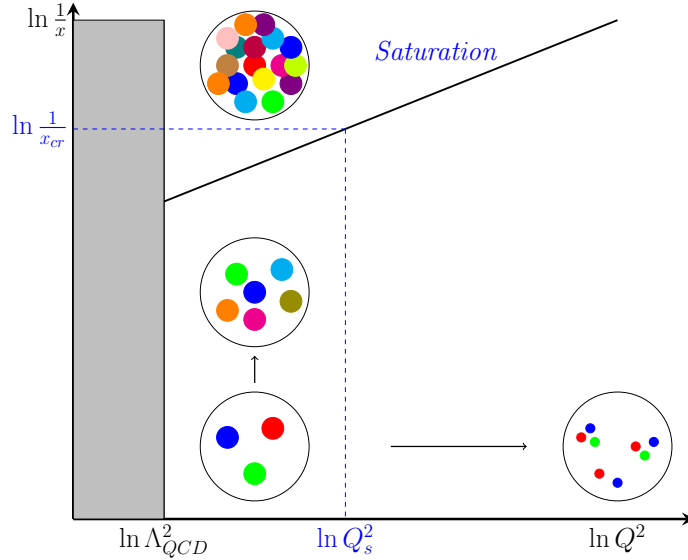
Figure 2.2: Schematic illustration of the parton distribution in the transverse plane as a function $\ln(1/x)$ and $\ln Q^2$. The black solid line represents the boundary between the dilute parton distribution and the saturated parton distribution

The above arguments in determining the transverse saturation momentum scale $Q_s^2(x, A)$ can also be used to determine a critical $x = x_{cr}(Q^2, A)$ as a function of the transverse scale Q^2 and the nuclear atomic number A. Figure 2.2 shows the

parton distributions in the transverse plane as a function of $\ln{(1/x)}$ and $\ln{Q^2}$. Given a specific value of x (fixing the collision energy), for larger and larger values of Q^2, one can probe smaller and smaller transverse size from the uncertainty principle $\Delta r_\perp \sim 1/Q$. On the other hand, for fixed value of Q^2, as we increase the collision energy (for smaller and smaller x), the number of partons with transverse size $1/Q$ increases and saturates when x is below x_{cr}. It is interesting to note that starting from the saturation regime, for fixed value of small x, as we increase the value of the transverse momentum scale Q^2, which is equivalent to zooming in our microscope, we see finer and finer transverse structure of the hadron and eventually we leave the saturation regime and enter the regime of a dilute parton distribution.

2.2.2 McLerran-Venugopalan Model

Now we turn to the effective field theory that describes the small-x part of the nuclear wavefunction which plays a dominant role in high energy collisions. Contributions from quarks can be ignored because their numbers are small compared to the gluon numbers in the small-x regime. Gluons dominate in the small-x regime. The saturated small-x gluon system can be approximately described by classical gluon fields [61, 62]. This is because when the occupation number of gluons in each momentum mode k becomes much larger than one $N_k \gg 1$, the difference between the ordering of creation and annihilation operators disappears $a_k^\dagger a_k \sim a_k a_k^\dagger \sim N_k$, we are in the classical regime. On the other hand, gluons and quarks that have relatively large values of x act as classical color sources radiating the small-x gluons. Therefore, the dynamical equation that describes the

small-x part of the nuclear wavefunction in the high energy limit is the classical Yang-Mills equation

$$[D_\mu, F^{\mu\nu}] = j^\nu. \tag{2.2}$$

Here the field strength tensor $F^{\mu\nu} = \partial^\mu A^\nu - \partial^\nu A^\mu - ig[A^\mu, A^\nu]$ and the covariant derivative $D_\mu = \partial_\mu - igA_\mu$. The classical gluon fields $A_\mu = A_\mu^a T^a$ describe the saturated gluon system. The color current $j^\nu = j^{a,\nu} T^a$ which comes from partons with large values of x needs further elaboration. First of all, the color current can be parameterized as

$$j^{a,\mu}(x) = \delta^{\mu+}\rho^a(x^-, \mathbf{x}_\perp). \tag{2.3}$$

Only the light cone "+" component of the color current is nonvanishing because the fast partons move along the light cone direction x^+. In addition, the color density $\rho^a(x^-, \mathbf{x}_\perp)$ does not rely on the light cone time coordinate x^+ as the fast partons look like static color sources to the small-x gluons due to time dilation. To be more precise, the lifetime of partons inside a nucleus can be estimated by the uncertainty principle using light cone variables: $\Delta x^+ \sim 1/\Delta k^- \sim 1/k^- = 2k^+/k_T^2 = 2xP^+/k_T^2$. Partons are assumed to be massless and have similar transverse momenta. Larger value of x means a longer lifetime. Fast partons have much longer lifetimes than small-x gluons. Within the lifetime of small-x gluons, fast partons are approximately static color sources. Second, the color density $\rho^a(x^-, \mathbf{x}_\perp)$ is a random field variable whose probability distribution is incorporated in a functional $W_\Lambda(\rho)$. Here Λ indicates the cut-off scale that separates the large x partons as color sources and the small x gluons produced by the color sources. The general probability distribution functional $W_\Lambda(\rho)$ satisfies a renormalization group equation called the JIMWLK equation [63, 64, 65, 66]. In the

McLerran-Venugopalan model [61, 62], the probability distribution functional is assumed to have a Gaussian form

$$W_\Lambda(\rho) = \mathcal{N} \exp\left\{ -\frac{1}{2} \int dx^- d^2\mathbf{x}_\perp \frac{\rho^a(x^-, \mathbf{x}_\perp)\rho^a(x^-, \mathbf{x}_\perp)}{\lambda(x^-, \mathbf{x}_\perp)} \right\}. \qquad (2.4)$$

Here $\lambda(x^-, \mathbf{x}_\perp)$ represents the spatially-dependent Gaussian width of the color charge fluctuations. Equations 2.2 -2.4 complete the effective theory of the McLerran-Venugopalan model. Given a color density $\rho^a(x^-, \mathbf{x}_\perp)$, one first solves the classical Yang-Mills equations. Then a statistical average over the Gaussian probability distribution has to be performed to obtain event-averaged physical quantities.

2.3 Nucleus-Nucleus Collisions in the CGC Framework

In high energy nucleus-nucleus collisions, the two colliding nuclei are propagating at speeds close to the speed of light in the center-of-momentum frame. They are highly Lorentz contracted and can be approximated as infinitely thin nuclear sheets after ignoring the longitudinal structures of the colliding nuclei. In the CGC framework, the wavefunction of each nucleus is dominated by the small-x gluons and is represented by the classical gluon fields. Therefore, the nucleus-nucleus collision at high energy is effectively the collision of two color glass condensates. Assuming the collision happens at space-time point $t = 0$ and $z = 0$, the two collding nuclei exchange color charges and lose energy and momentum instantaneously. After the collision, the two colliding nuclei are still propagating at speeds close to the speed of light. Saturated small-x gluons are formed in the region between the two receding nuclei. Now the fast partons inside the two nuclei serve as the color

sources for the saturated gluons in the central region. The saturated gluons in the central region are still described by the classical gluon fields $A^\mu(x)$ subject to the two receding color sources as boundaries. The physical picture resembles the situation where classical electromagnetic fields are generated between two electrically charged plates, the capacitor. In the nucleus-nucleus collision, classical gluon fields are generated between the two receding color charged nuclear plates. To understand the system created in the central region right after the nucleus-nucleus collision, we need to solve for the classical gluon fields in the central region.

2.3.1   Classical Gluon Fields from a Single Nucleus

Before the collision, each nucleus is associated with its own classical gluon fields from the small-x part of its wavefunction. These classical gluon fields can be obtained by solving the classical Yang-Mills equations. For the nucleus moving along the forward light cone direction x^+, the color charge density $\rho^a(x^-, \mathbf{x}_\perp)$ is independent of the light cone time x^+. We thus seek static solutions of the classical Yang-Mills equations Eq. 2.2 [61, 62, 67]. When the color source is moving at the speed of light, the solution in the *covariant gauge* $(\partial_\mu A^\mu = 0)$ is easy to obtain (inspired by the Weizsacker-Williams solution in classical electrodynamics)

$$A^\mu_{cov}(x^-, \mathbf{x}_\perp) = \delta^{\mu+}\alpha(x^-, \mathbf{x}_\perp) \tag{2.5}$$

with

$$\nabla^2\alpha(x^-, \mathbf{x}_\perp) = -\rho_{cov}(x^-, \mathbf{x}_\perp). \tag{2.6}$$

Here $\rho_{cov} = T^a \rho^a_{cov}$ is the color charge density in the covariant gauge. The classical gluon field in the covariant gauge is

$$A^+_{cov}(x^-, \mathbf{x}_\perp) = \int d^2\mathbf{x}'_\perp G(\mathbf{x}_\perp - \mathbf{x}'_\perp) \rho_{cov}(x^-, \mathbf{x}'_\perp) \tag{2.7}$$

with the Green function being

$$G(\mathbf{x}_\perp) = \int \frac{d^2\mathbf{k}_\perp}{(2\pi)^2} e^{i\mathbf{k}_\perp \cdot \mathbf{x}_\perp} \frac{1}{k^2 + m^2} = \frac{1}{2\pi} K_0(mx_\perp). \tag{2.8}$$

An infrared cut-off scale m has been introduced to regularize the singularity in the momentum integral. The $K_0(x)$ is the modified Bessel function of second kind of order zero and $x_\perp = |\mathbf{x}_\perp|$. Once we have one solution in the covariant gauge, we can obtain the solution in the *light cone gauge* $(A^+ = 0)$ by a gauge transformation. The reasons why we prefer the light cone gauge are: first, we can obtain gauge invariant quantities by doing the calculation in the light cone gauge and choosing appropriate boundary conditions and contour paths; second, results in the light cone gauge can be directly applied to the situation of nucleus-nucleus collisions. In the light cone gauge, the solutions are

$$\begin{aligned} A^+ &= A^- = 0 \,, \\ A^j(x^-, \mathbf{x}_\perp) &= \frac{i}{g} U(x^-, \mathbf{x}_\perp) \partial^j U^\dagger(x^-, \mathbf{x}_\perp) \,. \end{aligned} \tag{2.9}$$

Here $j = 1, 2$ represents the two transverse components. The gauge transformation can be represented by a path-ordered Wilson line

$$U(x^-, \mathbf{x}_\perp) = \mathcal{P} \exp\left[-ig \int_{-\infty}^{x^-} A^+_{cov}(z^-, \mathbf{x}_\perp) dz^- \right]. \tag{2.10}$$

Similar results can be obtained for the classical gluon fields of a single nucleus moving along the light cone direction x^- with the color current being $j^{\mu,a} = \delta^{\mu-} \rho^a(x^+, \mathbf{x}_\perp)$.

2.3.2 Yang-Mills Equations in Nucleus-Nucleus Collisions

For high energy nucleus-nucleus collisions, the two nuclei move along $+z$ and $-z$ directions. The collision happens at $z = 0$ when $t = 0$. In the collision, the color current becomes $j^\mu = j_1^\mu + j_2^\mu$ with $j_1^\mu = \delta^{\mu+}\rho(x^-, \mathbf{x}_\perp)$ representing the color current moving along the $+z$ direction at the speed of of light and $j_2^\mu = \delta^{\mu-}\rho(x^+, \mathbf{x}_\perp)$ representing the color current moving along the $-z$ direction at the speed of light. The structure of the color current holds both before and after the collision, assuming the nuclei still travel at the speed close to the speed of light even after the collision. In this situation, the solutions to the classical Yang-Mills equations have been first studied in [68, 69]. In Fock-Schwinger gauge $x^+ A^- + x^- A^+ = 0$, assuming boost-invariance so that the solutions are independent of the pseudorapidity η ($\eta = \frac{1}{2}\ln\frac{t+z}{t-z}$, see Appendix A for more detail about the Milne coordinates $(\tau, \eta, \mathbf{x}_\perp)$), the solution ansatz is

$$
\begin{aligned}
A^+(x) &= \theta(x^+)\theta(x^-)\, x^+ A(\tau, \mathbf{x}_\perp), \\
A^-(x) &= -\theta(x^+)\theta(x^-)\, x^- A(\tau, \mathbf{x}_\perp), \\
A^i(x) &= \theta(x^-)\theta(-x^+)A_1^i(\mathbf{x}_\perp) + \theta(x^+)\theta(-x^-)A_2^i(\mathbf{x}_\perp) \\
&\quad + \theta(x^+)\theta(x^-)A_\perp^i(\tau, \mathbf{x}_\perp).
\end{aligned}
\tag{2.11}
$$

Here $A_1^i(\mathbf{x}_\perp)$ and $A_2^i(\mathbf{x}_\perp)$ are the classical fields of a single nucleus before the collision. We are interested in solutions within the space-time region $x^+ > 0$, $x^- > 0$ after collision. Using the Milne coordinates $(\tau, \eta, \mathbf{x}_\perp)$, the gluon fields in the two coordinate systems are related by $\tau A^\tau = x^- A^+ + x^+ A^-$ and $\tau A^\eta = x^- A^+ - x^+ A^-$. The Fock-Schwinger gauge is equivalent to $A^\tau = 0$ and the only nonvanishing independent components are $A^\eta(\tau, \mathbf{x}_\perp)$ and $A_\perp^i(\tau, \mathbf{x}_\perp)$ in the Milne

coordinate system. The classical Yang-Mills equations Eq. (2.2) become

$$\frac{1}{\tau}\frac{\partial}{\partial\tau}\frac{1}{\tau}\frac{\partial}{\partial\tau}\tau^2 A^\eta - [D^i, [D^i, A^\eta]] = 0 \,,$$
$$\frac{1}{\tau}\frac{\partial}{\partial\tau}\tau\frac{\partial}{\partial\tau}A_\perp^i - ig\tau^2[A^\eta, [D^i, A^\eta]] - [D^j, F^{ji}] = 0 \,,$$

$$(2.12)$$

with the constraint equation

$$ig\tau[A^\eta, \frac{\partial}{\partial\tau}A^\eta] - \frac{1}{\tau}[D^i, \frac{\partial}{\partial\tau}A_\perp^i] = 0 \,. \qquad (2.13)$$

The dynamics before the collision, which involve the space-time regions $x^+ > 0$, $x^- < 0$ and $x^+ < 0$, $x^- > 0$, when analytically continuated to the space-time region $x^+ > 0$, $x^- > 0$ after the collision, provides initial conditions [68, 70] for the equations of motion Eq. (2.12)

$$A_\perp^i(\tau = 0, \mathbf{x}_\perp) = A_1^i(\mathbf{x}_\perp) + A_2^i(\mathbf{x}_\perp) \,,$$
$$A^\eta(\tau = 0, \mathbf{x}_\perp) = -\frac{ig}{2}[A_1^i(\mathbf{x}_\perp), A_2^i(\mathbf{x}_\perp)] \,,$$
$$\frac{\partial}{\partial\tau}A_\perp^i(\tau = 0, \mathbf{x}_\perp) = 0 \,,$$
$$\frac{\partial}{\partial\tau}A^\eta(\tau = 0, \mathbf{x}_\perp) = 0 \,.$$

$$(2.14)$$

Here $A_1^i(\mathbf{x}_\perp)$ and $A_2^i(\mathbf{x}_\perp)$ are the classical gluon fields produced by the single-nucleus color sources ρ_1 and ρ_2, respectively.

Studying the central region of high energy nucleus-nucleus collisions in the CGC framework is equivalent to solving the initial value problem Eqs. (2.12)-(2.14). Averaging over all the possible color configurations for the two color sources by the Gaussian distribution functional Eq. (2.4) can be equivalently implemented by the two-point function of color density

$$\langle\rho_a(x^-, \mathbf{x}_\perp)\rho_b(y^-, \mathbf{y}_\perp)\rangle = \frac{g^2}{d_A}\delta_{ab}\delta(x^- - y^-)\delta^{(2)}(\mathbf{x}_\perp - \mathbf{y}_\perp)\lambda(x^-, \vec{x}_\perp) \,. \qquad (2.15)$$

Here $d_A = N_c^2 - 1$ is the dimension of the adjoint representation of the SU(N_c) group and a, b are color indexes. The spatially dependent Gaussian width function $\lambda(x^-, \mathbf{x}_\perp)$, after integrating over the longitudinal direction $\mu(\mathbf{x}_\perp) = \int dx^- \lambda(x^-, \mathbf{x}_\perp)$, has the meaning of color charge squared per unit area. Notice that we adopt a different normalization in Eq. (2.15) compared with that used in [57].

2.3.3 Power Series Expansion in Proper Time

The initial value problem Eqs. (2.12)-(2.14) has been studied analytically in [68, 69] where the color sources were assumed weak so that a perturbative expansion in terms of the color sources ρ is justified. Another analytical approach proposed in [71, 72, 73] solves the classical Yang-Mills equations by the power series expansion in proper time τ. This approach is valid as long as we focus on early time (small τ) within the convergence radius set by the gluon saturation scale $1/Q_s$ and there is no initial singularity at $\tau = 0$. There are no generic analytic solutions although numerical solutions have been investigated by several groups [74, 75, 76, 77, 78]. We will follow the small-τ power series expansion method. The solutions are represented by

$$
\begin{aligned}
A^\eta(\tau, \mathbf{x}_\perp) &= \sum_{n=0}^\infty \tau^n A^\eta_{(n)}(\mathbf{x}_\perp) \,, \\
A^i_\perp(\tau, \mathbf{x}_\perp) &= \sum_{n=0}^\infty \tau^n A^i_{\perp(n)}(\mathbf{x}_\perp) \,.
\end{aligned}
\tag{2.16}
$$

Substituting into Eq. (2.12), one can check that coefficients with odd n vanish. We obtain the following recursion relations $(n \geq 1)$

$$
\begin{aligned}
A^{\eta}_{(2n)} &= \frac{1}{2n(2n+2)} \sum_{k+l+m=2n-2} \left[D^{i}_{(k)}, \left[D^{i}_{(l)}, A^{\eta}_{(m)} \right] \right], \\
A^{i}_{(2n)} &= \frac{1}{(2n)^2} \left(\sum_{k+l=2n-2} \left[D^{j}_{(k)}, F^{ji}_{(l)} \right] + ig \sum_{k+l+m=2n-4} \left[A^{\eta}_{(k)}, \left[D^{i}_{(l)}, A^{\eta}_{(m)} \right] \right] \right).
\end{aligned}
\tag{2.17}
$$

With the zeroth order coefficients given in Eq. (2.14), we can solve $A^{\eta}_{(2n)}$ and $A^{i}_{\perp(2n)}$ order by order in principle. Furthermore, the field strength tensor $F^{\mu\nu}$ can also be obtained as a power series expansion of τ using

$$
\begin{aligned}
F^{\tau\eta} &= \partial^{\tau} A^{\eta}, \\
F^{\tau i} &= \partial^{\tau} A^{i}, \\
F^{\eta i} &= -[D^{i}, A^{\eta}], \\
F^{ij} &= \partial^{i} A^{j} - \partial^{j} A^{i} - ig[A^{i}, A^{j}].
\end{aligned}
\tag{2.18}
$$

Denote $\tilde{F}^{\tau\eta} \equiv \tau F^{\tau\eta}$ and $\tilde{F}^{\eta i} \equiv \tau F^{\eta i}$ to avoid the coordinate singularities. The recursion relations for the field strength tensor components are

$$
\begin{aligned}
\tilde{F}^{\tau\eta}_{(2n)} &= (2n+2) A^{\eta}_{(2n)}, \\
F^{\tau i}_{(2n-1)} &= (2n) A^{i}_{(2n)}, \\
\tilde{F}^{\eta i}_{(2n-1)} &= - \left[D^{i}_{(0)}, A^{\eta}_{(2n-2)} \right] + ig \sum_{\substack{k+l=2n-2 \\ k \neq 0}} \left[A^{i}_{(k)}, A^{\eta}_{(l)} \right], \\
F^{ij}_{(2n-2)} &= \left[D^{i}_{(0)}, A^{j}_{(2n-2)} \right] - \left[D^{j}_{(0)}, A^{i}_{(2n-2)} \right] - ig \sum_{\substack{k+l=2n-2 \\ k \neq 0, l \neq 0}} \left[A^{i}_{(k)}, A^{j}_{(l)} \right].
\end{aligned}
\tag{2.19}
$$

At zeroth order, that is when $\tau = 0$, the only nonvanishing components of the field strength tensor are the longitudinal chromo-electric field E_0 and longitudinal

chromo-magnetic field B_0, specifically

$$E_0 = -\tilde{F}^{\tau\eta}_{(0)} = ig\delta^{ij}[A_1^i, A_2^j]\,,$$

$$B_0 = -F^{12}_{(0)} = ig\epsilon^{ij}[A_1^i, A_2^j]\,.$$

(2.20)

Here δ^{ij} and ϵ^{ij} are the two-dimensional Kronecker delta function and Levi-Civita symbol, respectively. With the recursive solutions to the classical Yang-Mills equations Eq. (2.17), Eq. (2.19) and the initial conditions Eq. (2.14), we can in principle calculate many interesting physical quantities of the classical gluon fields, like energy-momentum tensor[72], angular momentum tensor [79], etc.

2.4 Energy-Momentum Tensor of Glasma

The classical gluon fields we obtained in the above section describe the saturated gluon system in the central region right after a high energy heavy-ion collision. The gluons are strongly correlated and should be off-shell at the beginning. Equivalently speaking, the fields are strong in the sense that $A^\mu \sim 1/g$ and $\langle A^\mu A^\nu \rangle \sim 1/\alpha_s$. Here g is the strong coupling constant with $\alpha_s = g^2/4\pi$. As the system expands, the overoccupied gluon system eventually decoheres, gluons and quarks are liberated, and quark-gluon plasma is formed within a short time ($\tau \leq 1\,\mathrm{fm/c}$ [80]). This state of matter created soon after a heavy-ion collision and before the formation of quark-gluon plasma is dubbed Glasma (glass + plasma) [55] in the CGC framework. The question of how gluons are liberated as on-shell particles from the Glasma, as well as the production of quarks and their thermalization, is a challenging theoretical problem and is still under active research [81, 82, 83]. In this section, we will focus on one property of the Glasma state,

the event-averaged energy-momentum tensor $T^{\mu\nu}$, and explore its space-time evolution. Most of the work to be presented in this section can be found in the published paper [85]. The energy-momentum tensor of the classical gluon fields is defined as

$$T^{\mu\nu} = F^{\mu\lambda}F^{\nu}_{\ \lambda} + \frac{1}{4}g^{\mu\nu}F^{\kappa\lambda}F_{\kappa\lambda}\,, \tag{2.21}$$

with a trace over color indices taken implicitly as $AB = 2A^{a}B^{b}\operatorname{Tr}(\mathrm{T^{a}T^{b}})$. Assuming boost-invariance, the different components of the energy-momentum tensor can be expressed as

$$
\begin{aligned}
T^{00} &= \mathcal{A} + \mathcal{B}\cosh 2\eta + \mathcal{C}\sinh 2\eta\,, \\[4pt]
T^{0i} &= T^{i0} = \mathcal{E}_i\sinh\eta + \mathcal{F}_i\cosh\eta\,, \\[4pt]
T^{03} &= T^{30} = \mathcal{B}\sinh 2\eta + \mathcal{C}\cosh 2\eta\,, \\[4pt]
T^{11} &= \mathcal{A} + \mathcal{D}\,, \\[4pt]
T^{22} &= \mathcal{A} - \mathcal{D}\,, \\[4pt]
T^{12} &= T^{21} = \mathcal{G}\,, \\[4pt]
T^{i3} &= T^{3i} = \mathcal{F}_i\sinh\eta + \mathcal{E}_i\cosh\eta\,, \\[4pt]
T^{33} &= -\mathcal{A} + \mathcal{B}\cosh 2\eta + \mathcal{C}\sinh 2\eta\,.
\end{aligned}
\tag{2.22}
$$

where $i = (1,2)$ indicates the transverse components and $\mathcal{A}, \mathcal{B}, \mathcal{C}, \mathcal{D}, \mathcal{E}_i = (\mathcal{E}_1, \mathcal{E}_2)$, $\mathcal{F}_i = (\mathcal{F}_1, \mathcal{F}_2)$ and $\mathcal{G}$ are functions of proper time τ and transverse spatial coordinate $\mathbf{x}_\perp$ only. The dependence on pseudorapidity η factorizes into the hyperbolic

functions. They are related to the field strength tensor components

$$\mathcal{A} = \frac{1}{2}\left(\tilde{F}^{\tau\eta}\tilde{F}^{\tau\eta} + \frac{1}{2}F^{ij}F^{ij}\right),$$

$$\mathcal{B} = \frac{1}{2}(F^{i\tau}F^{i\tau} + \tilde{F}^{i\eta}\tilde{F}^{i\eta}),$$

$$\mathcal{C} = F^{i\tau}\tilde{F}^{i\eta},$$

$$\mathcal{D} = -\frac{1}{2}[F^{x\tau}F^{x\tau} - F^{y\tau}F^{y\tau} - (\tilde{F}^{x\eta}\tilde{F}^{x\eta} - \tilde{F}^{y\eta}\tilde{F}^{y\eta})], \qquad (2.23)$$

$$\mathcal{E}_i = F^{i\tau}\tilde{F}^{\tau\eta} - F^{ij}\tilde{F}^{j\eta},$$

$$\mathcal{F}_i = \tilde{F}^{i\eta}\tilde{F}^{\tau\eta} - F^{ij}F^{j\tau},$$

$$\mathcal{G} = -F^{x\tau}F^{y\tau} + \tilde{F}^{x\eta}\tilde{F}^{y\eta}.$$

In the general situation where the color charge fluctuation width $\mu(\mathbf{x}_\perp) = \int dx^-\lambda(x^-, \mathbf{x}_\perp)$ depends on the transverse coordinates $\mathbf{x}_\perp$, the energy-momentum tensor was solved up to fourth order in τ and first order in the gradients of $\mu(\mathbf{x}_\perp)$ [72]. At zeroth order, the initial energy-momentum tensor is diagonal $T_{(0)}^{\mu\nu} = \text{diag}\{\varepsilon_0, \varepsilon_0, \varepsilon_0, -\varepsilon_0\}$ with

$$\varepsilon_0(\mathbf{x}_\perp) = \frac{1}{2}\left(E_0^2 + B_0^2\right). \qquad (2.24)$$

Here the initial chromo-electric field E_0 and the chromo-magnetic field B_0 are given by Eq. (2.20). After statistically averaging over initial color charge configurations using the color density correlation function Eq. (2.15) one obtains

$$\varepsilon_0(\mathbf{x}_\perp) = 2\pi\alpha_s^3\frac{C_A}{d_A}\mu_1(\mathbf{x}_\perp)\mu_2(\mathbf{x}_\perp)\ln\left(\frac{Q_1^2}{m_1^2}\right)\ln\left(\frac{Q_2^2}{m_2^2}\right). \qquad (2.25)$$

Here $C_A = N_c$ is the Casimir operator of SU(N_c) in the adjoint representation and $d_A = N_c^2 - 1$. The $\alpha_s = g^2/4\pi$ is the strong coupling constant. The Q_i and m_i ($i = 1, 2$) are the transverse UV cut-off scale and transverse IR cut-off scale in the momentum space for the soft gluon (small-x) modes from the two nuclei.

For the nonequilibrium state of the gluon fields, we will denote the longitudinal pressure as $P_L = T^{33}$ and the transverse pressure as $P_T = (T^{11} + T^{22})/2$. With these definitions, one can see the highly anisotropic nature of the initial pressures $P_T = \varepsilon_0$ and $P_L = -\varepsilon_0$ and their relatively large value compared to a thermalized system, like $P = \varepsilon/3$ for a gas of relativistic particles. The negative value of the initial longitudinal pressure is consistent with our color capacitor picture. The produced gluon fields pull the two receding color nuclear plates back towards reach other so that the plates feel attractive forces. This attractive interaction explains the negative longitudinal pressure. One can see that the initial stage of the Glasma state is highly anisotropic and largely deviates from equilibrium.

In the following we focus on a simplified problem where the transverse color charge fluctuation width is homogeneous and isotropic $\mu(\vec{x}_\perp) = \mu$ and the two colliding nuclei are the same $\mu_1 = \mu_2$. Under the condition of transverse homogeneity and isotropy, the functions $\mathcal{C}, \mathcal{D}, \mathcal{E}_i, \mathcal{F}_i, \mathcal{G}$ in Eq. (2.22) vanish and the energy-momentum tensor reduces to

$$
T^{\mu\nu} = \begin{pmatrix} \mathcal{A} + \mathcal{B}\cosh 2\eta & 0 & 0 & \mathcal{B}\sinh 2\eta \\ 0 & \mathcal{A} & 0 & 0 \\ 0 & 0 & \mathcal{A} & 0 \\ \mathcal{B}\sinh 2\eta & 0 & 0 & -\mathcal{A} + \mathcal{B}\cosh 2\eta \end{pmatrix}. \tag{2.26}
$$

The energy and momentum of the Glasma itself are conserved as we assume the two receding nuclei still propagate at the speed of light and ignore the back-reaction of the classical fields on the nuclei. Implementing $\partial_\mu T^{\mu\nu} = 0$, we obtain the relation between $\mathcal{A}$ and $\mathcal{B}$

$$
\frac{\partial}{\partial\tau}(\tau^2 \mathcal{B}) + \tau^2 \frac{\partial \mathcal{A}}{\partial\tau} = 0. \tag{2.27}
$$

Plugging into the power series expansions of $\mathcal{A}(\tau)$ and $\mathcal{B}(\tau)$

$$\mathcal{A}(\tau) = \sum_{n=0}^{\infty} \tau^{2n} \mathcal{A}_{(2n)} \,,$$

$$\mathcal{B}(\tau) = \sum_{n=0}^{\infty} \tau^{2n} \mathcal{B}_{(2n)} \,. \tag{2.28}$$

we get the order-by-order relation

$$\mathcal{B}_{(2n)} = -\frac{2n}{2n+2} \mathcal{A}_{(2n)} \,. \tag{2.29}$$

Therefore, all we need to calculate are the coefficients $\mathcal{A}_{(2n)}$. The general expression for $\mathcal{A}_{(2n)}$ is

$$\mathcal{A}_{(2n)} \sim [D^{i_1}, [D^{i_2}, [D^{i_3}, \ldots, [D^{i_n}, [A_1^p, A_2^q]] \ldots,]]]$$

$$\times [D^{j_1}, [D^{j_2}, [D^{j_3}, \ldots, [D^{j_n}, [A_1^m, A_2^n] \ldots,]]] \,, \tag{2.30}$$

with event averaging using Eq. (2.15) in mind. There is a complicated overall prefactor that contracts with the spatial indexes $i_1, i_2, \ldots i_n; j_1, j_2, \ldots, j_n; m, n, p, q$; so that the final expression for $\mathcal{A}_{(2n)}$ is index free. It affects the coefficient of each term but will not influence the general structure of each term. In the expression for $\mathcal{A}_{(2n)}$, there are $2n$ covariant derivatives D^i which can be written in different ways: $D^i \equiv \partial^i - igA_1^i - igA_2^i = D_1^i - igA_2^i = D_2^i - igA_1^i$. We organize all terms contained in $\mathcal{A}_{(2n)}$ according to the number of covariant derivatives involved. Henceforth we employ the following correlation functions (we use A_1^i as an example, similar results hold for A_2^i).

$$\langle D_1^{i_1} D_1^{i_2} \ldots D_1^{i_k} A_1^p A_1^m \rangle \sim \frac{g^2}{d_A} \left(\frac{\mu}{4\pi}\right) Q^k \,,$$

$$\langle A_1^p A_1^m \rangle \sim \frac{g^2}{d_A} \left(\frac{\mu}{4\pi}\right) \ln\left(\frac{Q^2}{m^2}\right) \,, \tag{2.31}$$

$$\langle A_1^{i_1} A_1^{i_2} \ldots A_1^{i_k} \rangle \sim \sum_{\text{all combinations}} \langle A_1^{i_{p1}} A_1^{i_{p2}} \rangle \langle A_1^{i_{p3}} A_1^{i_{p4}} \rangle \ldots$$

(Formulas with the coefficients included are given in Appendix B). Here Q is a UV cut-off in transverse momentum space as can be seen from the explicit calculation of the correlation functions in Eq. (B.5). The m is an IR cut-off regulating the low energy behavior. We assume $Q^2 \gg m^2$ so that we only need to keep $(Q^2)^k$ terms and disregard $(m^2)^k \ln(Q^2/m^2)$ and $(Q^2)^l(m^2)^{k-l}$ terms in the calculation of the correlation functions. We further used the fact that only two-point correlations of color sources are nonvanishing [67, 84]. After calculating the first few orders, the general expression for $\mathcal{A}_{(2n)}$ can be written as

$$
\begin{aligned}
\mathcal{A}_{(2n)} = & \; g^6 \frac{C_A}{d_A} \left(\frac{\mu}{4\pi}\right)^2 \ln\left(\frac{Q^2}{m^2}\right) \sum_{k=1}^{n} \mathsf{F}_{2n}(k) \left(Q^2\right)^k \left[g^4 \frac{C_A}{d_A} \frac{\mu}{4\pi} \ln\left(\frac{Q^2}{m^2}\right)\right]^{n-k} \\
& + g^6 \frac{C_A}{d_A} \left(\frac{\mu}{4\pi}\right)^2 \sum_{k=2}^{n} \mathsf{G}_{2n}(k) \left(Q^2\right)^k \left[g^4 \frac{C_A}{d_A} \frac{\mu}{4\pi} \ln\left(\frac{Q^2}{m^2}\right)\right]^{n-k} \\
& + g^6 \frac{C_A}{d_A} \left(\frac{\mu}{4\pi}\right)^2 \ln^2\left(\frac{Q^2}{m^2}\right) \left[g^4 \frac{C_A}{d_A} \frac{\mu}{4\pi} \ln\left(\frac{Q^2}{m^2}\right)\right]^{n} \mathsf{H}_{2n} .
\end{aligned}
\tag{2.32}
$$

At each step, the number of covariant derivatives are reduced by two, and we have one additional factor $g^2 A_1 A_1$. That is why Q^2 is replaced by $g^4 C_A \mu/4\pi d_A \ln(Q^2/m^2)$ when its power index is descending. All the numerical coefficients $\mathsf{F}_{2n}(k), \mathsf{G}_{2n}(k), \mathsf{H}_{2n}$ have to be determined by detailed calculations which, in general, are very hard to achieve. In the following, we discuss an approximation that makes further computations possible.

2.4.1 Leading Q^2 Approximation

Within the CGC framework, the saturation scale Q_s is related to the color charge fluctuation measure μ at the lowest order by [86]

$$
Q_s^2 = g^4(Q_s^2) \frac{C_A}{d_A} \frac{\mu}{16\pi} \ln\left(\frac{Q_s^2}{m^2}\right) .
\tag{2.33}
$$

Here we explicitly write out the energy scale dependence of the strong coupling constant $g(Q_s^2)$. The lowest-order perturbative calculation of the running coupling constant is

$$\alpha_s(M^2) = \frac{g^2(M^2)}{4\pi} = \frac{1}{\beta_2 \ln(M^2/\Lambda_{QCD}^2)}, \qquad (2.34)$$

where $\beta_2 = (11N_c - 2N_f)/12\pi$ and N_f is the number of quark flavors. We choose the infrared scale $m^2 \sim \Lambda_{QCD}^2$. After substitution of μ from Eq. (2.33), replacing g with $g(Q^2)$, and using the expression for the initial energy density ε_0 from Eq. (2.25), Eq. (2.32) can be written as

$$
\begin{aligned}
\mathcal{A}_{(2n)} = {} & \frac{2\varepsilon_0}{\ln(Q^2/m^2)} \left[\frac{4Q_s^2 \ln(Q_s^2/m^2)}{\ln(Q^2/m^2)} \right]^n \sum_{k=1}^n \mathsf{F}_{2n}(k) \left[\frac{Q^2 \ln(Q^2/m^2)}{4Q_s^2 \ln(Q_s^2/m^2)} \right]^k \\
& + \frac{2\varepsilon_0}{\ln^2(Q^2/m^2)} \left[\frac{4Q_s^2 \ln(Q_s^2/m^2)}{\ln(Q^2/m^2)} \right]^n \sum_{k=2}^n \mathsf{G}_{2n}(k) \left[\frac{Q^2 \ln(Q^2/m^2)}{4Q_s^2 \ln(Q_s^2/m^2)} \right]^k \qquad (2.35) \\
& + 2\varepsilon_0 \left[\frac{4Q_s^2 \ln(Q_s^2/m^2)}{\ln(Q^2/m^2)} \right]^n \mathsf{H}_{2n}.
\end{aligned}
$$

In obtaining Eq. (2.35), we included the running coupling constant expression Eq. (2.34) at two energy scales $\alpha_s(Q^2)$ and $\alpha_s(Q_s^2)$. The UV cut-off scale Q sets the upper validity bound of the classical MV model which can not be determined by the model itself. The hard partons with transverse momentum $p_\perp > Q$ can be described by perturbative QCD and are responsible for minijet producton, while the soft partons with transverse momentum $p_\perp < Q$ can be effectively described by the classical fields and are responsible for the formation of the QGP. Physical quantities like the energy density should be insensitive to the cut-off chosen after the soft processes are matched with the hard processes, as pointed out in [71]. On the other hand, the saturation scale Q_s describes the typical transverse momentum scale of the saturated gluons. The scale is dynamically generated and depends

on the collision energy and the size of the colliding nuclei. In the McLerran-Venugopalan model, the large-x color sources are assumed to be uncorrelated on the transverse plane. This requires a finer resolution scale Q beyond the typical coherent soft gluon scale Q_s. Therefore, we assume that $Q^2 \gg Q_s^2$ [57, 66]. Then the summations in Eq. (2.35) can be approximated by keeping only the leading $k = n$ terms and the last line of Eq. (2.35) can be dropped. Hence

$$\mathcal{A}_{(2n)} \simeq 2\varepsilon_0 \mathsf{F}_{2n}(n)\frac{Q^{2n}}{\ln(Q^2/m^2)} + 2\varepsilon_0 \mathsf{G}_{2n}(n)\frac{Q^{2n}}{\ln^2(Q^2/m^2)} \,. \tag{2.36}$$

This is the expression for $\mathcal{A}_{(2n)}$ in the leading Q^2 approximation $Q^2 \gg Q_s^2 \gg m^2$ with which we work from now on.

Before calculating the numerical coefficients $\mathsf{F}_{2n}(n)$ and $\mathsf{G}_{2n}(n)$, we would like to discuss the problem of including running coupling effects by replacing α_s with $\alpha_s(M^2)$. First of all, if we absorb the strong coupling constant into the vector potential $gA_\mu \to A_\mu$, the pure gauge field sector of the QCD Lagrangian becomes $\mathcal{L}_G = -\frac{1}{4g^2}(F_{\mu\nu}^a)^2$. Then the equations of motion Eq. (2.12) and the constraint equation Eq. (2.13) have no explicit dependence on the strong coupling constant g. That means the time evolution of the *gauge fields* are free from the strong coupling constant and its running effects. Instead, the strong coupling constant is shuffled into the color charge sources $\rho_i \to g^2\rho_i$ ($i = 1, 2$). As a result, the initial conditions Eq. (2.14), via their dependence on A_1 and A_2, are functions of the strong coupling constant. Moreover, the expression for the energy-momentum tensor would change correspondingly to $T^{\mu\nu} \to \frac{1}{g^2}T^{\mu\nu}$. Here comes the subtle point. When we consider the time evolution of the pressures, the quantities we concentrate on are p_T/ε and p_L/ε. The prefactor $1/g^2$ before $T^{\mu\nu}$ and the dependence on color charge sources $g^2\rho_i$, which are both reflected in the initial energy density

ε_0, will cancel out. However, in arriving at Eq. (2.35), running coupling effects are encoded in the summations apart from the prefactor ε_0. As a consequence, we obtain the Q^{2n} factor in Eq. (2.36) under the leading Q^2 approximation. It will result in a Q_s^{2n} factor in the expression for $\mathcal{A}_{(2n)}$ if no running coupling effects are included. Keeping in mind the places where the running coupling constant plays a role, replacing α_s with $\alpha_s(M^2)$ implies the inclusion of quantum fluctuation effects in these places. This is in principle beyond the scope of a pure classical model (the McLerran-Venugopalan model). By the inclusion of a running coupling constant, we estimate the effects of quantum corrections in our classical description, specifically the initial dynamics at $\tau = 0$. We expect interactions involving gluons as well as quarks due to their contributions in the running coupling constant expression Eq.(2.34).

Now we begin evaluating the coefficients $\mathsf{F}_{2n}(n)$ and $\mathsf{G}_{2n}(n)$. The leading Q^2 approximation to $\mathcal{A}_{(2n)}$ from Eq. (2.36) is equivalent to keeping only the terms containing $2n$ derivatives in Eq. (2.30). As stated before, $D^i = D_1^i - ig A_2^i = D_2^i - ig A_1^i$, and terms in Eq. (2.30) are organized according to the number of derivatives D_1^i and D_2^i. To put it another way, the coupled nonlinear recursion solutions Eq. (2.17) become decoupled and linearized in the leading Q^2 approximation, namely

$$
\begin{aligned}
A_{(2n)}^\eta &= \frac{1}{2n(2n+2)} \left[D_{(0)}^i, \left[D_{(0)}^i, A_{(2n-2)}^\eta \right] \right] , \\
A_{(2n)}^i &= \frac{1}{(2n)^2} \left[D_{(0)}^j, F_{(2n-2)}^{ji} \right] .
\end{aligned}
\tag{2.37}
$$

The components of the field strength tensor $F^{\mu\nu}$ are consequently independent of

each other and are solved recursively.

$$\tilde{F}^{\tau\eta}_{(2n)} = -\frac{1}{[(2n)!!]^2} D^{\{2n\}} E_0 \,,$$

$$B_{(2n)} = \frac{1}{[(2n)!!]^2} D^{\{2n\}} B_0 \,,$$

$$\tilde{F}^{\eta i}_{(2n-1)} = \frac{2n}{[(2n)!!]^2} [D^i, D^{\{2n-2\}} E_0] \,,$$

$$F^{\tau i}_{(2n-1)} = \frac{2n}{[(2n)!!]^2} \epsilon^{ij} [D^j, D^{\{2n-2\}} B_0] \,.$$

$$(2.38)$$

Here we used $E_0 = \tilde{F}^{\tau\eta}_{(0)}$ and $B_0 = -\frac{1}{2}\epsilon^{ij} F^{ij}_{(0)}$. The double factorial is $(2n)!! = 2n \times (2n-2) \times (2n-4) \ldots \times 2$. The $D^{\{2n\}}$ represents nested commutators of 2n folds

$$D^{\{2n\}} E_0 = [D^{i_n}, [D^{i_n}, \ldots [D^{i_1}, [D^{i_1}, E_0]] \ldots]] \,. \qquad (2.39)$$

Substituting the above expressions into $\mathcal{A}_{(2n)}$ gives

$$\mathcal{A}_{(2n)} = \frac{1}{2} \sum_{k=0}^{n} \left(\tilde{F}^{\tau\eta}_{(2n-2k)} \tilde{F}^{\tau\eta}_{(2k)} + B_{(2n-2k)} B_{(2k)} \right)$$

$$= \frac{1}{2} (-1)^n f_{(2n)} \left[D^{\{n\}} E_0 D^{\{n\}} E_0 + D^{\{n\}} B_0 D^{\{n\}} B_0 \right] \,,$$

$$(2.40)$$

where $f_{(2n)} = \binom{2n}{n}/(2^n n!)^2$ contains the binomial coefficient $\binom{n}{k} = n!/(n-k)!k!$. After taking the statistical average and carrying out contractions for both color and spatial indexes, we find

$$\mathsf{F}_{2n}(n) = \frac{(-1)^n}{n} f_{(2n)} \,, \quad n \geq 1$$

$$\mathsf{G}_{2n}(n) = \frac{(-1)^n}{4} \mathcal{C}_{\pm}(2n) f_{(2n)} \,, \quad n \geq 2$$

$$(2.41)$$

In $\mathcal{C}_{\pm}(2n)$, the $\pm$ refers to even or odd values of n. For n an even integer $(n \geq 2)$

$$\mathcal{C}_{+}(2n) = 2\left[\sum_{k=0}^{n/2}\sum_{l=0}^{n/2}\sum_{i=0}^{k}\sum_{j=0}^{l}\frac{1}{n-k-l}\frac{1}{k+l}\binom{n/2}{k+i}\binom{k+i}{2i}\binom{n/2}{l+j}\binom{l+j}{2j}\binom{2i+2j}{i+j}\right.$$

$$+ \sum_{k=0}^{n/2-1}\sum_{l=0}^{n/2-1}\sum_{i=0}^{k}\sum_{j=0}^{l}\frac{1}{n-k-l-1}\frac{1}{k+l+1}\binom{n/2}{k+i+1}\binom{k+i+1}{2i+1}\binom{n/2}{l+j+1}$$

$$\left. \times \binom{l+j+1}{2j+1}\binom{2i+2j+2}{i+j+1}\right].$$

$$(2.42)$$

In the first line the term with $k = l = 0$ is excluded, and the term with $k = l = n/2$ is excluded. For n an odd integer $(n \geq 3)$

$$\mathcal{C}_{-}(2n) = 4\left[\sum_{k=0}^{(n-1)/2}\sum_{l=0}^{(n-1)/2}\left(\frac{1}{n-k-l-1}\right)\left(\frac{1}{k+l+1}\right)\right.$$

$$\times \left[\sum_{i=0}^{k}\sum_{j=0}^{l}\binom{(n-1)/2}{k+i}\binom{k+i}{2i}\binom{(n-1)/2}{l+j}\binom{l+j}{2j}\binom{2i+2j}{i+j}\right.$$

$$+ \frac{1}{2}\binom{(n-1)/2}{k+i}\binom{k+i}{2i}\binom{(n-1)/2}{l+j+1}\binom{l+j+1}{2j+1}\binom{2i+2j+2}{i+j+1}$$

$$+ \frac{1}{2}\binom{(n-1)/2}{k+i+1}\binom{k+i+1}{2i+1}\binom{(n-1)/2}{l+j}\binom{l+j}{2j}\binom{2i+2j+2}{i+j+1}$$

$$\left.\left.+ \binom{(n-1)/2}{k+i+1}\binom{k+i+1}{2i+1}\binom{(n-1)/2}{l+j+1}\binom{l+j+1}{2j+1}\binom{2i+2j+2}{i+j+1}\right]\right].$$

$$(2.43)$$

Also, the term with $k = l = (n-1)/2$ is excluded. To understand the general structure of $\mathcal{C}_{+}(2n)$ and $\mathcal{C}_{-}(2n)$, consider the first line of expression (2.42) as an example. At each order $2n$, we have n derivatives D^i to distribute between A_1^m and A_2^n, and another n derivatives to distribute between A_1^p and A_2^q. The number of derivatives acting on A_1^m and A_1^p in total has to be even, otherwise their statistical averages will vanish. The same is true for A_2^n and A_2^q. We have $n - 2k$ derivatives

D_1^i acting on A_1^m and $n - 2l$ derivatives D_1^i acting on A_1^p. But within the $n - 2k$ (or $n - 2l$) derivatives, we can choose either $D_1^i D_1^i$ or $D_1^i D_1^j$, which is why there are additional summation indexes i or j. The two prefactors $1/(n - k - l)$ and $1/k + l$ come from the momentum space integral $\int dp^2 (p^2)^{n-k-l}$ and $\int dp^2 (p^2)^{k+l}$ when evaluating correlation functions. Finally, the binomial coefficients $\binom{2i+2j}{i+j}$ are due to spatial index contractions. Using the expression for $\mathcal{A}_{(2n)}$ in Eq. (2.36), we can sum all the terms in the expression for $\mathcal{A}$ in Eq. (2.28) to get

$$\mathcal{A} = \varepsilon_0 + \frac{2\varepsilon_0}{\ln(Q^2/m^2)} \sum_{n=1}^{\infty} \mathsf{F}_{2n}(n)(Q\tau)^{2n} + \frac{2\varepsilon_0}{\ln^2(Q^2/m^2)} \sum_{n=2}^{\infty} \mathsf{G}_{2n}(n)(Q\tau)^{2n} . \quad (2.44)$$

The first summation can be expressed in closed form as

$$\sum_{n=1}^{\infty} \mathsf{F}_{2n}(n)(Q\tau)^{2n} = \sum_{n=1}^{\infty} \frac{(-1)^n}{n} f_{(2n)}(Q\tau)^{2n}$$

$$= -\frac{1}{2}(Q\tau)^2 \left[{}_3F_4\left(1, 1, \frac{3}{2}; 2, 2, 2, 2; -(Q\tau)^2\right) \right] . \quad (2.45)$$

Here ${}_pF_q(a_1, \ldots, a_p; b_1, \ldots, b_q; z)$ is the generalized hyper-geometric function

$$_pF_q(a_1, \ldots, a_p; b_1, \ldots, b_q; z) = \sum_{n=0}^{\infty} \frac{(a_1)_n \ldots (a_p)_n}{(b_1)_n \ldots (b_q)_n} \frac{z^n}{n!} . \quad (2.46)$$

However, the second summation does not have a closed form expression as far as we know. We will use $\mathsf{G}_A(Q\tau)$ to denote the second summation.

$$\mathsf{G}_A(Q\tau) = \sum_{n=2}^{\infty} \frac{(-1)^n}{4} \mathcal{C}_{\pm}(2n) f_{(2n)}(Q\tau)^{2n}$$

$$= \frac{1}{4}\left[8f_{(4)}(Q\tau)^4 - 18f_{(6)}(Q\tau)^6 + \frac{118}{3}f_{(8)}(Q\tau)^8 + \ldots \right] \quad (2.47)$$

Then we get our final expression for $\mathcal{A}$

$$\mathcal{A} = \varepsilon_0 + \frac{2\varepsilon_0}{\ln^2(Q^2/m^2)} \mathsf{G}_A(Q\tau) - \frac{\varepsilon_0}{\ln(Q^2/m^2)}(Q\tau)^2 \left[{}_3F_4\left(1, 1, \frac{3}{2}; 2, 2, 2, 2; -(Q\tau)^2\right) \right] . \quad (2.48)$$

With the relation Eq. (2.29) between $\mathcal{A}$ and $\mathcal{B}$ we immediately obtain

$$\mathcal{B} = \frac{2\varepsilon_0}{\ln(Q^2/m^2)} \left(1 - [J_0(Q\tau)]^2 - [J_1(Q\tau)]^2\right) + \frac{2\varepsilon_0}{\ln^2(Q^2/m^2)} \mathsf{G}_B(Q\tau) \qquad (2.49)$$

where $J_n(x)$ is the Bessel function of the first kind and

$$\begin{aligned}
\mathsf{G}_B(Q\tau) &= -\sum_{n=2}^{\infty} \frac{(-1)^n}{4} \frac{2n}{2n+2} C_\pm(2n) f_{(2n)}(Q\tau)^{2n} \\
&= -\left[\frac{4}{3} f_{(4)}(Q\tau)^4 - \frac{27}{8} f_{(6)}(Q\tau)^6 + \frac{118}{15} f_{(8)}(Q\tau)^8 + \ldots\right].
\end{aligned} \qquad (2.50)$$

Equations Eq. (2.48) and Eq. (2.49) are the main results in this subsection. They both contain two parts: one part can be expressed in closed form while the other part can only be expressed as an infinite power series.

2.4.2 Time Evolution of Energy Density and Pressures

In the central rapidity region where $\eta = 0$, the energy density and pressures from Eq. (2.26) are expressed as $\varepsilon = \mathcal{A} + \mathcal{B}$, $P_T = \mathcal{A}$ and $P_L = -\mathcal{A} + \mathcal{B}$. With the results for $\mathcal{A}$ in Eq. (2.48) and $\mathcal{B}$ in Eq. (2.49), we are ready to explore the time evolution of energy density and pressures. As functions of $Q\tau$, the only unknown parameter in $\mathcal{A}$ and $\mathcal{B}$ is $a \equiv \ln Q^2/m^2$ because the initial energy density ε_0 acts as an overall prefactor which can be rescaled out as long as we are not interested in the absolute values. The value of a has to be large as we assumed $Q^2 \gg m^2$, and we also work in the high-momentum regime where $Q^2 \gg Q_s^2$. In the following numerical calculations we choose $a = 6$. Then $Q = 4.0$ GeV when $m = \Lambda_{QCD} = 0.2$ GeV, and $Q_s \sim 1.2$ GeV. This will make $Q^2/m^2 \sim 400$ and $Q^2/Q_s^2 \sim 12$, which are consistent with our assumptions. We rescale energy density and pressures as $\varepsilon/\varepsilon_0$, P_T/ε_0, P_L/ε_0. In Fig. 2.3 the time evolution of the energy density is shown

with different calculated accuracy. We approximate $\mathsf{G}_A(Q\tau)$ and $\mathsf{G}_B(Q\tau)$ in Eqs. (2.48) and (2.49) up to the order of $(Q\tau)^{10}$, $(Q\tau)^{30}$, $(Q\tau)^{50}$, and $(Q\tau)^{100}$. The energy density decreases with time and sharply drops to negative values for a given order. Negative energy density is unphysical, we can only trust the time evolution of the energy density in the region where $\varepsilon > 0$. Moreover, increasing the order of accuracy makes the value of $Q\tau$ (when $\varepsilon = 0$) larger, thus enlarging the time interval for the validity of the energy density calculation. As we can see, the result at the order $(Q\tau)^{100}$ is sufficient to describe the time evolution within the interval $0 \leq Q\tau \leq 10$ chosen. Additional higher order terms will not change the behavior of the energy density in this interval. Results are only shown within this interval for two reasons. The $Q\tau = 10$ corresponds to $\tau \sim 0.5\,\mathrm{fm/c}$, later time evolution of the Glasma is dominated by quantum effects, which makes the prediction of the pure classical description questionable. Also, large values of $Q\tau$ in the power series expressions introduce large round-off errors in numerical precision which can result in unphysical behavior. Similar behavior is found in Fig. 2.4 for the transverse pressure P_T. Fig. 2.5 shows the rescaled longitudinal pressure P_L/ε_0 evolution. The initial negative value of P_L originates from the longitudinal motion of the two nuclei and their attractive interactions. The magnitude of the longitudinal pressure decreases as the nuclei recede from each other. From the results at the order of $2n = 100$, one can see the longitudinal pressure is still negative but tending towards zero. This implies that the classical gluon field description cannot realize pressure isotropization which requires the longitudinal pressure to become positive.
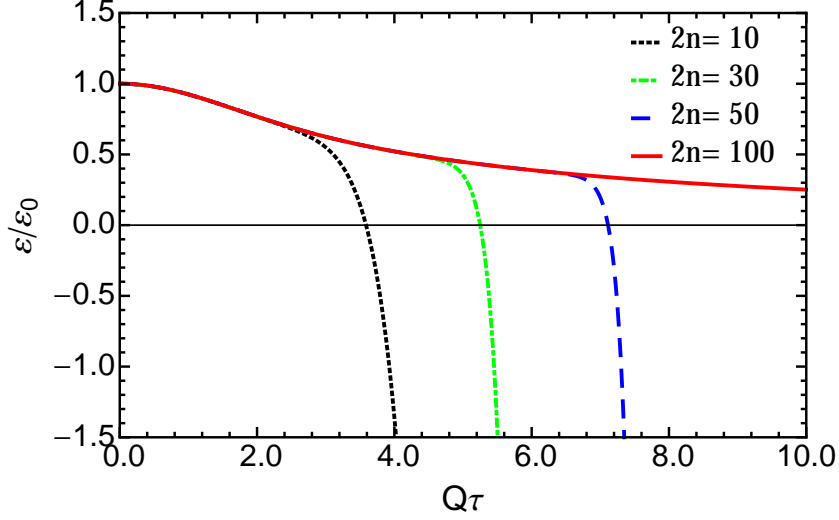
Figure 2.3: Energy density $\varepsilon/\varepsilon_0$ as a function of $Q\tau$ with different calculated accuracy. The black dotted line, green dot-dashed line, blue dashed line and the red solid line represent approximations of $\mathsf{G}_A(Q\tau)$ and $\mathsf{G}_B(Q\tau)$ to the order of $(Q\tau)^{10}$, $(Q\tau)^{30}$, $(Q\tau)^{50}$, and $(Q\tau)^{100}$, respectively.
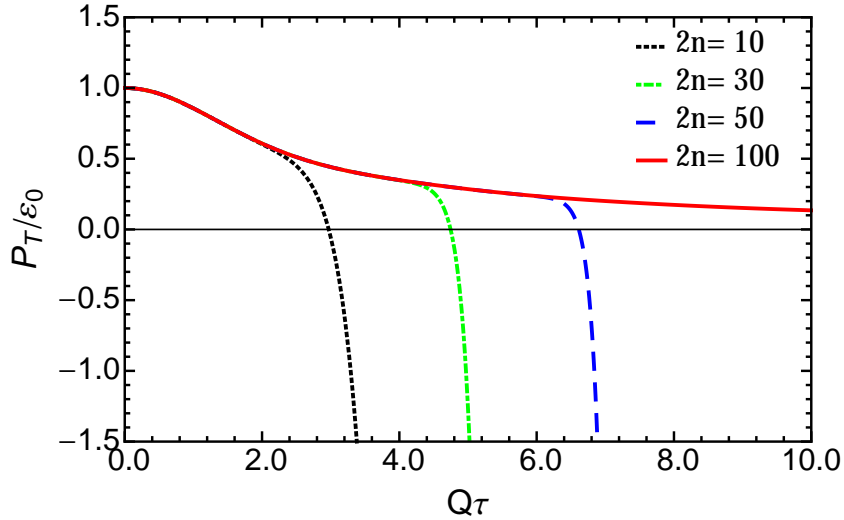
Figure 2.4: Transverse pressure P_T/ε_0 as a function of $Q\tau$ with different calculated accuracy. The notation is the same as in Fig. 2.3.
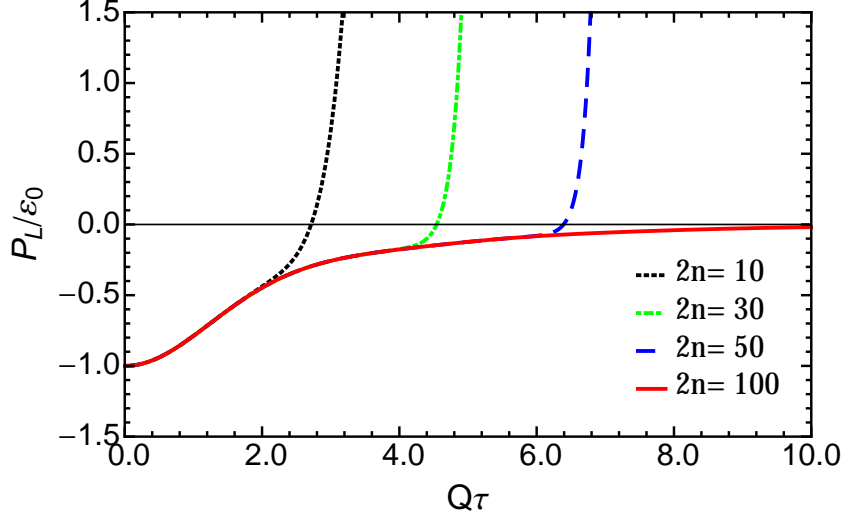
Figure 2.5: Longitudinal pressure P_L/ε_0 as a function of $Q\tau$ with different calculated accuracy. The notation is the same as in Fig. 2.3.

In Fig. 2.6 the time evolution of P_T/ε and P_L/ε are shown where $\mathsf{G}_A(Q\tau)$ and $\mathsf{G}_B(Q\tau)$ are truncated at the order of $2n = 100$. The ratio of the longitudinal and transverse pressures to the energy density are $P_T/\varepsilon \simeq 0.5$ and $P_L/\varepsilon \simeq 0$ at the time $Q\tau = 10.0$ ($\tau = 0.5\,\text{fm/c}$). The results obtained here are identical to those of [72] when all terms are truncated at order $(Q\tau)^4$ and the input parameter a is chosen appropriately. They are essentially the same as obtained in the classical SU(2) simulations in [87]. (There are small oscillations in their results which may be attributable to the finite lattice spacing or to the finite rapidity region of the space-time which was sampled and averaged over. Our solution assumes boost invariance.) When they include initial quantum fluctuations, and using a value of $g = 0.5$, they find a positive longitudinal pressure but still a sizable anisotropy of $P_L/P_T \sim 0.6$ at a time of 1 fm/c. For a smaller coupling of $g = 0.1$ the initial quantum fluctuations have very little effect on the classical solution.
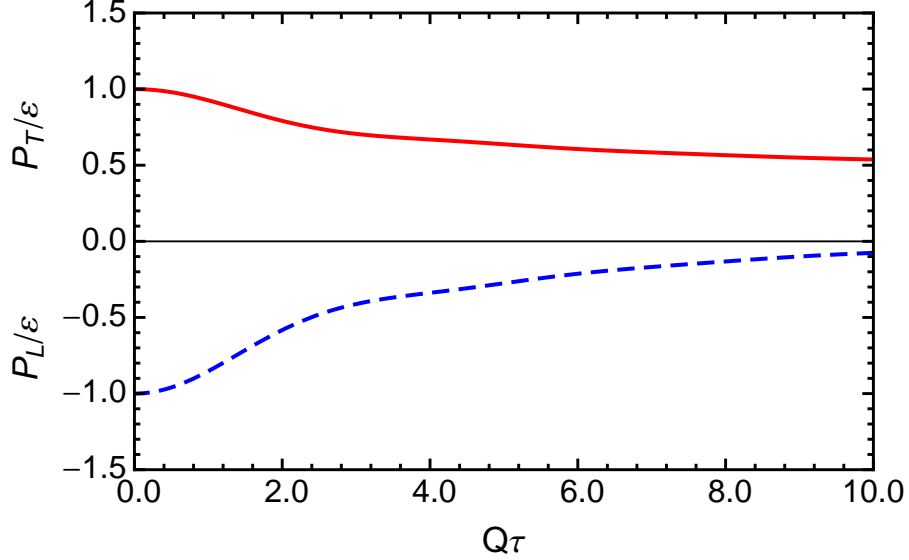
Figure 2.6: The pressures P_T/ε and P_L/ε as functions of $Q\tau$ with different calculated accuracy. The lines in the upper half plane represent P_T/ε while lines on the lower half plane represent P_L/ε. The notation is the same as in Fig. 2.3.

2.4.3 Leading Q^2 Approximation vs Abelian Approximation

To further understand the leading Q^2 approximation, we compare the differences between the leading Q^2 approximation and the Abelian approximation. Specifically, we compare the time evolution of energy density and pressures from these two approximations. The leading Q^2 approximation, as an improvement on the Abelian approximation, incorporates non-Abelian interactions minimally so that all order resummations are still feasible when full non-Ablian calculations are impossible to achieve. The leading Q^2 approximation predicts that the chromo-electric fields have larger contributions to the energy density than the chromo-magnetic fields do while in the Abelian approximation, the chromo-electric fields

and the chromo-magnetic fields contribute the same.

The classical Yang-Mills equations Eq. (2.2) are nonlinear equations for the gluon fields $A^\eta(\tau, \mathbf{x}_\perp)$ and $A^i_\perp(\tau, \mathbf{x}_\perp)$. The nonlinear terms reside in the commutators due to the non-Abelian feature of the $SU(3)$ color group. Ignoring the nonlinear terms in Eq. (2.2) results in solutions that are in contradiction with the initial conditions Eq. (2.14). Note that the initial conditions contain a non-Abelian feature. The Abelian approximation can be implemented by focusing on the field strength tensor $F^{\mu\nu}$ instead of the gluon fields A^μ. Starting from the recursive solutions of the field strength tensor Eq. (2.19), the Abelian approximation is implemented by ignoring the commutators in Eq. (2.19). The recursive solutions reduce to

$$
\begin{aligned}
\tilde{F}^{\tau\eta}_{(2n)}(\mathbf{x}_\perp) &= -\frac{1}{4^n (n!)^2} \, \partial^{2n} E_0(\mathbf{x}_\perp), \\
B^z_{(2n)}(\mathbf{x}_\perp) &= \frac{1}{4^n (n!)^2} \, \partial^{2n} B_0(\mathbf{x}_\perp), \\
\tilde{F}^{\eta i}_{(2n-1)}(\mathbf{x}_\perp) &= \frac{2n}{4^n (n!)^2} \partial^i \partial^{2n-2} E_0(\mathbf{x}_\perp), \\
F^{\tau i}_{(2n-1)}(\mathbf{x}_\perp) &= \frac{2n}{4^n (n!)^2} \epsilon^{ij} \partial^j \partial^{2n-2} B_0(\mathbf{x}_\perp),
\end{aligned}
\tag{2.51}
$$

with $\tilde{F}^{\tau\eta} = \tau F^{\tau\eta} = -\frac{1}{\tau} F_{\tau\eta}$, $\tilde{F}^{\eta i} = \tau F^{\eta i} = \frac{1}{\tau} F_{\eta i}$, $F^{\tau i} = -F_{\tau i}$ and $F^{ij} = F_{ij}$. Then the power series expansions can be cast into closed forms in momentum space

$$
\begin{aligned}
F_{\tau\eta}(\tau, \mathbf{k}_\perp) &= E_0(\mathbf{k}_\perp) \tau J_0(k_\perp \tau), \\
B^z(\tau, \mathbf{k}_\perp) &= B_0(\mathbf{k}_\perp) J_0(k_\perp \tau), \\
F_{\eta i}(\tau, \mathbf{k}_\perp) &= \frac{i k^i_\perp}{k_\perp} E_0(\mathbf{k}_\perp) \tau J_1(k_\perp \tau), \\
F^{\tau i}(\tau, \mathbf{k}_\perp) &= \frac{i \epsilon^{ij} k^j_\perp}{k_\perp} B_0(\mathbf{k}_\perp) J_1(k_\perp \tau).
\end{aligned}
\tag{2.52}
$$

Here $J_0(x)$ and $J_1(x)$ are Bessel functions of the first kind. The $E_0(\mathbf{k}_\perp)$ and $B_0(\mathbf{k}_\perp)$ are the Fourier transformation of the initial longitudinal chromo-electric field and the chromo-magnetic field Eq. (2.20), respectively

$$
\begin{aligned}
E_0(\mathbf{x}_\perp) &= \int \frac{d^2\mathbf{k}_\perp}{(2\pi)^2} e^{i\mathbf{k}_\perp \cdot \mathbf{x}_\perp} E_0(\mathbf{k}_\perp), \\
B_0(\mathbf{x}_\perp) &= \int \frac{d^2\mathbf{k}_\perp}{(2\pi)^2} e^{i\mathbf{k}_\perp \cdot \mathbf{x}_\perp} B_0(\mathbf{k}_\perp).
\end{aligned}
\tag{2.53}
$$

The energy density and pressures are related to the event-averaged correlation functions of the chromo-electric fields and the chromo-magnetic fields

$$
\begin{aligned}
\langle E^z(\tau, \mathbf{x}_\perp) E^z(\tau, \mathbf{x}_\perp) \rangle &= \langle \frac{1}{\tau^2} F_{\tau\eta} F_{\tau\eta} \rangle = \int \frac{d^2\mathbf{k}_\perp}{(2\pi)^2} G_{E_0}(\mathbf{k}_\perp) \left[J_0(k_\perp \tau) \right]^2 , \\
\langle B^z(\tau, \mathbf{x}_\perp) B^z(\tau, \mathbf{x}_\perp) \rangle &= \int \frac{d^2\mathbf{k}_\perp}{(2\pi)^2} G_{B_0}(\mathbf{k}_\perp) \left[J_0(k_\perp \tau) \right]^2 , \\
\langle E^i(\tau, \mathbf{x}_\perp) E^i(\tau, \mathbf{x}_\perp) \rangle &= \langle F_{\tau i} F_{\tau i} \rangle = \int \frac{d^2\mathbf{k}_\perp}{(2\pi)^2} G_{B_0}(\mathbf{k}_\perp) \left[J_1(k_\perp \tau) \right]^2 , \\
\langle B^i(\tau, \mathbf{x}_\perp) B^i(\tau, \mathbf{x}_\perp) \rangle &= \langle \frac{1}{\tau^2} F_{i\eta} F_{i\eta} \rangle = \int \frac{d^2\mathbf{k}_\perp}{(2\pi)^2} G_{E_0}(\mathbf{k}_\perp) \left[J_1(k_\perp \tau) \right]^2 .
\end{aligned}
\tag{2.54}
$$

with

$$
\begin{aligned}
G_{E_0}(\mathbf{k}_\perp) &= \int d^2\mathbf{r}_\perp e^{-i\mathbf{k}_\perp \cdot \mathbf{r}_\perp} \langle E_0(\mathbf{x}_\perp) E_0(\mathbf{y}_\perp) \rangle , \\
G_{B_0}(\mathbf{k}_\perp) &= \int d^2\mathbf{r}_\perp e^{-i\mathbf{k}_\perp \cdot \mathbf{r}_\perp} \langle B_0(\mathbf{x}_\perp) B_0(\mathbf{y}_\perp) \rangle .
\end{aligned}
\tag{2.55}
$$

The initial correlation functions are equal $\langle E_0(\mathbf{x}_\perp) E_0(\mathbf{y}_\perp) \rangle = \langle B_0(\mathbf{x}_\perp) B_0(\mathbf{y}_\perp) \rangle$ and only depend on $\mathbf{r}_\perp = \mathbf{x}_\perp - \mathbf{y}_\perp$. We will denote $G(\mathbf{k}_\perp) = G_{E_0}(\mathbf{k}_\perp) = G_{B_0}(\mathbf{k}_\perp)$. The final expressions for the energy density and pressures in the Abelian approximation are

$$
\begin{aligned}
\varepsilon(\tau) &= \int \frac{d^2\mathbf{k}_\perp}{(2\pi)^2} G(\mathbf{k}_\perp) \left[(J_0(k_\perp \tau))^2 + (J_1(k_\perp \tau))^2 \right] , \\
P_L(\tau) &= \int \frac{d^2\mathbf{k}_\perp}{(2\pi)^2} G(\mathbf{k}_\perp) \left[-(J_0(k_\perp \tau))^2 + (J_1(k_\perp \tau))^2 \right] , \\
P_T(\tau) &= \int \frac{d^2\mathbf{k}_\perp}{(2\pi)^2} G(\mathbf{k}_\perp) \left[(J_0(k_\perp \tau))^2 \right] .
\end{aligned}
\tag{2.56}
$$

The energy density and pressures in the Abelian approximation have been obtained by several different groups, either by solving the classical Yang-Mills equations assuming the color sources being weak [68, 69] or by perturbative QCD calculations at the lowest order [88, 89]. One advantage of the small-τ power series expansion method is that it naturally reproduces the Abelian approximation in a very simple and clear way.

In the leading Q^2 approximation, non-Abelian effects are minimally included, which appears to slow down the decreases of energy density and transverse pressure compared with results from the Abelian approximation, see Figs. 2.7 and 2.8. The increase of the longitudinal pressure is also slowed down in the leading Q^2 approximation in Fig. 2.9. In addition, chromo-electric fields and chromo-magnetic fields have the same contribution to the energy density in the Abelian approximation while in the leading Q^2 approximation, the chromo-electric fields have larger contribution to the energy density than the chromo-magnetic fields do as shown in Figs. 2.10 and 2.11. In numerical calculations of the Abelian approximation, we chose by trial and error the upper and the lower limits for the momentum space integrals to be $k_{\mathrm{max}} = 2.82\, Q$ and $k_{\mathrm{min}} = 0$, respectively, so that correct normalizations are maintained.

The discrepancy between the chromo-electric fields and the chromo-magnetic fields in their contributions to the energy density can be understood as follows. The initial condition Eq. (2.20) tells us that $E^z \neq B^z$ and $E^i = B^i = 0$ at $\tau = 0$ for a single event. However, after statistically averaging over all the configurations of color sources, $\langle E^z E^z \rangle = \langle B^z B^z \rangle$. Therefore, the contributions to the energy density from the chromo-electric fields and the chromo-magnetic fields are the
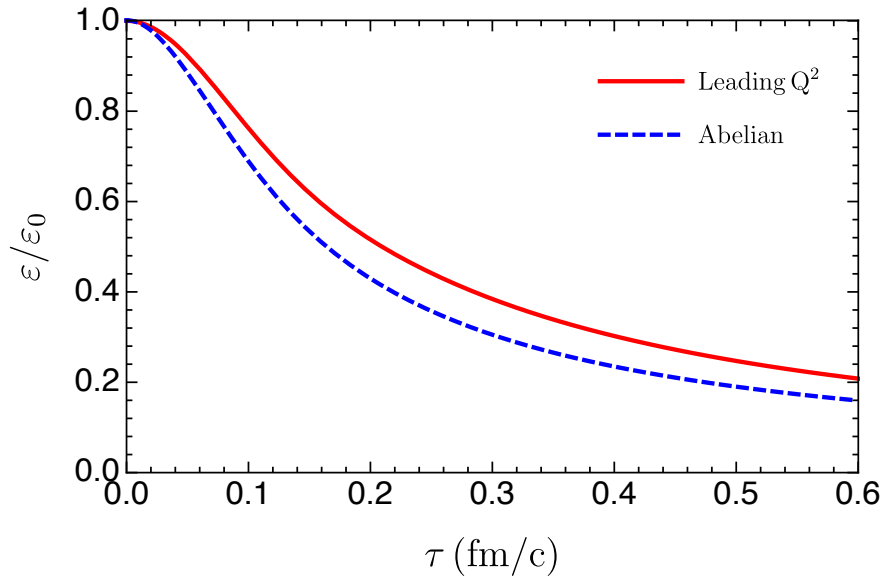
Figure 2.7: Comparison of the time evolution of energy density from the Abelian approximation and the leading Q^2 approximation.
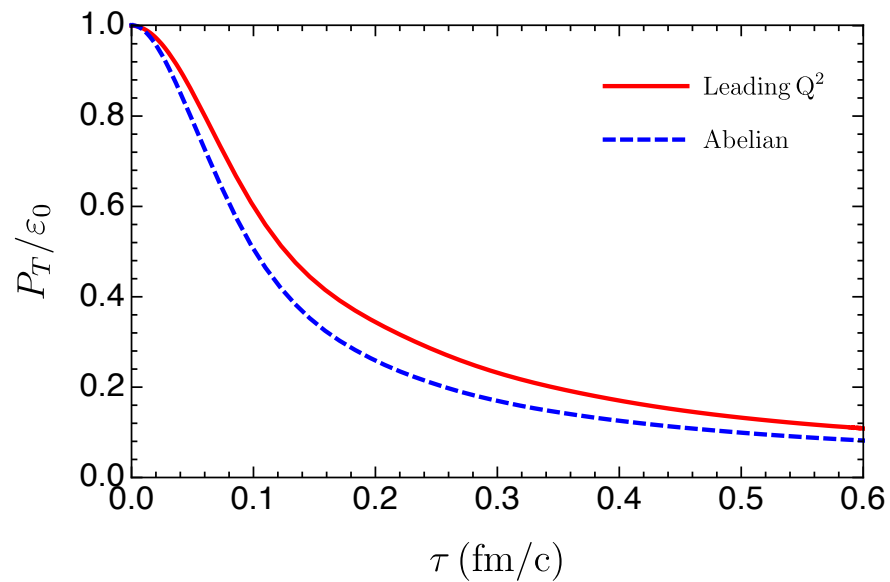
Figure 2.8: Comparison of the time evolution of transverse pressure from the Abelian approximation and the leading Q^2 approximation.
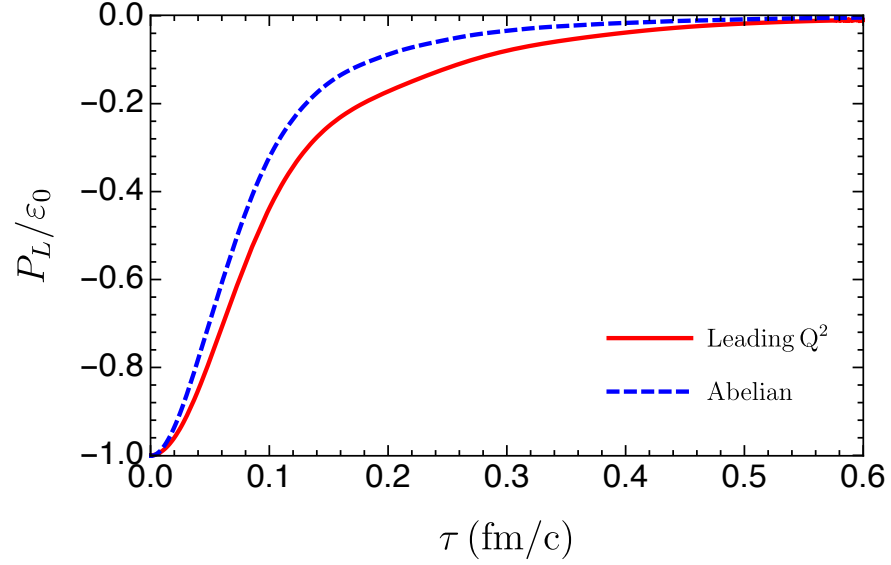
Figure 2.9: Comparison of the time evolution of longitudinal pressure from the Abelian approximation and the leading Q^2 approximation.
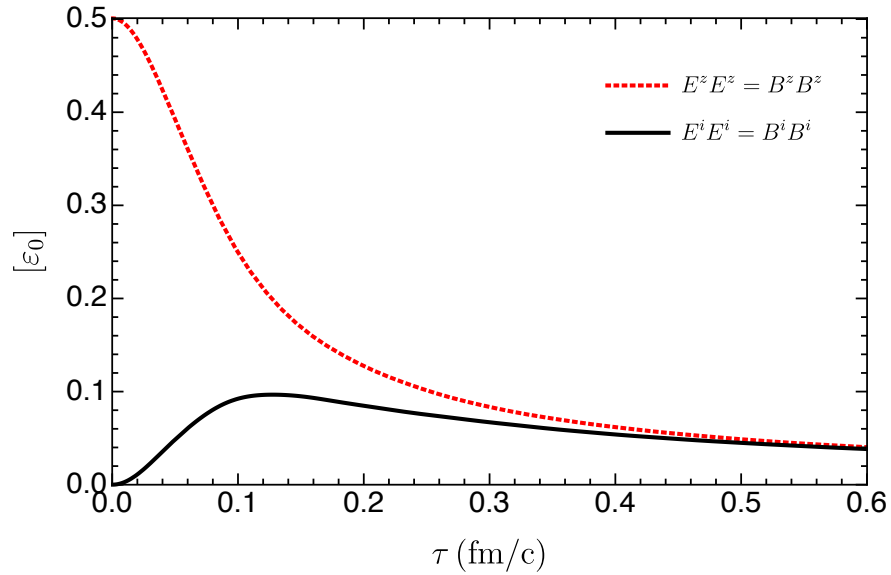
Figure 2.10: Time evolution of the chromo-electric fields and the chromo-magnetic fields as contributions to the energy density in the Abelian approximation.
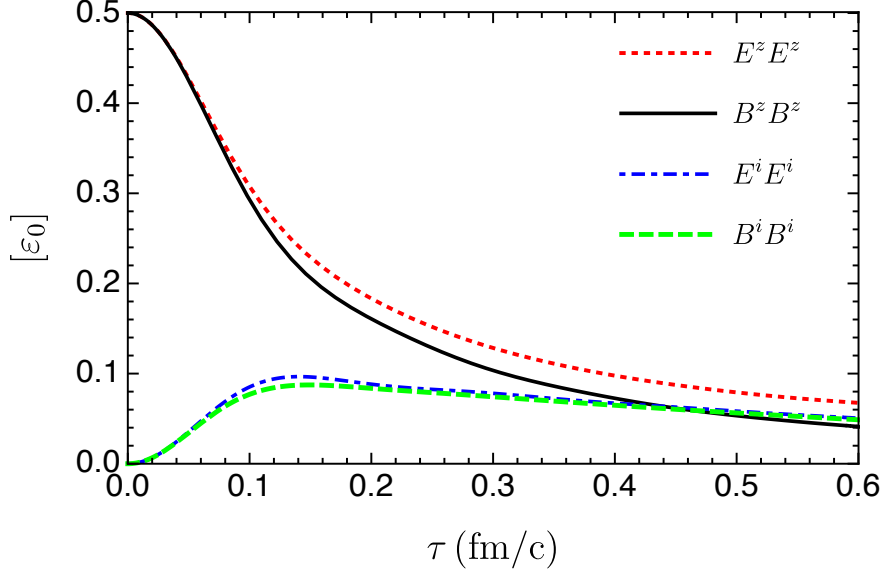
Figure 2.11: Time evolution of the chromo-electric fields and the chromo-magnetic fields as contributions to the energy density in the leading Q^2 approximation.

same at $\tau = 0$. This fact is also shown in Figs. 2.10 and 2.11.

- In the Abelian approximation, the chromo-electromagnetic fields for $\tau > 0$ are factorized into two parts. The initial magnitudes are determined by E_0 and B_0 while time evolution are governed by the Bessel functions, see Eq. (2.52). The chromo-electric fields and the chromo-magnetic fields are different event-by-event but their event averaged values are the same $\langle E^z E^z \rangle = \langle B^z B^z \rangle$ and $\langle E^i E^i \rangle = \langle B^i B^i \rangle$ see Eq. (2.54).

- In the leading Q^2 approximation, the chromo-electromagnetic fields for $\tau > 0$ can not be simply factorized any more due to the existence of non-Abelian commutators see Eq. (2.38). After averaging over initial color configurations, the initial difference between E_0 and B_0 are kept in the statistical averaging

due to the non-Abelian commutators. In other words, event-averaged time evolution of the chromo-electric fields and the chromo-magnetic fields are different. As a result, $\langle E^z E^z \rangle \neq \langle B^z B^z \rangle$ and $\langle E^i E^i \rangle \neq \langle B^i B^i \rangle$, see detailed expressions in [90]. The largeness of the chromo-electric fields can be traced back to the δ^{ij} in the initial E_0 compared to the ϵ^{ij} in the initial B_0. Spatial indexes are contracted with δ^{ij} and ϵ^{ij} respectively in the process of statistical averaging.

Apart from the bulk properties, like the energy density and pressures, the leading Q^2 approximation differs from the Abelian approximation in obtaining a reasonable gluon spectrum later in the Glasma evolution. In [90], the gluon spectrum in the leading Q^2 approximation was studied by the author. There the gluon spectrum is defined by

$$
\frac{dN}{d^2\mathbf{k}_\perp dy} = \frac{1}{2(2\pi)^2} \frac{1}{k_\perp} \left\{ \left[\tau F_{i\tau}(\tau, \mathbf{k}_\perp) F_{i\tau}(\tau, -\mathbf{k}_\perp) + \frac{1}{\tau} F_{\tau\eta}(\tau, \mathbf{k}_\perp) F_{\tau\eta}(\tau, -\mathbf{k}_\perp) \right] \right.
$$
$$
\left. + \left[\frac{\tau}{2} F_{ij}(\tau, \mathbf{k}_\perp) F_{ij}(\tau, -\mathbf{k}_\perp) + \frac{1}{\tau} F_{i\eta}(\tau, \mathbf{k}_\perp) F_{i\eta}(\tau, -\mathbf{k}_\perp) \right] \right\}.
$$
(2.57)

Using this definition, one can show the time evolution of different momentum modes. It was believed that gluons are liberated from the classical fields and form the quark-gluon plasma later on in the weakly coupling picture of thermalization [82]. To obtain a meaningful gluon spectrum at the moment when descriptions using classical gluon fields should be changed to descriptions using particle degrees of freedom, the gluon spectrum should not vary much. Therefore, a time-independent gluon spectrum is expected at late time in the Glasma evolution [76, 77]. From this perspective, the leading Q^2 approximation cures

the large oscillating features of the Abelian approximation within a proper time window $\tau < 0.6\,\text{fm/c}$; see Figs. 2.12 and Fig. 2.13. This is also an indication that non-Abelian effects have to be included in the study of gluon spectrum.
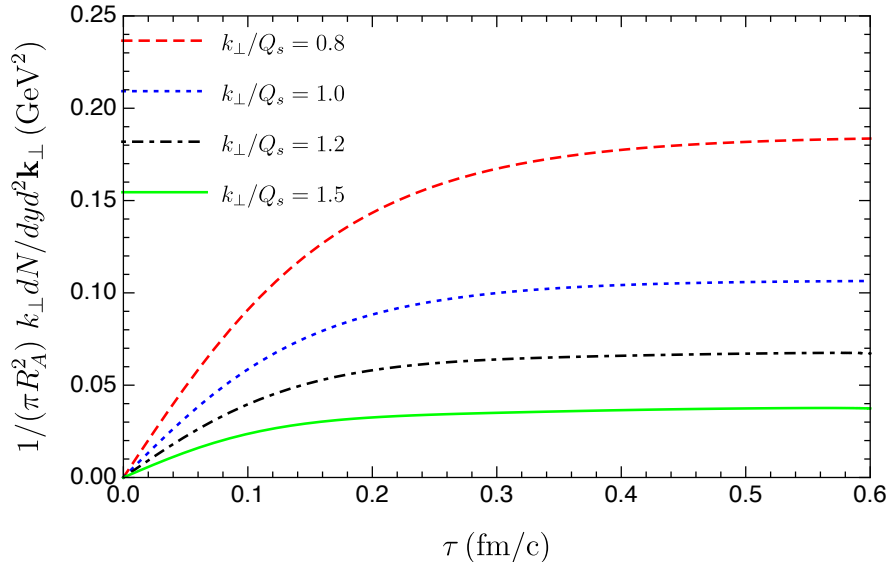
Figure 2.12: Time evolution of the gluon spectrum for different momentum modes in the leading Q^2 approximation.

2.5 Conclusion

In this chapter, we expanded the semi-analytic approach in solving the classical Yang-Mills equations using the power series expansion method proposed by Fries, Kapusta and Yang Li. Exact order-by-order calculations have only been done up to fourth order in proper time $(\mathcal{O}(\tau^4))$ and first order in gradient expansion of the transverse color fluctuation distributions. These results are important for understanding the very early time dynamics of high energy heavy-ion collisions
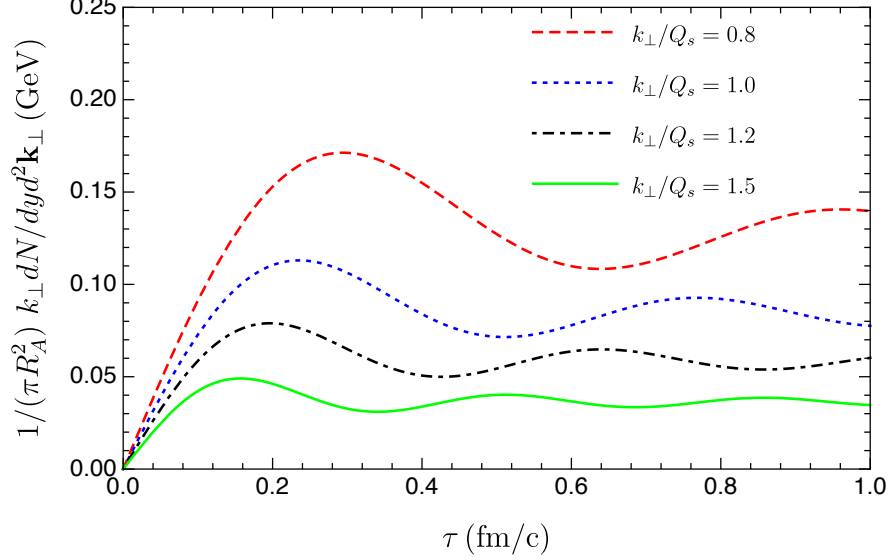
Figure 2.13: Time evolution of the gluon spectrum for different momentum modes in the Abelian approximation.

in the framework of CGC, particularly the initial energy density, pressures and the initial flows. However, the time window for the validity of these results is relatively small and late time properties of the classical gluon fields can not be probed. To generalize the calculations to higher orders in the power series expansion, we imposed isotropy and homogeneity in the transverse plane and assumed the transverse momentum scale separation $Q^2 \gg Q_s^2 \gg m^2$. Under these conditions, we were able to compute the solutions of classical Yang-Mills equations to all orders in the power series expansion in proper time. This leading Q^2 approximation incorporates a minimal amount of non-Abelian effects in the solutions and serves as the most simple improvement on the well known Abelian approximation. We calculated the energy-momentum tensor of the classical gluon fields. Our calculations showed that the energy density and the transverse pressure decrease

from initially positive values and stay positive values at late time. The longitudinal pressure however increases from initially negative value towards zero at late time. These results from the semi-analytic approach are consistent with the results from numerical simulations. Additionally, the leading Q^2 approximation predicts that the chromo-electric fields make a larger contribution to the energy density than the chromo-magnetic fields do during the time evolution. This is different from the situation in the Abelian approximation where the chromo-electric fields and the chromo-magnetic fields have the same contributions to the energy density. Finally, the leading Q^2 approximation can be used to study the gluon spectrum at late times of the Glasma evolution, while it is problematic for the Abelian approximation to properly define a time-independent distribution within the relevant time window.

The energy-momentum tensor calculated under the leading Q^2 approximation will be used to describe the central region of high energy heavy-ion collisions at the early stage before the formation of quark-gluon plasma in next chapter. Other special features of this energy-momentum tensor will be further discussed there.

Chapter 3

High Baryon Densities Achievable in the Fragmentation Regions of High Energy Heavy Ion Collisions

3.1 Introduction

As explained in Chapter 1 Sec. 1.3, kinematic nuclear compression in the fragmentation regions of high energy heavy-ion collisions result in enhanced baryon density Eq. (1.6). The enhancement factor $e^{\Delta y}$ involves the change of rapidity in the collision and is Lorentz boost invariant. To estimate the baryon density achievable in the fragmentation regions, one needs to compute the rapidity change Δy for the colliding nuclei in high energy heavy-ion collisions. This will be the main task in this chapter. Apart from the kinematic nuclear compression, there must be *nuclear excitation* accompanying it. This is easily understood as follows.

If the system are made of noninteracting particles, kinematic nuclear compression only reduces the inter-particle distances. However, if the system consists of particles strongly coupled with each other, kinematic nuclear compression also requires nuclear excitation at the same time because as the inter-particle distance changes, the potential energy between constituents will increase. Therefore, a proper modeling should incorporate both the nuclear stopping and the nuclear excitation energy.

In this chapter, we will use Au+Au collisions at center-of-momentum collision energy $\sqrt{s_{NN}} = 200\,\mathrm{GeV}$, the top RHIC collision energy, as a prototype and calculate the baryon density and energy density achievable in the fragmentation regions. In this way, we are calculating the change of rapidity Δy in the center-of-momentum frame rather than in the target rest frame where the nuclear compression formula is obtained. The Δy is Lorentz boost invariant and we exploit this freedom to our advantage. As alluded to in Chapter 2, we use the energy-momentum tensor of the Glasma in the central region. We consider the backreaction of the Glasma on the receding nuclei. Imposing energy and momentum conservation on the Glasma + nuclei system, the increase of energy and momentum for the Glasma should be equal to the decrease of the energy and momentum from the nuclei. Solving the energy momentum conservation equations gives us the anticipated rapidity loss and excitation energy for the colliding nuclei. Once we have the baryon density and energy density, we further estimate the corresponding temperature and baryon chemical potential in the fragmentation regions. This is done with the help of a realistic crossover equation of state that smoothly connects the quark-gluon plasma phase at high temperature and high

baryon chemical potential to the hadronic resonance gas phase at low temperature and small baryon chemical potential. With the prototype Au+Au collision at $\sqrt{s_{NN}} = 200\,\mathrm{GeV}$ at hand, we also explore other collision configurations, such as the asymmetric Cu+Au collision and collisions involving distorted nuclei like U+U collisions. Non-central collisions for Au+Au are also studied. In addition, we consider the Pb+Pb collisions at even higher energy at the LHC. Baryon densities achievable in the fragmentation regions for all these collision configurations will be presented.

The outline of this chapter is as follows. In Sec. 3.2 the formalism in implementing energy-momentum conservation for the Glasma + nuclei system is presented. Properties of the equations of motion and determining the input parameters are discussed. Section 3.3 is devoted to the high baryon densities in the fragmentation regions of the prototype Au+Au central collision at $\sqrt{s_{NN}} = 200\,\mathrm{GeV}$. In Sec. 3.4, systematic studies of the high baryon densities in high energy heavy-ion collisions are given. We consider the nuclear size dependence, the collision energy dependence and also collisions with non-zero impact parameter.

3.2 Baryon Rapidity Loss and Nuclear Excitation Energy

3.2.1 Equations of Motion

For high energy heavy-ion collisions in the center-of-momentum frame, the nuclei are highly Lorentz contracted and look like pancakes in shape. We neglect transverse dynamics, which should not be important during the fraction of a fm/c time

interval of relevance. Then the collision can be thought of as a sum of slab-slab collisions each taking place at a particular value of the transverse coordinate $\mathbf{r}_\perp$ with the beam along the z-axis. The projectile slab has a 4-momentum per unit area in the center-of-momentum frame denoted by $\mathcal{P}_P^\mu = (\mathcal{E}_P, 0, 0, \mathcal{P}_P)$. The slab loses energy and momentum to the classical color electric and magnetic fields produced in the region between the two receding slabs. This loss is quantified by

$$d\mathcal{P}_P^\mu = -T_{\text{glasma}}^{\mu\nu} d\Sigma_\nu \tag{3.1}$$

where $d\Sigma_\nu = (dz, 0, 0, -dt)$ is the infinitesimal four-vector perpendicular to the hypersurface spanned by dt, dz, and unit transverse area. The energy-momentum tensor of the Glasma has been calculated in Chapter 2 as

$$T_{\text{glasma}}^{\mu\nu} = \begin{pmatrix} \mathcal{A} + \mathcal{B}\cosh 2\eta & 0 & 0 & \mathcal{B}\sinh 2\eta \\ 0 & \mathcal{A} & 0 & 0 \\ 0 & 0 & \mathcal{A} & 0 \\ \mathcal{B}\sinh 2\eta & 0 & 0 & -\mathcal{A} + \mathcal{B}\cosh 2\eta \end{pmatrix}. \tag{3.2}$$

The $\mathcal{A}$ and $\mathcal{B}$ are functions of proper time $\tau = \sqrt{t^2 - z^2}$ (and other input parameters to be discussed in the following), while the dependence on space-time rapidity $\eta = \frac{1}{2}\ln[(t+z)/(t-z)]$ follows from the fact that $T_{\text{glasma}}^{\mu\nu}$ is a second-rank tensor in a boost-invariant setting. The longitudinal position of the slab z_P is a function of time, $z_P = z_P(t)$. The z_P is related to the time t via the velocity $v_P = dz_P/dt = \tanh y_P$, where y_P is the momentum-space rapidity of the slab. Hence all the quantities solely depend on t. Note that $T_{\text{glasma}}^{\mu\nu}$ must be evaluated

on the trajectory of the slab. Explicitly

$$d\mathcal{E}_{\mathrm{P}}(t, z_{\mathrm{P}}) = -T^{00}_{\mathrm{glasma}}(t, z_{\mathrm{P}})dz_{\mathrm{P}} + T^{03}_{\mathrm{glasma}}(t, z_{\mathrm{P}})dt \,,$$
$$d\mathcal{P}_{\mathrm{P}}(t, z_{\mathrm{P}}) = -T^{30}_{\mathrm{glasma}}(t, z_{\mathrm{P}})dz_{\mathrm{P}} + T^{33}_{\mathrm{glasma}}(t, z_{\mathrm{P}})dt \,. \tag{3.3}$$

It is useful to define the Lorentz invariant effective mass per unit area $\mathcal{M}_{\mathrm{P}}$ via the relations $\mathcal{E}_{\mathrm{P}} = \mathcal{M}_{\mathrm{P}} \cosh y_{\mathrm{P}}$ and $\mathcal{P}_{\mathrm{P}} = \mathcal{M}_{\mathrm{P}} \sinh y_{\mathrm{P}}$ so that

$$d\mathcal{E}_{\mathrm{P}} = \cosh y_{\mathrm{P}} \, d\mathcal{M}_{\mathrm{P}} + \mathcal{M}_{\mathrm{P}} \sinh y_{\mathrm{P}} \, dy_{\mathrm{P}} \,,$$
$$d\mathcal{P}_{\mathrm{P}} = \sinh y_{\mathrm{P}} \, d\mathcal{M}_{\mathrm{P}} + \mathcal{M}_{\mathrm{P}} \cosh y_{\mathrm{P}} \, dy_{\mathrm{P}} \,. \tag{3.4}$$

We then re-express the differential form of the energy momentum conservation Eq. (3.3) in terms of the Milne coordinates $(\tau, \mathbf{x}_\perp, \eta)$. Using the transformations $\tau = \sqrt{t^2 - z_{\mathrm{P}}^2}$ and $\eta_{\mathrm{P}} = \frac{1}{2} \ln[(t + z_{\mathrm{P}})/(t - z_{\mathrm{P}})]$, the pseudorapidity of the projectile slab η_{P} follows the equation

$$\tau \frac{d\eta_{\mathrm{P}}}{d\tau} = \tanh\left(y_{\mathrm{P}} - \eta_{\mathrm{P}}\right) \tag{3.5}$$

where the auxiliary relations between (t, z_{P}) and $(\tau, \eta_{\mathrm{P}})$

$$\frac{d\tau}{dt} = \frac{\cosh\left(y_{\mathrm{P}} - \eta_{\mathrm{P}}\right)}{\cosh y_{\mathrm{P}}} \,,$$
$$\frac{d\tau}{dz_{\mathrm{P}}} = \frac{\cosh\left(y_{\mathrm{P}} - \eta_{\mathrm{P}}\right)}{\sinh y_{\mathrm{P}}} \,, \tag{3.6}$$

have been used. Substituting Eqs. (3.2), (3.4), (3.6) into Eq. (3.3), we finally obtain the equations of motion for the rapidity y_{P} and the effective mass $\mathcal{M}_{\mathrm{P}}$ of the projectile slab in terms of Milne coordinates

$$-\mathcal{M}_{\mathrm{P}} \cosh\left(y_{\mathrm{P}} - \eta_{\mathrm{P}}\right)\frac{dy_{\mathrm{P}}}{d\tau} = \mathcal{A}(\tau) - \mathcal{B}(\tau) \cosh\left(2y_{\mathrm{P}} - 2\eta_{\mathrm{P}}\right),$$
$$\cosh\left(y_{\mathrm{P}} - \eta_{\mathrm{P}}\right)\frac{d\mathcal{M}_{\mathrm{P}}}{d\tau} = -\mathcal{B}(\tau) \sinh\left(2y_{\mathrm{P}} - 2\eta_{\mathrm{P}}\right). \tag{3.7}$$

Note that Eq. (3.7) should be supplemented by the equation for pseudorapidity η_P via Eq. (3.5). It is important to point out that y_P and $\mathcal{M}_P$ are dynamical variables while η_P is a geometric variable coming from the coordinate transformation. Equations (3.7) and (3.5) are coupled first order differential equations. Given the functions $\mathcal{A}(\tau)$ and $\mathcal{B}(\tau)$ from the Glasma energy-momentum tensor, initial conditions are needed to solve for y_P, $\mathcal{M}_P$ and η_P as functions of proper time τ. Before discussing the initial conditions and numerical solutions of the equations, a few important properties of Eqs. (3.5) and (3.7) are worth noting.

- First, if $\mathcal{B}(\tau) = 0$, the glasma energy-momentum tensor becomes diagonal $T^{\mu\nu}_{\text{glasma}} = \text{diag}(\mathcal{A}, \mathcal{A}, \mathcal{A}, -\mathcal{A})$ which is equivalent to the string rope model [91, 92]. In this situation, $d\mathcal{M}_P/d\tau = 0$ and the effective mass $\mathcal{M}_P$ does not change with time. No nuclear excitation happens. On the other hand, the rapidity y_P decreases with time. As long as $\mathcal{A}(\tau) \neq 0$, y_P decreases until it becomes negative when the yo-yo type motion in string rope models appear. Therefore, nonvanishing and finite $\mathcal{B}(\tau)$ is necessary to incorporate nuclear excitation energy and prevent the appearance of yo-yo type motion. The Glasma energy-momentum tensor predicts a nonvanishing $\mathcal{B}(\tau)$. Physically, the function $\mathcal{A}(\tau)$ represents contributions from the longitudinal chromo-electromagnetic fields E^z and B^z while the function $\mathcal{B}(\tau)$ represents contributions from the transverse chromo-electromangetic fields E^i and B^i. Initially at $\tau = 0$, $\mathcal{A} \neq 0$ and $\mathcal{B} = 0$, the initial transverse fields are zero while the initial longitudinal fields are nonzero. As the Glasma evolves, $\mathcal{B}$ gradually increases while $\mathcal{A}$ gradually decreases until they become very close at late time, see Figs. 2.10 and 2.11.

- Second, for nonvanishing and positive $\mathcal{B}(\tau)$, whether the effective mass $\mathcal{M}_{\mathrm{P}}(\tau)$ increases or decreases with time is controlled by the sign of $y_{\mathrm{P}}(\tau) - \eta_{\mathrm{P}}(\tau)$. To have excitation energy, that is $\mathcal{M}_{\mathrm{P}}(\tau)$ increasing with time, $y_{\mathrm{P}}(\tau) < \eta_{\mathrm{P}}(\tau)$ has to be maintained. From the definition $\tanh y_{\mathrm{P}} = dz_{\mathrm{P}}/dt$, one obtains $z_{\mathrm{P}} = \int_0^t \tanh y_{\mathrm{P}}(t')dt' > \tanh y_{\mathrm{P}}(t)\,t$ because the velocity of the projectile slab $v_{\mathrm{P}} = \tanh y_{\mathrm{P}}$ decreases with time. Therefore, with $\tanh \eta_{\mathrm{P}} = z_{\mathrm{P}}/t$, the condition $y_{\mathrm{P}} < \eta_{\mathrm{P}}$ is strictly guaranteed. In conclusion, positive values of $\mathcal{B}(\tau)$ predict increase of the effective mass, the nuclear excitation energy. In addition, as long as $y_{\mathrm{P}} \neq \eta_{\mathrm{P}}$, the effective mass always increases with time, which brings out the question of a cutoff time dependence of nuclear excitation energy. Physically, the increase of effective mass is governed by the strength of the transverse chromo-electromagnetic fields in the Glasma which gradually build up over time. It is worthy pointing out that this increase of transverse chromo-electromagnetic fields is not due to the decrease of the effective mass but comes from the decrease of the longitudinal chromo-electromagnetic fields.

- Third, for $y_{\mathrm{P}} < \eta_{\mathrm{P}}$, Eq. (3.5) predicts the pseudorapidity η_{P}, like y_{P}, also decreases with time. This decrease of η_{P} is purely kinematic in nature as a way to respond to any changes of y_{P}. On the other hand, Eq. (3.7) predicts the rate of momentum space rapidity loss $dy_{\mathrm{P}}/d\tau$ becomes smaller and smaller and finally saturates due to the time dependent properties of the functions $\mathcal{A}(\tau)$ and $\mathcal{B}(\tau)$.

To summarize, the nonvanishing and positive function $\mathcal{B}(\tau)$ in the glasma energy-momentum tensor, which is due to the transverse chromo-electromagnetic fields

that gradually build up, is responsible for the nuclear excitation and prevents the momentum space rapidity from forever decreasing.

3.2.2 Determining the Input Parameters

Initial conditions are easy to specify. For nucleus-nucleus collisions given by the center-of-momentum collision energy per nucleon pair $\sqrt{s_{NN}}$, the initial rapidity $y_{\rm P}(\tau = 0)$ is computed by

$$y_{\rm P}(\tau = 0) \equiv y_0 = \cosh^{-1}\left(\frac{\sqrt{s_{NN}}}{2m_N}\right) \tag{3.8}$$

where $m_N = 0.937(8)\,\text{GeV}$ is the nucleon mass. All the slabs have the same initial momentum space rapidity. The initial value of pseudorapidity $\eta_{\rm P}(\tau = 0)$ is undefined in principle, so we choose the initial value of $\eta_{\rm P}$ to be equal to y_0 and start numerical calculations at an infinitesimal initial time. Since we consider nucleus-nucleus collisions as a sum of slab-slab collisions at different $\mathbf{r}_\perp$, the initial effective mass, which is the mass per unit area, depends on the slab considered by

$$\mathcal{M}_{\rm P}(\mathbf{r}_\perp, \tau = 0) = T_A(\mathbf{r}_\perp)\, m_N. \tag{3.9}$$

Here $T_A(\mathbf{r}_\perp) = \int dz\, \rho_A(\mathbf{r}_\perp, z)$ is the nuclear thickness function for a nucleus with atomic mass number A. The $\rho_A(\mathbf{r}_\perp, z)$ is the Woods-Saxon distribution for a spherical nucleus.

Apart from the initial conditions, other input parameters come from the Glasma energy-momentum tensor. Specifically, the functions $\mathcal{A}(\tau)$ in Eq. (2.48) and $\mathcal{B}(\tau)$ in Eq. (2.49) factorize into two parts: the overall normalization ε_0 which is independent of time, and the time-dependent evolution functions. They can be

expressed as

$$\mathcal{A}(\tau) = \varepsilon_0 F_{\mathcal{A}} \left(\ln \left(Q^2/m^2 \right), Q\tau \right) ,$$

$$\mathcal{B}(\tau) = \varepsilon_0 F_{\mathcal{B}} \left(\ln \left(Q^2/m^2 \right), Q\tau \right) ,$$

(3.10)

The functions $F_{\mathcal{A}}$ and $F_{\mathcal{B}}$ depend on two free parameters, the ultraviolet cutoff scale Q and the infrared cutoff scale m on the transverse momentum. The ultraviolet cutoff scale characterizes the division between a description in terms of classical gluon fields and perturbative QCD . Larger values of Q attribute more energy and momentum to the classical fields whereas smaller values of Q attribute more to the production of partons or minijets. The infrared cutoff is identified as the Λ_{QCD} scale. The main complication comes from the initial energy density ϵ_0. To facilitate further discussions, we quote its expression here from Eq. (2.25)

$$\varepsilon_0(\mathbf{r}_\perp) = 2\pi\alpha_s^3 \frac{N_c}{N_c^2 - 1} \mu_1(\mathbf{r}_\perp)\mu_2(\mathbf{r}_\perp) \ln\left(\frac{Q_1^2}{m_1^2}\right) \ln\left(\frac{Q_2^2}{m_2^2}\right) .$$

(3.11)

Clearly, for different slab-slab collisions characterized by different values of $\mathbf{r}_\perp$, the initial energy densities $\varepsilon_0(\mathbf{r}_\perp)$ are different. This is due to the color charge fluctuation width $\mu(\mathbf{r}_\perp)$, which has the physical meaning of color charge squared per unit area and which is a function of the transverse location $\mathbf{r}_\perp$. Here $\mu_1(\mathbf{r}_\perp)$ and $\mu_2(\mathbf{r}_\perp)$ are the color charge fluctuation widths for the two colliding slabs. For a nucleus, we assume the color charge squared per unit area $\mu_A(\mathbf{r}_\perp)$ at the transverse location $\mathbf{r}_\perp$ is a sum of contributions from all the nucleons at $\mathbf{r}_\perp$, that is $\mu_A(\mathbf{r}_\perp) = T_A(\mathbf{r}_\perp)\mu_N$ [93, 94]. The μ_N, which characterizes the gluon saturation for a nucleon, particularly the proton, is related to the gluon saturation scale $Q_{s,N}^2$ up to a logarithmic modification [95]. The proton saturation scale $Q_{s,N}^2$ can be extracted from deep inelastic scattering experimental data [96]. With these

considerations, we relate the color charge squared per unit area for a slab at transverse position $\mathbf{r}_\perp$ to the slab at the central core region of the nucleus $\mathbf{r}_\perp = 0$ by

$$\frac{\mu_{\text{slab}}(\mathbf{r}_\perp)}{\mu_{\text{slab}}(\mathbf{r}_\perp = 0)} = \frac{T_A(\mathbf{r}_\perp)}{T_A(\mathbf{r}_\perp = 0)}. \tag{3.12}$$

As a consequence, the initial energy density for a slab-slab collision at transverse position $\mathbf{r}_\perp$ scales as

$$\frac{\varepsilon_0(\mathbf{r}_\perp)}{\varepsilon_0(\mathbf{r}_\perp = 0)} = \left[\frac{T_A(\mathbf{r}_\perp)}{T_A(\mathbf{r}_\perp = 0)}\right]^2. \tag{3.13}$$

In arriving at Eq. (3.13), we assume the ultraviolet cutoff Q and the infrared cutoff m are the same for all the slabs given the same two colliding nuclei for a fixed collision energy. For asymmetric collisions, the respective nuclear thickness function has to be used. To determine the initial energy density at the central core region $\varepsilon_0(\mathbf{r}_\perp = 0)$, initial conditions for hydrodynamic equations are invoked. Hydrodynamic equations require the initial value of the energy density $\varepsilon_{\text{hydro}}(\tau_0) \equiv \varepsilon_{\text{hydro}}(x = 0, y = 0; \tau = \tau_0)$ at spatial location $x = 0, y = 0$ with τ_0 the moment when hydrodynamics begins. Both $\varepsilon_{\text{hydro}}(\tau_0)$ and τ_0 are free input parameters of hydrodynamic simulations and are tuned to reproduce the experimental data. We assume the initial classical gluon fields from the glasma state are valid until $\tau = \tau_0$ when it is switched to the hydrodynamic state. This is in the same spirit with the IP-Glasma model [93, 94]. Therefore, the glasma energy density $\varepsilon_{\text{glasma}} = \mathcal{A}(\tau) + \mathcal{B}(\tau)$ (see Eq. (3.2)) at the central core region equals $\varepsilon_{\text{hydro}}(\tau_0)$ at $\tau = \tau_0$.

$$\varepsilon_0(\mathbf{r}_\perp = 0)\left[F_{\mathcal{A}}\left(\ln\left(Q^2/m^2\right), Q\tau_0\right) + F_{\mathcal{B}}\left(\ln\left(Q^2/m^2\right), Q\tau_0\right)\right] = \varepsilon_{\text{hydro}}(\tau_0). \tag{3.14}$$

Therefore $\varepsilon_0(\mathbf{r}_\perp = 0)$ can be solved once $\varepsilon_{\text{hydro}}(\tau_0)$ and τ_0 are given.

3.2.3   Numerical Results

In this subsection, we consider the most central Au+Au collision at the center-of-momentum collision energy $\sqrt{s_{NN}} = 200\,\mathrm{GeV}$. We focus on the slab-slab collision that comes from the central core region of the nucleus characterized by $\mathbf{r}_\perp = 0$ and compute the rapidity loss and nuclear excitation energy. The initial beam rapidity is $y_0 = 5.36$ from Eq. (3.8). For a gold nucleus, the nuclear atomic mass number is $A = 197$. The infrared cutoff is chosen to be $m = \Lambda_{QCD} = 0.2\,\mathrm{GeV}$. The initial mass per unit area is $\mathcal{M}_\mathrm{P}(\mathbf{r}_\perp = 0) = 2.03\,\mathrm{GeV/fm}^2$. We use the hydrodynamic initial energy density $\varepsilon_\mathrm{hydro}(\tau_0 = 0.6\,\mathrm{fm/c}) = 30.0\,\mathrm{GeV/fm}^3$, which has been adapted in the viscous hydrodynamic simulation in [97]. Depending on the ultraviolet cutoff chosen, $\varepsilon_0(\mathbf{r}_\perp)$ has values 123.2, 142.0 and 158.1 $\mathrm{GeV/fm}^3$ for $Q = 3.0$, 4.0 and 5.0 GeV, respectively; see Fig. 3.1. Different values of the ultraviolet cutoff Q only influence the time evolution of energy density at the very initial time period ($\tau \lesssim 0.15$); all the energy densities converge to the same values at later time when the transition to quark-gluon plasma is assumed. Typical time dependencies of $F_\mathcal{A}(\tau)$ and $F_\mathcal{B}(\tau)$ for $Q = 4.0\,\mathrm{GeV}$ are given in Fig. 3.2.

With these input parameters determined, we solve the equations of motion Eqs. (3.7) and (3.5) up to proper time $\tau = 0.6\,\mathrm{fm/c}$. Figure 3.3 shows the momentum-space rapidity y_P of the central core of a gold nucleus as a function of proper time τ. The beam rapidities in the center-of-momentum frame are ± 5.36 and the final rapidities are ± 2.47. The central core loses about three units of rapidity within the first 0.1-0.2 fm/c; this is a robust result, insensitive to the value of Q. The rate of rapidity loss decreases with time at the beginning and finally approaches
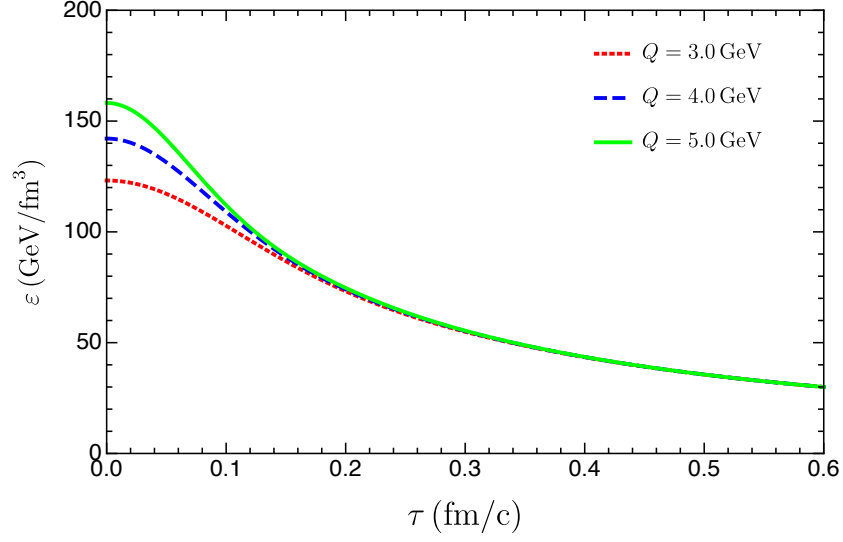
Figure 3.1: Time evolution of the energy density for different values of the ultraviolet cutoff scale Q given the hydrodynamic initial energy density $\varepsilon_{\mathrm{hydro}}(\tau_0 = 0.6\,\mathrm{fm/c}) = 30.0\,\mathrm{GeV/fm}^3$.
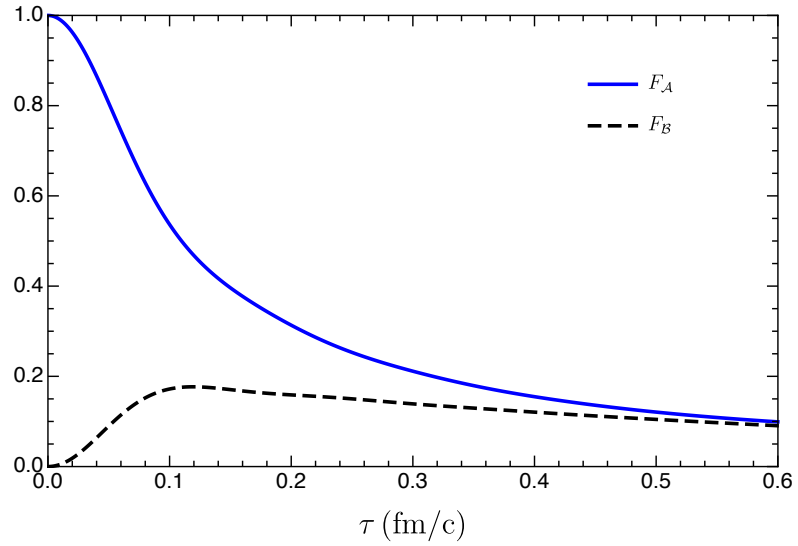
Figure 3.2: The dependence of $F_{\mathcal{A}}(\tau)$ and $F_{\mathcal{B}}(\tau)$ on proper time for $Q = 4.0\,\mathrm{GeV}$.

values close to zero, unlike the forever decreasing rapidity in string models. Figure 3.4 shows the excitation energy per baryon in units of the nucleon mass as a function of proper time. There is a slow but monotonic increase, unlike the rapidity loss whose asymptotic limit is reached within a few tenths of a fm/c. There is a weak dependence on Q. As can be seen from Eq. (3.7), the increasing rate of the nuclear excitation energy is determined by $2\mathcal{B}(\tau)\sinh(\eta_P - y_P)$. At late time, the $\mathcal{B}(\tau)$ maintains an almost constant positive value as shown in Fig. 3.2 while the difference $\eta_P - y_P$ slowly diminishes but maintains finite positive value as shown in Fig. 3.5. As a consequence, the increasing rate of the excitation energy gradually decreases. It is possible that the increase of the excitation energy saturates at large proper time outside the physical relevant range considered here. At $\tau = 0.6\,\mathrm{fm/c}$ the excitation energy reaches $\mathcal{M}_P/\mathcal{M}_P(\tau = 0) = 6.97$, approximately seven times larger than the nucleon rest mass. Finally, Fig. 3.6 shows the energy $\mathcal{E}_P = \mathcal{M}_P\cosh y_P$, momentum $\mathcal{P}_P = \mathcal{M}_P\sinh y_P$ and effective mass $\mathcal{M}_P$ as functions of proper time. The energy and momentum of the central core for a Au projectile nucleus decrease very quickly at the beginning due to the rapid decrease of y_P but then increase slowly due to the slow increase of effective mass and the almost constant y_P. In other words, in the interaction of the nuclei with the Glasma, the nuclei first lose energy and momentum to the Glasma in the form of rapidity loss and then slowly gain energy and momentum from the glasma in the form of nuclear excitation energy.
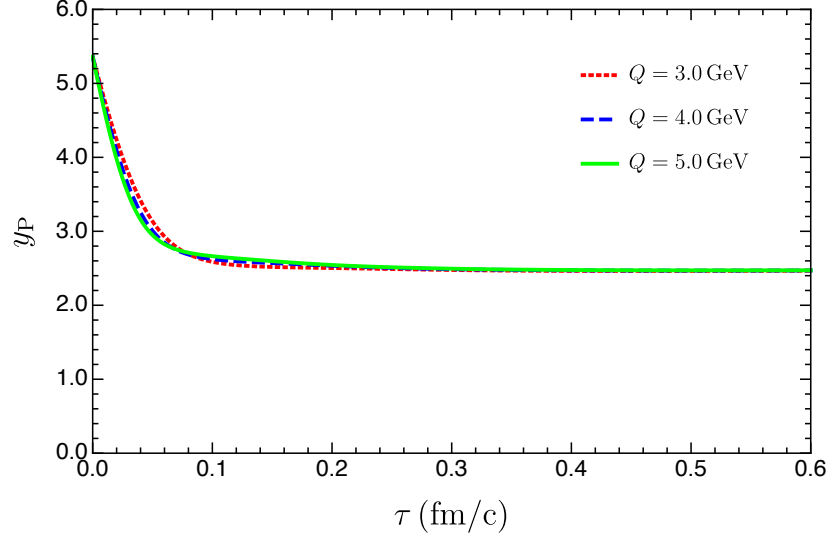
Figure 3.3: Rapidity of the central core of a Au projectile nucleus in the center-of-momentum frame for $\sqrt{s_{NN}} = 200\,\mathrm{GeV}$ as a function of proper time. The result is insensitive to the choice of Q in the physically relevant range.
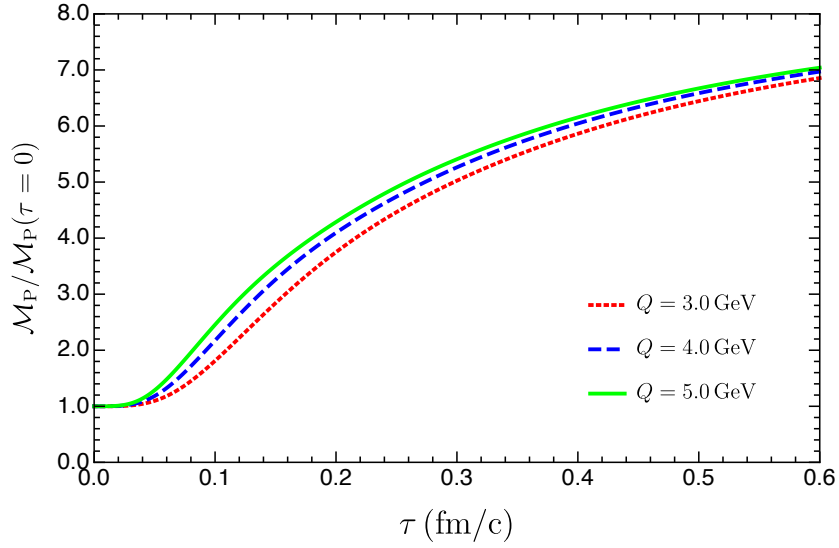
Figure 3.4: Excitation energy per baryon in the central core of a Au projectile nucleus in the center-of-momentum frame for $\sqrt{s_{NN}} = 200\,\mathrm{GeV}$ as a function of proper time. The result is mildly sensitive to the choice of Q in the physically relevant range.
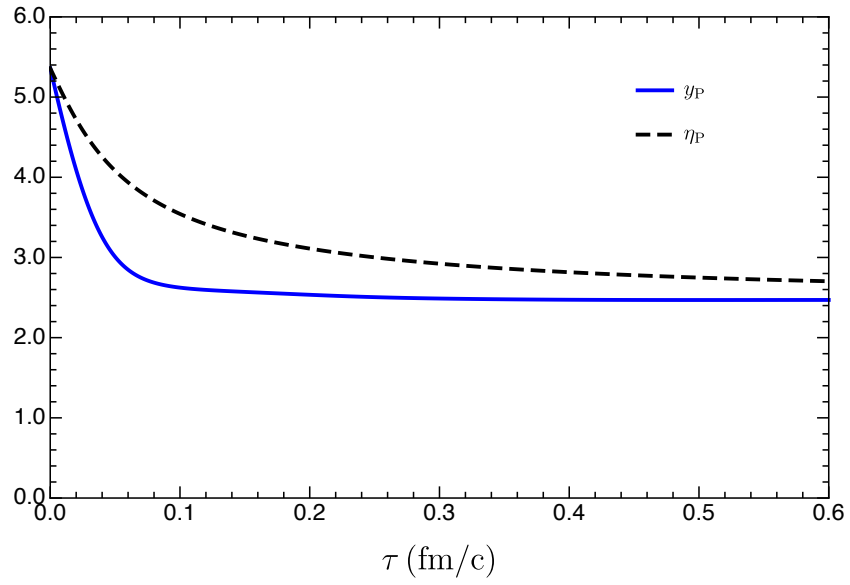
Figure 3.5: Momentum space rapidity y_P and coordinate space pseudorapidity η_P as functions of proper time for the central core of a Au projectile nucleus in the center-of-momentum frame for $\sqrt{s_{NN}} = 200\,\text{GeV}$. The ultraviolet cutoff is $Q = 4.0\,\text{GeV}$. The condition $y_P < \eta_P$ is maintained in the physically relevant proper time range.
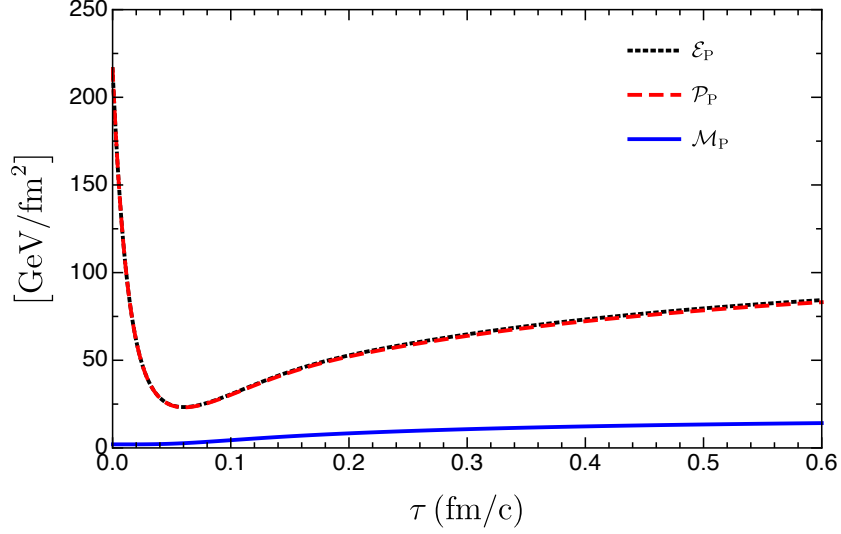
Figure 3.6: Energy $\mathcal{E}_{\mathrm{P}}$, momentum $\mathcal{P}_{\mathrm{P}}$ and effective mass $\mathcal{M}_{\mathrm{P}}$ per unit area as functions of proper time for the central core of a Au projectile nucleus in the center-of-momentum frame for $\sqrt{s_{NN}} = 200\,\mathrm{GeV}$. The ultraviolet cutoff is $Q = 4.0\,\mathrm{GeV}$.

3.3 High Baryon Density Achievable at Top RHIC Collision Energy

In the previous section, we calculated the rapidity loss and excitation energy for one single slab-slab collision that comes from the central core of the nucleus at $\mathbf{r}_\perp = 0$. In this section, we repeat the calculations for all the slab-slab collisions at different $\mathbf{r}_\perp$ with the help of Eqs. (3.9) and (3.13) for Au+Au central collision at $\sqrt{s_{NN}} = 200\,\mathrm{GeV}$. Different slab-slab collisions characterized by $\mathbf{r}_\perp$ will produce different rapidity losses $y_{\mathrm{P}}(\mathbf{r}_\perp, \tau)$ and different excitation energies $\mathcal{M}_{\mathrm{P}}(\mathbf{r}_\perp, \tau)$. Once $y_{\mathrm{P}}(\mathbf{r}_\perp, \tau)$ and $\mathcal{M}_{\mathrm{P}}(\mathbf{r}_\perp, \tau)$ have been obtained, average rapidity loss is readily computed so that it is constrained by the experimental data from the BRAHMS collaboration [48, 49]. Furthermore, rapidity loss and excitation energy predict

the baryon density and energy density that can be achieved. Additional thermo-dynamic properties of the high baryon density matter like temperature and baryon chemical potential can be calculated with the help of an appropriate equation of state.

3.3.1 Net-Baryon Rapidity Distribution

By collecting all the baryons at different $\mathbf{r}_\perp$ after the collision at proper time τ_0 and record their final rapidity $y_P(\mathbf{r}_\perp, \tau_0)$, one obtains the net-baryon rapidity distribution at that time. Let $y_P(\mathbf{r}_\perp)$ denote the rapidity for the projectile slab at $\mathbf{r}_\perp$ at proper time $\tau_0 = 0.6\,\mathrm{fm/c}$. The net-baryon rapidity distribution dN_B/dy is computed by summing up all the baryons at different $\mathbf{r}_\perp$ that have rapidity y

$$\frac{dN_B}{dy} = \int_0^{2\pi} d\phi \int_0^{R_A} r_\perp dr_\perp \, T_A(\mathbf{r}_\perp) \, \delta(y - y_P(\mathbf{r}_\perp)) = \frac{2\pi r_\perp T_A(r_\perp)}{|dy_P/dr_\perp|}\bigg|_{r_\perp = r_\perp(y)}. \quad (3.15)$$

Here R_A is the radius of the nucleus and and $T_A(\mathbf{r}_\perp)$ the nuclear thickness function. We assumed azimuthal symmetry in the transverse plane. The total number of baryons should be equal to the nuclear atomic number $A = \int_0^{y_0} \frac{dN_B}{dy} dy$ with y_0 the initial beam rapidity. The average rapidity loss follows from

$$\langle \delta y \rangle = y_0 - \frac{1}{A} \int_0^{y_0} y \, \frac{dN_B}{dy} dy. \quad (3.16)$$

Figure 3.7 shows the net-baryon rapidity distribution at $\tau = 0.6\,\mathrm{fm/c}$ after the collision of Au nuclei at $\sqrt{s_{NN}} = 200\,\mathrm{GeV}$. The initial beam rapidities are $y_0 = \pm 5.36$ and the final rapidities for the central core of the Au nucleus are $y_P(\mathbf{r}_\perp = 0) = \pm 2.47$. The central core of the Au nucleus experiences the largest rapidity loss while the peripheral part $(\mathbf{r}_\perp \sim R_A)$ of the Au nucleus experiences the smallest rapidity loss. We ignore possible thermal motions of baryons inside the

nuclear slabs so that all the baryons at $\mathbf{r}_\perp$ have the same rapidity $y_{\mathrm{P}}(\mathbf{r}_\perp)$. That is why there is the sharp vertical line at $y = 2.47$. The average rapidity loss is computed to be $\langle \delta y \rangle = 2.4$. The BRAHMS collaboration [48, 49] was the only detector at the RHIC that could measure particle production anywhere near the fragmentation regions. The coverage was limited to $|y| \leq 3.1$, so the uncertainty in the rapidity loss estimate was large. For 0-5% centrality BRAHMS found an average rapidity loss of about $2.05 + 0.4/0.6$. This is consistent with our result, especially since we focus on 0% centrality for illustration.
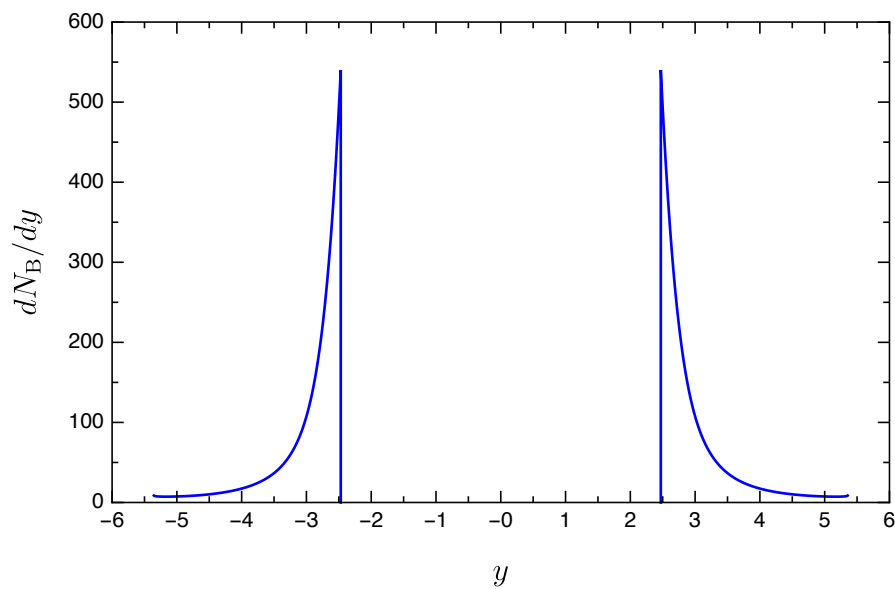
Figure 3.7: Net-baryon rapidity distribution at $\tau = 0.6\,\mathrm{fm/c}$ in the center-of-momentum frame after the collision for Au+Au at $\sqrt{s_{NN}} = 200\,\mathrm{GeV}$. The initial beam rapidities are $y_0 = \pm 5.36$.

3.3.2   High Baryon Density and Large Energy Density

With the rapidity loss $y_{\mathrm{P}}(\mathbf{r}_\perp, \tau)$ and the excitation energy $\mathcal{M}_{\mathrm{P}}(\mathbf{r}_\perp, \tau)$, we are able to calculate the baryon density and the energy density. The baryon density at proper time τ_0 is computed by Eq. (1.6)

$$n_B(r_\perp, z', \tau_0) = e^{\Delta y(r_\perp, \tau_0)}\, \rho_A(r_\perp, z'\, e^{\Delta y(r_\perp, \tau_0)}), \tag{3.17}$$

where $z' = z - z_{\mathrm{P}}(r_\perp, \tau_0)$ is the longitudinal coordinate in the local rest frame of the fireball characterized by $r_\perp$. The change of rapidity $\Delta y(r_\perp, \tau_0) = y_0 - y_{\mathrm{P}}(r_\perp, \tau_0)$ depends on the transverse position $r_\perp$. Different parts of the colliding nucleus characterized by $r_\perp$ have different time dependent rapidity $y_{\mathrm{P}}(r_\perp, \tau)$ and different longitudinal trajectory $z_P(r_\perp, \tau)$ as viewed in the center-of-momentum frame. Those slabs that are close to the central core of the nucleus experience larger rapidity loss and travel to a smaller longitudinal distance $z_{\mathrm{P}}(r_\perp \sim 0, \tau_0)$ at time τ_0 while those slabs close to the peripheral region of the nucleus experience small rapidity loss and travel to a larger longitudinal distance $z_{\mathrm{P}}(r_\perp \sim R_A, \tau_0)$ at time τ_0. Therefore different slabs characterized by different $r_\perp$ are separated along the longitudinal direction due to different $z_{\mathrm{P}}(r_\perp, \tau_0)$ at τ_0 and the spherical shape of the nucleus before the collision will no longer be maintained after the collision. Since $y_{\mathrm{P}}(r_\perp, \tau)$ also depends on $r_\perp$, there is no single reference frame that is the local rest frame for all the slabs characterized by different $r_\perp$. Each nuclear slab has its own local rest frame by boosting the center-of-momentum frame to the frame moving at rapidity $y_{\mathrm{P}}(r_\perp, \tau_0)$. Multiplying the baryon density by the nuclear excitation energy, one obtains the energy density

$$\varepsilon(r_\perp, z', \tau_0) = \frac{\mathcal{M}_{\mathrm{P}}(r_\perp, \tau_0)}{\mathcal{M}_{\mathrm{P}}(r_\perp, \tau = 0)}\, m_N\, n_B(r_\perp, z', \tau_0). \tag{3.18}$$

The energy density relies on the excitation energy which slowly increases with time, see Fig. 3.4. Therefore the energy density depends on the proper time chosen to evaluate its value.

Figure 3.8 shows the proper energy density and baryon density as functions of the transverse coordinate at $\tau = 0.6 \, \mathrm{fm/c}$ for $z' = 0$. It should be noted that the maximum baryon density, about 3 baryons/fm^3, is 20 times greater than the normal matter density of 0.155 nucleons/fm^3. The maximum energy density is about $20 \, \mathrm{GeV/fm}^3$, much larger than the critical energy density $\sim 1.0 \, \mathrm{GeV/fm}^3$ for the formation of quark-gluon plasma. Figure 3.9 is a contour plot of the proper baryon density. The contours are drawn at $n_\mathrm{B} = 3$, 2, 1, 0.5, and 0.15 baryons/fm^3. The shapes of the contours arise for the following reasons. The diameter of a gold nucleus $2R_A$ is about 14 fm. The core centered at $r_\perp = 0$ along the z axis contains the most matter, suffers the greatest deceleration, and hence the greatest compression. Moving outward with increasing $r_\perp$, the length of the tube is decreased to $2\sqrt{R_A^2 - r_\perp^2}$, and the deceleration, and hence compression, are reduced. These opposing effects approximately cancel each other, giving rise to roughly rectangular contours in the $r_\perp - z'$ plane. Care must be taken when interpreting this figure. Since the rapidity loss depends on $r_\perp$ it means that there is a shear in the $r_\perp$ direction, and there is no single global frame of reference for all elements of the fireball. It should be emphasized that the baryon densities calculated here are more robust than the energy densities. The reason can be seen by comparing Figs. 3.3 and 3.4. The rapidity loss and therefore compression are determined mostly within the first few tenths of a fm/c when the Glasma dominates the dynamics. The excitation energy continues its slow growth as time

goes on. If the transition from Glasma to quark-gluon plasma happens earlier than 0.6 fm/c, it would reduce the excitation energy but hardly affect the compression. Exactly how the transition occurs is a topic of much current interest and activity. This should be kept in mind in the following discussions.
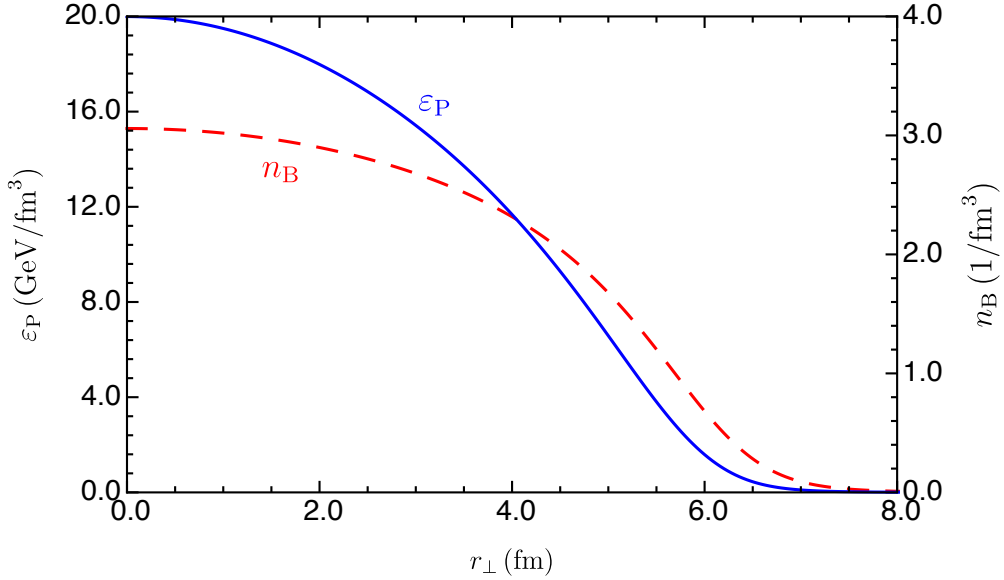
Figure 3.8: The energy density and baryon density at $\tau = 0.6\,\mathrm{fm/c}$ as functions of the transverse distance for central collisions of Au nuclei at $\sqrt{s_{NN}} = 200\,\mathrm{GeV}$.

Both the baryon density Eq. (3.17) and the energy density Eq. (3.18) are evaluated in the local rest frames of the fireball characterized by $r_\perp$. In this representation, Fig. 3.9 displays the volume information of the fireball. To present the distributions in the center-of-momentum frame where the spatial distribution of baryons is apparent requires making Lorentz boosts from the individual local rest frame characterized by $r_\perp$ to the center-of-momentum frame. Note that
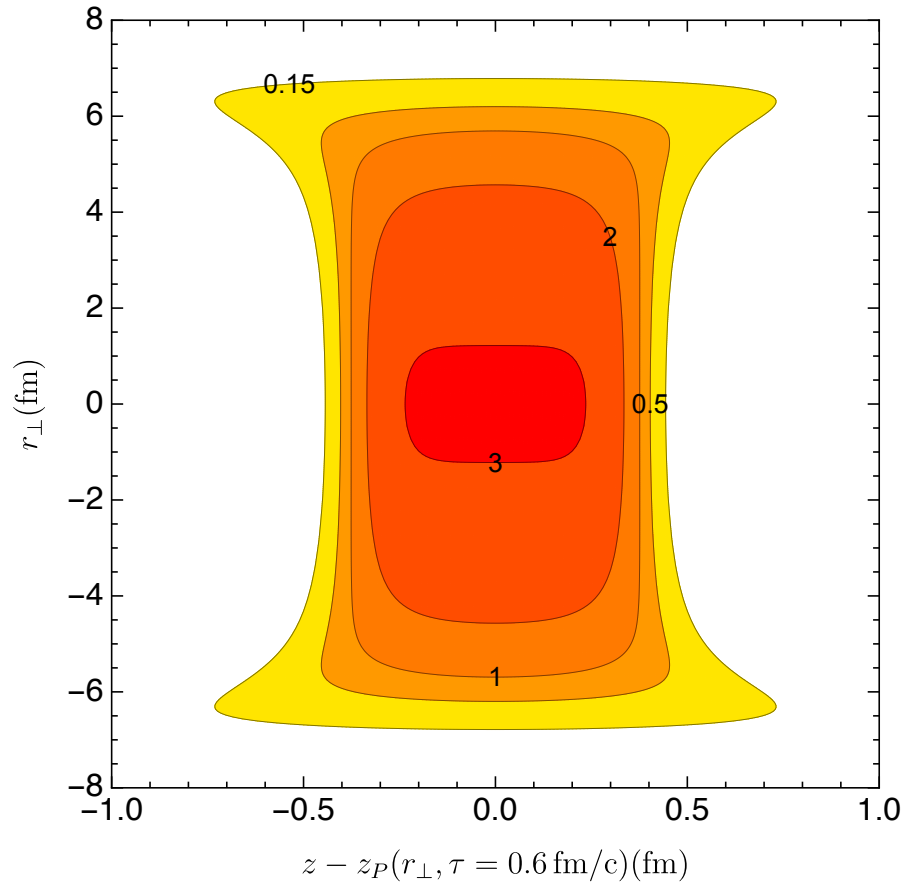
Figure 3.9: Contour plot of the proper baryon density for central collisions of Au nuclei at $\sqrt{s_{NN}} = 200\,\text{GeV}$. The numbers are in units of baryons per fm^3. The horizontal axis measures the distance along the beam direction in the local rest frame. Care must be taken when interpreting this plot since the rapidity of the matter and therefore the frame of reference depend on $r_\perp$.

the baryons shown in Fig. 3.9 share the same proper time τ instead of the same Cartesian coordinate time t. Figure 3.10 shows the schematic picture of the central core nuclear slab after collision in its local rest frame. Let (t^*, z^*) denote Cartesian coordinates in the center-of-momentum frame and (t', z') denote Cartesian coordinates in the local rest frame of the nuclear slab. Making the Lorentz transformation one gets

$$z'_L = \gamma_{\mathrm{P}}(z_L^* - \beta_{\mathrm{P}} t_L^*), \tag{3.19}$$

where $\gamma_{\mathrm{P}} = \cosh y_{\mathrm{P}}$ and $\beta_{\mathrm{P}} = \tanh y_{\mathrm{P}}$ with y_{P} the rapidity of the nuclear slab. The baryons all have the same proper time τ viewed in the center-of-momentum frame so that $z_L^* = \tau \sinh \eta_L$ and $t_L^* = \tau \cosh \eta_L$. Here η_L is the pseudorapidity defined in the center-of-momentum frame. Then $z'_L = \tau \sinh(\eta_L - y_{\mathrm{P}})$ which, compared with $z^* = \tau \cosh \eta_L$, is just a shift of rapidity from η_L to $\eta_L - y_{\mathrm{P}}$. Therefore, the space-time pseudorapidity η_L of the baryon labeled by L in the center-of-momentum frame is related the the corresponding local coordinate z'_L in the local rest frame by

$$\eta_L = \sinh^{-1}\left(\frac{z'_L}{\tau}\right) + y_{\mathrm{P}}. \tag{3.20}$$

A potential problem with Eq. (3.20) is that for $z'_o = 0$ it predicts $\eta_o = y_{\mathrm{P}}$ which is not exactly true since η_o slightly deviates from y_{P}, see Fig. 3.5. Here "o" indicates the center of the nuclear slab in Fig. 3.10. However, this probably only slightly influence the absolute position of the pseudorapidity for the center of the nuclear slab; the span of the pseudorapidity remains unchanged.

Figure 3.11 is the baryon distribution on the $r_\perp - \eta$ plane converted using Eq. (3.20). The central core region spans about 1.5 units of rapidity. This distribution will be used to perform hydrodynamic simulations in space and time in the next

$$e^{-\Delta y}\, 2R_A$$

L R

o

z'_L $\quad$ 0 $\quad$ z'_R $\quad$ z'
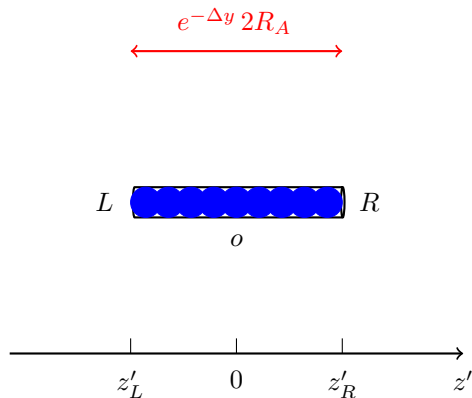
Figure 3.10: Schematic picture of the nuclear slab for the central core of a nucleus in its local rest frame.

chapter.

3.3.3 Temperature and Baryon Chemical Potential

The previous results and discussions have not assumed the fireballs in the fragmentation regions to be thermalized. We calculated the baryon density and energy density achievable in the fragmentation regions at proper time $\tau = 0.6\,\text{fm/c}$ for Au+Au collisions at $\sqrt{s_{NN}} = 200\,\text{GeV}$. The baryon density is found to be more than ten times larger than the normal atomic nuclear density and the energy density is also found to be more than ten times larger than the typical critical energy density for the formation of quark-gluon plasma. However, high baryon density and large energy density are only necessary but not sufficient conditions for the formation of quark-gluon plasma. The question of thermalization is even harder to tell. The proper time $\tau = 0.6\,\text{fm/c}$ is the typical time when quark-gluon plasma is believed to be formed in the *central region* of Au+Au collision at $\sqrt{s_{NN}} = 200\,\text{GeV}$ and is also the time when the matter in the central region is
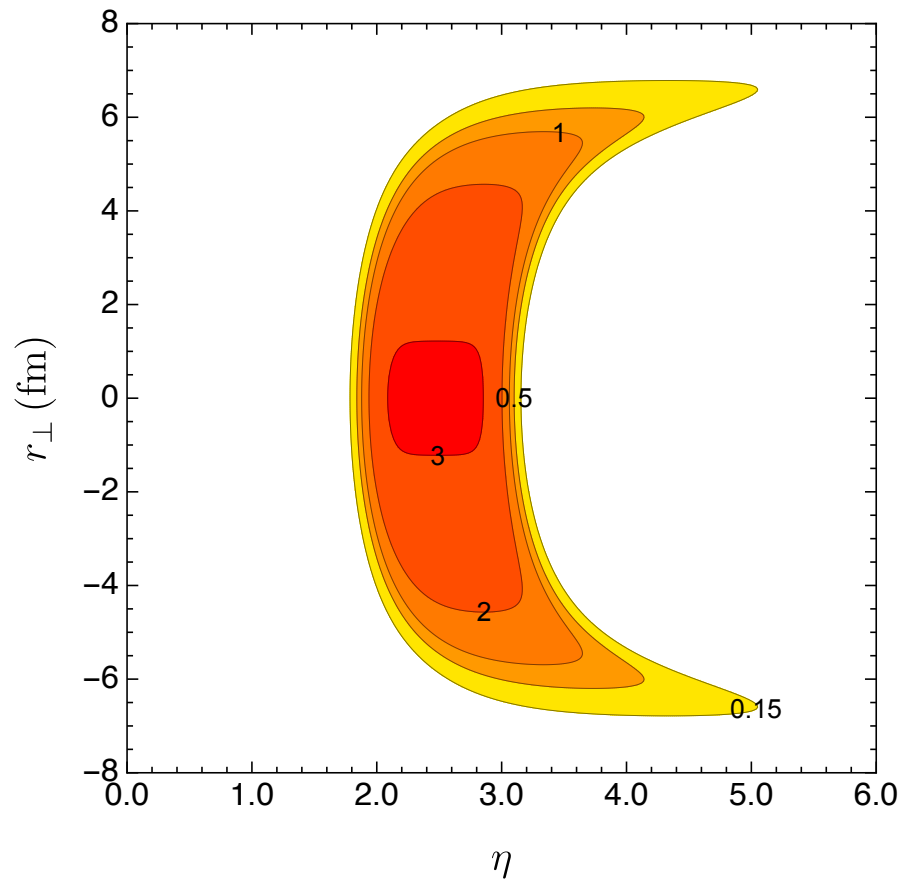
Figure 3.11: Contour plot of the proper baryon density for central collisions of Au nuclei at $\sqrt{s_{NN}} = 200\,\text{GeV}$. The numbers are in units of baryons per fm^3. The horizontal axis is the space-time pseudorapidity in the center-of-momentum frame.

assumed to be thermalized. Exactly how the quark-gluon plasma in the central region equilibrates and thermalizes has not reached a definite conclusion yet and is still under active research [83]. The practical approach is to assume the thermalization has been reached and tune the input parameters at $\tau = 0.6\,\mathrm{fm/c}$ so as to reproduce experimental data. The exact mechanism for the thermalization is actually not so relevant as long as it predicts the required initial conditions at $\tau = 0.6\,\mathrm{fm/c}$ constrained by experimental data. As for the fragmentation regions, Anishetty, Koehler and McLerran [50] argued that the matter in the fireballs of the fragmentation regions could thermalize due to interactions of secondary particles. Since then, there has been very little research concerning the fragmentation regions, not to mention the thermalization problem. Thermalization in the fragmentation regions, if it is possible, could be as challenging as the thermalization problem in the central region and beyond the scope of the current thesis. Just like what has been practiced in the central region, we assume the fireballs in the fragmentation regions have reached thermalization and explore the consequences.

For thermalized matter that contains large baryon density, what are the temperature and baryon chemical potential? We need an equation of state. In the limit of very high temperature and baryon density, for a thermalized system of quarks and gluons, the equation of state can be calculated using perturbative QCD in thermal field theory [98, 99]. On the other hand, in the low temperature and small baryon density regime, the degrees of freedom become hadrons. For a thermalized system of hadrons, the hadron resonance gas model gives a very good description of the thermodynamic properties of the system. Furthermore, first

principle calculations based on lattice QCD provides robust results for the equation of state of a system of quarks and gluons in a very wide range of temperature for zero baryon chemical potential [9, 103]. Extending to finite baryon chemical potential has the notorious sign problem. Currently, much effort has been devoted to extending the lattice calculations to finite baryon chemical potential [100]. In the following, we will use a crossover equation of state [101, 102] that smoothly connects the quark-gluon plasma phase and the hadronic resonance gas phase in consistent with lattice data [103, 104]. This equation of state does not contain a first order phase transition line or critical point. Instead, the transition from the quark-gluon plasma phase to the hadronic resonance gas phase is a rapid, smooth crossover both for zero baryon chemical potential and for nonzero baryon chemical potentials. The crossover equation of state [101, 102] has the form

$$P(T,\mu) = S(T,\mu)P_{\mathrm{qg}}(T,\mu) + [1 - S(T,\mu)] P_{\mathrm{h}}(T,\mu). \qquad (3.21)$$

with the switching function

$$S(T,\mu) = \exp\{-\theta(\mathrm{T},\mu)\}, \quad \theta(\mathrm{T},\mu) = \left[\left(\frac{\mathrm{T}}{\mathrm{T_0}}\right)^{\mathrm{r}} + \left(\frac{\mu}{\mu_0}\right)^{\mathrm{r}}\right]^{-1}. \qquad (3.22)$$

Here P_{qg} represents the perturbative QCD results for the pressure of the quark-gluon plasma phase while P_{h} represents pressure from the excluded volume model of the hadronic resonance gas phase. The switching function $S(T,\mu)$ asymptotically approaches 1 for very large T and μ and asymptotically approaches 0 for very small T and μ. The free parameters T_0, μ_0 and r are optimized to be consistent with lattice data.

Given the energy and baryon density distributions for $z' = 0$ shown in Fig. 3.8, we compute the corresponding temperature and baryon chemical potential

distributions using the crossover equation of state from Eqs. (3.21) and (3.22).
Figure 3.12 shows the temperatures and baryon chemical potentials for different
rapidities y_P instead of $r_\perp$. Note that there is a one-to-one correspondence be-
tween $r_\perp$ and y_P by $y_P = y_P(r_\perp)$. Only those with energy densities larger than
$1.0\,\mathrm{GeV/fm^3}$ have been displayed. We focus on $z' = 0$ as defined in Eq. (3.17).
In the range of rapidity from 2.47 to 3.45, the value of the baryon chemical po-
tential increases from $655\,\mathrm{MeV}$ to $1020\,\mathrm{MeV}$ while the value of the temperature
correspondingly decreases from $328\,\mathrm{MeV}$ to $155\,\mathrm{MeV}$. The baryon chemical po-
tential to temperature ratio ranges from 2.0 to 6.5 as shown in Fig. 3.13. The
same data shown in the $\mu_B - T$ plane is given in Fig. 3.14. The initial baryon
chemical potentials achievable in the fragmentation regions of Au+Au collision at
$\sqrt{s_{NN}} = 200\,\mathrm{GeV}$ are estimated to be larger than $600\,\mathrm{MeV}$ which is much larger
than the baryon chemical potential found in the central region of about $25\,\mathrm{MeV}$.
If we assume the subsequent expansion of the thermalized high baryon density
matter after $\tau = 0.6\,\mathrm{fm/c}$ is approximately adiabatic, just like in the central re-
gion, then typical phase trajectories in the $\mu_B - T$ plane are shown in Fig. 3.15
for three different entropy per baryon ratios. The entropy per baryon ratio is a
conserved quantity in the adiabatic expansion. Also the corresponding momen-
tum space rapidities are specified. These phase trajectories tilt to the right after
changing from the quark-gluon plasma phase to the hadronic gas phase. In the
transition region, the temperature decreases very fast while the baryon chemical
potential decreases very slowly. From these phase trajectories, it is possible that
the expansion of the high baryon density matter in the fragmentation regions
might go through or near the region on the $\mu_B - T$ plane where a first order

phase transition line or a critical point are conjectured to be located [105, 106]. As shown in Fig. 3.16, the entropy per baryon ratio might be in the right range so that a scan through the momentum space rapidity may locate the critical point.
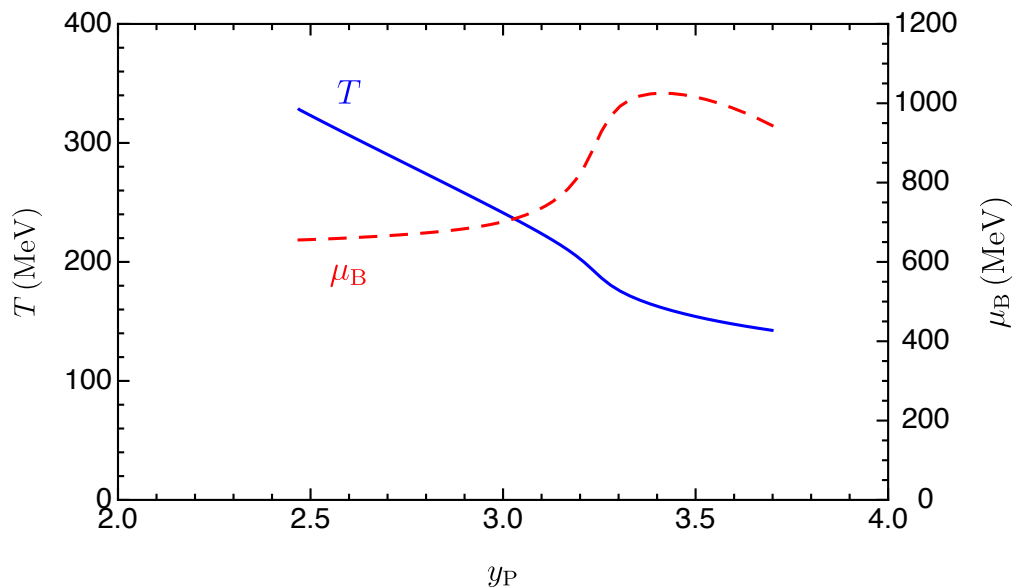
Figure 3.12: The temperature and baryon chemical potential in the fragmentation regions as a function of momentum space rapidity at $\tau = 0.6\,\mathrm{fm/c}$. Values are calculated for $z' = 0$ as defined in Eq. (3.17). Only those with energy densities larger than $1.0\,\mathrm{GeV/fm}^3$ have been displayed.
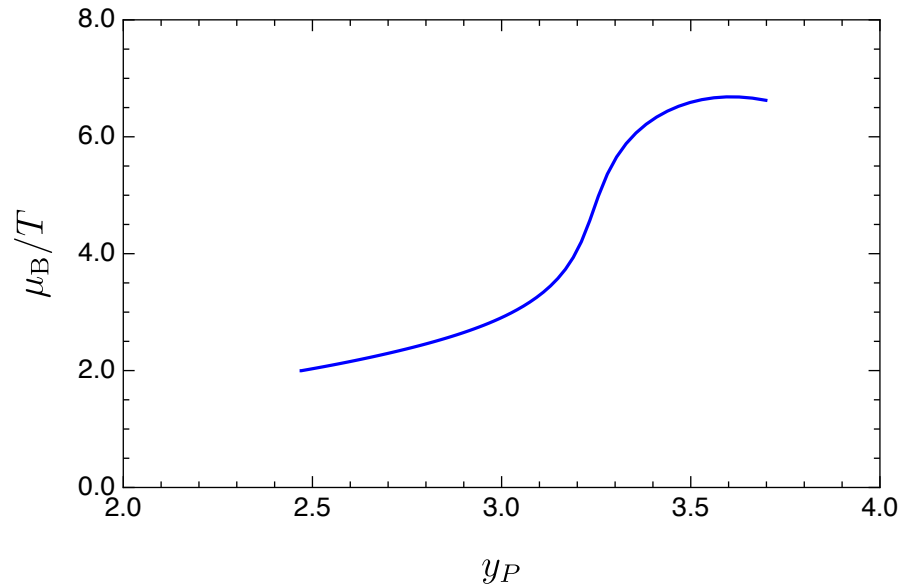
Figure 3.13: Ratio of baryon chemical potential to temperature as a function of rapidity.
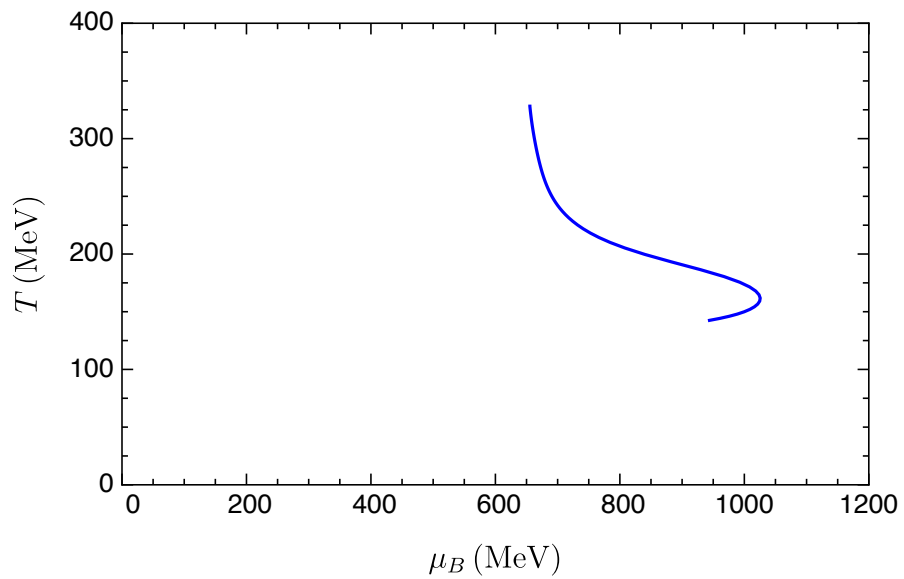
Figure 3.14: The initial temperatures and baryon chemical potentials in the fragmentation regions at $\tau = 0.6\,\mathrm{fm/c}$ with energy density larger than $1.0\,\mathrm{GeV/fm^3}$. Values are calculated for $z' = 0$ as defined in Eq. (3.17).
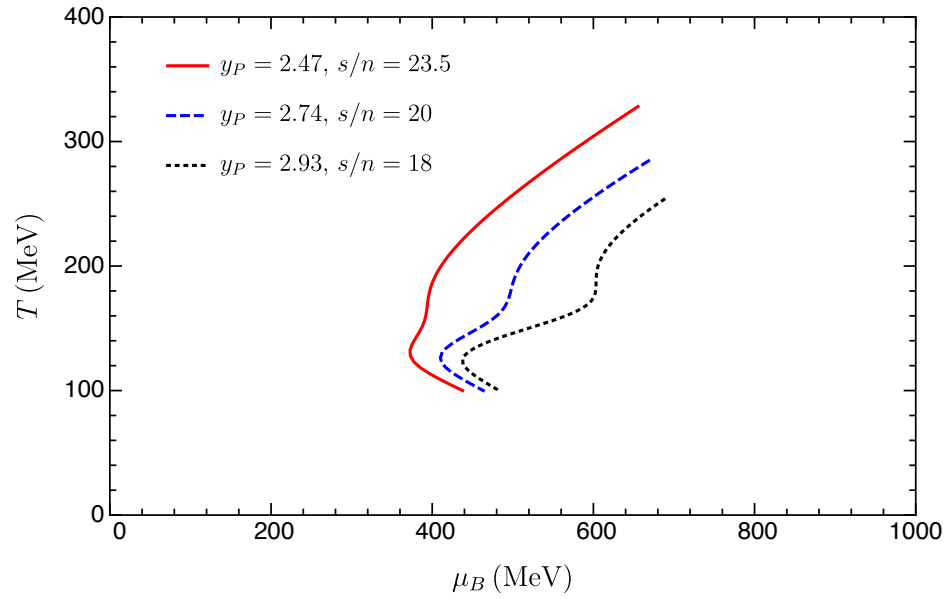
Figure 3.15: Phase trajectories of adiabatic expansion at three different rapidities and entropy per baryon ratios.
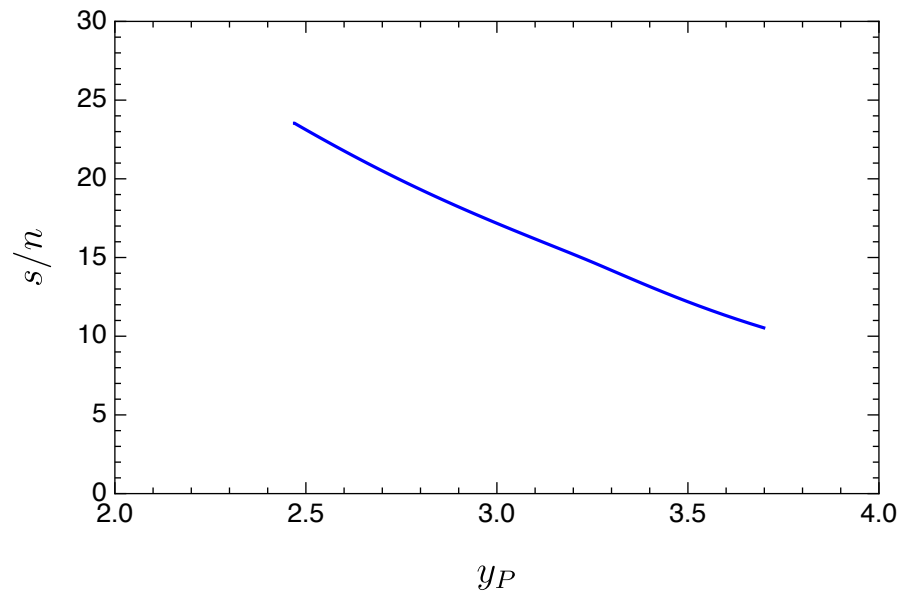
Figure 3.16: Entropy per baryon ratio as a function of the rapidity. A scan through the momentum space rapidity may locate the critical point.

3.4 High Baryon Density Achievable in Other Collision Configurations

To extend the previous analysis of the high baryon densities in the fragmentation regions of Au+Au collision at $\sqrt{s_{NN}} = 200\,\text{GeV}$ to other heavy-ion collision configurations involving different nuclear sizes, different collision energies or different impact parameters, the crucial step is to determine the initial energy density of the Glasma $\varepsilon_0(\mathbf{r}_\perp)$ for these different collision configurations. In the case of central Au+Au collision at $\sqrt{s_{NN}} = 200\,\text{GeV}$, the $\varepsilon_0(\mathbf{r}_\perp)$ is determined by $\varepsilon_0(\mathbf{r}_\perp = 0)$ through the nuclear thickness function $T_A(\mathbf{r}_\perp)$ while $\varepsilon_0(\mathbf{r}_\perp = 0)$ is fixed by the initial energy density of hydrodynamics at $\tau_0 = 0.6\,\text{fm/c}$ assuming that the classical gluon fields are valid up to the time when hydrodynamic evolution of the quark-gluon plasma begins. In principle, we can repeat this procedure to determine $\varepsilon_0(\mathbf{r}_\perp)$ for other collision configurations as long as we know the starting time of hydrodynamics τ_0 and the initial energy density at that time $\varepsilon(\mathbf{r}_\perp = 0, \tau_0)$ for these collisions. These two quantities are usually optimized to reproduce bulk experimental data after running hydrodynamic simulations. In the following analysis, however, we take a different approach in determining $\varepsilon_0(\mathbf{r}_\perp)$ for other collision configurations. We assume Eq. (3.11) is the formula that determines the initial energy density $\varepsilon_0(\mathbf{r}_\perp)$. Rewritten more explicitly, the initial energy density

$$\varepsilon_0(\mathbf{r}_\perp) \equiv \varepsilon_0 \left[\mu_i(\mathbf{r}_\perp, \sqrt{s}), Q_i(\mathbf{r}_\perp, \sqrt{s}) \right] \tag{3.23}$$

is a functional of $\mu_i(\mathbf{r}_\perp, \sqrt{s})$ and $Q_i(\mathbf{r}_\perp, \sqrt{s})$ with $i = 1, 2$ indicating the two colliding nuclei. We assume the infrared cutoffs to be the same $m_1 = m_2 = \Lambda_{QCD}$ for the two colliding nuclei. Both the color charge squared per unit area μ_i and

the ultraviolet cutoff Q_i, in principle, depend on the transverse position $\mathbf{r}_\perp$ and the center-of-momentum collision energy $\sqrt{s}$. The color charge squared per unit area for a nucleus is related to that of a nucleon by

$$\mu_A(\mathbf{r}, \sqrt{s}) = T_A(\mathbf{r}_\perp)\mu_N(\sqrt{s}). \tag{3.24}$$

We assume, for a given nucleus-nucleus collision, the ultraviolet cut-off is independent of the transverse position $\mathbf{r}_\perp$ so that

$$Q_A(\mathbf{r}_\perp, \sqrt{s}) = Q_A(\sqrt{s}). \tag{3.25}$$

The central Au+Au collision at $\sqrt{s_{NN}} = 200\,\mathrm{GeV}$ will serve as a reference collision configuration for other collisions involving different nuclear sizes, different collision energies and different impact parameters.

3.4.1 Nuclear Size Dependence

In this subsection, we consider heavy-ion collisions at fixed center-of-momentum collision energy $\sqrt{s_{NN}} = 200\,\mathrm{GeV}$. We will study Cu+Cu, Cu+Au, and U+U collisions in addition to Au+Au collisions. The Relativistic Heavy-Ion Collider at BNL has already run Cu+Cu, Au+Au, and Cu+Au collisions at $\sqrt{s_{NN}} = 200\,\mathrm{GeV}$ and run U+U collisions at $\sqrt{s_{NN}} = 193\,\mathrm{GeV}$. For a fixed center-of-momentum collision energy, the initial energy density for a general nucleus-nucleus central collision can be obtained with reference to the Au+Au collision

$$\varepsilon_{0,A}(\mathbf{r}_\perp) = \left[\frac{T_A(\mathbf{r}_\perp)}{T_{\mathrm{Au}}(\mathbf{r}_\perp = 0)}\right]^2 \varepsilon_{0,\mathrm{Au}}(\mathbf{r}_\perp = 0). \tag{3.26}$$

The initial energy density for Au+Au collision is $\varepsilon_{0,\mathrm{Au}}(\mathbf{r}_\perp = 0) = 142.0\,\mathrm{GeV/fm}^3$ for the ultraviolet cutoff $Q = 4.0\,\mathrm{GeV}$, see Fig. 3.1. Since the rapidity loss is

insensitive to the ultraviolet cutoff, we choose $Q = 4.0\,\mathrm{GeV}$ for all the collisions at $\sqrt{s_{NN}} = 200\,\mathrm{GeV}$.

The computation of nuclear thickness functions involves the Woods-Saxon nuclear distribution function. For spherical nuclei, such as Au and Cu, the Woods-Saxon distributions $\rho_A(r)$ are spherically symmetric. For deformed nuclei like U, we use the following parameterization of Woods-Saxon distribution [107, 108]

$$\rho_A(\mathbf{r}) = \frac{\rho_0}{1 + e^{\frac{r - R_A \Omega(\theta)}{\xi}}}. \tag{3.27}$$

Here $\rho_0 = 0.166\,\mathrm{fm}^{-3}$, $\xi = 0.44\,\mathrm{fm}$, $R_A = 6.86\,\mathrm{fm}$ and $\Omega(\theta) = 1 + \beta_2 Y_0^2(\theta) + \beta_4 Y_0^4(\theta)$ with $\beta_2 = 0.280$ and $\beta_4 = 0.093$. The $Y_m^l(\theta)$ are spherical harmonic functions. The angle θ is related the the Cartesian coordinates by $\sin\theta = r_\perp/r$ and $\cos\theta = z/r$. The $\theta = 0$ corresponds to the direction of the longest axis while $\theta = \pi/2$ corresponds to the direction of the shortest axis. Equation (3.27) describes an ellipsoid like shape. In central U+U collisions, depending on the orientations of the uranium nuclei, there could be many different collision configurations. In the following discussion, we only consider the *tip-tip* collision configuration where the longest axes of the uranium nuclei align with the beam directions.

Table 3.1 presents several physical quantities associated with the three collisions of different nuclear sizes at $\sqrt{s_{NN}} = 200\,\mathrm{GeV}$, which are Cu+Cu, Au+Au and U+U (tip-tip) collisions. They all have the same initial beam rapidity $y_0 = 5.36$ due to the same collision energy. The average rapidity loss $\langle \delta y \rangle$ increases with the increase of nuclear atomic mass. This can be understood from the slab-slab collision at the central cores of the colliding nuclei where the remaining quantities y_P, n_B, ε_P, T and μ_B are evaluated. In the three collisions, the central core of a projectile starts with initial rapidity y_0 and ends with rapidity y_P. For collisions

involving nuclei of larger atomic mass, like U+U, the final rapidity $y_{\rm P}$ is smaller and the rapidity loss experienced is therefore larger. This point is encoded in the equations of motion Eq. (3.7) where $\mathcal{M}_{\rm P} \sim T_A(r_\perp)$ and $\mathcal{A}, \mathcal{B} \sim [T_A(r_\perp)]^2$ so that the rate of rapidity change $dy/d\tau \sim T_A(r_\perp)$. When averaging over all the collisions at different $r_\perp$, collisions of nuclei with bigger nuclear size have larger average rapidity loss. The average rapidity loss in Au+Au collisions at $\sqrt{s_{NN}} = 200\,{\rm GeV}$ for the centrality class $0-5\%$ has been measured and estimated to be in the range from 1.45 to 2.45 by the BRAHMS collaboration [48]. However, the average rapidity losses for the Cu+Cu collision and the U+U (tip-tip) collision have not been measured experimentally. The values in Table 3.1 are the theoretical estimations. The largest baryon densities achieved in these three collisions are 2.04, 3.01 and 3.94 baryons/fm^3, respectively. Baryon densities increase with increasing nuclear atomic mass in accordance with the rapidity losses because the baryon density is proportional to the exponential of the rapidity loss. These maximal baryon densities are all more than ten times larger than the normal nuclear density. The maximal energy densities $\varepsilon_{\rm P}$ obtained in the fragmentation regions of the three collisions are smaller than the respective energy densities $\varepsilon_{\rm hydro}$ in the central rapidity region at $\tau = 0.6\,{\rm fm/c}$ when hydrodynamics begins. This is consistent with the expectation that energy density achieved in the central region of high energy heavy-ion collisions is larger than the energy density achieved in the fragmentation regions so that quark-gluon plasma is more likely to be created in the central region than the fragmentation regions. The temperature T and baryon chemical potential $\mu_{\rm B}$ corresponding the largest baryon density $n_{\rm B}$ and energy density $\varepsilon_{\rm P}$ for the three collisions are also given in Table 3.1. Finally, the largest entropy

per baryon ratios s/n_B that can be achieved in the fragmentation regions of the three collisions are 18.33, 23.53 and 27.82 which increases with the nuclear atomic mass.

$\sqrt{s_{NN}} = 200\,\mathrm{GeV}$	Cu+Cu	Au+Au	U+U (tip-tip)
Atomic Mass	63	197	238
$\varepsilon_{\mathrm{hydro}}(\mathrm{GeV/fm}^3)$	13.3	30.0	52.3
y_0	5.36	5.36	5.36
$\langle \delta y \rangle$	1.93	2.40	2.67
y_{P}	2.87	2.47	2.19
$n_{\mathrm{B}}(1/\mathrm{fm}^3)$	2.04	3.01	3.94
$\varepsilon_{\mathrm{P}}(\mathrm{GeV/fm}^3)$	9.0	20.0	33.8
$T\,(\mathrm{MeV})$	264.1	328.1	376.0
$\mu_{\mathrm{B}}(\mathrm{MeV})$	693.0	655.4	643.9
s/n_{B}	18.33	23.53	27.82

Table 3.1: Three different collision configurations at $\sqrt{s_{NN}} = 200\,\mathrm{GeV}$. Here $\varepsilon_{\mathrm{hydro}}$ is the initial energy density in the central rapidity region with $x = y = 0$ at $\tau = 0.6\,\mathrm{fm/c}$ when hydrodynamics starts. The y_0 is the initial beam rapidity and $\langle \delta y \rangle$ is the average rapidity loss. The y_{P} is the final rapidity of the central core of the nucleus at $r_\perp = 0$, which experiences the largest rapidity loss. Other thermodynamic quantities $n_{\mathrm{B}}, \varepsilon_{\mathrm{P}}, T, \mu_B$ and s are also evaluated in the central core of the fireball.

Figures 3.17, 3.18, 3.19 and 3.20 show the baryon density, energy density, baryon chemical potential and temperature achievable in the fragmentation regions of the three collisions as functions of $r_\perp$ with $z' = 0$. The temperature and baryon chemical potential are displayed only in the regions with energy density larger than $1.0\,\mathrm{GeV/fm}^3$. In Fig. 3.19, the baryon chemical potential increases as $r_\perp$ increases. After reaching peak values, the baryon chemical potential decreases. This peculiar feature is due to the equation of state used because the
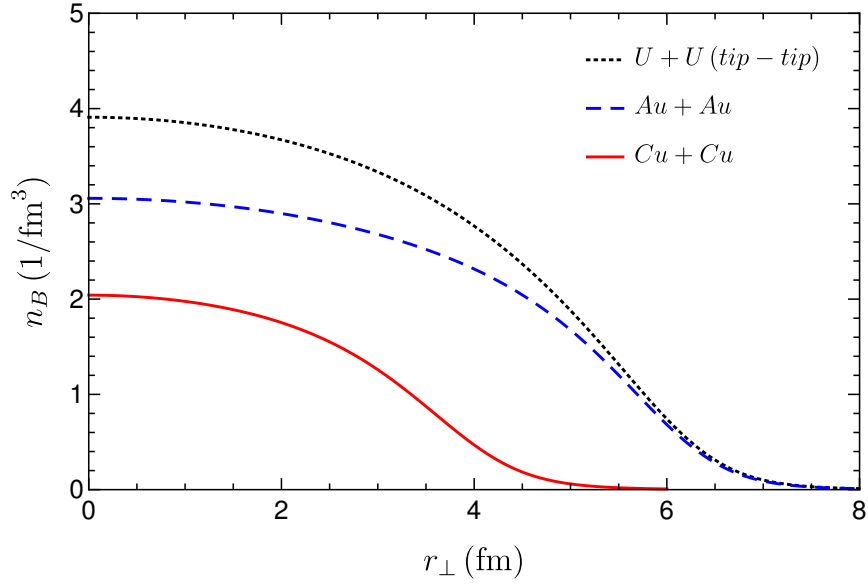
Figure 3.17: Baryon density achievable in the fragmentation regions as a function of $r_\perp$ with $z' = 0$ for three different collisions at $\sqrt{s_{NN}} = 200\,\text{GeV}$.
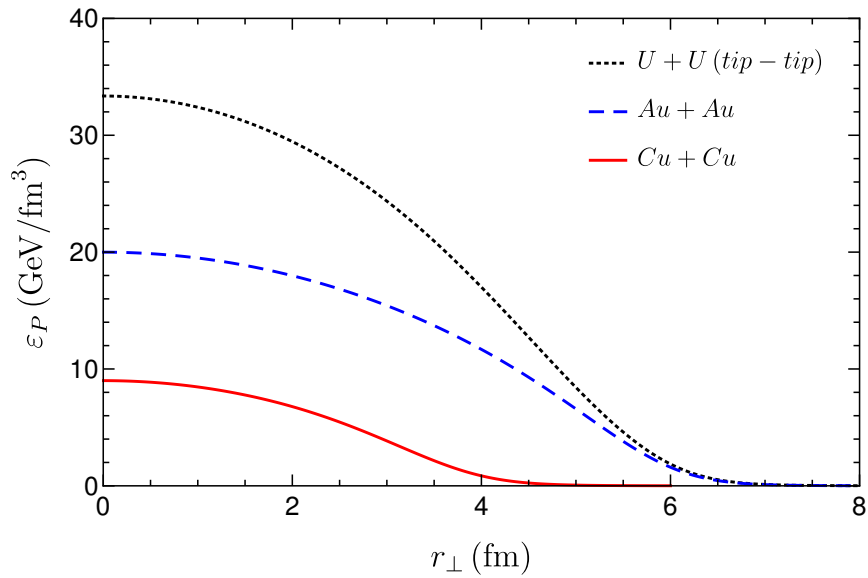
Figure 3.18: Energy density achievable in the fragmentation regions as a function of $r_\perp$ with $z' = 0$ for three different collisions at $\sqrt{s_{NN}} = 200\,\text{GeV}$.
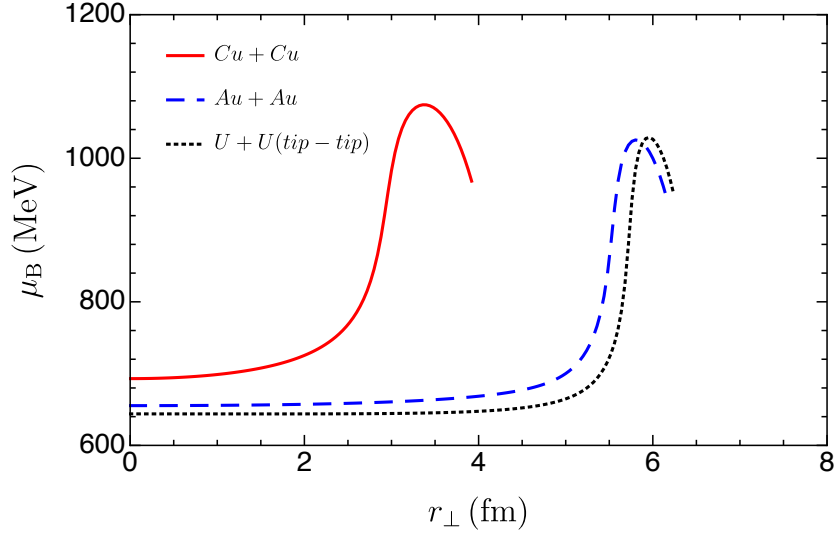
Figure 3.19: Baryon chemical potential achievable in the fragmentation regions as a function of $r_\perp$ with $z' = 0$ for three different collisions at $\sqrt{s_{NN}} = 200\,\mathrm{GeV}$. Only regions with energy density larger than $1.0\,\mathrm{GeV/fm}^3$ have been displayed.
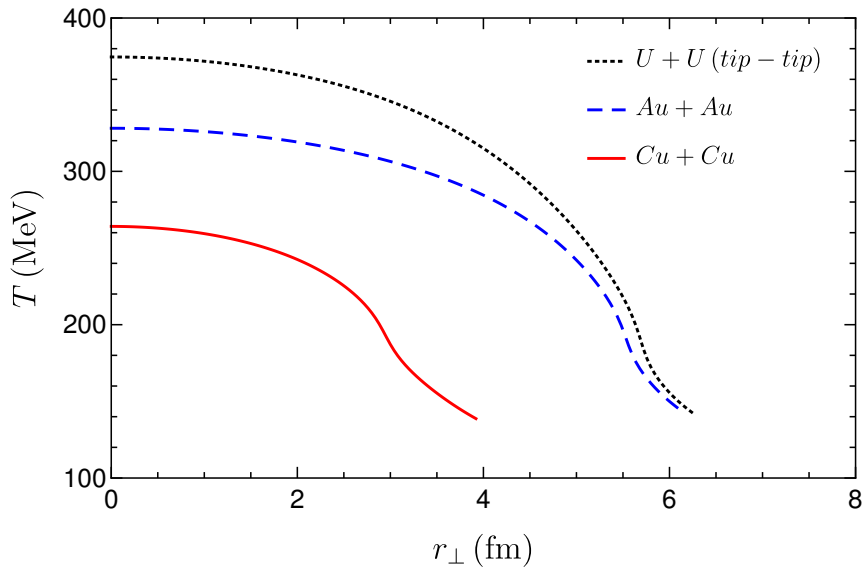
Figure 3.20: Temperature achievable in the fragmentation regions as a function of $r_\perp$ with $z' = 0$ for three different collisions at $\sqrt{s_{NN}} = 200\,\mathrm{GeV}$. Only regions with energy density larger than $1.0\,\mathrm{GeV/fm}^3$ have been displayed.

corresponding temperatures in these regions are in the transition regions from the quark-gluon plasma to the hadronic resonance gas. Figures 3.21 and 3.22 show the baryon density distributions in the fragmentation regions in the local rest frame of the fireballs for Cu and U, respectively. The longitudinal sizes are around 1 fm. Figures 3.23 and 3.24 shows the baryon density distributions in the fragmentation regions in the center-of-momentum frame. Here η is the space-time pseudorapidity. For Cu+Cu collisions, the pseudorapidity spans about 1.5 unit around the central core regions while for U+U collision, the pseudorapidity spans about 1.0 unit.

For asymmetric central collisions of Cu+Au at $\sqrt{s_{NN}} = 200\,\text{GeV}$, the Au nucleus has a larger diameter than the Cu nucleus so that the transverse overlap size is only the cross sectional area of the Cu nucleus. Peripheral regions of the Au nucleus play the role of spectators and do not participate in the collision. To solve the equations of motion Eq. (3.7) for the Cu fireball and the Au fireball after the collision, one has to generalize the initial energy density Eq. (3.26) to incorporate contributions from two different nuclei as

$$\varepsilon_{0,AA'}(\mathbf{r}_\perp) = \frac{T_A(\mathbf{r}_\perp)T_{A'}(\mathbf{r}_\perp)}{[T_{\text{Au}}(\mathbf{r}_\perp = 0)]^2}\,\varepsilon_{0,\text{Au}}(\mathbf{r}_\perp = 0). \tag{3.28}$$

Here A and A' indicate the two colliding nuclei. As a consequence, the functions $\mathcal{A}, \mathcal{B}$ in the equations of motion Eq. (3.7) scale as $T_A T_{A'}$. For the Cu nucleus in the Cu+Au collision, after canceling out T_{Cu} from the two sides of equations in Eq. (3.7)(note that $\mathcal{M}_{\text{P,Cu}} \sim T_{\text{Cu}}$), the equations of motion are only determined by the thickness function T_{Au}. These equations of motion are exactly the same as the equations of motion for the Au nucleus in symmetric Au+Au collision of the same energy. Likewise, the equations of motion for a Au nucleus in Cu+Au
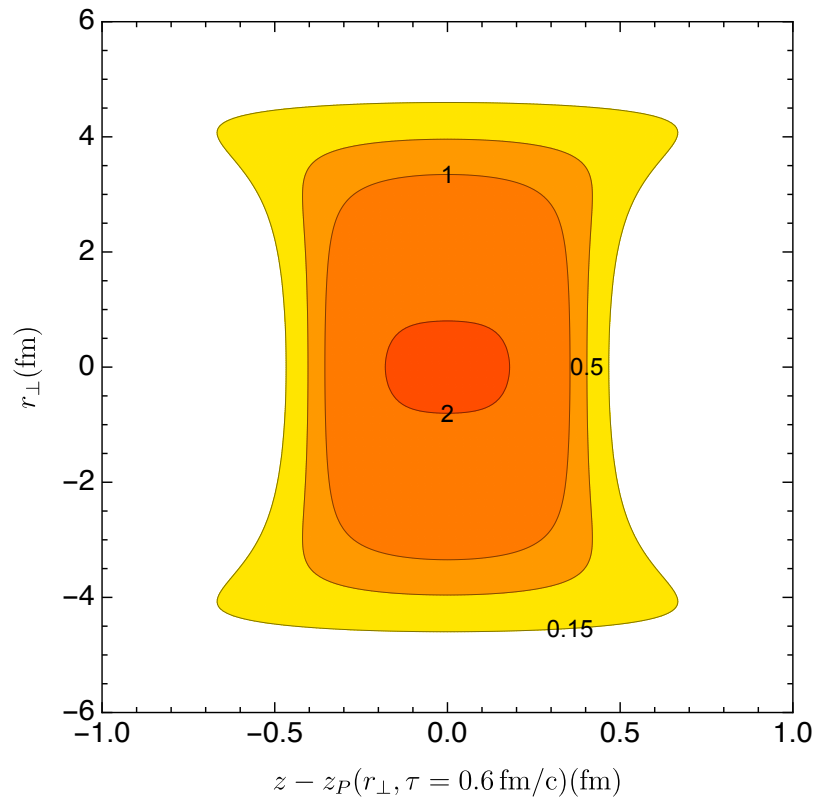
Figure 3.21: Contour plot of the proper baryon density for central collisions of Cu nuclei at $\sqrt{s_{NN}} = 200\,\mathrm{GeV}$. The numbers are in units of baryons per fm^3. The horizontal axis measures the distance along the beam direction in the local rest frame. Care must be taken when interpreting this plot since the rapidity of the matter and therefore the frame of reference depends on $r_\perp$.
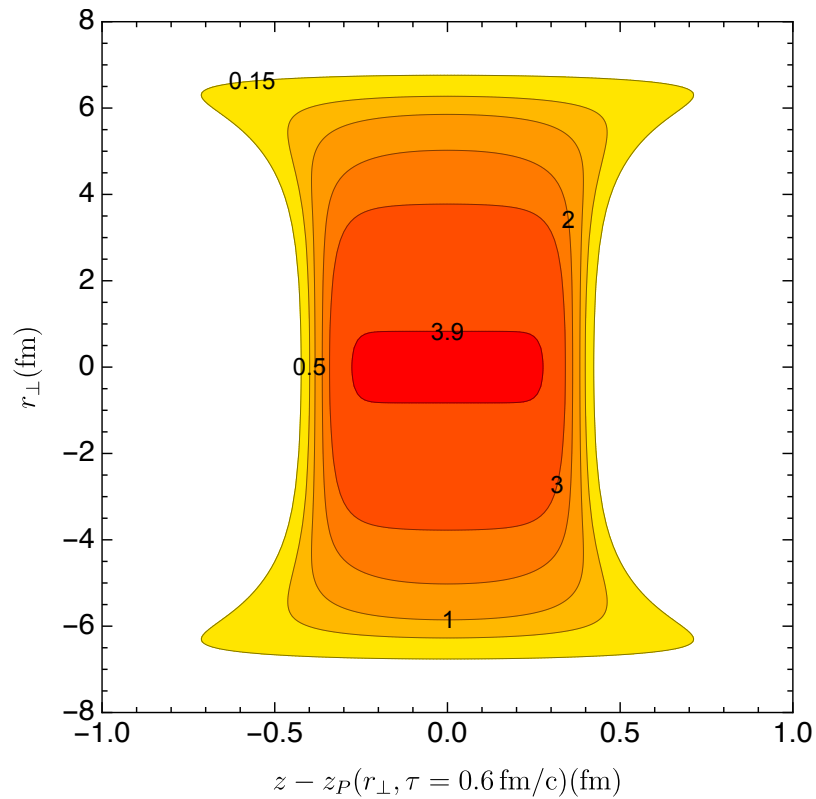
Figure 3.22: Contour plot of the proper baryon density for central collisions of U nuclei at $\sqrt{s_{NN}} = 200\,\mathrm{GeV}$. The numbers are in units of baryons per fm³. The horizontal axis measures the distance along the beam direction in the local rest frame. Care must be taken when interpreting this plot since the rapidity of the matter and therefore the frame of reference depend on $r_\perp$.
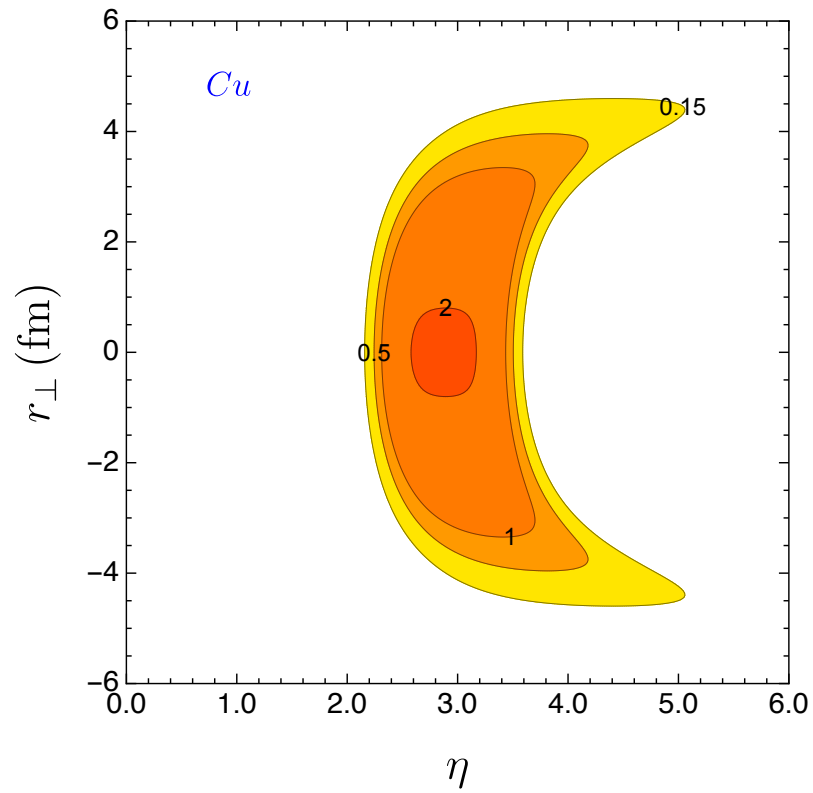
Figure 3.23: Contour plot of the proper baryon density for central collisions of Cu nuclei at $\sqrt{s_{NN}} = 200\,\mathrm{GeV}$. The numbers are in units of baryons per fm³. The horizontal axis is the space-time pseudorapidity in the center-of-momentum frame.
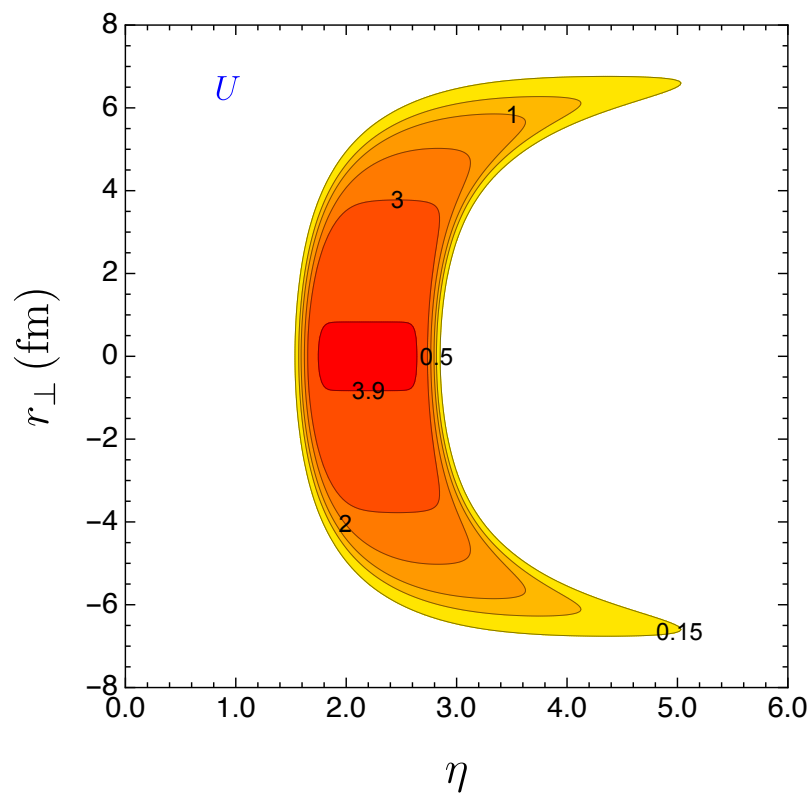
Figure 3.24: Contour plot of the proper baryon density for central collisions of U nuclei at $\sqrt{s_{NN}} = 200\,\text{GeV}$. The numbers are in units of baryons per fm³. The horizontal axis is the space-time pseudorapidity in the center-of-momentum frame.

collisions are exactly the same as the equations of motion governing the Cu nucleus in Cu+Cu collision at the same energy. In other words, concerning the rapidity loss and the excitation energy, the following equivalences are valid.

- Cu in Cu+Au central collision at $\sqrt{s_{NN}} = 200\,\mathrm{GeV} \iff$ Au in Au+Au central collision at $\sqrt{s_{NN}} = 200\,\mathrm{GeV}$.

- Au in Cu+Au central collision at $\sqrt{s_{NN}} = 200\,\mathrm{GeV} \iff$ Cu in Cu+Cu central collision at $\sqrt{s_{NN}} = 200\,\mathrm{GeV}$.

Therefore, the maximal baryon density achievable in the Cu fireball after the Cu+Au collision is about $3.01\,\mathrm{baryons/fm^3}$ while the maximum baryon density in the Au fireball is about $2.04\,\mathrm{baryons/fm^3}$; see Table 3.2 and Table 3.1. The Cu fireball is denser and hotter than the Au fireball in high energy Cu+Au collision. On the other hand, the average rapidity loss $\langle \delta y \rangle$ for the Cu nucleus in Cu+Au collisions is different from that of the Au nucleus in Au+Au collisions because of the different nuclear thickness functions.

Figure 3.25 shows the net baryon rapidity distribution in Cu+Au central collisions at $\sqrt{s_{NN}} = 200\,\mathrm{GeV}$ without including a thermal smearing effect. Peripheral regions of the Au nucleus do not participate in the collision so that their rapidities are the same as the beam rapidity $y_0 = -5.36$. The net baryon distribution on the Cu side of the Cu+Au collision shown in Fig. 3.25 has a smaller magnitude and narrower width compared to the net baryon distribution in Au+Au collision shown in Fig. 3.7, but they have the same smallest rapidity cutoff at $y = 2.47$.

Finally, Figures 3.26 and 3.27 show the contour plots of proper baryon density for the Cu fireball and the Au fireball in their respective local rest frames. The Cu

Cu+Au Collision	Au	Cu
Atomic Mass	197	63
$R_A(\text{fm})$	6.4	4.2
y_0	5.36	5.36
$\langle \delta y \rangle$	1.34	2.71
y_{P}	2.87	2.47
$n_{\text{B}}(1/\text{fm}^3)$	2.04	3.01
$\varepsilon_{\text{P}}(\text{GeV}/\text{fm}^3)$	9.0	20.0
$T\,(\text{MeV})$	264.1	328.1
$\mu_{\text{B}}(\text{MeV})$	693.0	655.4
s/n_{B}	18.33	23.53

Table 3.2: Asymmetic Cu+Au collisions at $\sqrt{s_{NN}} = 200\,\text{GeV}$. The y_0 is the initial beam rapidity and $\langle \delta y \rangle$ is the average rapidity loss. The y_{P} is the final rapidity of the central core of the nucleus at $r_\perp = 0$, which experiences the largest rapidity loss. Other thermodynamic quantities $n_{\text{B}}, \varepsilon_{\text{P}}, T$, μ_B and s are also evaluated at the central core of the nucleus.
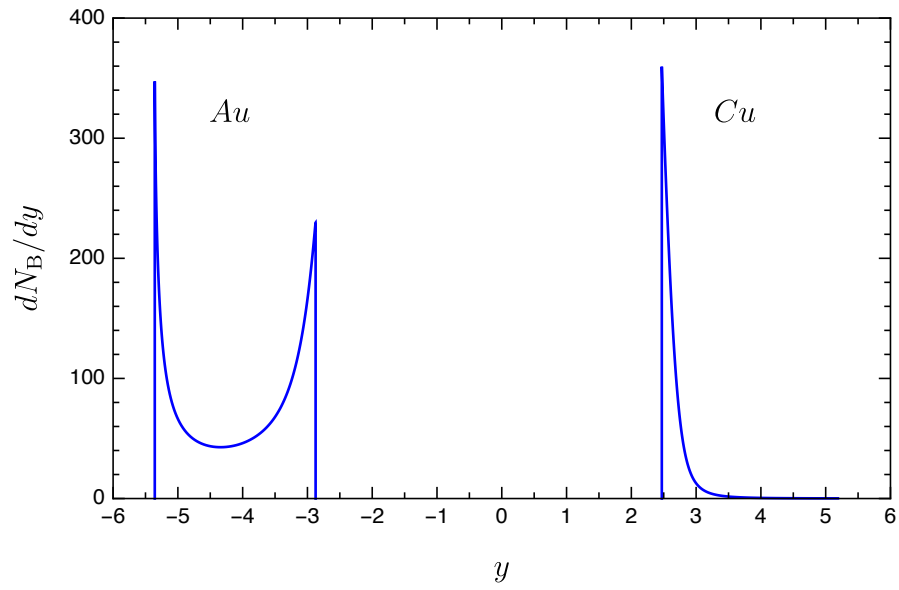
Figure 3.25: Net baryon rapidity distribution in Cu+Au central collision at $\sqrt{s_{NN}} = 200\,\mathrm{GeV}$. The initial beam rapidities are ± 5.36. Peripheral regions of the Au nucleus do not participate in the collision.
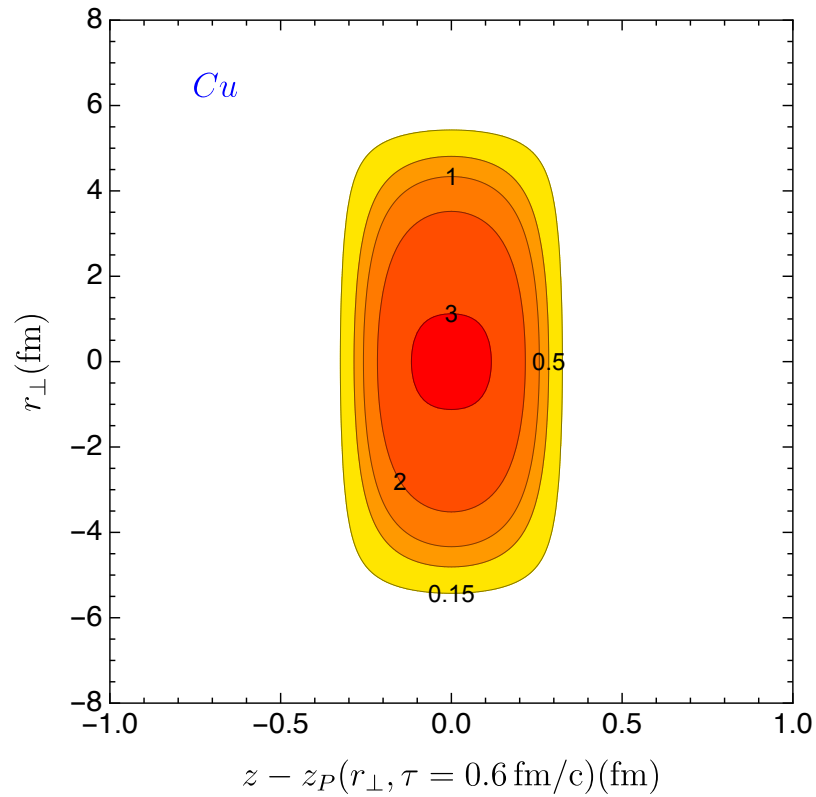
Figure 3.26: Contour plot of the proper baryon density for the Cu fireball in the central collision of Cu+Au at $\sqrt{s_{NN}} = 200\,\mathrm{GeV}$. The numbers are in units of baryons per fm^3. The horizontal axis measures the distance along the beam direction in the local rest frame. Care must be taken when interpreting this plot since the rapidity of the matter and therefore the frame of reference depend on $r_\perp$.

Figure 3.27: Contour plot of the proper baryon density for the Au fireball in the central collision of Cu+Au at $\sqrt{s_{NN}} = 200\,\mathrm{GeV}$. The numbers are in units of baryons per fm³. The horizontal axis measures the distance along the beam direction in the local rest frame. Care must be taken when interpretting this plot since the rapidity of the matter and therefore the frame of reference depend on $r_\perp$..

fireball in Cu+Au collisions has a smaller longitudinal extension $\sim 0.6\,\mathrm{fm}$ in the central core shown in Fig. 3.26 compared to the Au fireball in Au+Au collision with longitudinal extension $\sim 0.9\,\mathrm{fm}$ shown in Fig. 3.9. On the contrary, the Au fireball in Cu+Au collision has a larger longitudinal extension $\sim 1.4\,\mathrm{fm}$ in the central core shown in Fig. 3.27 compared to the Cu fireball in the Cu+Cu collision with longitudinal extension $\sim 1.0\,\mathrm{fm}$ shown in Fig. 3.21.

It is important to note that the Cu fireball is denser and hotter than the Au fireball in the asymmetric central collision of Cu+Au at $\sqrt{s_{NN}} = 200\,\mathrm{GeV}$. On the other hand, the charged particle pseudorapidity distribution in asymmetric central collision of Cu+Au at $\sqrt{s_{NN}} = 200\,\mathrm{GeV}$ tilts to the side of the Au fireball [109]. The central region of the Cu+Au collision is not boost invariant any more.

3.4.2   Collision Energy Dependence

In this section, we study the high baryon densities in the fragmentation regions of high energy heavy-ion collisions with different collision energies. Specifically, we focus on Au+Au central collisions at $\sqrt{s_{NN}} = 62.4\,\mathrm{GeV}$, Au+Au central collisions at $\sqrt{s_{NN}} = 200\,\mathrm{GeV}$, Pb+Pb central collisions at $\sqrt{s_{NN}} = 2.76\,\mathrm{TeV}$ and Pb+Pb central collisions at $\sqrt{s_{NN}} = 5.02\,\mathrm{TeV}$. The Au+Au collisions at these two different collision energies have been carried out at RHIC while the LHC has collided Pb+Pb at $2.76\,\mathrm{TeV}$ and $5.02\,\mathrm{TeV}$. The Au nucleus has atomic mass number 197 and the Pb nucleus has atomic mass number 208, so nuclear size differences would be minor. It should be pointed out that the McLerran-Venugopalan model that describes the central region of high energy heavy-ion collisions using

classical gluon fields becomes more and more applicable with increasing center-of-momentum collision energy. For the Au+Au collision at $\sqrt{s_{NN}} = 62.4\,\mathrm{GeV}$, whether the McLerran-Venugopalan model is still applicable needs more detailed study, which is beyond the scope of this thesis. Here we explore the Au+Au collision at $\sqrt{s_{NN}} = 62.4\,\mathrm{GeV}$ as an extrapolating application of our method. Importantly, the average baryon rapidity loss and net proton rapidity distribution have been measured for Au+Au collision at $\sqrt{s_{NN}} = 62.4\,\mathrm{GeV}$ [49].

To solve for the rapidity loss and excitation energy from Eq. (3.7) for collisions at different energies, one needs to generalize the calculation of initial energy density Eq. (3.26) to include the collision energy dependence. With the help of Eqs. (3.24)

$$\frac{\varepsilon_{0,A}(r_\perp, \sqrt{s_{NN}})}{\varepsilon_{0,Au}(r_\perp = 0, \sqrt{s_{NN}} = 200\,\mathrm{GeV})} = \left[\frac{T_A(r_\perp)}{T_{Au}(r_\perp = 0)}\right]^2 \left[\frac{\mu_N(\sqrt{s_{NN}})}{\mu_N(\sqrt{s_{NN}} = 200\,\mathrm{GeV})}\right]^2 \tag{3.29}$$

In obtaining this expression, we ignore the collision energy dependence of the ultraviolet cutoff (3.25) which appears as $\ln Q^2/m^2$ in the initial energy density Eq. (3.11). In principle the ultraviolet cutoff Q has to be adjusted when the saturation scale Q_s changes with collision energy. This is to make sure that the scale separation $Q^2 \gg Q_s^2$ is satisfied so that the semi-analytic expression of the Glasma energy-momentum tensor we obtained in the leading Q^2 approximation can be used. In Au+Au collisions at $\sqrt{s_{NN}} = 200\,\mathrm{GeV}$, we used the value $Q_s = 1.2\,\mathrm{GeV}$ and $Q = 4.0\,\mathrm{GeV}$. As it will become clear in the following, the saturation scale at LHC energy $5.02\,\mathrm{TeV}$ is approximately $Q_s \sim 1.8\,\mathrm{GeV}$ and an ultraviolet cutoff of $Q \sim 6.0\,\mathrm{GeV}$ only contributes approximately 10% change in the energy density after taking the logarithm. This logarithmic change of the ultraviolet

cutoff in the expression for the energy density should be minor compared to the power law changes in the $\mu_N(\sqrt{s_{NN}})$. Note that μ_N is related to the saturation scale of the nucleon Q^2_{sN} up to a logarithmic correction Eq. (2.33). The collision energy dependence of the saturation scale $Q^2_{sN}(x)$ can be parameterized as [110, 111, 112]

$$Q^2_{sN}(x) = Q^2_0 \left(\frac{x_0}{x}\right)^\lambda \tag{3.30}$$

with $Q^2_0 = 1.0\,\mathrm{GeV}^2$, $x_0 = 3 \times 10^{-4}$ and $\lambda = 0.288$. This parameterization provides a successful description of the HERA data on deep inelastic scattering. At central rapidity $y = 0$, the small x parameter is related to the center-of-momentum collision energy by $x = Q_{sN}/\sqrt{s_{NN}}$, and one obtains [113]

$$\frac{Q^2_{sN}(\sqrt{s_{NN}})}{Q^2_{sN}(\sqrt{s_0})} = \left(\frac{\sqrt{s_{NN}}}{\sqrt{s_0}}\right)^{\bar\lambda} \tag{3.31}$$

with $\bar\lambda = \frac{\lambda}{1+\lambda/2} = 0.252$ with $\sqrt{s_0}$ some reference collision energy. Therefore, the final expression for the collision energy dependent initial energy density is

$$\frac{\varepsilon_{0,A}(r_\perp, \sqrt{s_{NN}})}{\varepsilon_{0,Au}(r_\perp = 0, \sqrt{s_{NN}} = 200\,\mathrm{GeV})} = \left[\frac{T_A(r_\perp)}{T_{Au}(r_\perp = 0)}\right]^2 \left[\frac{\sqrt{s_{NN}}}{200\,\mathrm{GeV}}\right]^{2\bar\lambda}. \tag{3.32}$$

Using this simple parameterization of the collision energy dependence, we compute the initial energy density of the Glasma and the hydrodynamic initial energy density for the different collision energies; the results are given in Table 3.3

With the help of Eq. (3.32) we calculate the baryon and energy densities achieved in the target fireball in the fragmentation region of Au+Au collisions and Pb+Pb collisions at different energies. Table 3.4 shows a few characteristic values of physical quantities. The average rapidity loss for Au+Au at $\sqrt{s_{NN}} = 62.4\,\mathrm{GeV}$ is found to be 1.85, which is close to the lower bound of $1.85 \leq \langle \delta y \rangle \leq 2.17$ measured by the BRAHMS collaboration [49]. The average rapidity losses for

Collision	Au+Au	Au+Au	Pb+Pb	Pb+Pb
$\sqrt{s_{NN}}(\mathrm{GeV})$	62.4	200	2760	5020
$Q_{sA}(\mathrm{GeV})$	1.04	1.20	1.69	1.82
$\varepsilon_0(\mathrm{GeV/fm}^3)$	78.9	142.0	553.6	748.5
$\varepsilon_{\mathrm{hydro}}(\mathrm{GeV/fm}^3)$	16.7	30.0	116.9	158.0
$\varepsilon_{\mathrm{hydro}}^{\mathrm{MC-Glauber}}(\mathrm{GeV/fm}^3)$	25.5	42.5	104.5	132.3

Table 3.3: The initial energy density of the glasma and the initial energy density for hydrodynamics for different collision energies from Eq. (3.32). The hydrodynamic initial energy densities obtained from the Monte Carlo Glauber model for the 0-5% centrality are listed as reference [114]. The gluon saturation scale of the nucleus at different collision energies are also estimated.

Pb+Pb collisions at 2.76 TeV and 5.02 TeV are 3.73 and 4.02, respectively. As a consequence of the rapidity losses, the maximum baryon density achievable in the fragmentation regions of Au+Au collision at $\sqrt{s_{NN}} = 62.4$ GeV is 1.71 baryons/fm^3, which is about 11 times larger than normal nuclear density. Furthermore, for Pb+Pb collisions at $\sqrt{s_{NN}} = 2.76$ TeV and 5.02 TeV, the maximal baryon densities achievable are 11.66 baryons/fm^3 and 15.77 baryons/fm^3, which are about 75 times and 101 times larger than normal nuclear density. These are extremely large baryon densities. The maximal energy density in the target fireball for Au+Au collision at $\sqrt{s_{NN}} = 62.4$ GeV is 6.34 GeV/fm^3 which is smaller than the energy density at the central region 16.7 GeV/fm^3 shown in Fig. 3.3. However, the energy density in the fragmentation regions of Pb+Pb collisions at $\sqrt{s_{NN}} = 2.76$ TeV and 5.02 TeV are 288.67 GeV/fm^3 and 527.50 GeV/fm^3 which are much larger than the corresponding energy densities in the central region, 116.9 GeV/fm^3 and 158.0 GeV/fm^3 given in Table 3.3. As the collision

energy increases, the maximum temperature achievable in the fragmentation regions increases monotonically. The baryon chemical potential however increases very slowly. Consequently, the maximal entropy per baryon increases with the collision energy, as one would expect.

Collision	Au+Au	Au+Au	Pb+Pb	Pb+Pb
$\sqrt{s_{NN}}(\text{GeV})$	62.4	200	2760	5020
y_0	4.2	5.36	7.99	8.59
$\langle \delta y \rangle$	1.85	2.41	3.73	4.02
y_{P}	1.89	2.47	3.76	4.06
$n_{\text{B}}(1/\text{fm}^3)$	1.71	3.01	11.66	15.77
$\varepsilon_{\text{P}}(\text{GeV}/\text{fm}^3)$	6.34	20.00	288.67	527.50
$T(\text{MeV})$	236.6	328.1	642.4	745.9
$\mu_{\text{B}}(\text{MeV})$	748.3	655.4	673.7	680.8
s/n	16.3	23.5	49.6	58.2

Table 3.4: Central collisions of Au+Au and Pb+Pb at center-of-momentum energies $\sqrt{s_{NN}} = 62.4, 200\,\text{GeV}$ and $\sqrt{s_{NN}} = 2.76, 5.02\,\text{TeV}$. The final rapidity y_{P}, baryon density n_{B} , energy density ε_{P} , temperature T, baryon chemical potential μ_B and the entropy per baryon ratio s/n are given for the central core $r_{\perp} = 0$ of the target fireball at $z' = 0$.

The baryon distributions in the local rest frame of the fireballs for Au+Au collisions at $\sqrt{s_{NN}} = 61.4\,\text{GeV}$ and for Pb+Pb collisions at $\sqrt{s_{NN}} = 2.76\,\text{TeV}$ and $5.02\,\text{TeV}$ are shown in Figs. 3.28, 3.29 and 3.30. Compared to Au+Au collisions at $\sqrt{s_{NN}} = 200\,\text{GeV}$, less nuclear compression happens in Au+Au collisions at $\sqrt{s_{NN}} = 62.4\,\text{GeV}$. In the local rest frame of the fireball, the longitudinal extension in the central core is about $\Delta z' \sim 1.6\,\text{fm}$ as shown in Fig. 3.28. On the other hand, in Pb+Pb collisions at $\sqrt{s_{NN}} = 2.76\,\text{TeV}$ and $5.02\,\text{TeV}$, very large nuclear compression result in much smaller longitudinal extensions of $\Delta z' \sim 0.3\,\text{fm}$ and

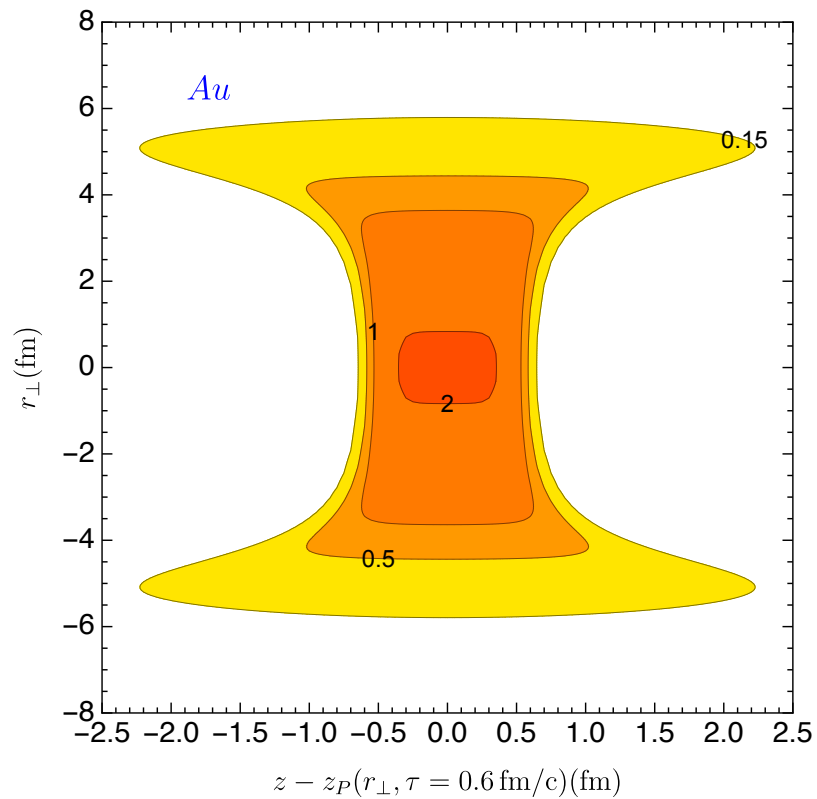$\Delta z' \sim 0.2\,\mathrm{fm}$, as shown in Fig. 3.29 and Fig. 3.30, respectively.
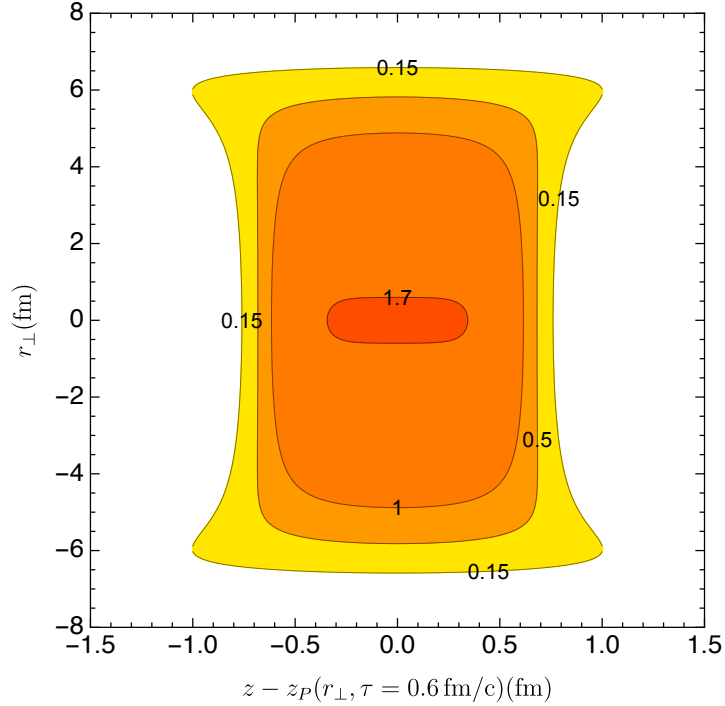
Figure 3.28: Contour plot of the proper baryon density for the Au fireball in central collisions of Au+Au at $\sqrt{s_{NN}} = 62.4\,\mathrm{GeV}$. The numbers are in units of baryons per fm^3. The horizontal axis measures the distance along the beam direction in the local rest frame. Care must be taken when interpreting this plot since the rapidity of the matter and therefore the frame of reference depend on $r_\perp$.

In Fig. 3.31, the adiabatic phase trajectories for the central core regions of the fireballs of Au+Au collisions with $\sqrt{s_{NN}} = 62.4\,\mathrm{GeV}$, $200\,\mathrm{GeV}$ and Pb+Pb collisions with $\sqrt{s_{NN}} = 2.76\,\mathrm{TeV}, 5.02\,\mathrm{TeV}$ are plotted. Increasing the collision energy increases the temperatures inside the fireballs in the fragmentation regions while the baryon chemical potentials change very little, leading to larger and larger entropy per baryon ratios.
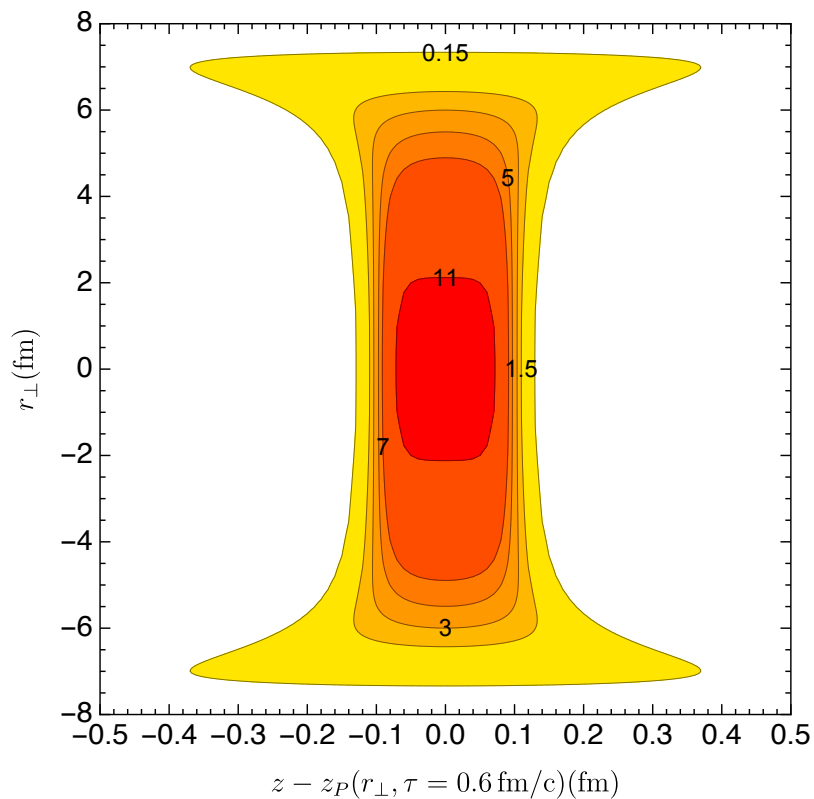
Figure 3.29: Contour plot of the proper baryon density for the Pb fireball in central collisions of Pb+Pb at $\sqrt{s_{NN}} = 2.76\,\mathrm{TeV}$. The numbers are in units of baryons per fm³. The horizontal axis measures the distance along the beam direction in the local rest frame. Care must be taken when interpreting this plot since the rapidity of the matter and therefore the frame of reference depend on $r_\perp$.
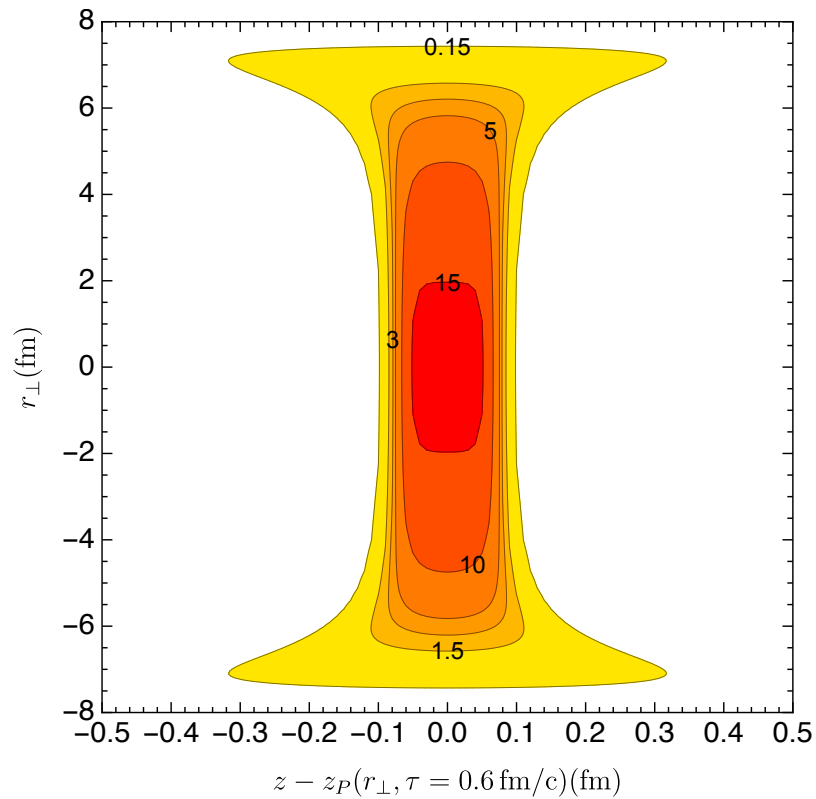
Figure 3.30: Contour plot of the proper baryon density for the Pb fireball in central collisions of Pb+Pb at $\sqrt{s_{NN}} = 5.02\,\text{TeV}$. The numbers are in units of baryons per fm³. The horizontal axis measures the distance along the beam direction in the local rest frame. Care must be taken when interpreting this plot since the rapidity of the matter and therefore the frame of reference depend on $r_\perp$.
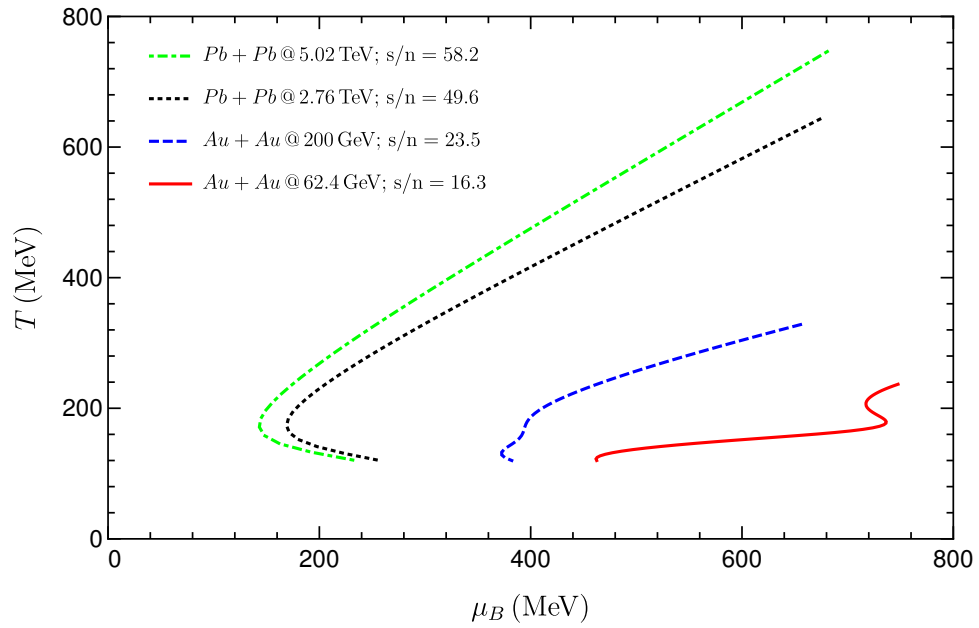
Figure 3.31: Adiabatic phase trajectories for the central core regions of the target fireball in the Au+Au collisions at $\sqrt{s_{NN}} = 62.4, 200\,\text{GeV}$ and in the Pb+Pb collisions at $\sqrt{s_{NN}} = 2.76, 5.02\,\text{TeV}$.

3.4.3   Non-Central Collisions

Apart from colliding heavy ions of different nuclear sizes and at different collision energies, realistic heavy-ion collisions also measure observables at different centralities. The centrality characterizes the impact parameter of the two colliding nuclei. From the most central collisions with impact parameter $b \sim 0$ to the most peripheral collisions with impact parameter $b \sim 2R_A$, the value of centrality increases from 0% to 100%. The initial impact parameter however cannot be directly measured in heavy-ion experiments. It is noted that the observed particle multiplicity decreases from central collisions to peripheral collisions. Therefore, experimentalists measure the particle multiplicity and categorize these events using centrality values in the range $0\% - 100\%$. With the help of a geometric model, like the Glauber model, one can then relate the centrality to the initial impact parameter. A few examples are given in Table 3.5 as calculated by the PHENIX collaboration [115], we will explore the impact parameter dependence of the high baryon densities in the fragmentation regions of high energy heavy-ion collisions.

Centrality Class	0-5%	5%-10%	10%-15%	15%-20%	20%-25%
Impact parameter (fm)	2.3	4.1	5.2	6.2	7.0

Table 3.5: Correspondence between centrality classes and average impact parameters from calculations within the Glauber model [115].

To characterize non-central collisions in the transverse spatial dimensions, we use cylindrical coordinates. Figure 3.32 is a schematic illustration of the transverse overlap region of two equal size nuclei colliding at non-zero impact parameter b. All the vectors here are 2-dimensional in the x-y plane. Let the projectile P be located at $\mathbf{b}/2$ and the target T at $-\mathbf{b}/2$ with $\mathbf{b} = (0, b)$. An arbitrary point is

labeled by $\mathbf{r}_\perp = r_\perp(\cos\phi, \sin\phi) = (x, y)$. The distance from the centers of the nuclei to that point are

$$r_{\mathrm{P}}^2 = r_\perp^2 + \frac{1}{4}b^2 - br_\perp \sin\phi,$$
$$r_{\mathrm{T}}^2 = r_\perp^2 + \frac{1}{4}b^2 + br_\perp \sin\phi, \tag{3.33}$$

The thickness functions T_{P} and T_{T} depend only on r_{P} and r_{T}, respectively. Consider the baryon distribution arising from the projectile; a similar formula applies to the target. Let $y_{\mathrm{P}}(r_\perp, \phi, b)$ denote the final rapidity of a piece of projectile located at the position $\mathbf{r}_\perp$. Then the baryon rapidity distribution is a generalization of Eq. (3.15) taking into account the non-zero impact parameter,

$$\frac{dN_P}{dy} = \int_0^\infty dr \int_0^{2\pi} d\phi T_{\mathrm{P}}(r_\perp, \phi, b) r_\perp \delta(y - y_{\mathrm{P}}(r_\perp, \phi, b)). \tag{3.34}$$

For central collisions of spherical nuclei, which need not be identical, there is no dependence on ϕ, and there is a one-to-one correspondence between y_{P} and r. Then we can replace $\delta(y - y_{\mathrm{P}}(r_\perp))$ with $\delta(r_\perp - r_{\perp\mathrm{P}}(y))$ along with the relevant Jacobian to reproduce the expression in Eq. (3.15).

For $b \neq 0$ it is probably better to discretize both r and ϕ. Assuming uniform spacings Δr and $\Delta\phi$ which satisfy $N_r \times \Delta r = \tilde{R}$ and $(N_\phi + 1) \times \Delta\phi = 2\pi$, respectively. Here $\tilde{R}$ characterizes the radius of a circular area chosen for the discretization. The discretized points are labeled by (r_i, ϕ_j) with

$$r_i = i\Delta r, \qquad i = 1, 2, \ldots, N_r$$
$$\phi_j = j\Delta\phi, \qquad j = 0, 1, 2, \ldots, N_\phi. \tag{3.35}$$

The point $(0, 0)$ is treated separately. Also, $\phi_j = 0$ is the same as $\phi_j = 2\pi$. For points in the overlap region, their coordinates (r_i, ϕ_j) satisfy $r_{\mathrm{P}(i,j)}^2 \leq R_A^2$
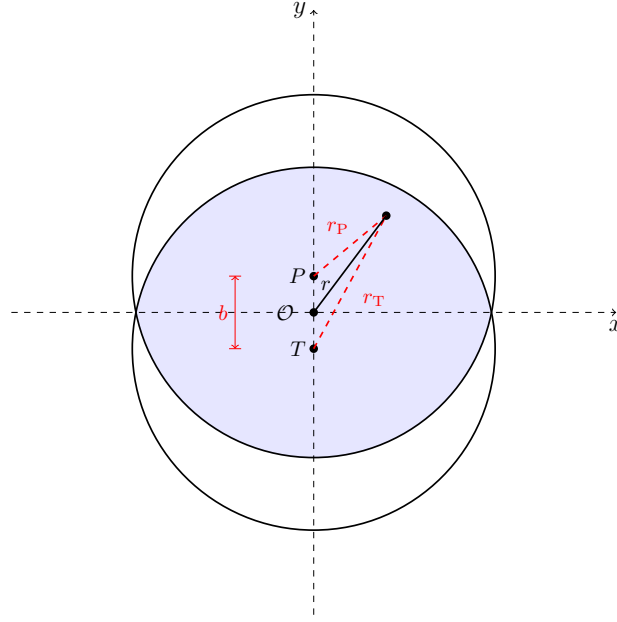
Figure 3.32: Schematic picture of the transverse overlap region for non-central collisions of two nuclei.

and $r^2_{\mathrm{T}(i,j)} \leq R^2_A$. For the slab-slab collisions at the position (r_i, ϕ_j), the mass per unit area is obtained by the thickness functions $\mathcal{M}_{\mathrm{P}(i,j)} = m_N T_A(r_{\mathrm{P}(i,j)})$ and $\mathcal{M}_{\mathrm{T}(i,j)} = m_N T_A(r_{\mathrm{T}(i,j)})$ and the initial energy is proportional to the product of the two nuclear thickness functions $\varepsilon_{0(i,j)} \sim T_A(r_{\mathrm{P}(i,j)}) T_A(r_{\mathrm{T}(i,j)})$. We can then solve for the final rapidity $y_{\mathrm{P}(i,j)}$ and the nuclear excitation energy $\mathcal{M}_{\mathrm{P}(i,j)}$. The number of baryon charges inside the projectile slab at position (r_i, ϕ_j) is $\Delta N_{\mathrm{P}(i,j)} = r_i T_{\mathrm{P}(i,j)} \Delta r \Delta \phi$. To calculate the baryon rapidity distribution for $b \neq 0$, we perform the integration over the Dirac delta function while fixing the value of ϕ

$$
\begin{aligned}
\frac{dN_{\mathrm{P}}}{dy} &= \sum_j \Delta \phi \int_0^\infty dr_\perp T_{\mathrm{P}}(r_\perp, \phi_j, b) r_\perp \delta(y - y_{\mathrm{P}}(r_\perp, \phi_j, b)) \\
&= \sum_j \frac{T_{\mathrm{P}}(r_\perp, \phi_j, b) r_\perp \Delta \phi}{|dy_{\mathrm{P}}/dr_\perp|} \Bigg|_{r_\perp = r_\perp(y, \phi_j, b)}
\end{aligned}
\tag{3.36}
$$

Figure 3.33 shows the net-baryon distribution as a function of momentum

space rapidity for Au+Au collisions at $\sqrt{s_{NN}} = 200\,\text{GeV}$. Results for two impact parameters $b = 0$ and $b = 2.3\,\text{fm}$ are presented. Here $b = 2.3\,\text{fm}$ corresponds to the $0 - 5\%$ centrality class. Compared to the most central collision with $b = 0$, the collision with average impact parameter $b = 2.3\,\text{fm}$ has some spectator baryons that do not participate in the collision. These baryons are located in the peripheral regions along the direction of the impact parameter vector (see Fig. 3.32) and maintain their original beam rapidities ± 5.36. That is why the dN_{B}/dy distribution has baryon excess around $y = \pm 5.36$ for $b = 2.3\,\text{fm}$ in Fig. 3.33. Since fewer baryons participate in the collisions with non-zero impact parameter, the average rapidity loss is smaller. For Au+Au collisions at $\sqrt{s_{NN}} = 200\,\text{GeV}$ with $b = 0$, our prediction is $\langle \delta y \rangle \simeq 2.4$. For $b = 2.3\,\text{fm}$, the average rapidity loss is calculated to be $\langle \delta y \rangle \simeq 2.14$. These values should be compared with the experimental measurements from the BRAHMS collaboration, $1.45 \leq \langle \delta y \rangle \leq 2.45$ for the centrality class $0 - 5\%$ [48].

In Figs. 3.34 and 3.35, the proper baryon density distribution of the projectile fireball in the transverse plane for the longitudinal slice $z' = 0$ are given for $b = 0$ and $b = 2.3\,\text{fm}$, respectively. For zero impact parameter, the baryon distribution is azimuthally symmetric in the transverse plane and the center of the fireball achieves the largest baryon density of about $3\,\text{baryons/fm}^3$. On the contrary, in collisions with non-zero impact parameter $b = 2.3\,\text{fm}$, the baryon distribution on the transverse plane is not azimuthally symmetric anymore. Even the region where the largest baryon density is achieved has been shifted away from the center of the projectile fireball (the center of the fireball corresponds to $(x = 0, y = 0)$). The region with largest baryon density is surrounding the point $(x = 0, y =$
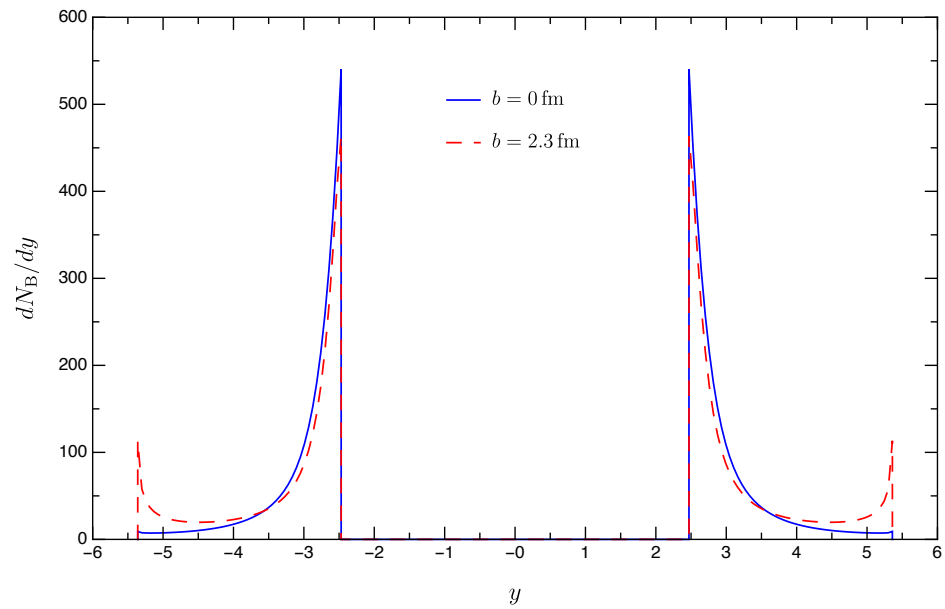
Figure 3.33: Net-baryon rapidity distribution for Au+Au collisions at $\sqrt{s_{NN}} = 200\,\mathrm{GeV}$ with two impact parameters, $b = 0$ and $b = 2.3\,\mathrm{fm}$. The initial beam rapidities are ± 5.36.

2.3 fm) which is the transverse location of the center of the *target fireball* when the projectile nucleus and the target nucleus overlap. This is easy to understand from our previous discussion on the asymmetric Cu+Au collision. When two nuclear slabs collide, the nuclear slab with less baryon charge experiences larger nuclear compression while the nuclear slab with more baryon charge experiences less nuclear compression.
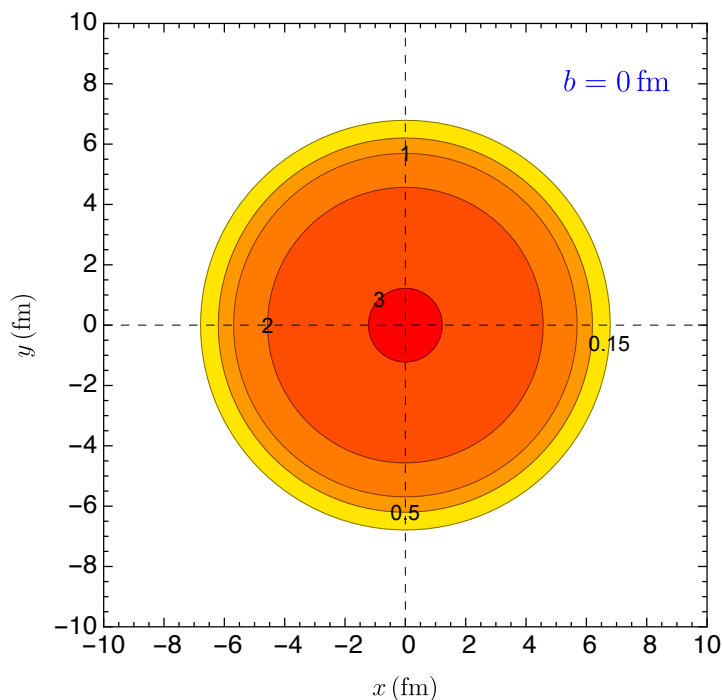
Figure 3.34: Contour plot of the proper baryon density for the Au *projectile fireball* in the transverse plane for the slice $z' = 0$. The collision is Au+Au at $\sqrt{s_{NN}} = 200\,\mathrm{GeV}$ with impact parameter $b = 0\,\mathrm{fm}$. The numbers are in units of baryons per fm^3. The position $x = 0, y = 0$ corresponds to the center of the fireball.

Figures 3.36 and 3.37 show the baryon density distribution in the $r_\perp - z'$ plane for azimuthal angle $\phi = \pi/2$ and $\phi = 3\pi/2$. This is the direction along the impact
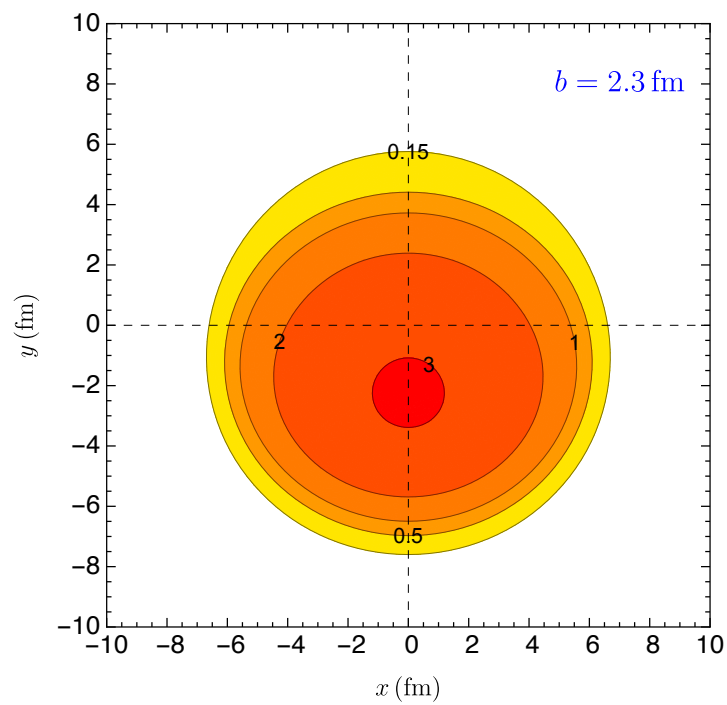
Figure 3.35: Contour plot of the proper baryon density for the Au *projectile fireball* in the transverse plane for the slice $z' = 0$. The collision is Au+Au at $\sqrt{s_{NN}} = 200\,\text{GeV}$ with impact parameter $b = 2.3\,\text{fm}$. The numbers are in units of baryons per fm^3. The position $x = 0, y = 0$ corresponds to the center of the fireball.

parameter vector. For collisions with zero impact parameter, the baryon density distribution is symmetric with respect to $\phi = \pi/2$ and $\phi = 3\pi/2$. Also the largest baryon density region is around the center of the projectile fireball. On the other hand, for collisions with non-zero impact parameter $b = 2.3\,\mathrm{fm}$, the baryon density distribution is no longer symmetric along the direction of the impact parameter vector. In Fig. 3.37, the position $(r_\perp = 0, z' = 0)$ corresponds to the center of the projectile fireball. The region of the projectile nucleus that overlaps with the central region of the target nucleus experiences the largest nuclear compression while the regions of the projectile nucleus that overlap with the peripheral region of the target nucleus experiences less and less nuclear compression.

3.5 Conclusion

In this chapter we have systematically studied the high baryon densities in the fragmentation regions of high energy heavy-ion collisions within the McLerran-Venugopalan model. The off-diagonal term in the energy-momentum tensor of the Glasma, which comes from the transverse chromo-electromagnetic fields, is responsible for the nuclear excitation energy in this model. For Au+Au central collisions at $\sqrt{s_{NN}} = 200\,\mathrm{GeV}$, the highest baryon density $3.0\,\mathrm{baryons/fm}^3$ in the fragmentation regions is found to be more than ten times larger than normal nuclear density, and the largest energy density $20\,\mathrm{GeV/fm}^3$ is also more than ten times larger than the critical energy density for the formation of quark-gluon plasma. Using a crossover equation of state, the temperature is found to be above $200\,\mathrm{MeV}$ and the baryon chemical potentials are larger than $600\,\mathrm{MeV}$. The entropy per baryon ratios are found to be in the range of $10 - 23.5$, inversely
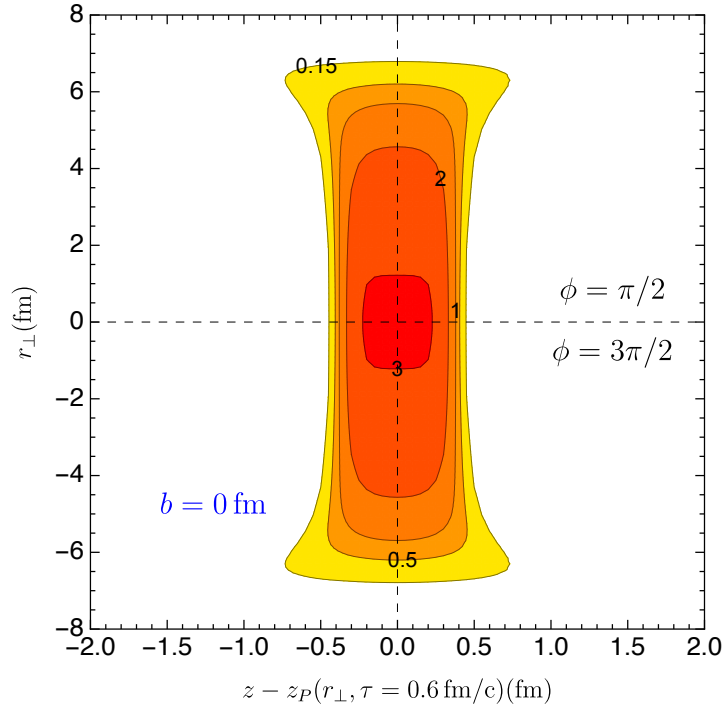
Figure 3.36: Contour plot of the proper baryon density for the Au *projectile fireball* in the $r_\perp - z'$ plane. The angle ϕ is chosen to align with the direction of the impact parameter so that the upper half is for $\phi = \pi/2$ and the lower half is for $\phi = 3\pi/2$. The collision is Au+Au at $\sqrt{s_{NN}} = 200\,\text{GeV}$ with impact parameter $b = 0\,\text{fm}$. The numbers are in units of baryons per fm^3. The position $r_\perp = 0, z' = 0$ corresponds to the center of the fireball.
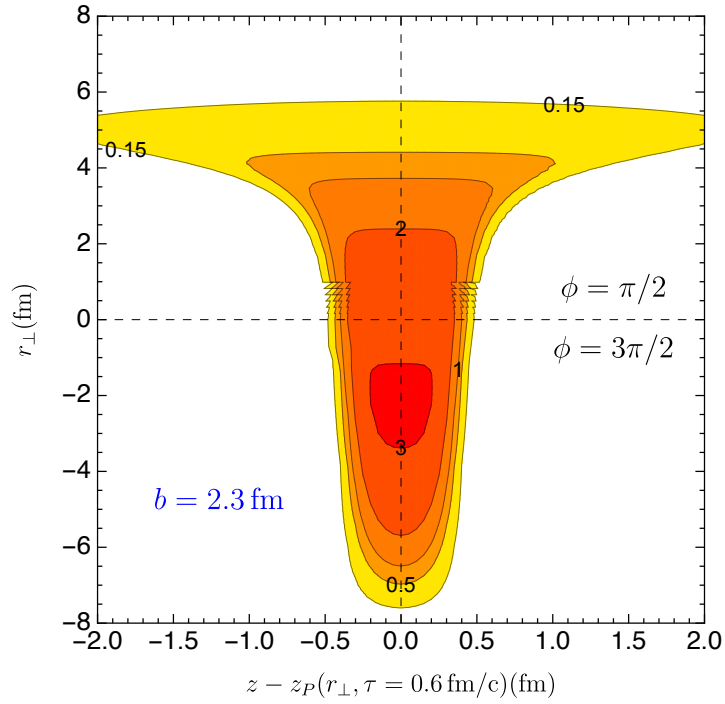
Figure 3.37: Contour plot of the proper baryon density for the Au *projectile fireball* in the $r_\perp - z'$ plane. The angle ϕ is chosen to align with the direction of the impact parameter so that the upper half is for $\phi = \pi/2$ and the lower half is for $\phi = 3\pi/2$. The collision is Au+Au at $\sqrt{s_{NN}} = 200\,\mathrm{GeV}$ with impact parameter $b = 2.3\,\mathrm{fm}$. The numbers are in units of baryons per fm^3. The position $r_\perp = 0, z' = 0$ corresponds to the center of the fireball.

corresponding to the momentum space rapidity range $2.5 - 3.7$. The entropy per baryon ratios might be in the right range so that a scan through rapidity may locate the critical point of QCD phase diagram for central collisions. For central collision at fixed beam energy, the highest baryon density achievable in the fragmentation regions increases with nuclear size. In Cu+Cu, Au+Au and U+U (tip-tip) collisions at $\sqrt{s_{NN}} = 200\,\text{GeV}$, the highest baryon densities are $2.0, 3.0$ and $4.0\,\text{baryons/fm}^3$, respectively. In asymmetric Cu+Au collisions, the Cu nucleus is compressed more than the Au nucleus so that the Cu fireball achieves the higher baryon densities. For central collisions at fixed nuclear size, the highest baryon density achievable increases with collision energy. In Au+Au collisions at $\sqrt{s_{NN}} = 62.4\,\text{GeV}$, Au+Au collisions at $\sqrt{s_{NN}} = 200\,\text{GeV}$, Pb+Pb collisions at $\sqrt{s_{NN}} = 2.76\,\text{TeV}$, and Pb+Pb collisions at $\sqrt{s_{NN}} = 5.02\,\text{TeV}$, the highest baryon densities are $1.76, 3.01, 11.66$ and $15.77\,\text{baryons/fm}^3$, respectively. For non-central collisions with finite impact parameter, the average rapidity loss is reduced due to the spectator baryons in the peripheral region of the colliding nuclei. For Au+Au collisions at $\sqrt{s_{NN}} = 200\,\text{GeV}$ with $0 - 5\%$, our calculations predict the average rapidity loss to be about 2.14. This is in agreement with measurement by the BRAHMS collaboration.

Chapter 4

Hydrodynamic Evolution of High Baryon Density Matter

4.1 Introduction

The idea of using hydrodynamics to describe particle production in high energy hadronic collisions has a long history and dates back to L. D. Landau in 1950s [116]. Although there were many efforts in studying heavy-ion collisions using hydrodynamics before the RHIC era [117, 118, 119, 120], it is only when the RHIC experiments discovered the large collective flow and the azimuthally anisotropic particle emission patterns, which can be well described by ideal hydrodynamic modeling, that the hydrodynamical description of the QGP evolution became one part of the standard space-time picture of heavy-ion collisions that is being widely accepted [121, 80]. Theoretical efforts to correctly include viscosities into the relativistic ideal hydrodynamics were also carried out at the same time [122,

123, 140, 125]. In 2004, studies from the Anti-de Sitter/Conformal Field Theory (AdS/CFT) approach predicted a lower bound on the ratio of the shear viscosity to the entropy density $\eta/s = 1/4\pi$ for a strongly interacting quantum system [126]. Since then relativistic viscous hydrodynamics has been implemented and improved in numerical simulations to compare with experimental data from high energy heavy-ion collisions [127, 128, 129]. Currently, the 3+1D event-by-event hydrodynamics with initial state fluctuation [130, 131] is the state-of-art in the hydrodynamic modeling of heavy-ion collisions (see recent reviews in [132, 133, 134]).

The discovery that the space-time evolution of the QGP created in the central region of high energy heavy-ion collisions follows the principles of fluid mechanics is astonishing. Indeed, the typical size of QGP created in nucleus-nucleus collisions is on the order of 10 fm and the time duration is on the order of $10 - 20$ fm/c. The validity and effectiveness of hydrodynamics for such a small system having so short lifetime where quantum mechanics should play an important role is far from clear. To emphasize the situation, there are studies [135] showing that for even smaller systems created in proton+proton collisions and proton+lead collisions at the LHC can also be described by hydrodynamics. However, how QGP is formed after the first encounter of the two colliding nuclei is still a challenging open question, not to mention the microscopic effective degrees of freedom that could explain the strongly interacting nature behind the QGP. In practice, the hydrodynamic modeling of high energy heavy-ion collisions begins by assuming the QGP is formed at some initial proper time τ_0 after the collision. With appropriate model-dependent initial conditions, the relativistic viscous hydrodynamic

equations are numerically solved using an equation of state either from lattice QCD calculations or from theoretical models. As the system expands and cools, the mean free path of constituents in the QGP increases until it is comparable to the size of the system so that hydrodynamics breaks down. Conversion from the description of a hydrodynamical continuous medium to the description involving individual hadrons, like the kinetic theory approach, follows in order to compare with experimental data.

Following this practice in the central region of high energy heavy-ion collisions, we assume the high baryon density matter in the fragmentation regions also evolves according to relativistic hydrodynamic equations. The questions of how thermalization is reached and how QGP with high baryon density is formed in the fragmentation regions are beyond the scope of the thesis. After assuming the hydrodynamic evolution of the high baryon density matter in the fragmentation regions, we will focus on the phenomenological consequences. Specifically, we solve the 1+1D (temporal + longitudinal) hydrodynamic equations together with the baryon diffusion equation. The initial conditions are the high baryon density initial conditions for the fragmentation regions developed in the previous Chapter in combination with the boost-invariant initial conditions for the central region. We will explore the baryon transport phenomena and momentum space rapidity dependent observables.

The chapter is organized as follows. A general discussion of the relativistic hydrodynamic equations with viscous and diffusive effects is given in Sec. 4.2. The equations are written explicitly for the 1+1D situation. Section 4.3 includes the inputs to the 1+1D diffusive hydrodynamic equations, like the initial conditions,

the equation of state, the baryon transport coefficient and the freezeout mechanism. Numerical results from solving the 1+1D diffusive hydrodynamic equations are presented in Sec. 4.4. The baryon diffusion dynamics and rapidity dependent observables are explained in detail.

4.2 Relativistic Hydrodynamic Equations

4.2.1 Viscous and Diffusive Hydrodynamic Equations

Relatvistic hydrodynamic equations, which in general describe the long wavelength degrees of freedom of a system in the relativistic realm, govern the space-time evolution of QGP and the production of soft hadrons in nuclear collisions. They are about the conservation of energy and momentum and the conservation of charges, like electric charge, baryon charge, etc. In high energy heavy-ion collisions, we are particularly interested in the baryon current as baryon charges are conserved in the strong interaction and the QCD phase diagram is controlled by the baryon doping in the system. There are plenty of review papers on the relativistic hydrodynamic equations in the context of high energy heavy-ion collisions [125, 132, 134, 136]; the discussion in this section closely follows the papers [133, 138]. The hydrodynamic equations are

$$\partial_\mu T^{\mu\nu} = 0,$$
$$\partial_\mu J_B^\mu = 0. \tag{4.1}$$

The general energy-momentum tensor $T^{\mu\nu}$ for an relativistic viscous fluid has the expression

$$T^{\mu\nu} = \varepsilon u^\mu u^\nu - (P + \Pi)\Delta^{\mu\nu} + \pi^{\mu\nu}. \tag{4.2}$$

Here $\varepsilon \equiv \varepsilon(x)$, $P \equiv P(x)$, $\Pi \equiv \Pi(x)$, $u^\mu \equiv u^\mu(x)$ and $\pi^{\mu\nu} \equiv \pi^{\mu\nu}(x)$ are the local energy density, the thermal pressure, the bulk viscous pressure, the velocity field and the shear stress tensor, respectively. The time-like velocity field u^μ is chosen to be along the energy current satisfying $T^\mu_\nu u^\nu = \varepsilon u^\mu$, the so-called Landau frame. The velocity field is further normalized to be $u^\mu u_\mu = 1$. Raising or lowering tensor indexes are through the Minkowski metric $g_{\mu\nu} = \mathrm{diag}(1, -1, -1, -1)$. The $\Delta^{\mu\nu} = g^{\mu\nu} - u^\mu u^\nu$ is a symmetric projection operator orthogonal to the velocity field $\Delta^{\mu\nu} u_\nu = \Delta^{\mu\nu} u_\mu = 0$. The shear stress tensor $\pi^{\mu\nu}$ is by construction symmetric, traceless and also orthogonal to the velocity field $\pi^{\mu\nu} u_\mu = 0$. The bulk viscous pressure $\Pi(x)$ and the shear stress tensor $\pi^{\mu\nu}(x)$ are the viscous corrections to the ideal hydrodynamics energy-momentum tensor $T^{\mu\nu}_{\mathrm{id}} = (\varepsilon + P)u^\mu u^\nu - Pg^{\mu\nu}$. The baryon current is expressed as

$$J^\mu_B = n_B u^\mu + V^\mu \tag{4.3}$$

with $n_B \equiv n_B(x)$ being the local baryon density field and $V^\mu \equiv V^\mu(x)$ the diffusive baryon current. The diffusive part of the baryon current is perpendicular to the four velocity $u_\mu V^\mu = 0$. Also, the $V^\mu(x)$ is the diffusive correction to the baryon current of ideal fluid $J^\mu_{B,\mathrm{id}} = n_B u^\mu$. With these constraints, in 3+1 dimensions, there are fifteen variables to be solved in the energy-momentum tensor Eq. (4.2) and the baryon current Eq. (4.3); they are $\varepsilon(x), n_B(x), P(x), \Pi(x), u^\mu(x), V^\mu(x)$ and $\pi^{\mu\nu}(x)$. But there are only five differential equations in Eqs. (4.1). We need ten more equations or constraints to solve for the variables.

Generalizations of the well-known non-relativistic Navier-Stokes equations of fluid mechanics to the relativistic realm result in a few constitutive equations for the viscous corrections and the diffusive correction: $\Pi = -\zeta\theta$, $\pi^{\mu\nu} = 2\eta\sigma^{\mu\nu}$ and

$V^\mu = \kappa_B I^\mu$. Here ζ, η and κ_B are the bulk viscosity, shear viscosity and baryon transport coefficient, respectively. The scalar $\theta = \partial_\mu u^\mu$ and the symmetric tensor $\sigma^{\mu\nu} = \frac{1}{2}(\nabla^\mu u^\nu + \nabla^\nu u^\mu) - \frac{1}{3}\Delta^{\mu\nu}\theta$ with the space-like gradient $\nabla^\mu = \Delta^{\mu\nu}\partial_\nu$ come from the gradients of the velocity field. The vector $I^\mu = \nabla^\mu(\mu_B/T)$ with μ_B and T the baryon chemical potential and temperature is due to the gradient of the fugacity. However, the relativistic Navier-Stokes equations suffer from the problems of acausality and numerical instability because it assumes instantaneous responses of the viscous flows and diffusive current to the gradients of the hydrodynamical variables (the velocity field, baryon chemical potential and temperature) as expressed in the constitutive equations. Relativistic causal fluid equations can be achieved by promoting the constitutive equations to dynamical equations, the Israel-Stewart theory [137]. The bulk viscous pressure $\Pi(x)$, the shear stress tensor $\pi^{\mu\nu}(x)$ and the baryon diffusive current $V^\mu(x)$ follow their own dynamical equations that asymptotically approach their Navier-Stokes limits

$$\tau_\Pi D\Pi + \Pi = -\zeta\theta + \mathcal{X}\,,$$
$$\tau_\pi \Delta^{\mu\nu}{}_{\alpha\beta} D\pi^{\alpha\beta} + \pi^{\mu\nu} = 2\eta\sigma^{\mu\nu} + \mathcal{X}^{\mu\nu}\,, \tag{4.4}$$
$$\tau_V \Delta^{\mu\nu} DV_\nu + V^\mu = \kappa_B I^\mu + \mathcal{X}^\mu\,.$$

The τ_Π, τ_π and τ_V are the relaxation times for the bulk viscous pressure, the shear stress tensor and the baryon diffusive current, respectively. The comoving time derivative $D = u^\mu\partial_\mu$ reduces to ∂_t in the fluid local rest frame where $u^\mu = (1,0,0,0)$. Here $\Delta^{\mu\nu}{}_{\alpha\beta} = \frac{1}{2}(\Delta^\mu_\alpha \Delta^\nu_\beta + \Delta^\mu_\beta \Delta^\nu_\alpha) - \frac{1}{3}\Delta^{\mu\nu}\Delta_{\alpha\beta}$. The $\mathcal{X}, \mathcal{X}^{\mu\nu}, \mathcal{X}^\mu$ represent other possible terms that can be higher order gradients of hydrodynamical and thermodynamical variables. For example, Israel and Stewart [137] predicted there are terms $-\frac{4}{3}\tau_\Pi\theta\Pi$, $-\frac{4}{3}\tau_\pi\theta\pi^{\mu\nu}$ and $-\tau_V\theta V^\mu$ in $\mathcal{X}$, $\mathcal{X}^{\mu\nu}$ and $\mathcal{X}^\mu$,

respectively. How many terms there are and what the relative importance of these terms to the study of QGP are still under active research and debate [139, 140]. Most of the derivations of relativistic viscous hydrodynamic equations follow the kinetic theory approach starting from the Boltzmann equation for a single particle distribution function. This approach has a long history dating back to the works of Chapman-Enskog [141], Grad [143, 144] and Israel and Stewart[137]. The problem is how to organize the terms either in the gradient expansion of hydrodynamical and thermodynamical variables or in the moment expansion of the single particle distribution function. There is also the question whether results from the kinetic theory approach, which is generally valid for dilute systems, can be applied to strongly interacting systems like the QGP created in high energy heavy-ion collisions.

The final constraint on the fifteen variables is the Equation of State (EoS) $P = P(T, \mu_B)$, which relates the energy density and the baryon density to the pressure. The relaxation time $\tau_\Pi, \tau_\pi, \tau_V$, the bulk viscosity ζ, the shear viscosity η, the baryon transport coefficient κ_B and the EoS store information on the microscopic dynamics specific to the QGP. Hydrodynamics as a universal framework is used to describe many different physical systems, but only the coefficients in the hydrodynamic equations and the EoS carry information about the particular system under study. One important purpose of using hydrodynamics to study the QGP is to constraint the EoS and extract information on the microscopic physics underlying the QGP. The $\tau_\Pi, \tau_\pi, \tau_V, \zeta, \eta, \kappa_B$ and the EoS are external inputs to the hydrodynamic equations.

4.2.2   Validity of Hydrodynamics

Hydrodynamics as a macroscopic description of certain physical systems usually assumes the system is not far from local thermal equilibrium. For a perfect fluid, local thermal equilibrium is strictly enforced in the rest frame of each fluid element and the fluid looks isotropic to a comoving observer with the fluid element. In dissipative fluids, local thermal equilibrium is required to be maintained in the rest frame of each fluid element but the fluid does not look isotropic anymore to a comoving observer. Frictional forces (viscosities), heat conduction and particle transport between fluid elements ruin the isotropy in the local rest frame of the fluid element and modify the local thermal equilibrium state. Requiring local thermal equilibrium for hydrodynamics, both for perfect fluids and imperfect fluids, makes sure that the equation of state of the system is well-defined: for example, the thermal pressure is related to the local energy density and particle number density $P \equiv P(\varepsilon, n)$. For a fluid element which is physically small but contains a sufficiently large number of particles, the mean free path of a particle has to be much smaller than the typical physical size of the fluid element. Otherwise the kinetic theory approach would be more appropriate than the hydrodynamic approach, or more coarse-grained fluid elements have to be used to stay in the fluid regime. The ratio of the mean free path to the macroscopic length scale, defined as the Knudsen number $Kn = \lambda_{\mathrm{mfp}}/L_{\mathrm{mac}}$, characterizes the validity of hydrodynamics. The Knudsen number has to be small.

In the case of dissipative fluids, dissipative effects come from the gradients of thermodynamic variables and the velocity field. The fluid element has to adjust its local thermal equilibrium in response to the dissipative forces. These dissipative

perturbations to the local thermal equilibrium have to be small to allow the fluid element to rest onto a new thermal equilibrium. The inverse Reynolds numbers, defined as $R_\Pi^{-1} = |\Pi|/P, R_V^{-1} = |V^\mu|/P, R_\pi^{-1} = |\pi^{\mu\nu}|/P$ characterize the relative size of the dissipative effects to the thermodynamic variables in equilibrium. If the Reynolds numbers are much larger than one, that is, the gradients are very large, local thermal equilibrium cannot be maintained and hydrodynamics breaks down. The Israel-Stewart theory, which allows finite relaxation time for the fluid element to rest onto a new thermal equilibrium, contains second orders in the gradient expansions. When the gradients are large, certain resummations over the all-order gradient expansions can be achieved that partially alleviate the divergent nature of the gradient expansion in deriving hydrodynamic equations [134]. For dissipative hydrodynamics to be applicable, the Reynolds numbers also have to be small.

4.2.3   1+1D Diffusive Hydrodynamic Equations

The study of the QGP in the central region using hydrodynamics usually ignores the baryon current conservation equation in Eq. (4.1) and the associated baryon diffusion equation Eq. (4.4) because the net baryon charges are close to zero and boost-invariance is usually assumed in high energy heavy-ion collisions. Most of the efforts are focused on the effects of shear viscosity in reproducing the anisotropic flow data and extracting the temperature dependence of shear viscosity over entropy density [125, 145]. With the high baryon density initial conditions in the fragmentation regions of high energy heavy-ion collisions, baryon

conservation and diffusion equations must be included in the hydrodynamic description of the QGP evolution, and the boost-invariance assumption becomes invalid. A full 3+1D numerical computation of Eqs. (4.1) and (4.4) with high baryon density initial conditions are challenging. Instead, we focus on the 1+1D (temporal+longitudinal) situation and study the longitudinal dynamics of the high baryon density matter, given the initial conditions. We also ignore the viscous effects and focus on the baryon diffusion effect. This is complementary to the conventional hydrodynamic simulations of the QGP evolution in high energy heavy-ion collision which usually ignore the longitudinal dynamics by assuming boost-invariance and not taking into account the high baryon densities in the fragmentation regions. We hope this 1+1D study will give us a physical picture of the longitudinal dynamics of the baryons before a full 3+1D description is developed.

There are several studies on the 1+1D hydrodynamics for high energy heavy-ion collisions without assuming boost-invariance [146, 147, 148, 149]. However, none of these studies take into account the high baryon density initial conditions in the fragmentation regions. We only keep the ideal part of the energy-momentum tensor in Eq. (4.2). For the baryon diffusion equation in Eq. (4.4), only the fugacity gradient term is kept on the right hand side ignoring the $\mathcal{X}^\mu$ terms. We rewrite the equations using Milne coordinates (τ, η) defined from the Cartesian coordinates by $\tau = \sqrt{t^2 - z^2}$ and $\eta = \frac{1}{2}\ln\left(\frac{t+z}{t-z}\right)$. The set of equations we are

solving in terms of the Milne coordinates are

$$\partial_\tau(\tau T^{\tau\tau}) + \partial_\eta \tilde{T}^{\tau\eta} + \tilde{T}^{\eta\eta} = 0,$$

$$\partial_\tau(\tau \tilde{T}^{\tau\eta}) + \partial_\eta \tilde{T}^{\eta\eta} + \tilde{T}^{\tau\eta} = 0,$$

$$\partial_\tau(\tau J^\tau) + \partial_\eta(\tau J^\eta) = \mathcal{S}_B,$$

$$\partial_\tau(\tilde{V}^\eta) + \partial_\eta\left(\frac{u^\eta}{u^\tau}\tilde{V}^\eta\right) = \mathcal{S}_V.$$

(4.5)

with the source terms being

$$\mathcal{S}_B = -\partial_\tau\left(\frac{\tau^2 u^\eta}{u^\tau}\tilde{V}^\eta\right) - \partial_\eta\tilde{V}^\eta,$$

$$\mathcal{S}_V = \frac{\tilde{V}^\eta}{u^\tau}(\partial_\tau u^\tau + \partial_\eta u^\eta) - \frac{1}{\tau_V}\frac{\tilde{V}^\eta}{u^\tau} - \frac{\kappa_B}{\tau_V}[u^\tau\tau^{-1}\partial_\eta + \tau u^\eta\partial_\tau]\left(\frac{\mu_B}{T}\right).$$

(4.6)

Here

$$T^{\tau\tau} = (\varepsilon + P)u^\tau u^\tau - P,$$

$$\tilde{T}^{\tau\eta} = \tau T^{\tau\eta} = (\varepsilon + P)\tau u^\tau u^\eta,$$

$$\tilde{T}^{\eta\eta} = \tau^2 T^{\eta\eta} = (\varepsilon + P)\tau^2 u^\eta u^\eta + P,$$

$$J^\tau = n_B u^\tau,$$

$$J^\eta = n_B u^\eta,$$

$$\tilde{V}^\eta = \tau V^\eta.$$

(4.7)

and the velocity fields are

$$u^\tau = u^t \cosh\eta - u^z \sinh\eta,$$

$$\tau u^\eta = u^z \cosh\eta - u^t \sinh\eta.$$

(4.8)

The 1+1D hydrodynamics equations Eq. (4.5) are written in a form that is suitable for numerical calculations using the Central-Upwind scheme (Kurganov-Tadmor scheme) [150, 151, 152]. Hydrodynamic equations play important roles in many

different areas of physics and have a long history in their numerical implementations. For different algorithms in solving the relativistic hydrodynamic equations for heavy-ion collisions, the reader is referred to [153]. The Kurganov-Tadmor scheme is a finite-volume method in solving hyperbolic partial differential equations and is used in the MUSIC package [154, 130, 155] for a 3+1D simulation of heavy-ion collisions. A brief explanation of the Kurganov-Tadmor scheme and its implementation in the 1+1D situation are given in the Appendix C and Appendix D.

4.3   Inputs to 1+1D Diffusive Hydrodynamic Equations

In high energy heavy-ion collisions, in the early stage before the formation of the QGP, hydrodynamics is not valid as the system is still far from equilibrium. Usually, hydrodynamics in the central region is assumed to start at some initial time τ_0 after the encounter of the two colliding nuclei. At late times of the QGP evolution, the system is sufficiently dilute and the temperature is low enough that the mean free path of individual constituent could be larger than the typical macroscopic length scale. Then hydrodynamics breaks down. Therefore, one has to determine when to stop the hydrodynamic evolution of the QGP. Physics at the initial time and at the ending time are external inputs to the hydrodynamic equations to be solved. We will discuss the initial conditions when the hydrodynamics begins and the final freezeout mechanism when the hydrodynamics ceases. In addition, as an indispensable part to close the hydrodynamic equations, we need the EoS of the

QGP at finite baryon densities and the transport coefficient related to the baryon diffusion. The EoS and the transport coefficient that will be used in the numerical calculations will also be discussed in this section.

4.3.1 Initial Conditions

We assume the hydrodynamic evolution of the high baryon density matter starts from $\tau_0 = 0.6\,\mathrm{fm/c}$ for central Au+Au collision at $\sqrt{s_{NN}} = 200\,\mathrm{GeV}$. This is the typical starting time chosen to simulate the almost baryon-free central region of high energy heavy-ion collisions using hydrodynamics [97]. To initialize the 1+1D diffusive hydrodynamic equations Eqs. (4.5), one needs specify the energy density $\varepsilon(\eta)$, the baryon density $n_B(\eta)$, the velocity field $u^\tau(\eta)$ and the baryon diffusion current $V^\eta(\eta)$ as functions of the pseudorapidity η at the initial time τ_0.

The high baryon density initial conditions developed in Chapter 3 only concern the forward/backward large rapidity regions but do not say anything about the central region around $\eta \sim 0$. Usually, at high collision energies, boost-invariance is assumed in the central region so that Lorentz scalars like the energy density and baryon density are independent of η. Boost-invariance generally becomes invalid at lower collision energies. For central Au+Au collisions at $\sqrt{s_{NN}} = 200\,\mathrm{GeV}$ we assume boost-invariance in the central region. The magnitude of the energy density is chosen to be $\varepsilon(\eta = 0) = 30\,\mathrm{GeV/fm}^3$ [97] while the net baryon density is chosen to be $n_B(\eta = 0) = 0$. The velocity fields are $u^\tau = \cosh{(y - \eta)}$ and $\tau u^\eta = \sinh{(y - \eta)}$ from Eqs. (4.8) with the momentum rapidity $y = y(\eta)$. In the central region, boost-invariance also requires $y = \eta$ so that $u^\tau = 1$ and $u^\eta = 0$.

In the forward/backward rapidity regions where the high baryon densities are

located, the boost-invariance assumption is invalid and the pseudorapidity dependence of $\varepsilon(\eta)$, $n_B(\eta)$ and $y(\eta)$ are given by the high baryon density initial conditions in Chapter 3. We have to combine the forward/backward rapidity regions with the central region to obtain the initial distributions across the whole range of the pseudorapidity. In principle, a detailed dynamical study of the interplay between the forward/backward rapidity regions and the central regions is needed to give a realistic initial distributions. However, this is beyond the scope of the current thesis and should be the topic for future study. Instead, we take a more practical approach by smoothly connecting the forward/backward rapidity regions to the central regions using a half-Gaussian distribution. The center and the width of the half-Gaussian distribution are free parameters chosen appropriately in the numerical calculations. The half-Gaussian distribution has the expression [154, 156, 157]

$$
H(\eta) = \exp\left[-\frac{(|\eta| - \eta_f/2)^2}{2\sigma_\eta^2}\theta(|\eta| - \eta_f/2)\right].
\tag{4.9}
$$

Here η_f characterizes the range of the central boost-invariant region and σ_η is the Gaussian width at the boundaries $\pm\eta_f/2$ between the central region and the forward/backward rapidity regions. The $\theta(x)$ is the Heaviside step function.

For 1+1D studies of central Au+Au collisions at $\sqrt{s_{NN}} = 200\,\mathrm{GeV}$, we focus on the position $r_\perp = 0$ in the transverse plane. The initial energy density distribution $\varepsilon(\eta)$ at $\tau_0 = 0.6\,\mathrm{fm/c}$ is shown in Fig. 4.1. The range of the central boost-invariant region is chosen to be $\eta_f = 3.6$ and the Gaussian width is chosen to be $\sigma_\eta = 0.1$. In the central region, the energy density is $30\,\mathrm{GeV/fm}^3$ and smoothly connects to the forward/backward rapidity regions where the largest energy density is around

$20\,\text{GeV/fm}^3$. The rapidity regions $1.8 \leq |\eta| \leq 3.2$ are where the high baryon densities are located. Figure 4.2 shows the initial baryon density distribution. The half-Gaussian connection has not been used for the baryon density distribution as the baryon density in the central region is also assumed to be zero in the discussions in Chapter 3. The momentum space rapidity $y(\eta)$ which characterizes the velocity fields is shown in Fig. 4.3. For $|\eta| \leq 1.8$, the boost-invariance distribution $y = \eta$ is used. For $1.8 \leq |\eta| \leq 3.2$, the rapidity is the same as the final rapidity of the central core of the baryonic fireball $y = 2.47$ (see Fig. 3.3). Thermal motions of baryons inside the baryonic fireballs are ignored and this constant momentum rapidity reflects the overall velocities of the receding baryonic fireballs. The above rapidity regions are connected by the same half-Gaussian distribution as in the energy distribution in Fig. 4.1. Large rapidity regions $|\eta| > 3.2$ where both the baryon density and energy density vanish are the vacuum. Their rapidities should be zero but are also assumed to be 2.47 here to avoid any additional artificial connection. As will be demonstrated later in the numerical calculations, the matter in the central regions is pushed to the large rapidity regions as the system evolves and the rapidity distributions in the vacuum are quickly adjusted to be close to the boost-invariant distribution for the velocity field when the matter enters. In addition, we will find out that the half-Gaussian connection might not be a good choice for the velocity field.

4.3.2   Equation of State and Transport Coefficient

The QGP created in the central region of high energy heavy-ion collisions has almost zero baryon chemical potential and its EoS has been well understood from
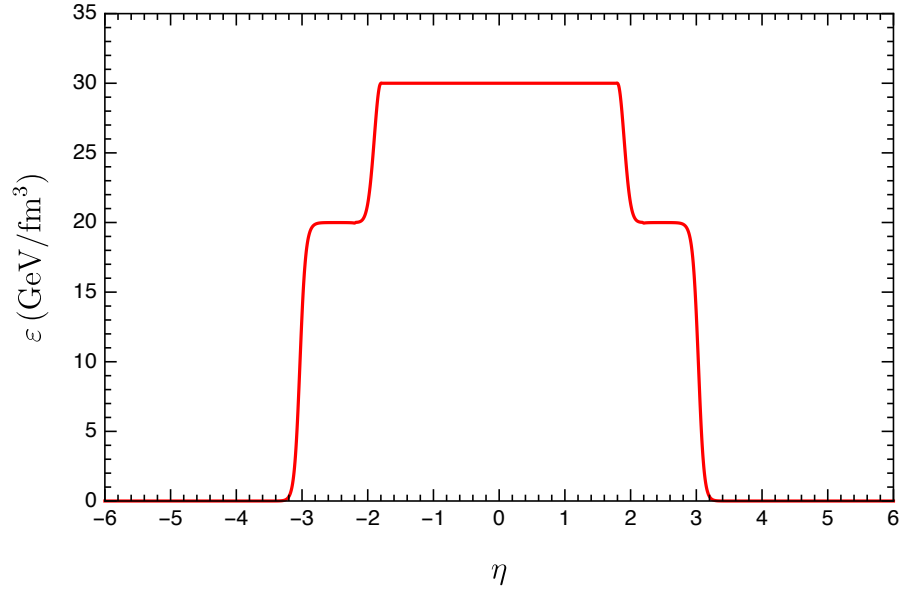
Figure 4.1: 1+1D initial energy density distribution $\varepsilon(\eta)$ at $\tau_0 = 0.6\,\mathrm{fm/c}$.
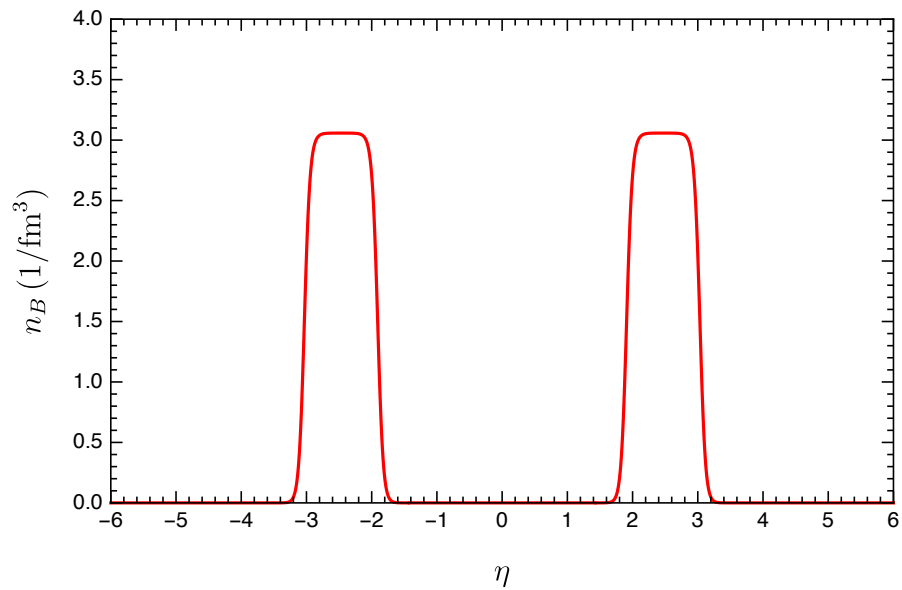
Figure 4.2: 1+1D initial baryon density distribution $n_B(\eta)$ at $\tau_0 = 0.6\,\mathrm{fm/c}$.
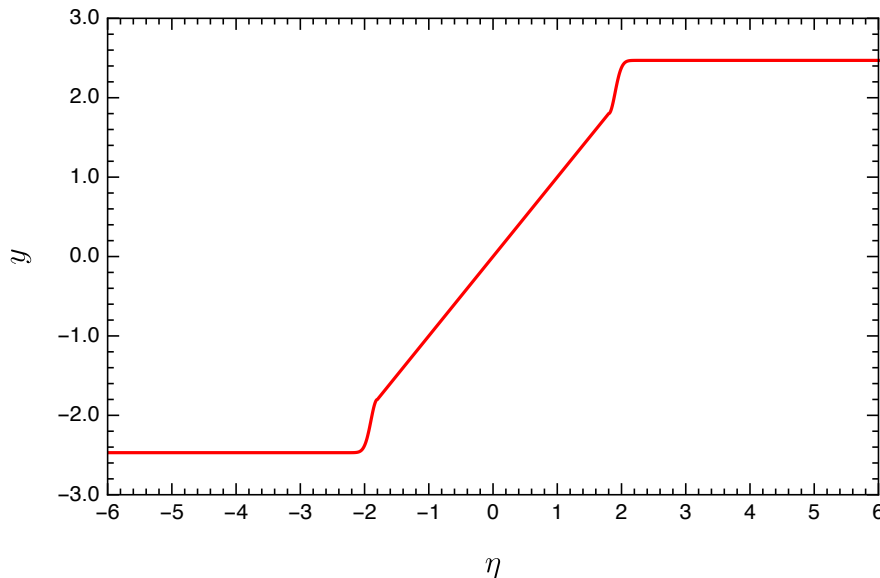
Figure 4.3: 1+1D initial momentum space rapidity distribution $y(\eta)$ at $\tau_0 = 0.6\,\mathrm{fm/c}$.

lattice simulations [9, 158]. The transition from the deconfined states of quarks and gluons to the confined states is a rapid smooth crossover for zero baryon chemical potential. Therefore the EoS at zero baryon chemical potential does not contain any phase transitions. On the other hand, the high baryon density matter created in the forward/backward rapidity regions has very large baryon chemical potentials. Its EoS is far from being well understood. Lattice calculations have their own intrinsic problem in extending the equation of state to finite baryon chemical potential. Many efforts are devoted to calculating the QGP EoS at finite baryon chemical potential in the lattice QCD community [104, 100, 159]. In addition, it is expected that the QCD phase diagram at finite baryon chemical potential might have a critical point and a first order phase transition line. Therefore, the EoS of the QGP at finite baryon chemical potential is believed

to contain a critical point and a first order phase transition line, although the exact locations of the critical point and the first order phase transition line are still under experimental search. To study the space-time evolution of the matter created both in the central region and the forward/backward rapidity regions at the same time in high energy heavy-ion collisions, the EoS should include the features both at zero baryon chemical potential and finite baryon chemical potential. Unfortunately, such an EoS has not been obtained from lattice calculations, although there are some model-dependent theoretical parameterizations [160]. In the numerical study of the hydrodynamic evolution of the high baryon density matter, we will instead use the crossover EoS Eqs. (3.21) and (3.22) developed by Albright, Kapusta and Young [101, 102]. This EoS has been used in Chapter 3 to calculate the temperatures and baryon chemical potentials given the energy densities and baryon densities. The crossover EoS is valid for finite baryon chemical potential and does not contain any critical points or first order phase transitions. Although it might not be a realistic EoS due to the lack of the critical point and the first order phase transition line, it is smooth and analytic at finite baryon chemical potential and is sufficient for our study of high baryon density matter as long as we are not focused on the critical phenomena.

Apart from the equation of state, we also need expressions for the baryon transport coefficient κ_B and the relaxation time τ_V at finite baryon chemical potential. Like the equation of state, κ_B and τ_V are determined by the microscopic dynamics of the high baryon density matter and are calculable should we knew the microscopic degrees of freedom and their interactions. However, first principle calculations of κ_B and τ_V at finite baryon chemical potential are very difficult if near

impossible. There are expressions for κ_B and τ_V at finite baryon chemical potential from weakly coupled theory using the kinetic theory approach [161, 162, 163, 164] and strongly coupled theory using the AdS/CFT correspondence [165, 166]. In [164], the Boltzmann equation for the single particle distribution function is solved in the relaxation time approximation using the Chapman-Enskog expansion. In the massless limit using the classical Boltzmann distribution for equilibrium distribution, the baryon transport coefficient has the form

$$\kappa_B = \tau_V n_B \left(\frac{1}{3} \coth \left(\frac{\mu_B}{T} \right) - \frac{n_B T}{\varepsilon + P} \right). \tag{4.10}$$

The relaxation time τ_V is assumed to be inversely proportional to the temperature $\tau_V = C_B/T$ with a free parameter C_B. It is worth emphasizing that the baryon transport coefficient Eq. (4.10) comes from the kinetic theory approach. The kinetic theory approach serves as a good description of the hadronic phase particularly in a hadronic quasi-particle model [161]. This approach might be still applicable in the extremely large temperature and/or baryon chemical potential regions where the quark-gluon plasma can be approximated as a weakly-coupled system so that perturbative QCD approach is justified [162, 167, 168, 169, 170, 171]. However, one should not expect this approach to be applicable in the strongly coupled QGP regime. Unlike the equation of state, there are no known results of the baryon transport coefficient from the Lattice QCD calculations. Our current understanding of the baryon transport coefficient in the QGP phase across a wide range of temperatures and baryon chemical potentials is very little [172].

In [165] the thermal conductivity of an R-charged $\mathcal{N} = 4$ supersymmetric

Yang-Mills theory was calculated using the AdS/CFT correspondence. Translating into the baryon transport coefficient, it has the expression

$$\kappa_B = 2\pi \frac{Ts}{\mu_B^2} \left(\frac{n_B T}{\varepsilon + P} \right)^2.$$
(4.11)

It should be noticed that the $\mathcal{N} = 4$ supersymmetric Yang-Mills theory has no direct connection with the QGP and the hadronic matter created in heavy-ion collisions. The strongly coupled nature of the QGP created in high energy heavy-ion collisions makes it very difficult to study. The AdS/CFT provides an approach to study strongly coupled quantum system in 4-dimensional flat spacetime by studying the dual black hole in higher dimension Anti-de Sitter space. People in the heavy-ion collision community are interested in results from AdS/CFT, which might hint at some correct physics. Expression (4.11) is quoted here and will be used in the numerical simulation of the 1+1D diffusive hydrodynamics merely to compare with results obtained when using Eq. (4.10).

4.3.3 Freeze-Out

At late times of the hydrodynamic evolution of the QGP, the temperature decreases and the system becomes dilute. The deconfined quarks and gluons recombine into confined states of hadrons. The hadronic system expands further until the mean free path of the constituent particles becomes comparable to the typical macroscopic length size, and hydrodynamics breaks down. It would be more appropriate to describe the subsequent evolution of the hadronic system using kinetic theory, such as the hadronic cascade model UrQMD [173, 174]. As the system continues expanding, the chemical freeze-out and kinetic freeze-out follow when inelastic collisions, particle decays and elastic collisions gradually stop. The

resulting stable particles freely travel to the detectors. While it is more realistic to use a hybrid model (hydrodynamics + transport model) to describe the particle productions, we use the simple Cooper-Frye freeze-out mechanism [175] to estimate the final particle distribution which comes directly from the end of the hydrodynamics without the subsequent hadron transport. We also take into account of the resonance decay contribution to the particle production.

Direct Thermal Production

At the moment that hydrodynamics breaks down, particles are thermally emitted from the individual fluid cells. The momentum space distributions of the emitted particles are given by the Cooper-Frye formula [175]

$$E\frac{dN_i^{th}}{d^3\mathbf{p}} = \frac{dN_i^{th}}{dyd^2\mathbf{p}_T} = \frac{g_i}{(2\pi)^3}\int_\Sigma f^i(x,p)\,p^\mu d^3\Sigma_\mu. \tag{4.12}$$

Here Σ represents the freeze-out hypersurface in the four dimensional spacetime. The $d^3\Sigma_\mu$ is the normal four vector of the hypersurface. Its magnitude tells the size of the infinitesimal hypersurface patch while the four vector tells the direction of the normal vector associated with each of these hypersurface patches. For the particle species labeled by i, the g_i is the degeneracy factor and $f^i(x,p)$ is the phase space distribution which can be decomposed into the equilibrium part and the nonequilibrium correction

$$f^i(x,p) = f_0^i(x,p) + \delta f^i(x,p)\,. \tag{4.13}$$

The local equilibrium distribution $f_0^i(x,p)$ is

$$f_0^i(x,p) = \frac{1}{e^{(u^\mu p_\mu - b_i\mu_B)/T} \pm 1} \tag{4.14}$$

We only focus on the baryon charge; the b_i represents the number of baryon charges that the particle species i carries. For example, the proton carries $+1$ unit of baryon charge while the antiproton carries -1 unit of baryon charge. Here $u^\mu(x)$, $\mu_B(x)$ and $T(x)$ are macroscopic functions of spacetime representing flow velocity, baryon chemical potential and temperature pertaining to the local fluid cell at x. The nonequilibrium correction to the distribution function $\delta f^i(x, p)$ depends on specific models used to describe the nonequilibrium processes. We only consider the baryon diffusion process. Within a kinetic theory approach in the relaxation approximation, it has the form [164]

$$\delta f^i(x,p) = f_0^i(x,p)(1 \pm f_0^i(x,p)) \left(\frac{n_B}{\varepsilon + P} - \frac{b_i}{u^\mu p_\mu} \right) \frac{p^\mu V_\mu}{\kappa_B / \tau_V} \qquad (4.15)$$

Here $n_B(x)$, $\varepsilon(x)$ and $P(x)$ are the baryon density, energy density and pressure pertaining to the fluid cell at x. The $V^\mu(x)$ represents the baryon diffusive current of the total baryon current $j^\mu = n_B u^\mu + V^\mu$. Also the κ_B is the baryon diffusion coefficient and τ_V is the relaxation time.

The freeze-out hypersurface is practically determined by comparing the local energy density $\varepsilon(x)$ with some prescribed freeze-out energy density ε_{FO}. Therefore, only three of the four components of spacetime coordinates (t_f, x_f, y_f, z_f) are independent. They satisfy the condition $\varepsilon(t_f, x_f, y_f, z_f) = \varepsilon_{FO}$. This is how the profile of the freeze-out hypersurface $\Sigma^\mu = (t_f, x_f, y_f, z_f)$ is determined. After determining the profile of the freeze-out hypersurface, one needs to construct the normal vector to the hypersurface $d^3\Sigma_\mu$. If the hypersurface is parameterized by three independent locally orthogonal coordinates u, v, w, then the normal vectors in the Cartesian coordinate system are computed by

$$d^3\Sigma_\mu = -\epsilon_{\mu\nu\lambda\rho} \frac{\partial\Sigma^\nu}{\partial u} \frac{\partial\Sigma^\lambda}{\partial v} \frac{\partial\Sigma^\rho}{\partial w} du\, dv\, dw. \qquad (4.16)$$

Here $\epsilon_{\mu\nu\lambda\rho}$ is the totally antisymmetric tensor of rank four. Using Milne coordinates (τ, x, y, η), the freeze-out hypersurface can be represented by $\tau_f = \tau_f(x_f, y_f, \eta_f)$ with the three independent coordinates being x, y, η. In the 1+1D situation, the hypersurface reduces to $\tau_f = \tau_f(\eta_f)$ and normal vectors in the Cartesian coordinates are

$$d\Sigma_0 = \left(\tau_f \cosh \eta_f + \frac{\partial \tau_f}{\partial \eta_f} \sinh \eta_f \right) d^2 \mathbf{x}_\perp d\eta_f, \qquad (4.17)$$

$$d\Sigma_3 = - \left(\tau_f \sinh \eta_f + \frac{\partial \tau_f}{\partial \eta_f} \cosh \eta_f \right) d^2 \mathbf{x}_\perp d\eta_f \qquad (4.18)$$

and $d\Sigma_1 = d\Sigma_2 = 0$. Now it is an easy exercise to obtain the normal vectors in the Milne coordinates

$$d\Sigma_a = \left(1, 0, 0, -\frac{\partial \tau_f}{\partial \eta_f} \right) \tau_f d\eta_f d^2 \mathbf{x}_\perp \qquad (4.19)$$

with $a = (\tau, x, y, \eta)$.

The momentum of the emitted particle $p^\mu = (E, p^x, p^y, p^z)$ can be expressed as $E = m_T \cosh y_p$ and $p^z = m_T \sinh y_p$ with $y_p = \frac{1}{2} \ln \frac{E+p^z}{E-p^z}$ being the momentum space rapidity of the emitted particle and $m_T = \sqrt{p_\perp^2 + m^2}$ being the transverse mass. With the help of $p^\tau = m_T \cosh(y_p - \eta)$ and $p^\eta = m_T \sinh(y_p - \eta)/\tau$, one obtains

$$u^\mu p_\mu = u^\tau p^\tau - \tau^2 u^\eta p^\eta = m_T \cosh(y - y_p). \qquad (4.20)$$

Here $y \equiv y(x)$ is a function of spacetime representing the fluid velocity $u^\mu(x) = (\cosh y, 0, 0, \sinh y)$. Particles are emitted from each fluid cell at x. In addition, one calculates

$$p^\mu d^3 \Sigma_\mu = m_T \left[\tau_f \cosh(y_p - \eta_f) - \frac{\partial \tau_f}{\partial \eta_f} \sinh(y_p - \eta_f) \right] d\eta_f d^2 \mathbf{x}_\perp. \qquad (4.21)$$

Therefore, in the 1+1D situation, the rapidity distribution of the emitted particles
is separated into the equilibrium part and the nonequilibrium diffusive correction

$$
\begin{aligned}
\frac{dN^{th}}{dy} &= \left(\frac{dN^{th}}{dy}\right)_{\text{eq}} + \left(\frac{dN^{th}}{dy}\right)_{\text{diff}} \\
&= \frac{g_i}{(2\pi)^3} S_\perp \int d\eta_f \left[\tau_f \cosh\left(y_p - \eta_f\right) - \frac{\partial \tau_f}{\partial \eta_f} \sinh\left(y_p - \eta_f\right)\right] \\
&\quad \times \int d^2 \mathbf{p}_\perp m_T \left(f_0^i(x,p) + \delta f^i(x,p)\right) .
\end{aligned}
\tag{4.22}
$$

To further simplify the integration over the transverse momentum, the particle is
considered as classical and the phase space distribution function is taken as the
relativistic Boltzmann distribution

$$
f_0^i(x,p) = e^{b_i \mu_B/T} e^{-u^\mu p_\mu/T} .
\tag{4.23}
$$

Then the transverse momentum integral of the equilibrium part can be worked
out analytically

$$
\begin{aligned}
\int d^2 \mathbf{p}_\perp m_T f_0^i(x,p) &= (2\pi) e^{b_i \mu_B/T} \int_m^\infty dm_T\, m_T^2 e^{-m_T \cosh(y-y_p)/T} \\
&= (2\pi) e^{b_i \mu_B/T} (2\xi^2 + 2m\xi + m^2) \xi e^{-m/\xi}
\end{aligned}
\tag{4.24}
$$

with

$$
\xi = \frac{T}{\cosh(y - y_p)}.
\tag{4.25}
$$

To calculate the diffusive part, we notice that

$$
p^\mu V_\mu = p^\tau V^\tau - \tau^2 p^\eta V^\eta = m_T \sinh(y - y_p)\left(\frac{\tau V^\eta}{u^\tau}\right)
\tag{4.26}
$$

where orthogonality $u^\mu V_\mu = 0$ is used. The non-equilibrium distribution then

follows

$$\delta f^i(x,p) = e^{b_i \mu_B/T} e^{-m_T \cosh(y-y_p)/T} \left(\frac{\tau V^\eta}{u^\tau}\right) \frac{1}{\kappa_B/\tau_V}$$
$$\times \left(\frac{n_B}{\varepsilon + p} m_T \sinh(y - y_p) - b_i \tanh(y - y_p)\right). \tag{4.27}$$

Plugging into the transverse momentum integral of the nonequilibrium diffusive correction, one gets

$$\int d^2 \mathbf{p}_\perp m_T \, \delta f^i(x,p) = (2\pi) e^{b_i \mu_B/T} \left(\frac{\tau V^\eta}{u^\tau}\right) \frac{1}{\kappa_B/\tau_V}$$
$$\times \left[\frac{n_B}{\varepsilon + p} \sinh(y - y_p) \int_m^\infty dm_T \, m_T^3 e^{-m_T/\xi} \right.$$
$$\left. - b_i \tanh(y - y_p) \int_m^\infty dm_T \, m_T^2 e^{-m_T/\xi}\right]. \tag{4.28}$$

The auxiliary integrals are

$$\int_m^\infty dm_T \, m_T^3 e^{-m_T/\xi} = \xi(6\xi^3 + 6m\xi^2 + 3m^2\xi + m^3)e^{-m/\xi} \tag{4.29}$$

and

$$\int_m^\infty dm_T \, m_T^2 e^{-m_T/\xi} = \xi(2\xi^2 + 2m\xi + m^2)e^{-m/\xi}. \tag{4.30}$$

Finally

$$\int d^2 \mathbf{p}_\perp m_T \, \delta f^i(x,p) = (2\pi) e^{b_i \mu_B/T} \left(\frac{\tau V^\eta}{u^\tau}\right) \frac{1}{\kappa_B/\tau_V}$$
$$\times \left[\frac{n_B}{\varepsilon + p} \sinh(y - y_p)\xi(6\xi^3 + 6m\xi^2 + 3m^2\xi + m^3)e^{-m/\xi} \right.$$
$$\left. - b_i \tanh(y - y_p)\xi(2\xi^2 + 2m\xi + m^2)e^{-m/\xi}\right] \tag{4.31}$$

After obtaining the transverse momentum integration in Eq. (4.22), one needs the analytic expression for the freeze-out hypersurface $\tau_f = \tau_f(\eta_f)$ to perform the

integrals over η_f. However, it is difficult to construct an analytical expression of the freeze-out surface $\tau_f = \tau_f(\eta_f)$ that is not singular. In practice, we directly calculate the particle spectrum by summing over all the discrete freeze-out points without asking the analytic expression $\tau_f = \tau_f(\eta_f)$. This involves the factor

$$
\begin{aligned}
p^\mu d^3\Sigma_\mu &\sim \left[\tau_f \cosh\left(y_p - \eta_f\right) - \frac{\partial \tau_f}{\partial \eta_f} \sinh\left(y_p - \eta_f\right) \right] d\eta_f \\
&\sim \Delta\eta_f \tau_f \cosh\left(y_p - \eta_f\right) - \Delta\tau_f \sinh\left(y_p - \eta_f\right).
\end{aligned}
\tag{4.32}
$$

This trick of changing the $\Delta\eta_f$ element to the proper time element $\Delta\tau_f$ in the second term circumvents the possible infinity associated with the derivative $\partial\tau_f/\partial\eta_f$ in trying constructing an analytic expression $\tau_f = \tau_f(\eta_f)$. In addition, we have to make sure that $p^\mu d^3\Sigma_\mu \geq 0$ because the particle that freezes out has to align with the normal direction of the freeze-out hypersurface so that it decouples from the QGP medium rather than flowing back into the QGP medium. It is possible that for given particle rapidity y_p at certain spatial freeze-out point η_f, the integration measure becomes negative $p^\mu d^3\Sigma_\mu < 0$. What we did in numerical implementation is to disregard contributions from these possibilities as their contributions turn out to be very small.

We assume the particles freeze out when the energy densities of the fluid cells become smaller than some prescribed freeze-out energy density $\varepsilon_{\mathrm{FO}}$ (for example $\varepsilon_{\mathrm{FO}} = 0.5\,\mathrm{GeV/fm^3}$). At the initial time $\tau = \tau_0$, we have to take into account of the freeze-out of particles from the fluid cells at the edge of the system where the local energy densities are smaller than the freeze-out energy density $\varepsilon_{\mathrm{FO}}$. All the particles freeze out simultaneously at time τ_0. For these fluid cells, the integration measure in the Cooper-Frye formula is

$$
p^\mu d^3\Sigma_\mu \sim \Delta\eta_f \tau_f \cosh\left(y_p - \eta_f\right).
\tag{4.33}
$$

The summation of the freeze out points are for spatial regions $|\eta_f| > |\eta_f(\tau = \tau_0)|$.

Resonance Decay Production

The Cooper-Frye mechanism not only gives the direct thermal distribution of stable hadrons such as proton and pions, it also predicts the distribution of unstable resonance particles such as the nucleon resonances N^* and the Δ baryons. Ultimately, we will be interested in the final proton spectrum which partly comes from direct thermal production and partly comes from the decays of resonance baryons. For example, the decay channel $\Delta^+(1232) \rightarrow p + \pi^0$ contributes to the proton spectrum. Consider the decay process that a resonance particle labeled by "R" decays to the particle of interest labeled by "i" and other unidentified N particles

$$R \longrightarrow i + 1 + 2 + \cdots N \,. \tag{4.34}$$

The decay width of this channel is computed by

$$d\Gamma_i = \frac{1}{2E_R}|\mathcal{M}|^2 d\Phi_f(i, 1, \ldots, N) \,. \tag{4.35}$$

Here E_R is the energy of the decaying particle, which reduces to the m_R in the resonance's rest frame. The $\mathcal{M}$ is the decay matrix element of the process. The phase space factor is defined by

$$d\Phi_f(i, 1, \ldots, N) = (2\pi)^4 \delta^{(4)}(p_R - (p_i + p_1 + \cdots + p_N)) \frac{d^3\mathbf{p}_i}{(2\pi)^3 2E_i} \frac{d^3\mathbf{p}_1}{(2\pi)^3 2E_1} \cdots \frac{d^3\mathbf{p}_N}{(2\pi)^3 2E_N} \,. \tag{4.36}$$

The Lorentz-invariant momentum spectrum of particle " i " due to resonance decay channel (4.34) is [176, 177, 178, 179, 180]

$$E_i \frac{dN_i^{res}}{d^3\mathbf{p}_i} = \int_0^\infty dm\, W(m) \int \frac{d^3\mathbf{p}_R}{E_R} \left(E_R \frac{dN_R^{th}}{d^3\mathbf{p}_R} \right) \left[Br \times \left(\frac{1}{\Gamma_i} \right) \times \left(E_i \frac{d\Gamma_i}{d^3\mathbf{p}_i} \right) \right].$$
(4.37)

Here

$$\mathrm{Prob}(E_i, \mathbf{p}_i; E_R, \mathbf{p}_R) = Br \times \left(\frac{1}{\Gamma_i} \right) \times \left(E_i \frac{d\Gamma_i}{d^3\mathbf{p}_i} \right). \tag{4.38}$$

is the probability density for a resonance particle with energy and momentum E_R and $\mathbf{p}_R$ decays to the particle " i " which happens to have energy and momentum E_i and $\mathbf{p}_i$. The " Br " is the branching ratio of the decay channel $Br = \Gamma_i/\Gamma_R$ with Γ_R the total decay width of the resonance particle. The thermal spectrum of the resonance particle $E_R dN_R^{th}/d^3\mathbf{p}_R$ is computed by the Cooper-Frye formula Eq. (4.12). The $W(m)$ integration describes the finite width effect of the resonance particle. The standard functional form of $W(m)$ is chosen to be the Breit-Wigner distribution. In the zero width limit, it reduces to the Dirac delta function. For simplicity, we will chose $W(m) = \delta(m - m_R)$. A recent discussion on the finite width effects can be found in [181]. In the following, we will mainly focus on two-body decays. One crucial step is to compute the probability density $\mathrm{Prob}(E_i, \mathbf{p}_i; E_R, \mathbf{p}_R)$ associated with each decay channel. This may seem intimidating as each decay channel has its own decay matrix element $\mathcal{M}$ which in general depends on all the momenta of the particles involved in the decay process. Therefore, a rigorous treatment is to analyze the dynamics of each decay channel in detail to obtain the exact decay matrix element $\mathcal{M}$. A less rigorous but more practical approach, which has been adopted in several previous works, is to assume certain properties of the decay matrix element $\mathcal{M}$ to simplify the computation of

the probability density $\text{Prob}(E_i, \mathbf{p}_i; E_R, \mathbf{p}_R)$. For example, the decay matrix $\mathcal{M}$ is assumed to be independent of momenta of the particles involved at the tree level. Under this assumption, the probability density reduces to

$$\text{Prob}(E_i, \mathbf{p}_i; E_R, \mathbf{p}_R) \simeq Br \times \left(\frac{1}{\Phi_f}\right) \times \left(E_i \frac{d\Phi_f}{d^3\mathbf{p}_i}\right). \tag{4.39}$$

Microscopic dynamics of the decay process completely drops out of the formula leaving only the phase space factor. With this assumption, analytic expressions of the probability density for two-body decays and three-body decays can be achieved. For a two-body decay channel $R \rightarrow i + 1$, assuming the resonance particle " R " is a spinless particle so that there's no preferred direction of decay in its own rest frame, the probability density is

$$\text{Prob}^{(2)}(E_i, \mathbf{p}_i; E_R, \mathbf{p}_R) \simeq Br \times \frac{\delta(E_i^* - \bar{E}_i^*)}{4\pi \bar{p}_i^*}. \tag{4.40}$$

Here $E_i^* = (E_i E_R - \mathbf{p}_i \cdot \mathbf{p}_R)/m_R$ is the energy of the decay particle " i " in the rest frame of the resonance particle " R ". The $\bar{p}_i^*$ and $\bar{E}_i^*$ are fully determined by the masses of the particles involved in the decay

$$\bar{p}_i^* = \sqrt{(\bar{E}_i^*)^2 - m_i^2}, \quad \bar{E}_i^* = \frac{m_R^2 + m_i^2 - m_1^2}{2m_R}. \tag{4.41}$$

The thermal distribution of the resonance particle $E_R dN_R^{th}/d^3\mathbf{p}_R$ has contributions from the equilibrium part and the non-equilibrium part of the local phase space integration as shown in Eqs. (4.12) and (4.13). The non-equilibrium diffusive contribution turns out to be negligible compared to that of the equilibrium part. Therefore we focus on the equilibrium part using the classical Boltzmann distribution

$$E_R \frac{dN_R^{th}}{d^3\mathbf{p}_R} = \frac{g_R}{(2\pi)^3} \int_\Sigma \text{Exp}\left[-\frac{p_R^\mu u_\mu - b_R \mu_B}{T}\right] p_R^\mu d^3\Sigma_\mu. \tag{4.42}$$

In this situation, the integration over the momenta of the resonance $\int d^3\mathbf{p}_R/E_R$ can be carried out to obtain a simplified analytic expression [182]. The simplified expression of Eq. (4.37) is

$$E_i \frac{dN_i^{res}}{d^3\mathbf{p}_i} = \frac{Br}{4\pi \bar{p}_i^*} \frac{g_R}{(2\pi)^3} \int d\Sigma_\mu e^{b_R \mu_B/T} (\mathcal{A}p_i^\mu + \mathcal{B}u^\mu) \qquad (4.43)$$

with

$$\begin{aligned}
\mathcal{A} &= \frac{2\pi T m_R}{p_i'^3} \left[m_R \bar{E}_i^* - E_i'(T + E_R'^{(+)}) \right] e^{-E_R'^{(+)}/T} - \left(E_R'^{(+)} \to E_R'^{(-)} \right), \\
\mathcal{B} &= \frac{2\pi T m_R}{p_i'^3} \left[m_i^2(T + E_R'^{(+)}) - m_R \bar{E}_i^* E_i' \right] e^{-E_R'^{(+)}/T} - \left(E_R'^{(+)} \to E_R'^{(-)} \right).
\end{aligned} \qquad (4.44)$$

Here

$$E_i' = p_i^\mu u_\mu, \quad p_i' = \sqrt{E_i'^2 - m_i^2} \qquad (4.45)$$

and

$$E_R'^{(\pm)} = \frac{m_R}{m_i^2} (E_i' \bar{E}_i^* \pm p_i' \bar{p}_i^*). \qquad (4.46)$$

The formula Eq. (4.43) will be used in the numerical calculation of the final particle spectrum due to resonance decays.

4.4 Longitudinal Dynamics of High Baryon Density Matter

In this section, results from numerical calculations of the 1+1D diffusive hydrodynamic equations with the high baryon density initial conditions are presented and discussed. We first test the validity of the codes by numerically checking the conservation of energy and baryon number, as well as the increase of entropy.

Problems associated with the half-Gaussian connections between the central region and the forward/backward rapidity regions are explained. This is followed by the discussion of the baryon diffusion and rapidity dependent observables.

4.4.1 Validation of the Codes

Before discussing the main results from solving these 1+1D diffusive hydrodynamic equations, we would like to check the validity of the codes and assess the accuracy of the numerical calculations. First of all, a few numerical setups. The range of the spatial rapidity is chosen to be $-6 \leq \eta \leq 6$. The space-time grids have spacing $\Delta\eta = 0.04$ and $\Delta\tau = 0.02\,\mathrm{fm/c}$. The free parameter C_B in the baryon transport coefficient and the relaxation time is chosen to be $C_B = 0.4$ for illustrative purpose. In the numerical calculations, the energy conservation and the baryon conservation should be respected. The total energy defined by $E^{\mathrm{tot}} = \int T^{\mu 0} d^3\sigma_\mu$ with the hypersurface at constant proper time τ being $d^3\sigma_\mu = (\cosh\eta, 0, 0, -\sinh\eta)\tau d\eta d^2\mathbf{x}_\perp$ has the explicit expression

$$E^{\mathrm{tot}} = S_A \int \tau d\eta \left(T^{\tau\tau}\cosh\eta + \tau T^{\tau\eta}\sinh\eta\right). \tag{4.47}$$

Here S_A is the transverse area. The total number of baryons defined by $N_B^{\mathrm{tot}} = \int J^\mu d^3\sigma_\mu$ has a contribution from the diffusive current

$$N_B^{\mathrm{tot}} = S_A \int \tau d\eta \left(n_B u^\tau + V^\tau\right). \tag{4.48}$$

In addition, the total entropy, which is defined by $S^{\mathrm{tot}} = \int s^\mu d^3\sigma_\mu$ with $s^\mu = su^\mu - \frac{\mu_B}{T}V^\mu$, should also be conserved for an ideal fluid and should not decrease for diffusive hydrodynamics. Its explicit expression is

$$S^{\mathrm{tot}} = S_A \int \tau d\eta \left[su^\tau - \left(\frac{\mu_B}{T}\right)V^\tau\right]. \tag{4.49}$$

In the ideal fluid situation when the diffusive current is turned off $V^\mu = 0$, the E^{tot}/S_A, N_B^{tot}/S_A and S^{tot}/S_A are constants. Their initial values are $284.49\,\text{GeV/fm}^2$, $4.2857\,\text{fm}^{-2}$ and $339.16\,\text{fm}^{-2}$, respectively. We check their values at each time step. Baryons are conserved to a very high precision. The total energy is conserved with less than 0.1% numerical violations while the entropy is conserved with less than 0.2% numerical violations. These tiny increases of the total energy and the total entropy are mainly due to the numerical viscosities of the Central-Upwind scheme in solving hydrodynamic equations. Further improvements of the algorithm can be found in [151].

In the diffusive hydrodynamics with V^μ included, E^{tot}/S_A and N_B^{tot}/S_A are still expected to be constants while the entropy per transverse area S^{tot}/S_A is expected to increase. The total energy in this situation is almost the same as in the perfect fluid situation. The total number of baryons, however, increases up to 2% at the ending time of the hydrodynamic evolution. This 2% percentage violation of baryon conservation is the accuracy of the numerical results on quantities related to baryons. There are several sources this small violation of baryon conservation can come from. After introducing the baryon diffusion current, the source terms Eqs. (4.6) contain time derivatives. This structure in principle violates the Central-Upwind scheme. The treatment of these time derivatives by the finite difference method in the codes could introduce uncertainties in the numerical results. In addition, the baryon diffusion current V^μ is theoretically expected to be smaller than the ideal part of the total baryon current J_{id}^μ. However, in numerically solving the baryon diffusion equation governing the time evolution of V^μ, there is no small controlling parameter that guarantees $|V^\mu| \lesssim |J_{\text{id}}^\mu|$. As

a result, the V^μ can be comparable or larger than J^μ_{id}, especially in the spatial regions close to the edges of the system where the baryon densities are small. The baryon diffusion currents V^μ are regulated so as to make them smaller in these regions.

Figures 4.4 and 4.5 show the profiles of the proper energy density and temperature, respectively, at four different proper times $\tau = 0.6, 1.0, 2.0, 3.0\,\text{fm/c}$. The peculiarity in the time evolution of the energy density profile and the temperature profile are the deep-valley structures developed in the connecting areas ($\eta \sim \pm 2$) between the central region and the forward/backward rapidity regions. There is no physical reason to expect cold spots in these connecting areas. It is unphysical and comes from the peculiar initial longitudinal flow profile Fig. 4.3 we used. Specifically, the hydrodynamic equation for energy density is written explicitly as $D\varepsilon = -(\varepsilon + P)\partial_\mu u^\mu$ with $u^\mu = (\cosh y, 0, 0, \sinh y)$. Large gradients of y in the connecting areas as shown in Fig. 4.3 cause a large decrease of the energy density at these areas. The problem associated with the initial flow profile in Fig. 4.3 is that the high baryon density regions are assumed to have the same rapidity $y = \pm 2.47$. Thermal motions of the baryons inside of the fireball, which might modify the rapidity profile, are ignored. In addition, we used the half-Gaussian function to connect the central region with the forward/backward rapidity regions. This might be a good approximation for thermodynamic quantities like the energy density, but is not a good approximation for the initial flow profile as small changes of the initial flow profile could be amplified and revealed in the profiles of the thermodynamic quantities. The time evolution of the initial flow profile is shown in Fig. 4.6. The initial flow profile is adjusting itself to be close to

the $y = \eta$ boost-invariant flow profile at the forward/backward rapidity regions as the system evolves. Therefore, to avoid the unphysical deep-valley structure, we will adopt the initial rapidity distribution as $y = \eta$ in the numerical calculations. The regions with high baryon densities will adjust themselves according to the hydrodynamic equations to the appropriate rapidity distributions as the system evolves. Of course, a more realistic modeling of the fragmentation regions and the interactions of the central region with the fragmentation regions is needed to formulate the realistic initial flow profile. This is beyond the scope of the thesis and will be the work of future study.

Figure 4.4: Profile of the proper energy density $\varepsilon(\eta)$ as it evolves with time hydrodynamically assuming the initial flow profile in Fig. 4.3.

The profiles of the proper energy density and the temperature assuming initial flow $y = \eta$ are given in Figs. 4.7 and 4.8, respectively. On each side of the rapidity profile ($\eta > 0$ or $\eta < 0$), the energy density $\varepsilon(\eta)$ and the temperature $T(\eta)$
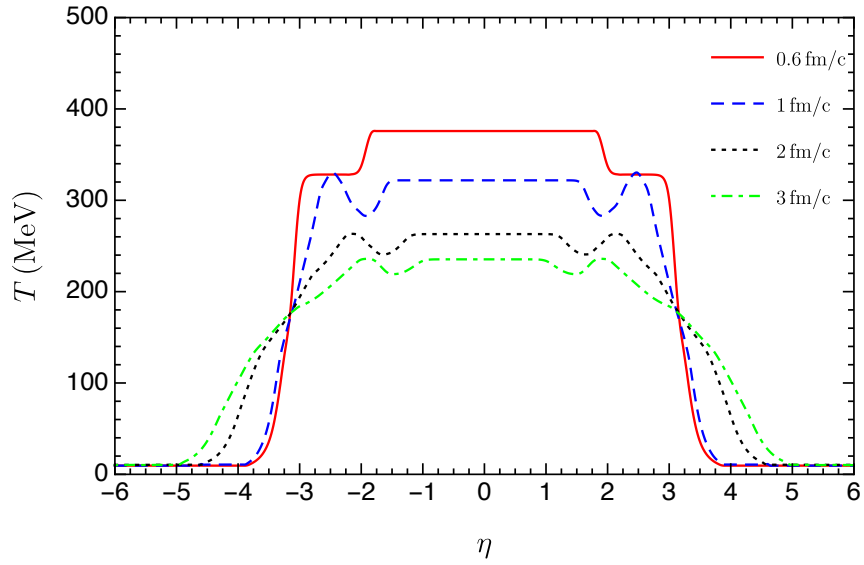
Figure 4.5: Profile of the temperature $T(\eta)$ as it evolves with time hydrodynamically assuming the initial flow profile in Fig. 4.3.
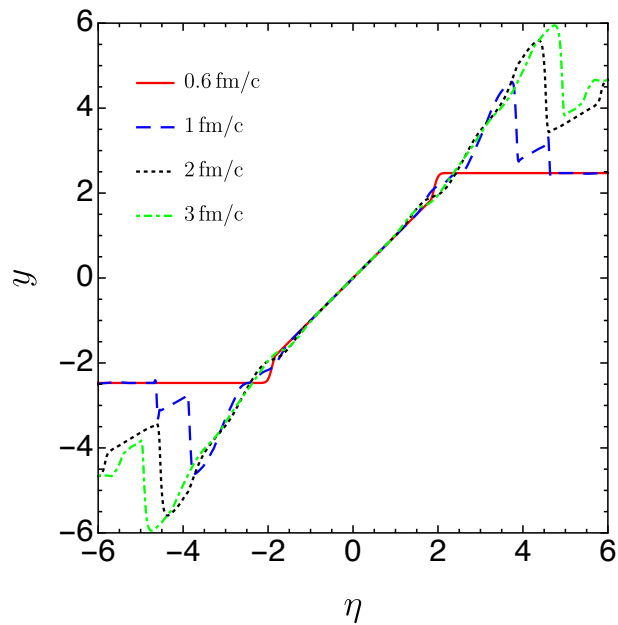
Figure 4.6: Profile of the initial flow $y(\eta)$ as it evolves with time hydrodynamically.

are monotonic functions of η. The rapidity profiles $y(\eta)$ are shown in Fig. 4.9. Even though the initial flow file is boost-invariant, the high baryon density matter adjusts itself to be away from the $y = \eta$ distribution at large rapidity regions as the system evolves.
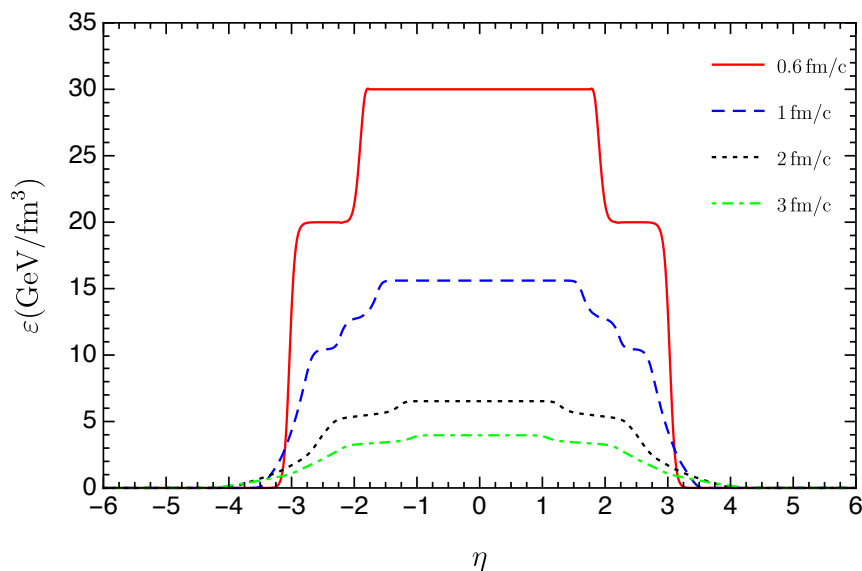
Figure 4.7: Profile of the proper energy density $\varepsilon(\eta)$ as it evolves with time hydrodynamically assuming the initial flow profile $y = \eta$.

4.4.2 Baryon Diffusion

After checking the conservation laws numerically and arguing for a more reasonable initial flow profile, results from numerically solving the 1+1D diffusive hydrodynamic equations are presented in this section. The proper baryon densities at $\tau = 0.6, 1.0, 2.0, 3.0$ fm/c are shown in Fig. 4.10. Note that the area under the curve $n_B(\eta)$ is not the total number of baryons per unit area. The total number of baryons per unit area have to be computed using Eq. (4.48). As can be
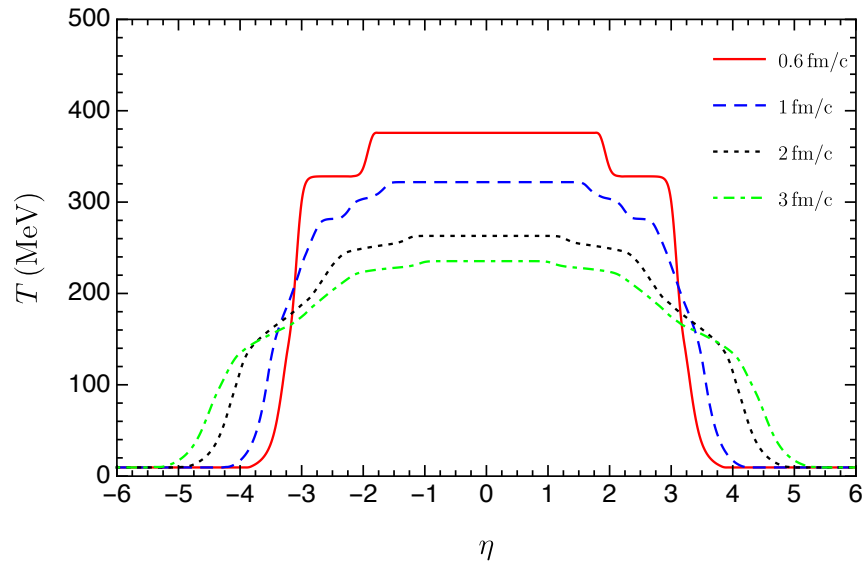
Figure 4.8: Profile of the temperature $T(\eta)$ as it evolves with time hydrodynamically assuming the initial flow profile $y = \eta$.
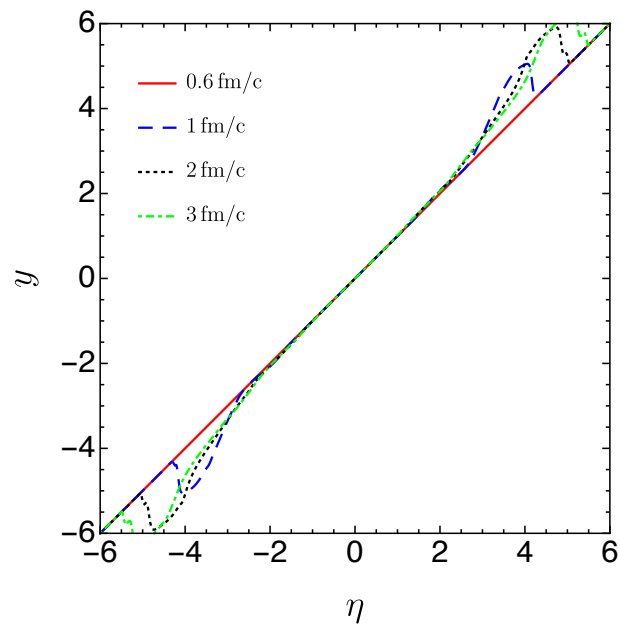
Figure 4.9: Profile of the rapidity $y(\eta)$ as it evolves with time hydrodynamically assuming the initial flow profile $y = \eta$.

seen from Fig. 4.10, the magnitude of the proper baryon density decreases very fast at the early stage of the hydrodynamic expansion. It drops from the initial $3.0\,\text{baryons/fm}^3$ at $\tau = 0.6\,\text{fm/c}$, which is around 20 times larger than the normal nuclear density to around $0.4\,\text{baryons/fm}^3$ at $\tau = 3\,\text{fm/c}$ which is less than three times larger than the normal nuclear density. As will be shown later, the total time of the hydrodynamic evolution is around $\tau_{\text{tot}} \sim 18\,\text{fm/c}$. In Fig. 4.10, the baryon distribution spreads to both the smaller rapidity regions $|\eta| \lesssim 2$ and the larger rapidity regions $|\eta| \gtrsim 3$ as the system evolves. There are two factors that determine the change of the baryon distribution during the hydrodynamic evolution. One is the longitudinal hydrodynamic expansion driven by the gradient of the pressure. The other is the baryon diffusion driven by the gradient of the fugacity. The effects of the longitudinal hydrodynamic expansion push the baryons to larger spatial rapidity regions as shown in Fig. 4.11 where the baryon diffusion current is turned off: $V^\mu = 0$. No baryons spread to the central region in the ideal fluid dynamical evolution. The pressure profiles are shown in Fig. 4.12. In the ideal fluid, the change of baryon density is governed by $Dn_B = -n\theta$ and $Du^\mu = \nabla^\mu P/(\varepsilon + P)$. Figure 4.13 shows the proper baryon density distributions at $\tau = 10\,\text{fm/c}$ from the ideal hydrodynamics and the diffusive hydrodynamics. Baryon diffusion causes the baryons to be transported from the backward/forward rapidity regions to the central region. However, baryon diffusion to larger rapidity regions $|\eta| \gtrsim 3$ are suppressed. The spreading of baryons to the $|\eta| \gtrsim 3$ regions are mainly caused by the hydrodynamical expansion. Close to the edge of the system $|\eta| \gtrsim 3.8$, the two distributions overlap because of the regulation of the baryon diffusion current V^μ in these regions.
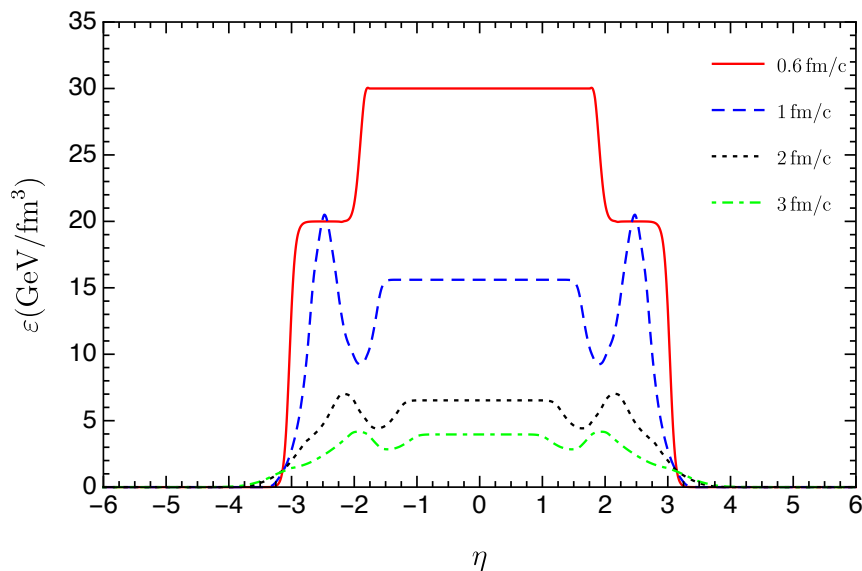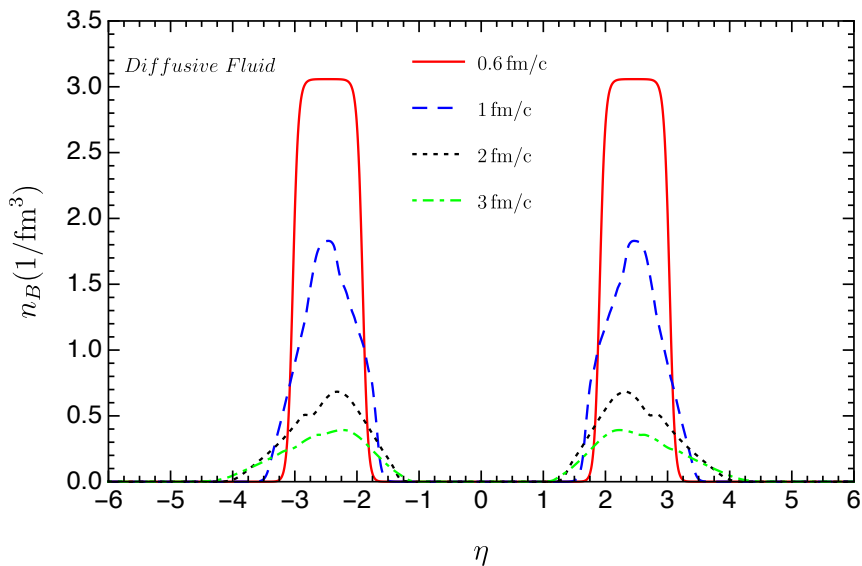
Figure 4.10: Profile of the proper baryon density $n_B(\eta)$ as it evolves with time hydrodynamically assuming the initial flow profile $y = \eta$.
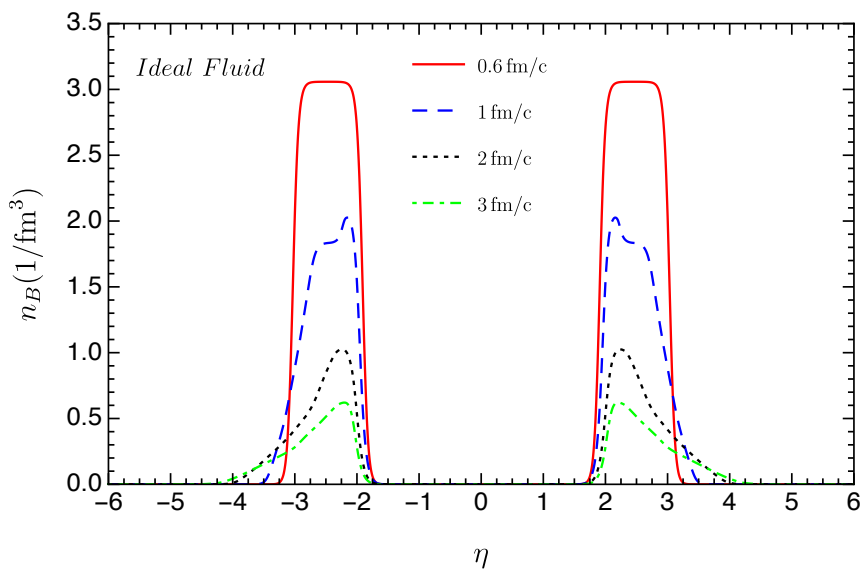
Figure 4.11: Profile of the proper baryon density $n_B(\eta)$ as it evolves with time according to the ideal fluid hydrodynamic equations assuming the initial flow profile $y = \eta$.
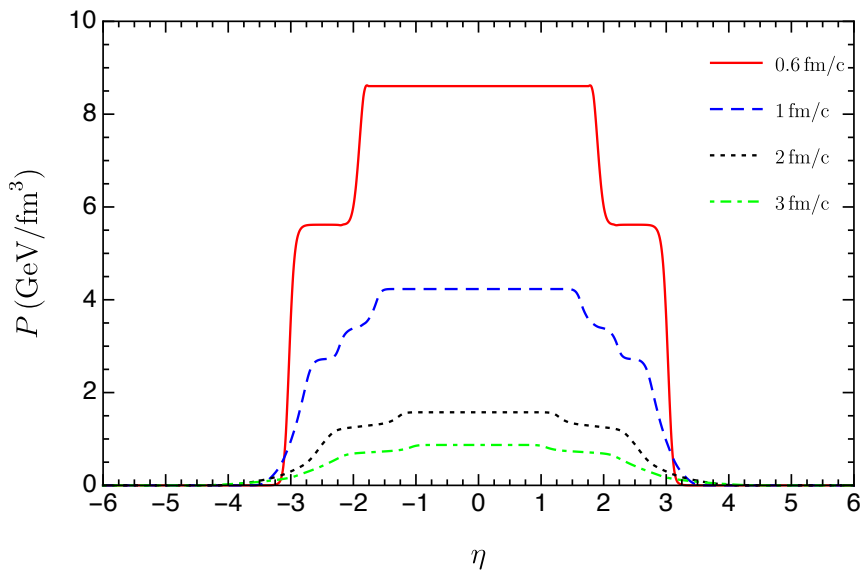
Figure 4.12: Profile of the pressure P as it evolves with time according to the diffusive hydrodynamic equations assuming the initial flow profile $y = \eta$.
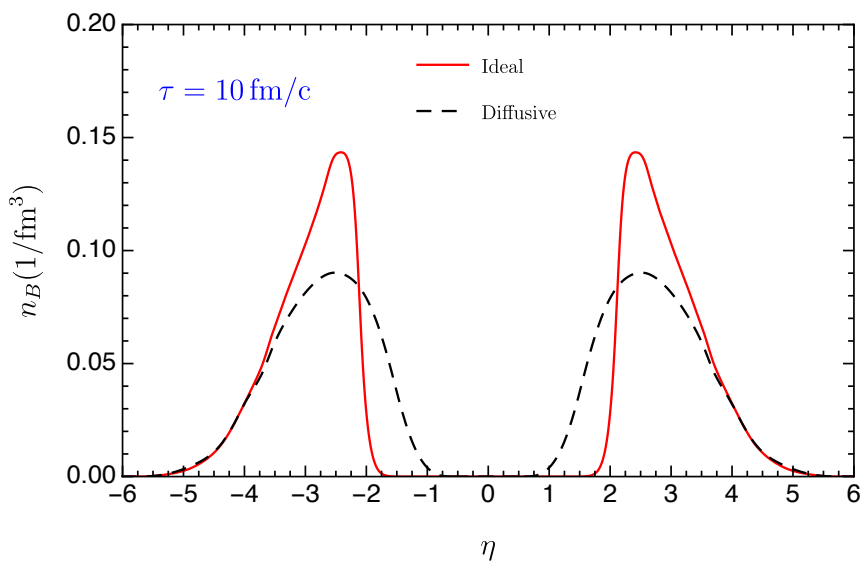
Figure 4.13: The proper baryon density distribution $n_B(\eta)$ at $\tau = 10\,\mathrm{fm/c}$ from the ideal hydrodynamics and from the diffusive hydrodynamics.

The baryon diffusion currents at four different proper times $\tau = 0.7, 1.0, 1.4, 2.0 \,\mathrm{fm/c}$ are plotted in Fig. 4.14. The baryon diffusion current is assumed to be zero at the initial time $\tau = 0.6 \,\mathrm{fm/c}$. The direction and magnitude of the baryon diffusion are determined by the fugacity gradient. In the relativistic Navier-Stokes limit, we have $V^\mu = \kappa_B \nabla^\mu(\frac{\mu_B}{T})$. Therefore, in the 1+1D situation

$$\tau V^\eta = V^z \cosh \eta - V^t \sinh \eta$$
$$\sim -\kappa_B \cosh (y - \eta) \left[\tau u^\eta \partial_\tau + u^\tau \tau^{-1} \partial_\eta \right] \left(\frac{\mu_B}{T} \right) \tag{4.50}$$
$$\sim -\kappa_B \left[\cosh (y - \eta) \right]^2 \frac{1}{\tau} \partial_\eta \left(\frac{\mu_B}{T} \right)$$

where in the last line we only focus on the spatial gradient term. The baryon diffusion current τV^η is inversely proportional to the rapidity gradient of μ_B/T and is scaled by $1/\tau$. The factor $1/\tau$, which is the same as the expansion rate $\partial_\mu u^\mu$ in the boost-invariant case, indicates that the magnitude of τV^η is larger at early times and becomes smaller and smaller at late times due to the hydrodynamical expansion. The explicit profiles of μ_B/T as a function of η are shown in Fig. 4.15. Around $\eta \sim 2$, the value of μ_B/T increases from zero to about two at $\tau = 0.7 \,\mathrm{fm/c}$. This is a general feature of the space-time picture of high energy heavy-ion collisions where very few baryons are left in the central region and most of the baryons are carried away by the nuclear remnants. Taking derivative of μ_B/T, one gets the "plateau-valley-plateau" structure in the τV^η profile in the connecting area between the central region and the fragmentation regions as shown in Fig. 4.14. We want to emphasize again that this is a general feature of high energy heavy-ion collisions. In the extreme case of low collision energy where the two colliding nuclei are completely stopped, baryons are concentrated in the central region. The μ_B/T instead should be decreasing from the central

region to the fragmentation regions. As a consequence, one gets the "plateau-hill-plateau" structure in the baryon diffusion current τV^η which indicates that the baryons diffuse from the central region to the fragmentation regions. For the μ_B/T profiles shown in Fig. 4.15, as baryons diffuse from the fragmentation regions to the central regions, the μ_B/T distribution is lowered and spread around $\eta \sim 2$. The deep valley in the τV^η profile correspondingly becomes shallower and more flat. The region around $\eta \sim 3$ in Fig. 4.15 needs more explanation. This is the connecting area between the high baryon density matter and the vacuum, which is different from the connecting area around $\eta \sim 2$ where high baryon density matter and the QGP with zero baryon densities are connected. The value of μ_B/T first decreases and then quickly increases to infinity around $\eta \sim 3$ at $\tau = 0.7\,\mathrm{fm/c}$. The values of μ_B and T are determined by the equation of state, given the values of the energy density ε and the baryon density n_B. Around $\eta \sim 3$, both ε and n_B are small while around $\eta \sim 2$, the n_B is small but ε is vary large. The feature of μ_B/T around $\eta \sim 3$ thus reflects the property of the equation of state at small n_B and ε. See also similar structure using a different equation of state in [164]. This particular feature of μ_B/T results in a small hill structure around $\eta \sim 3$ in the τV^η profile as shown in Fig. 4.14. Baryons are thus diffused from the fragmentation regions to even larger rapidity regions where the vacuum locates. Gradually, this small hill structure in τV^η around $\eta \sim 3$ is flattened as the system expands and the baryons diffuse; we are left with a monotonic increasing rapidity profile of μ_B/T.

The reason why baryons diffuse from the fragmentation regions to the central region given the "plateau-valley-plateau" structure of the baryon diffusion current
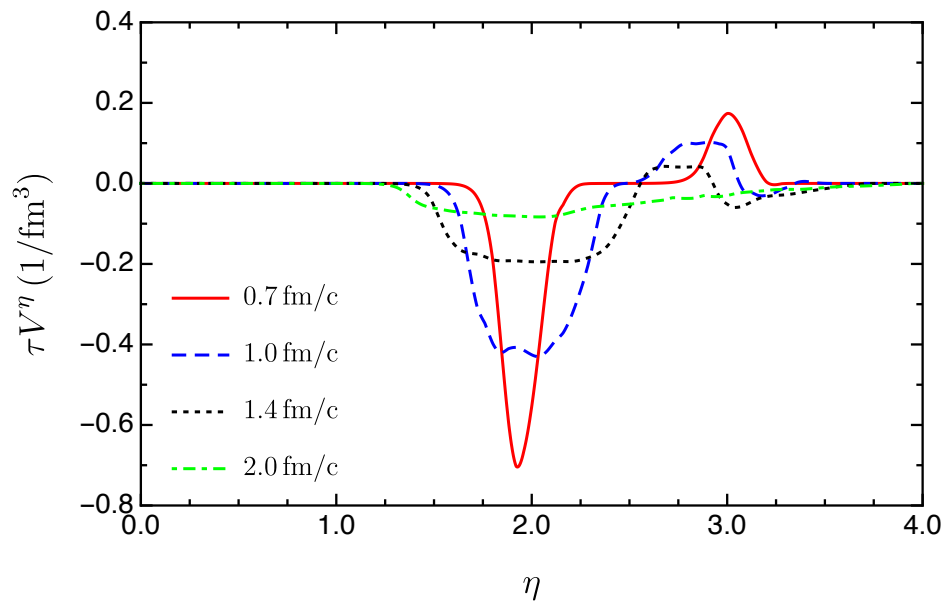
Figure 4.14: The baryon diffusion current τV^η as it evolves with time hydrodynamically. Only the postive rapidity region is shown.

Figure 4.15: The μ_B/T profile evolve with time hydrodynamically. Only the positive rapidity region is shown.

τV^η are explicitly shown in Fig. 4.16. The source term S_B in the baryon conservation equation Eqs. (4.5) has a rapidity gradient term $S_B \sim -\partial_\eta(\tau V^\eta)$ as shown in Eqs. (4.6). The change of the proper baryon density n_B after one time step due to the rapidity gradient of the baryon diffusion current can be approximated as

$$\Delta n_B \sim -\frac{1}{u^\tau}\frac{\Delta\tau}{\tau}\partial_\eta(\tau V^\eta). \tag{4.51}$$

Therefore, the "plateau-valley-plateau" structure of the τV^η causes the baryons to increase on one side of the valley and the baryons to decrease on the other side of the valley. Overall, one sees the baryons are transported from the fragmentation regions to the central region. Likewise, as the system expands and the baryons diffuse, the deep valley becomes more flat. Baryon diffusion still happens on the edge of the valley but the magnitudes are reduced due to the expansion of the system and the shallowness of the valley, as shown in Fig. 4.16.

4.4.3   Rapidity Dependent Observables

In the numerical calculations, we chose the freezeout energy density to be $\varepsilon_{FO} = 0.5\,\mathrm{GeV/fm}^3$ and found that the whole system freezes out at $\tau = 17.42\,\mathrm{fm/c}$. Particle momentum space distributions can then be computed by the Cooper-Frye formula and by including contributions from the resonance decays. We focus on particles that carry baryon charges. Neutral particles like the neutrons are difficult to measure experimentally. The BRAHMS collaboration has measured the proton, antiproton and net-proton rapidity distribution dN/dy for y up to 3.1 for Au+Au collision at $\sqrt{s_{NN}} = 200\,\mathrm{GeV}$ in the $0-5\%$ centrality bin [48]. Our calculation is not the full 3+1D case, thus detailed quantitative comparisons with the experimental data are not practical. However, the experimentally measured
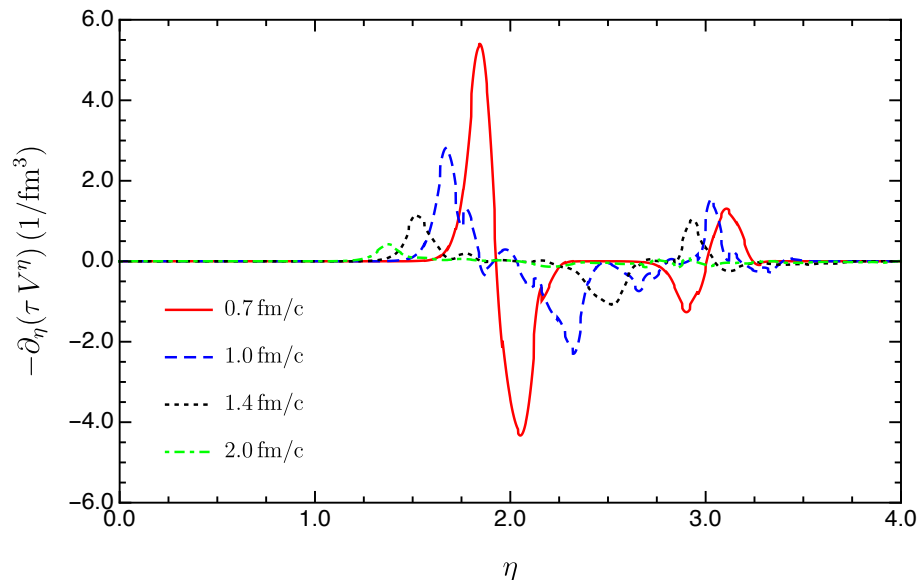
Figure 4.16: The gradient of baryon diffusion current $-\partial_\eta(\tau V^\eta)$ as it evolves with time hydrodynamically. Only the postive rapidity region is shown.

rapidity distributions of proton, antiproton and net-proton can put a qualitative constrain on the longitudinal dynamics of the high baryon density matter predicted by the 1+1D diffusive hydrodynamics.

Figure 4.17 shows the net-proton rapidity distribution and the contributions from the direct thermal production and from the resonance decays. Resonance decays contribute more on the production of proton than the direct thermal emission. Including the resonance decays increases the magnitude of the net-proton rapidity distribution while the shape of the rapidity distribution remains unchanged. It would be crucial to include the resonance decays when one compares theoretical predictions with experimental data. Note that the dN/dy has unit of $1/\mathrm{fm}^2$, as we consider a unit transverse area around the central core of the nuclei. Bulk variables are counted as per unit area. Figure 4.18 shows the

net-proton rapidity distributions from three different resonance decays. The reso-nances $\Delta(1232)$, Λ and Σ^+, whose masses are $m_\Delta = 1232\,\mathrm{MeV}$, $m_\Lambda = 1115.7\,\mathrm{MeV}$ and $m_\Sigma = 1189.4\,\mathrm{MeV}$, are the baryons that have the lowest masses besides the proton and neutron. The $\Delta(1232) \to p\pi$ actually consists of three channels $\Delta^{++}(1232) \to p\pi^+$, $\Delta^+(1232) \to p\pi^0$ and $\Delta^0(1232) \to p\pi^-$. Other two-body decays that contribute to the production of protons and antiprotons are detailed in the Appendix F.
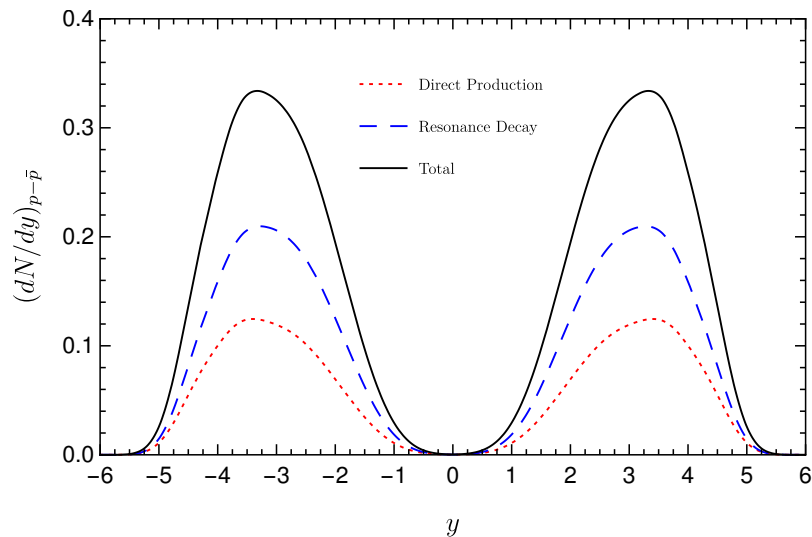
Figure 4.17: Comparison of the net-proton rapidity distributions from the direct thermal production and the resonance decays.

As shown in Fig. 4.19, the net-proton distribution has the double peak struc-ture which is in qualitative agreement with experimental findings. The difference lies in the valley between the two peaks around $y \sim 0$. Experimental data reveals that there is a small amount of baryon charge existing in the central region around $y \sim 0$ with the baryon chemical potential about $25\,\mathrm{MeV}$ at the chemical freezeout. As a consequence, in the experimental data, the net-proton rapidity distribution
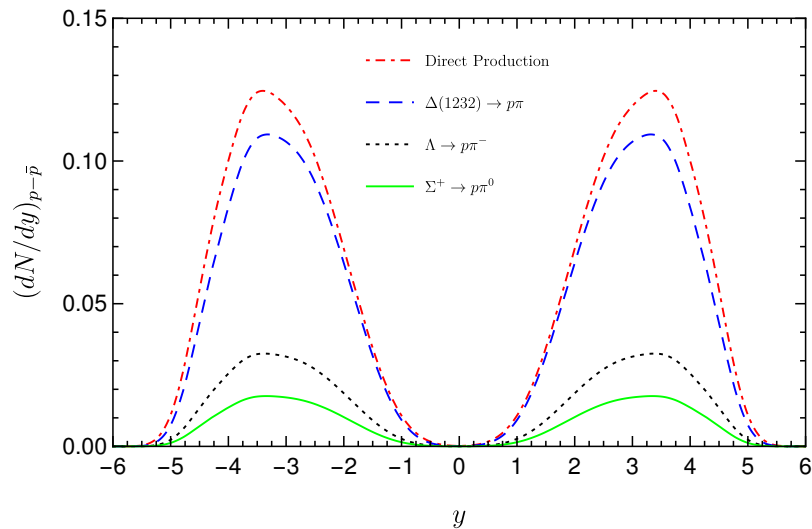
Figure 4.18: Comparison of the net-proton rapidity distributions from the direct thermal production and three resonance decays $\Delta(1232) \to p\pi$, $\Lambda \to p\pi^-$ and $\Sigma^+ \to p\pi^0$.

has nonzero values around $y \sim 0$ and the valley between the two peaks is found to be shallower and more flat. In addition, this small baryon chemical potential around $y \sim 0$ predicts slightly larger proton rapidity distribution than the antiproton rapidity distribution at $y \sim 0$. In Fig. 4.19, the $(dN/dy)_p$ and $(dN/dy)_{\bar{p}}$ are the same around $y \sim 0$ because $\mu_B \simeq 0$ there. Antiprotons are not existing before the collision of the two nuclei, they come from pair production associated with the protons or from hadronization. Finally, the baryons are distributed as Dirac delta functions around $y = \pm 2.47$ in the momentum space at the initial time $\tau = 0.6 \, \text{fm/c}$. Hydrodynamic expansions and baryon diffusion spread the net baryon distribution over an wide range of y in the momentum space as illustrated in Fig. 4.19.

Where does the small amount of net baryons at $y \sim 0$ come from? Are they
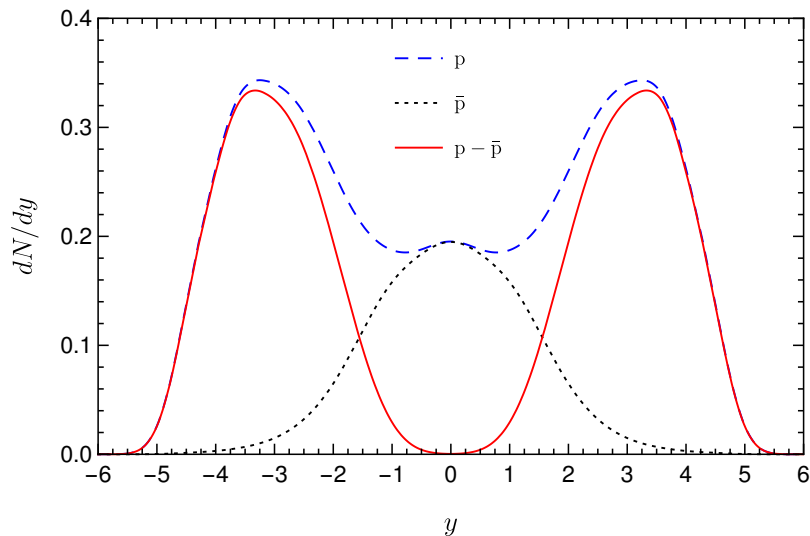
Figure 4.19: The proton, antiproton and net-proton rapidity distribution after the freezeout. Both the direct thermal production and contributions from the resonance decays are included.

already there at the initial time $\tau = 0.6\,\mathrm{fm/c}$ because the collision is not fully transparent even at $\sqrt{s_{NN}} = 200\,\mathrm{GeV}$? Or do the baryons come from diffusion from the fragmentation regions to the central region during the hydrodynamic evolution? Our modeling and calculations cannot evaluate the first possibility as full transparency was assumed. The second possibility, that would require an extraordinary strength of baryon diffusion. Given the initial conditions, the strength of the baryon diffusion is controlled by the baryon transport coefficient κ_B. However, the κ_B can not be arbitrarily large as the requirement $|V^\mu| \lesssim |J^\mu_{\mathrm{id}}|$ has to be satisfied, otherwise the diffusive hydrodynamics breaks down. Figure 4.20 shows the net-proton distributions after the Cooper-Frye freezeout for three different values of κ_B (the C_B is a prefactor in the expression of κ_B in Eq. 4.10). As one increases the value of κ_B, more baryons diffuse to the central region.

However, we have checked that a very large value $C_B = 2$ still can not reproduce the expected net baryons at $y \sim 0$. Also the hydrodynamic codes become unstable. Our calculations therefore do not favor the second possibility.
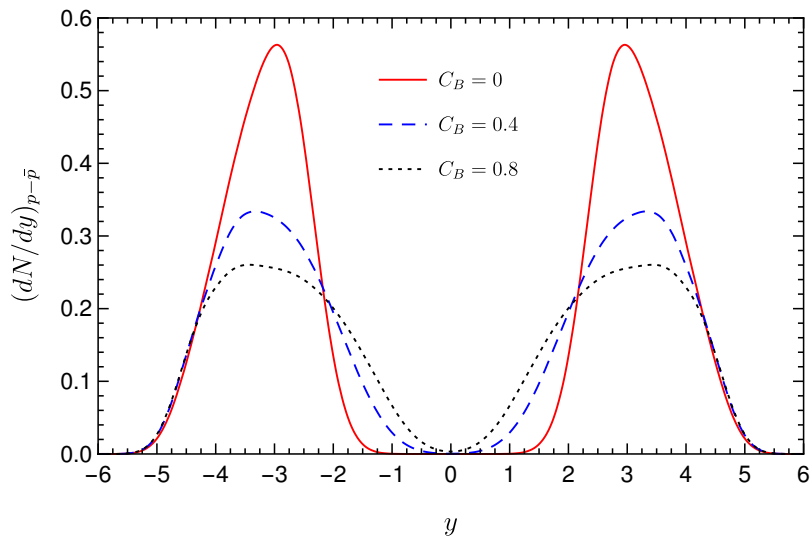
Figure 4.20: The net-proton distributions after freezeout for three different values of C_B.

Figure 4.21 shows the temperature and the baryon chemical potential as functions of the rapidity y at the Cooper-Frye freezeout. The values of temperature and baryon chemical potential at the chemical freezeout can be reconstructed from the thermal statistical model in fitting hadron yields and hadron yield ratios. An attempted extraction of the rapidity dependence of T and μ_B for Au+Au collision at $\sqrt{s_{NN}} = 200\,\text{GeV}$ using the data from the BRAHMS collaboration is presented in [183], where the parabolic form of the baryon chemical potential $\mu_B = 26 + 12y^2$ was assumed. Again, our results show the baryon chemical potentials are zero around $y \sim 0$ while the parabolic parameterization has $\mu_B = 26\,\text{MeV}$ there. At the moment of freezeout, from the central region to the fragmentation

regions, the baryon chemical potential increases while the temperature decreases. The distribution of T and μ_B as functions of rapidity y indicate that a rapidity scan would cover a wide range of (T, μ_B) points on the QCD phase diagram and can be used to search for the critical point in high energy heavy-ion collisions, which is different from the low energy Beam Energy Scan.
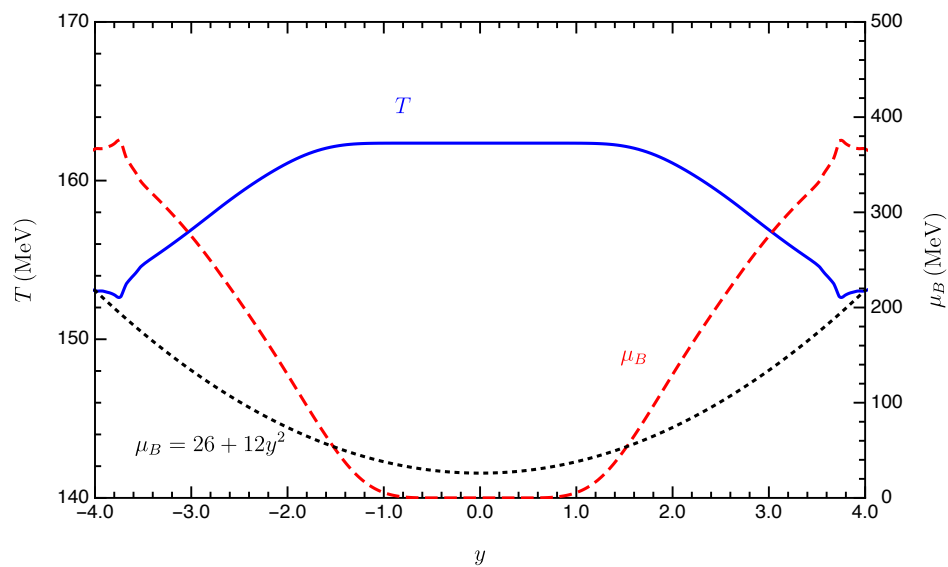
Figure 4.21: The temperature T and the baryon chemical potential μ_B as functions of rapidity y at the Cooper-Fye freezeout. The form $\mu_B = 26 + 12y^2$ from [183] is plotted for reference.

4.4.4   Comparing Different κ_B

The baryon transport coefficient κ_B is not well known at finite baryon chemical potential. In the above numerical results, we used the expression of κ_B from

Eq. (4.10) which was derived using the kinetic theory approach. In this section, we will compare numerical results from using a different baryon transport coefficient Eq. (4.11), which was suggested by the AdS/CFT approach. The κ_B from the kinetic theory approach is not completely determined by the thermodynamic quantities as its magnitude is controlled by a free parameter C_B. The κ_B from the AdS/CFT approach however is completely fixed by the thermodynamic state. In the comparison, we assume the relaxation time is the same $\tau_V = C_B/T$ and we pick $C_B = 0.4$. Figure 4.22 shows the two baryon transport coefficients as functions of η at the initial time $\tau = 0.7\,\mathrm{fm/c}$. Both κ_B have similar values in the limit of vanishing baryon density. The κ_B from the kinetic theory approach has larger values than that from the AdS/CFT approach at non-zero baryon densities. As a consequence, the baryon diffusion is stronger when using the κ_B from the kinetic theory approach. However, Figure 4.23 shows the baryon density distributions at late times of the hydrodynamic evolution are almost the same for the two κ_B. This is easy to understand as the baryon diffusion is more efficient at early times of the hydrodynamic evolution. At late times, hydrodynamic expansion plays a dominant role, leaving the differences resulting from the two different κ_B very small. Figure 4.24 presents the net-proton rapidity distribution after freezeout using the two different κ_B. The $(dN/dy)_{p-\bar{p}}$ has a slightly larger peak value when using κ_B from the AdS/CFT approach. Other than that, the two distributions overlap with each other. Although these two baryon transport coefficients come from completely different approaches, the physics at late times of the hydrodynamic evolution is not very sensitive to their differences.
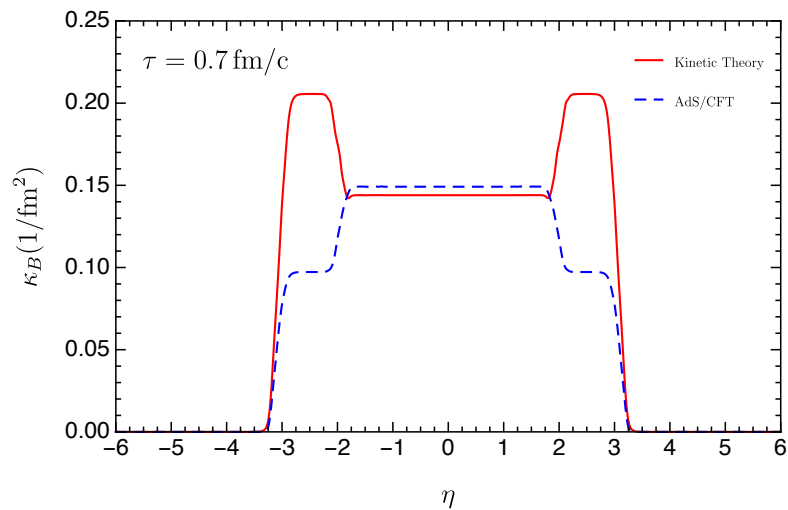
Figure 4.22: The initial profiles of the baryon transport coefficient κ_B obtained from the kinetic theory approach and the AdS/CFT approach.
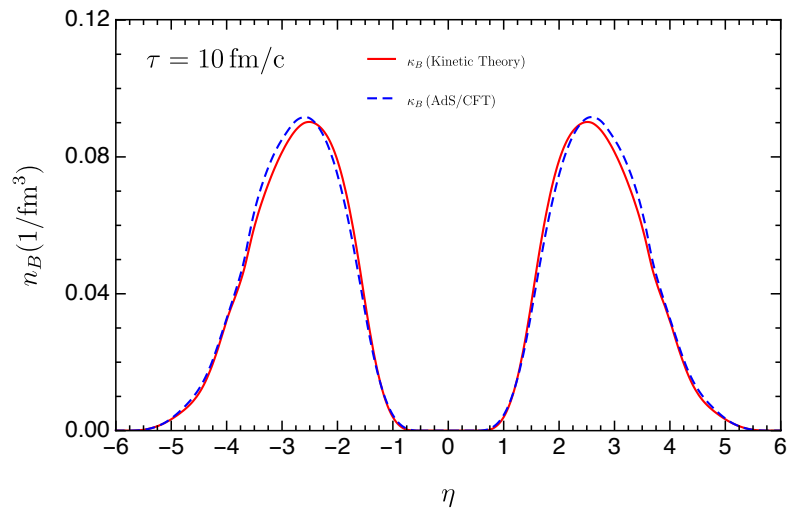
Figure 4.23: The baryon density spatial distribution at late time of the hydrodynamic evolution from two different baryon transport coefficients κ_B.
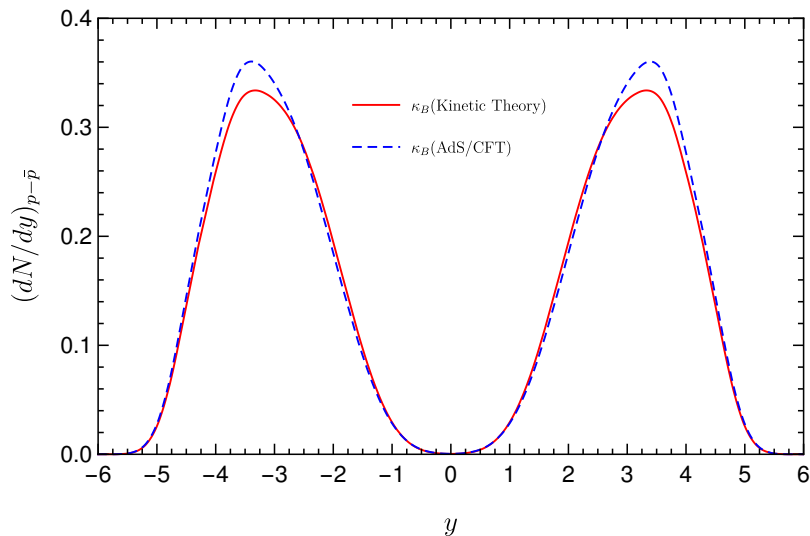
Figure 4.24: The net-proton rapidity distributions after freezeout from two different baryon transport coefficients κ_B.

4.5   Conclusion

In this chapter, we have performed the numerical calculations of the 1+1D diffusive hydrodynamic equations given the high baryon density initial conditions for Au+Au central collision at $\sqrt{s_{NN}} = 200\,\mathrm{GeV}$. We gave detailed discussions on the dynamics of baryon diffusion. Baryons are found to diffuse from the fragmentation regions to the central region overcoming the counter-force of hydrodynamic expansion, which has the effect of pushing baryons from the fragmentation regions to even larger rapidity regions. The amount of baryons transported to the central region is controlled by the baryon transport coefficient. It is difficult to achieve the observed number of baryons in the central region by purely baryon diffusion because the baryon transport coefficient can not be arbitrarily large before hydrodynamics break down. The proton, antiproton and net-proton rapidity

distributions after the freezeout are in qualitative agreement with experimental findings. We have the predicted temperature and baryon chemical potential as functions of rapidity y at freezeout which indicates that a rapidity scan might be helpful in searching for the critical point. This rapidity scan at high energy heavy-ion collisions is different from the beam energy scan at low collision energies.

In the future, numerical calculations of the full 3+1D hydrodynamics including both viscous and diffusive effects, together with the high baryon density initial conditions are needed to understand the three dimensional dynamics of baryon diffusion and to quantitatively compare with experimental data.

Chapter 5

Conclusions and Outlooks

In this thesis, we proposed an initial state model that deals with the fragmentation regions of high energy heavy-ion collisions. This initial state model predicts that very high baryon densities, more than ten times larger than normal atomic nuclear density, can be achieved in the fragmentation regions of the central $Au + Au$ collision at $\sqrt{s_{NN}} = 200\,\mathrm{GeV}$. In this model, the central region of high energy heavy-ion collisions is described by classical gluon fields using the McLerran-Venugopalan model in the Color Glass Condensate framework. We first computed the energy-momentum tensor of the classical gluon fields by solving the classical Yang-Mills equations semianalytically with a power series expansion. Calculations to all orders in the leading Q^2 approximation are obtained. With this energy-momentum tensor, we further consider the action of the classical gluon fields on the receding nuclear remnants by imposing energy and momentum conservation. The final rapidities and excitation energies of the nuclear remnants are calculated by solving the conservation equations. The peculiar features of the gluon energy-momentum tensor are the off-diagonal terms which come from

the transverse components of the color-electromagnetic fields. These off-diagonal terms are responsible for the nuclear excitation. The nuclear compression in the collision is characterized by the exponential of the change of rapidity and gives the enhancement of the baryon density. Energy densities achievable are computed by taking into account both the nuclear compression and the thermal excitation energy. It is found that the energy densities achievable are also more than ten time larger than the critical energy density, above which the deconfined state of quarks and gluons are formed. With these large energy and baryon densities, we assume QGP with high baryon density is formed in the fragmentation regions. Using a crossover EoS, the corresponding temperature and baryon chemical potentials in the fragmentation regions are found. The values of the temperature and baryon chemical potential are found to be in the right range relevant to the search for the possible critical point and the first order phase transition line of the QCD phase diagram. Therefore, a rapidity scan in high energy heavy-ion collisions focusing on the fragmentation regions might be helpful in locating the possible critical point and the first order phase transition. This rapidity scan at high collision energies is different from the low energy beam energy scan approach currently being carried out on the RHIC at BNL. Systematic studies of the high baryon densities in the fragmentation regions for other collision configurations, such as asymmetric collisions, collisions at different energies, and non-central collisions were presented. These discussions only concern the early times of the high energy heavy-ion collisions. To explore the subsequent spacetime evolution of the high baryon density matter in the fragmentation regions after their formation, we performed a 1+1D hydrodynamic simulation focusing on their longitudinal dynamics. We found that

baryons diffuse from the fragmentation regions to the central region due to the gradient of the fugacity while competing against the hydrodynamic expansion from the gradient of the pressure. Our calculations, however, do not favor the scenario that the tiny amount of net-baryons at the central region of Au+Au collision at $\sqrt{s_{NN}} = 200\,\text{GeV}$ are purely from baryon diffusion. At the freezeout, the baryon chemical potential increases from 0 up to $400\,\text{MeV}$ while the temperature decreases from about $165\,\text{MeV}$ to $150\,\text{MeV}$ as the rapidity increases from $y = 0$ to $y = 4$. These values reinforce the idea of a rapidity scan in high energy heavy-ion collisions to explore the QCD phase diagram.

Unfortunately, experimental measurements of particle production at large rapidity y are very challenging in the collider mode. The BRAHMS collaboration at RHIC had the capability of measuring (anti)protons, kaons and pions up to rapidity $y \sim 3.1$. A detailed rapidity scan has not been performed yet. It is desired that experimentalists can identify particles' identities (thus knowing their masses) and measure their transverse momenta while scanning through the momentum space rapidity. A more promising approach in measuring the fragmentation regions could be fixed target experiments. For example, the AFTER@LHC project [184, 185], a fixed target experiment using the 2.76 TeV Pb beam which is equivalent to the $\sqrt{s_{NN}} = 72\,\text{GeV}$ Pb+Pb collision in the center-of-momentum frame, is under study. In a fixed target experiment, detectors are located in the forward rapidity region behind the target in the Lab frame. This forward rapidity region in a fixed target experiment corresponds to one of the fragmentation regions in the collider mode. It is worth emphasizing that the major difficulty in measuring the large rapidity regions is particle identification (PID). In design the BRAHMS

detector, the largest rapidity $y = 4$ is equivalent to 2° away from the beam direction. With particles produced in directions so close to the beam direction, signals are easily buried in the original beam particles. It is also worth noting that there are dedicated experimetns, the LHCf and the RHICf experiments, that measure the neutrons in the forward direction.

For future theoretical work, we plan to make improvements to the initial state model, implement the full 3+1D hydrodynamics simulations, study baryon diffusion in non-central collisions, and possibly extrapolate our initial state model to the intermediate energy collisions like $\sqrt{s_{NN}} = 72\,\text{GeV}$.

References

[1] C. Patrignani *et al.* [Particle Data Group], Chin. Phys. C **40**, no. 10, 100001 (2016).

[2] D. J. Gross and F. Wilczek, Phys. Rev. Lett. **30**, 1343 (1973).

[3] H. D. Politzer, Phys. Rev. Lett. **30**, 1346 (1973).

[4] R. Hagedorn, Nuovo Cim. Suppl. **3**, 147 (1965).

[5] J. C. Collins and M. J. Perry, Phys. Rev. Lett. **34**, 1353 (1975).

[6] N. Cabibbo and G. Parisi, Phys. Lett. **59B**, 67 (1975).

[7] M. A. Stephanov, PoS LAT **2006**, 024 (2006)

[8] K. Fukushima and T. Hatsuda, Rept. Prog. Phys. **74**, 014001 (2011)

[9] Y. Aoki, G. Endrodi, Z. Fodor, S. D. Katz and K. K. Szabo, Nature **443**, 675 (2006)

[10] C. DeTar and U. M. Heller, Eur. Phys. J. A **41**, 405 (2009)

[11] G. F. Chapline, M. H. Johnson, E. Teller and M. S. Weiss, Phys. Rev. D **8** (1973) 4302.

[12] T. D. Lee and G. C. Wick, Phys. Rev. D **9**, 2291 (1974).

[13] G. F. Chapline and A. K. Kerman, M I T Cambridge - CTP-695 (78,REC.APR) 10p

[14] S. A. Chin, Phys. Lett. **78B**, 552 (1978).

[15] J. D. Bjorken, Phys. Rev. D **27**, 140 (1983).

[16] I. Arsene *et al.* [BRAHMS Collaboration], Nucl. Phys. A **757**, 1 (2005)

[17] B. B. Back *et al.*, Nucl. Phys. A **757**, 28 (2005)

[18] J. Adams *et al.* [STAR Collaboration], Nucl. Phys. A **757**, 102 (2005)

[19] K. Adcox *et al.* [PHENIX Collaboration], Nucl. Phys. A **757**, 184 (2005)

[20] R. Nouicer *et al.* [PHOBOS Collaboration], Eur. Phys. J. C **33** (2004) S606

[21] R. Nouicer, Eur. Phys. J. Plus **131**, no. 3, 70 (2016)

[22] A. Andronic, P. Braun-Munzinger, K. Redlich and J. Stachel, Nucl. Phys. A **904-905**, 535c (2013)

[23] M. Nasim [STAR Collaboration], Nucl. Phys. A **904-905**, 413c (2013)

[24] J. Adams *et al.* [STAR Collaboration], Phys. Rev. C **72**, 014904 (2005)

[25] A. Adare *et al.* [PHENIX Collaboration], Phys. Rev. Lett. **98**, 162301 (2007)

[26] P. F. Kolb, P. Huovinen, U. W. Heinz and H. Heiselberg, Phys. Lett. B **500**, 232 (2001)

[27] P. Huovinen, P. F. Kolb, U. W. Heinz, P. V. Ruuskanen and S. A. Voloshin, Phys. Lett. B **503**, 58 (2001)

[28] S. S. Adler *et al.* [PHENIX Collaboration], Phys. Rev. Lett. **96**, 202301 (2006)

[29] I. Vitev and M. Gyulassy, Phys. Rev. Lett. **89**, 252301 (2002)

[30] J. Adams *et al.* [STAR Collaboration], Phys. Rev. Lett. **91**, 072304 (2003)

[31] J. Adams *et al.* [STAR Collaboration], Phys. Rev. Lett. **95**, 152301 (2005)

[32] E. Shuryak, Prog. Part. Nucl. Phys. **62**, 48 (2009)

[33] E. Shuryak, Rev. Mod. Phys. **89**, 035001 (2017)

[34] [STAR Collaboration], " Studying the Phase Diagram of QCD Matter at RHIC" (2014).

[35] D. H. Rischke, Y. Pursun, J. A. Maruhn, H. Stoecker and W. Greiner, Acta Phys. Hung. A **1**, 309 (1995)

[36] H. Stoecker, Nucl. Phys. A **750**, 121 (2005)

[37] L. Adamczyk *et al.* [STAR Collaboration], Phys. Rev. Lett. **112**, 162301 (2014)

[38] M. A. Stephanov, K. Rajagopal and E. V. Shuryak, Phys. Rev. Lett. **81**, 4816 (1998)

[39] M. A. Stephanov, K. Rajagopal and E. V. Shuryak, Phys. Rev. D **60**, 114028 (1999)

[40] M. A. Stephanov, Phys. Rev. Lett. **102**, 032301 (2009)

[41] M. M. Aggarwal *et al.* [STAR Collaboration], Phys. Rev. Lett. **105** (2010) 022302

[42] L. Adamczyk *et al.* [STAR Collaboration], Phys. Rev. C **96**, 044904 (2017)

[43] A. Aduszkiewicz [NA61/SHINE Collaboration], Nucl. Phys. A **967**, 35 (2017)

[44] M. Lorenz [HADES Collaboration], Nucl. Phys. A **967**, 27 (2017).

[45] P. Senger [CBM Collaboration], Nucl. Phys. A **967**, 892 (2017).

[46] V. Kekelidze, A. Kovalenko, R. Lednicky, V. Matveev, I. Meshkov, A. Sorin and G. Trubnikov, Nucl. Phys. A **967**, 884 (2017).

[47] T. Sakaguchi [J-PARC-HI Collaboration], Nucl. Phys. A **967**, 896 (2017).

[48] I. G. Bearden *et al.* [BRAHMS Collaboration], Phys. Rev. Lett. **93**, 102301 (2004)

[49] I. C. Arsene *et al.* [BRAHMS Collaboration], Phys. Lett. B **677**, 267 (2009)

[50] R. Anishetty, P. Koehler and L. D. McLerran, Phys. Rev. D **22**, 2793 (1980).

[51] K. Kajantie and L. D. McLerran, Nucl. Phys. B **214**, 261 (1983).

[52] K. Kajantie, R. Raitio and P. V. Ruuskanen, Nucl. Phys. B **222**, 152 (1983)

[53] M. Gyulassy and L. P. Csernai, Nucl. Phys. A **460**, 723 (1986).

[54] R. D. Woods and D. S. Saxon, Phys. Rev. **95**, 577 (1954).

[55] T. Lappi and L. McLerran, Nucl. Phys. A **772**, 200 (2006)

[56] L. D. McLerran, Lect. Notes Phys. **583**, 291 (2002)

[57] E. Iancu and R. Venugopalan, In *Hwa, R.C. (ed.) et al.: Quark gluon plasma* 249-3363

[58] M. Froissart, Phys. Rev. **123**, 1053 (1961).

[59] L. V. Gribov, E. M. Levin and M. G. Ryskin, Phys. Rept. **100**, 1 (1983).

[60] A. H. Mueller and J. w. Qiu, Nucl. Phys. B **268**, 427 (1986).

[61] L. D. McLerran and R. Venugopalan, Phys. Rev. D **49**, 2233 (1994)

[62] L. D. McLerran and R. Venugopalan, Phys. Rev. D **49**, 3352 (1994)

[63] J. Jalilian-Marian, A. Kovner, A. Leonidov and H. Weigert, Phys. Rev. D **59**, 014014 (1998)

[64] J. Jalilian-Marian, A. Kovner and H. Weigert, Phys. Rev. D **59**, 014015 (1998)

[65] E. Iancu, A. Leonidov and L. D. McLerran, Nucl. Phys. A **692**, 583 (2001)

[66] E. Ferreiro, E. Iancu, A. Leonidov and L. McLerran, Nucl. Phys. A **703**, 489 (2002)

[67] Y. V. Kovchegov, Phys. Rev. D **54**, 5463 (1996)

[68] A. Kovner, L. D. McLerran and H. Weigert, Phys. Rev. D **52**, 6231 (1995)

[69] A. Kovner, L. D. McLerran and H. Weigert, Phys. Rev. D **52**, 3809 (1995)

[70] M. Gyulassy and L. D. McLerran, Phys. Rev. C **56**, 2219 (1997)

[71] R. J. Fries, J. I. Kapusta and Y. Li, nucl-th/0604054.

[72] G. Chen, R. J. Fries, J. I. Kapusta and Y. Li, Phys. Rev. C **92**, no. 6, 064912 (2015)

[73] H. Fujii, K. Fukushima and Y. Hidaka, Phys. Rev. C **79**, 024909 (2009)

[74] A. Krasnitz and R. Venugopalan, Phys. Rev. Lett. **84**, 4309 (2000)

[75] A. Krasnitz and R. Venugopalan, Phys. Rev. Lett. **86**, 1717 (2001)

[76] A. Krasnitz, Y. Nara and R. Venugopalan, Phys. Rev. Lett. **87**, 192302 (2001)

[77] T. Lappi, Phys. Rev. C **67**, 054903 (2003)

[78] T. Lappi, Phys. Lett. B **643**, 11 (2006)

[79] R. J. Fries, G. Chen and S. Somanathan, Phys. Rev. C **97**, 034903 (2018)

[80] P. F. Kolb and U. W. Heinz, In *Hwa, R.C. (ed.) et al.: Quark gluon plasma* 634-714

[81] R. Baier, A. H. Mueller, D. Schiff and D. T. Son, Phys. Lett. B **502**, 51 (2001)

[82] A. Kurkela and Y. Zhu, Phys. Rev. Lett. **115**, 182301 (2015)

[83] K. Fukushima, Rept. Prog. Phys. **80**, 022301 (2017)

[84] K. Fukushima and Y. Hidaka, JHEP **0706**, 040 (2007)

[85] M. Li and J. I. Kapusta, Phys. Rev. C **94**, 024908 (2016)

[86] E. Iancu, A. Leonidov and L. McLerran, "The Color glass condensate: An Introduction," hep-ph/0202270.

[87] T. Epelbaum and F. Gelis, Phys. Rev. Lett. **111**, 232301 (2013)

[88] Y. V. Kovchegov and D. H. Rischke, Phys. Rev. C **56**, 1084 (1997)

[89] Y. V. Kovchegov, Nucl. Phys. A **762**, 298 (2005)

[90] M. Li, Phys. Rev. C **96**, 064904 (2017)

[91] I. N. Mishustin and J. I. Kapusta, Phys. Rev. Lett. **88**, 112501 (2002)

[92] C. Shen and B. Schenke, Phys. Rev. C **97**, 024907 (2018)

[93] B. Schenke, P. Tribedy and R. Venugopalan, Phys. Rev. Lett. **108**, 252301 (2012)

[94] B. Schenke, P. Tribedy and R. Venugopalan, Phys. Rev. C **86**, 034908 (2012)

[95] T. Lappi, Eur. Phys. J. C **55**, 285 (2008)

[96] J. L. Albacete and C. Marquet, Prog. Part. Nucl. Phys. **76**, 1 (2014)

[97] H. Song, S. A. Bass and U. Heinz, Phys. Rev. C **83**, 024912 (2011)

[98] J. I. Kapusta and C. Gale, "Finite-temperature field theory: Principles and applications," Cambridge University Press, 2011.

[99] A. Kurkela and A. Vuorinen, Phys. Rev. Lett. **117**, 042501 (2016)

[100] A. Bazavov *et al.*, Phys. Rev. D **95**, 054504 (2017)

[101] M. Albright, J. Kapusta and C. Young, Phys. Rev. C **90**, 024915 (2014)

[102] M. Albright, J. Kapusta and C. Young, Phys. Rev. C **92**, 044904 (2015)

[103] S. Borsanyi, G. Endrodi, Z. Fodor, A. Jakovac, S. D. Katz, S. Krieg, C. Ratti and K. K. Szabo, JHEP **1011**, 077 (2010)

[104] S. Borsanyi, G. Endrodi, Z. Fodor, S. D. Katz, S. Krieg, C. Ratti and K. K. Szabo, JHEP **1208**, 053 (2012)

[105] C. Nonaka and M. Asakawa, Phys. Rev. C **71**, 044904 (2005)

[106] M. Asakawa, S. A. Bass, B. Muller and C. Nonaka, Phys. Rev. Lett. **101**, 122302 (2008)

[107] B. Schenke, P. Tribedy and R. Venugopalan, Phys. Rev. C **89**, 064908 (2014)

[108] C. Shen, Z. Qiu, H. Song, J. Bernhard, S. Bass and U. Heinz, Comput. Phys. Commun. **199**, 61 (2016)

[109] P. Boek, Phys. Lett. B **717**, 287 (2012)

[110] K. J. Golec-Biernat and M. Wusthoff, Phys. Rev. D **59**, 014017 (1998)

[111] K. J. Golec-Biernat and M. Wusthoff, Phys. Rev. D **60**, 114023 (1999)

[112] A. M. Stasto, K. J. Golec-Biernat and J. Kwiecinski, Phys. Rev. Lett. **86**, 596 (2001)

[113] D. Kharzeev, E. Levin and M. Nardi, Nucl. Phys. A **747**, 609 (2005)

[114] Chun Shen, private communication.

[115] K. Regers [Phenix Collaboration], "Glauber Monte-Carlo Calculations for Au+Au Collisions at sNN = 200 GeV." (2003)

[116] L. D. Landau, Izv. Akad. Nauk Ser. Fiz. **17**, 51 (1953).

[117] H. Stoecker and W. Greiner, Phys. Rept. **137**, 277 (1986).

[118] J. P. Blaizot and J. Y. Ollitrault, Nucl. Phys. A **458**, 745 (1986).

[119] L. P. Csernai, Chichester, UK: Wiley (1994) 310 p

[120] D. H. Rischke, Lect. Notes Phys. **516**, 21 (1999)

[121] P. Huovinen, In *Hwa, R.C. (ed.) et al.: Quark gluon plasma* 600-633

[122] A. Muronga, Phys. Rev. Lett. **88**, 062302 (2002) Erratum: [Phys. Rev. Lett. **89**, 159901 (2002)]

[123] A. Muronga, Phys. Rev. C **69**, 034903 (2004)

[124] R. Baier, P. Romatschke, D. T. Son, A. O. Starinets and M. A. Stephanov, JHEP **0804**, 100 (2008)

[125] P. Romatschke, Int. J. Mod. Phys. E **19**, 1 (2010)

[126] P. Kovtun, D. T. Son and A. O. Starinets, Phys. Rev. Lett. **94**, 111601 (2005)

[127] H. Song and U. W. Heinz, Phys. Rev. C **77**, 064901 (2008)

[128] M. Luzum and P. Romatschke, Phys. Rev. C **78**, 034915 (2008) Erratum: [Phys. Rev. C **79**, 039903 (2009)]

[129] H. Song, S. A. Bass, U. Heinz, T. Hirano and C. Shen, Phys. Rev. Lett. **106**, 192301 (2011) Erratum: [Phys. Rev. Lett. **109**, 139904 (2012)]

[130] B. Schenke, S. Jeon and C. Gale, Phys. Rev. Lett. **106**, 042301 (2011)

[131] C. Gale, S. Jeon, B. Schenke, P. Tribedy and R. Venugopalan, Phys. Rev. Lett. **110**, 012302 (2013)

[132] C. Gale, S. Jeon and B. Schenke, Int. J. Mod. Phys. A **28**, 1340011 (2013)

[133] S. Jeon and U. Heinz, Int. J. Mod. Phys. E **24**, no. 10, 1530010 (2015)

[134] P. Romatschke and U. Romatschke, arXiv:1712.05815 [nucl-th].

[135] R. D. Weller and P. Romatschke, Phys. Lett. B **774**, 351 (2017)

[136] A. Jaiswal and V. Roy, Adv. High Energy Phys. **2016**, 9623034 (2016)

[137] W. Israel and J. M. Stewart, Annals Phys. **118**, 341 (1979).

[138] G. S. Denicol, E. Molnr, H. Niemi and D. H. Rischke, Eur. Phys. J. A **48**, 170 (2012)

[139] G. S. Denicol, H. Niemi, E. Molnar and D. H. Rischke, Phys. Rev. D **85**, 114047 (2012) Erratum: [Phys. Rev. D **91**, no. 3, 039902 (2015)]

[140] R. Baier, P. Romatschke, D. T. Son, A. O. Starinets and M. A. Stephanov, JHEP **0804**, 100 (2008)

[141] S. Chapman, T. G. Cowling, "The mathematical thoery of non-uniform gas", Cambridge University Press, 1970.

[142] S. R. De Groot, W. A. Van Leeuwen and C. G. Van Weert, "Relativistic Kinetic Theory. Principles and Applications," Amsterdam, Netherlands: North-holland (1980) 417p

[143] H. Grad "On the kinetic theory of rarefied gases", Commun. Pure Appl. Math. **2**, 331 (1949).

[144] H. Grad "On the N-dimensional Hermite Polynomials", Commun. Pure Appl. Math. **2**, 325 (1949).

[145] H. Song, Nucl. Phys. A **904-905**, 114c (2013)

[146] L. M. Satarov, A. V. Merdeev, I. N. Mishustin and H. Stoecker, Phys. Rev. C **75**, 024903 (2007)

[147] P. Bozek, Phys. Rev. C **77**, 034911 (2008)

[148] A. Monnai, Phys. Rev. C **86**, 014908 (2012)

[149] W. Florkowski, R. Ryblewski, M. Strickland and L. Tinti, Phys. Rev. C **94**, 064903 (2016)

[150] A. Kurganov "Central Schemes: A Powerful Black-Box Solver for Nonlinear Hyperbolic PDEs", In R. Abgrall and C-W. Shu (ed.) "Handbook of Numerical Analysis" (2016). p525-584.

[151] A. Kurganov and C-T. Lin "On the Reduction of Numerical Dissipation in Central-Upwind Schems", Commun. Comput. Phys. Vol. **2**, No. 1, pp. 141-163 (2007)

[152] A. Kurganov and E. Tadmor "New High-Resoluton Central Schemes for Nonlinear Conservation Laws and Convection-Diffusion Equations", J. Compu. Phys. **160**, 241-282 (2000)

[153] Y. Akamatsu, S. i. Inutsuka, C. Nonaka and M. Takamoto, J. Comput. Phys. **256**, 34 (2014)

[154] B. Schenke, S. Jeon and C. Gale, Phys. Rev. C **82**, 014903 (2010)

[155] J. F. Paquet, C. Shen, G. S. Denicol, M. Luzum, B. Schenke, S. Jeon and C. Gale, Phys. Rev. C **93**, 044906 (2016)

[156] T. Hirano, Phys. Rev. C **65**, 011901 (2002)

[157] T. Hirano and K. Tsuda, Phys. Rev. C **66**, 054905 (2002)

[158] A. Bazavov *et al.* [HotQCD Collaboration], Phys. Rev. D **90**, 094503 (2014)

[159] J. N. Guenther, R. Bellwied, S. Borsanyi, Z. Fodor, S. D. Katz, A. Pasztor, C. Ratti and K. Szabo, PoS CPOD **2017**, 032 (2018).

[160] P. Parotto *et al.*, "Lattice-QCD-based equation of state with a critical point," arXiv:1805.05249 [hep-ph].

[161] M. Albright and J. I. Kapusta, Phys. Rev. C **93**, 014903 (2016)

[162] A. Jaiswal, B. Friman and K. Redlich, Phys. Lett. B **751**, 548 (2015)

[163] M. Greif, J. A. Fotakis, G. S. Denicol and C. Greiner, arXiv:1711.08680 [hep-ph].

[164] G. S. Denicol, C. Gale, S. Jeon, A. Monnai, B. Schenke and C. Shen, arXiv:1804.10557 [nucl-th].

[165] D. T. Son and A. O. Starinets, JHEP **0603**, 052 (2006)

[166] R. Rougemont, J. Noronha and J. Noronha-Hostler, Phys. Rev. Lett. **115**, 202301 (2015)

[167] P. Danielewicz and M. Gyulassy, Phys. Rev. D **31**, 53 (1985).

[168] A. Hosoya and K. Kajantie, Nucl. Phys. B **250**, 666 (1985).

[169] S. Gavin, Nucl. Phys. A **435**, 826 (1985).

[170] H. Heiselberg and C. J. Pethick, Phys. Rev. D **48**, 2916 (1993).

[171] J. W. Chen, Y. F. Liu, S. Pu, Y. K. Song and Q. Wang, Phys. Rev. D **88**, 085039 (2013)

[172] S. Floerchinger and M. Martinez, Phys. Rev. C **92**, 064906 (2015)

[173] S. A. Bass *et al.*, Prog. Part. Nucl. Phys. **41**, 255 (1998)

[174] M. Bleicher *et al.*, J. Phys. G **25**, 1859 (1999)

[175] F. Cooper and G. Frye, Phys. Rev. D **10**, 186 (1974).

[176] J. I. Kapusta, Phys. Rev. C **16**, 1493 (1977).

[177] J. Sollfrank, P. Koch and U. W. Heinz, Phys. Lett. B **252**, 256 (1990).

[178] J. Sollfrank, P. Koch and U. W. Heinz, Z. Phys. C **52**, 593 (1991).

[179] M. I. Gorenstein, M. S. Tsai and S. N. Yang, Phys. Rev. C **51**, 1465 (1995).

[180] P. M. Lo, Phys. Rev. C **97**, 035210 (2018)

[181] P. Huovinen, P. M. Lo, M. Marczenko, K. Morita, K. Redlich and C. Sasaki, Phys. Lett. B **769**, 509 (2017)

[182] L. M. Satarov, I. N. Mishustin, A. V. Merdeev and H. Stoecker, Phys. Atom. Nucl. **70**, 1773 (2007)

[183] F. Becattini and J. Cleymans, J. Phys. G **34**, S959 (2007)

[184] A. Rakotozafindrabe *et al.*, Nucl. Phys. A **904-905**, 957c (2013)

[185] S. J. Brodsky, F. Fleuret, C. Hadjidakis and J. P. Lansberg, Phys. Rept. **522**, 239 (2013)

Appendix A

Light Cone and Milne Coordinates

In the high energy limit, particles move at speeds very close to the speed of light. It is convenient to use light cone coordinates when describing particles moving in the forward light cone on the space-time diagram. The light cone coordinates are defined as:

$$x^+ = \frac{1}{\sqrt{2}}(t+z), \qquad x^- = \frac{1}{\sqrt{2}}(t-z), \qquad \mathbf{x}_\perp = (x, y) \tag{A.1}$$

where x^+ is interpreted as the time component of the light cone coordinates. The x^- is the longitudinal spatial coordinate and $\mathbf{x}_\perp$ are the transverse spatial coordinates. The metric $g_{\mu\nu}$ in the light cone coordinate system is obtained from $ds^2 = g_{\mu\nu}dx^\mu dx^\nu = 2dx^+dx^- - d^2\mathbf{x}_\perp$. The nonvanishing components of $g_{\mu\nu}$ are $g_{+-} = g_{-+} = 1$ and $g_{xx} = g_{yy} = -1$. Likewise, the four-momentum p^μ are written in light cone coordinates:

$$p^+ = \frac{1}{\sqrt{2}}(E+p_z), \qquad p^- = \frac{1}{\sqrt{2}}(E-p_z), \qquad \mathbf{p}_T = (p_x, p_y) \tag{A.2}$$

where p^- is interpreted as the energy component. The p^+ is the longitudinal momentum and $\mathbf{p}_T$ are the transverse momentums. The above interpretation is consistent with the inner product $x \cdot p = x^+ p^- + x^- p^+ - \mathbf{x}_\perp \cdot \mathbf{p}_T$. Moreover, the uncertainty principles are:

$$\Delta x^\pm \Delta p^\mp \sim 1 \tag{A.3}$$

The on-shell condition now becomes $p^2 = 2p^+ p^- - p_T^2 = m^2$ and $p^- = (p_T^2 + m^2)/2p^+$.

In high energy heavy-ion collisions, the collision is usually assumed to occur at $z = 0$ when $t = 0$. For describing physics after the collision, the Milne coordinate system is convenient to use. The longitudinal dynamics and transverse dynamics are treated separately. Instead of the Cartesian coordinates (t, x, y, z) or the light cone coordinates (x^+, x^-, x, y), one defines the Milne coordinates:

$$\tau = \sqrt{t^2 - z^2} = \sqrt{2x^+ x^-}, \qquad \eta = \frac{1}{2} \ln \left(\frac{t+z}{t-z} \right) = \frac{1}{2} \ln \left(\frac{x^+}{x^-} \right), \qquad \mathbf{x}_\perp = (x, y) \tag{A.4}$$

where τ is the proper time and η the space-time pseudorapidity. The Milne coordinates are only meaningful for $t > 0$ and $z < t$. The metric g_{mn} in the Milne coordinate system is defined by $ds^2 = g_{mn} dx^m dx^n$ for $m, n = (\tau, x, y, \eta)$. Then $g_{mn} = \mathrm{diag}(1, -1, -1, -\tau^2)$ and the inverse of the metric is $g^{mn} = \mathrm{diag}(1, -1, -1, -\tau^{-2})$.

The four-vectors, such as the gluon field A^μ and tensors like the field strength $F^{\mu\nu}$, and the energy-momentum tensor $T^{\mu\nu}$ in different coordinate systems are related by the transformation rules

$$
\begin{aligned}
V_\mu &= \frac{\partial x^m}{\partial x^\mu} V_m \,, \\
T_{\mu\nu} &= \frac{\partial x^m}{\partial x^\mu} \frac{\partial x^n}{\partial x^\nu} T_{mn} \,.
\end{aligned}
\tag{A.5}
$$

The transformation rules apply to the covariant vectors and tensors. For contravariant vectors and tensors, we use the metric to raise the indexes after the transformation.

Appendix B

Gluon Correlation Functions

The method of calculating higher twist gluon correlation functions is described in Ref. [72]. We sketch the main steps here. All the correlation functions are expressed in terms of gradients of $\gamma(\vec{x}_\perp, \vec{y}_\perp)$ [73]

$$\gamma(\vec{x}_\perp, \vec{y}_\perp) = \mu \int \frac{d^2\vec{k}_\perp}{(2\pi)^2} e^{i\vec{k}_\perp(\vec{x}_\perp - \vec{y}_\perp)} \frac{1}{(k_\perp^2 + m^2)^2} \ . \tag{B.1}$$

A few examples are

$$\langle A_a^i(\vec{x}_\perp) A_b^j(\vec{x}_\perp) \rangle = \delta_{ab} \frac{g^2}{d_A} \nabla_x^i \nabla_y^j \gamma(\vec{x}_\perp, \vec{y}_\perp)|_{\vec{y}_\perp \to \vec{x}_\perp} \ , \tag{B.2}$$

$$\langle (D^k A^i)_a(\vec{x}_\perp)(D^l A^j)_b(\vec{x}_\perp) \rangle = \delta_{ab} \frac{g^2}{d_A} \times \nabla_x^k \nabla_y^l \nabla_x^i \nabla_y^j \gamma(\vec{x}_\perp, \vec{y}_\perp)|_{\vec{y}_\perp \to \vec{x}_\perp} \ , \tag{B.3}$$

and

$$\langle (D^k D^l A^i)_a(\vec{x}_\perp)(D^m D^n A^j)_b(\vec{x}_\perp) \rangle = \delta_{ab} \frac{g^2}{d_A} \nabla_x^k \nabla_x^l \nabla_y^m \nabla_y^n \nabla_x^i \nabla_y^j \gamma(\vec{x}_\perp, \vec{y}_\perp)|_{\vec{y}_\perp \to \vec{x}_\perp} \ . \tag{B.4}$$

We only consider terms containing even numbers of covariant derivatives because terms with odd numbers of covariant derivatives vanish by homogeneity and isotropy. This can be seen from explicit calculations like

$$
\begin{aligned}
\nabla^k_{x,y} \nabla^l_{x,y} \nabla^i_x \nabla^j_y & \gamma(\vec{x}_\perp, \vec{y}_\perp)|_{\vec{y}_\perp \to \vec{x}_\perp} \\
&= -\mu \int \frac{d^2 \vec{k}_\perp}{(2\pi)^2} e^{i\vec{k}_\perp (\vec{x}_\perp - \vec{y}_\perp)} \frac{k^k_\perp k^l_\perp k^i_\perp k^j_\perp}{(k^2_\perp + m^2)^2} \\
&= -\mu \int \frac{d^2 \vec{k}_\perp}{(2\pi)^2} \frac{k^4_\perp}{(k^2_\perp + m^2)^2} \frac{1}{8} (\delta^{kl} \delta^{ij} + \delta^{ki} \delta^{lj} + \delta^{kj} \delta^{li}) \\
&= -\frac{\mu}{32\pi} \int^{Q^2} dk^2_\perp \frac{k^4_\perp}{k^4_\perp} (\delta^{kl} \delta^{ij} + \delta^{ki} \delta^{lj} + \delta^{kj} \delta^{li}) \\
&= -\frac{\mu}{32\pi} Q^2 (\delta^{kl} \delta^{ij} + \delta^{ki} \delta^{lj} + \delta^{kj} \delta^{li}) \,.
\end{aligned}
\tag{B.5}
$$

In the above integration, we only kept the leading Q^2 terms due to the assumption that $Q^2 \gg m^2$. Higher twist correlation functions have more spatial indexes to deal with, for example

$$
\begin{aligned}
\nabla^k_x \nabla^l_x \nabla^m_y \nabla^n_y \nabla^i_x \nabla^j_y & \gamma(\vec{x}_\perp, \vec{y}_\perp)|_{\vec{y}_\perp \to \vec{x}_\perp} \\
&= \mu \int \frac{d^2 \vec{k}_\perp}{(2\pi)^2} e^{i\vec{k}_\perp (\vec{x}_\perp - \vec{y}_\perp)} \frac{k^k_\perp k^l_\perp k^m_\perp k^n_\perp k^i_\perp k^j_\perp}{(k^2_\perp + m^2)^2} \\
&= \frac{\mu}{4\pi} \frac{Q^4}{2} \frac{1}{48} \Delta^{klmnij} \,,
\end{aligned}
\tag{B.6}
$$

where the tensor Δ^{klmnij} is defined below. The momentum indices can be grouped as

$$
\begin{aligned}
k^k_\perp k^l_\perp k^m_\perp k^n_\perp k^i_\perp k^j_\perp = \frac{k^6_\perp}{48} \Big(& \delta^{ij} \delta^{kl} \delta^{mn} + \delta^{ij} \delta^{km} \delta^{ln} + \delta^{ij} \delta^{kn} \delta^{lm} \\
+ \delta^{ik} \delta^{jl} \delta^{mn} & + \delta^{ik} \delta^{jm} \delta^{ln} + \delta^{ik} \delta^{jn} \delta^{lm} + \delta^{il} \delta^{jk} \delta^{mn} + \delta^{il} \delta^{jm} \delta^{kn} + \delta^{il} \delta^{jn} \delta^{km} \\
+ \delta^{im} \delta^{jk} \delta^{ln} & + \delta^{im} \delta^{jl} \delta^{kn} + \delta^{im} \delta^{jn} \delta^{lk} + \delta^{in} \delta^{jk} \delta^{lm} + \delta^{in} \delta^{jl} \delta^{km} + \delta^{in} \delta^{jm} \delta^{lk} \Big) \,.
\end{aligned}
\tag{B.7}
$$

Therefore, we have to address the problem of complicated spatial index contractions during the resummation. We define $\Delta^{i_1 i_2 \cdots i_{2n}}$ as the summation of all possible

products of Kronecker delta functions with spatial indexes $i_1, i_2, \ldots, i_{2n}$. A few examples are

$$\Delta^{mp} \equiv \delta^{mp},$$

$$\Delta^{ijmp} \equiv \delta^{ij}\Delta^{mp} + \delta^{im}\Delta^{jp} + \delta^{ip}\Delta^{jm},$$

$$\Delta^{klijmp} \equiv \delta^{kl}\Delta^{ijmp} + \delta^{ki}\Delta^{ljmp} + \delta^{kj}\Delta^{limp}$$

$$+ \delta^{km}\Delta^{lijp} + \delta^{kp}\Delta^{lijm}.$$

(B.8)

In general, the normalized expression is proportional to

$$\frac{1}{(2n)!!}\Delta^{i_1 i_2 \ldots i_{2n}}$$

(B.9)

Notice that $\Delta^{i_1 i_2 \ldots i_{2n}}$ is totally symmetric under exchange of any two indexes. After explicit calculation, we obtain the following contraction identity which is used throughout the resummation process.

$$(\delta^{mn}\delta^{pq} + \epsilon^{mn}\epsilon^{pq})\frac{1}{(2n)!!}\Delta^{i_1 i_2 \ldots i_{2n-2}mp}\frac{1}{(2n)!!}\Delta^{i_1 i_2 \ldots i_{2n-2}nq} = \frac{(2n-2)!}{[(2n-2)!!]^2} \quad (B.10)$$

Appendix C

Central-Upwind Scheme

The central-upwind scheme is a finite-volume method in solving conservation and balance laws. The discussion in this appendix closely follows references [150, 151], see also [154, 133]. For 1+1D, the hyperbolic conservation laws to be solved are

$$\mathbf{q}_t + \mathbf{f}(\mathbf{q})_x = \mathbf{0}, \tag{C.1}$$

with the given initial conditions at t_0

$$\mathbf{q}(x, t_0) = \mathbf{q}_0(x). \tag{C.2}$$

Here $\mathbf{q} = \mathbf{q}(x, t)$ is a vector of variables to be solved and $\mathbf{f}(\mathbf{q})$ is the flux vector. After setting up the space-time grid $t_n = t_0 + n\Delta t$ and $x_i = x_0 + i\Delta x$, instead of evolving the values $\mathbf{q}(x_i, t_0)$ at the discrete grid points x_i to the next time step, the finite-volume method evolves the volume average $\bar{\mathbf{q}}_i = \frac{1}{\Delta x} \int_{x_i}^{x_i + \Delta x} q(x, t_0) dx$ within each spatial volume to the next time step. Values of the variables $\mathbf{q}(x, t)$ within the spatial volume $[x_i, x_i + \Delta x]$ are reconstructed from the volume average $\bar{\mathbf{q}}_i$ using interpolants; usually linear interpolants are used. As a finite-volume method,

214

the central-upwind scheme solves the integral form of the conservation laws Eq. (C.1). Take a small space-time control volume $[x - \Delta x/2, x + \Delta x/2] \times [t, t + \Delta t]$ and integrate Eq. (C.1) over this control volume

$$\bar{\mathbf{q}}(x, t + \Delta t) = \bar{\mathbf{q}}(x, t) - \frac{\Delta t}{\Delta x} \left[\hat{\mathbf{f}} \left(x + \frac{\Delta x}{2}, t \right) - \hat{\mathbf{f}} \left(x - \frac{\Delta x}{2}, t \right) \right], \qquad \text{(C.3)}$$

with the volume average

$$\bar{\mathbf{q}}(x, t) = \frac{1}{\Delta x} \int_{x - \Delta x/2}^{x + \Delta x/2} \mathbf{q}(x', t) dx'. \qquad \text{(C.4)}$$

and the average flux in the time interval $[t, t + \Delta t]$

$$\hat{\mathbf{f}}(x, t) = \frac{1}{\Delta t} \int_{t}^{t + \Delta t} \mathbf{f}(\mathbf{q}(x, t')) dt'. \qquad \text{(C.5)}$$

The integral form Eq. (C.3) is the starting point of the central-upwind scheme. In implementing the central-upwind scheme, the one dimensional volume – the cell – is labeled by $\mathcal{C}_j = (x_{j-\frac{1}{2}}, x_{j+\frac{1}{2}})$. The two boundaries of the cell $\mathcal{C}_j$ are $x_{j-\frac{1}{2}}$ and $x_{j+\frac{1}{2}}$ with $x_{j+\frac{1}{2}} - x_{j-\frac{1}{2}} = \Delta x$. The center of the cell $\mathcal{C}_j$ is labeled as $x_j = x_{j-\frac{1}{2}} + \Delta x/2$. Instead of evolving the cell average for each cell $\mathcal{C}_j$, the central-upwind scheme further divides each cell and doubles the total number of cells. Around each boundary $x_{j+\frac{1}{2}}$, two new boundaries are inserted: $x_{j+\frac{1}{2},l} = x_{j+\frac{1}{2}} + a_{j+\frac{1}{2}}^{-} \Delta t$ and $x_{j+\frac{1}{2},r} = x_{j+\frac{1}{2}} + a_{j+\frac{1}{2}}^{+} \Delta t$. Here $a_{j+\frac{1}{2}}^{\pm}$ are the maximum and minimum eigenvalues of the Jacobian $\mathbf{A}(\mathbf{q}) = \partial \mathbf{f}/\partial \mathbf{q}$ at the boundary $x_{j+\frac{1}{2}}$. They are one-sided local propagation speeds of waves generated at the cell boundaries. Now the cell numbers are doubled with $\left[x_{j-\frac{1}{2},r}, x_{j+\frac{1}{2},l} \right] \bigcup \left[x_{j+\frac{1}{2},l}, x_{j+\frac{1}{2},r} \right]$. The central-upwind scheme evolves the two cell averages within the cells $\left[x_{j-\frac{1}{2},r}, x_{j+\frac{1}{2},l} \right]$ and $\left[x_{j+\frac{1}{2},l}, x_{j+\frac{1}{2},r} \right]$ simultaneously at each time step according to Eq. (C.3), and then reconstructs from them the cell average for the original cell $[x_{j-\frac{1}{2}}, x_{j+\frac{1}{2}}]$. It

is important to note that for the cell splitting to be meaningful, the spatial and temporal spacing have to satisfy the following condition

$$\max\left(a^+_{j+\frac{1}{2}}, -a^-_{j+\frac{1}{2}}\right) < \frac{\Delta x}{2\Delta t}, \quad \forall j \tag{C.6}$$

The final result of the central-upwind scheme written in a semi-discrete form is

$$\frac{d}{dt}\bar{\mathbf{q}}_j(t) = -\frac{\mathbf{H}_{j+\frac{1}{2}}(t) - \mathbf{H}_{j-\frac{1}{2}}(t)}{\Delta x} \tag{C.7}$$

with the approximated flux term

$$\mathbf{H}_{j+\frac{1}{2}}(t) = \frac{\mathbf{f}(\mathbf{q}^+_{j+\frac{1}{2}}) + \mathbf{f}(\mathbf{q}^-_{j+\frac{1}{2}})}{2} - \frac{a_{j+\frac{1}{2}}}{2}\left(\mathbf{q}^+_{j+\frac{1}{2}} - \mathbf{q}^-_{j+\frac{1}{2}}\right) \tag{C.8}$$

Here $a_{j+\frac{1}{2}} = a^+_{j+\frac{1}{2}} = -a^-_{j+\frac{1}{2}}$ is assumed for the local propagation speed. The $\mathbf{q}^+_{j+\frac{1}{2}}$ and $\mathbf{q}^-_{j+\frac{1}{2}}$ are the right-sided value and the left-sided value of $\mathbf{q}(x,t)$ at the boundary $x_{j+\frac{1}{2}}$, respectively. This is because the value of $\mathbf{q}(x,t)$ at the boundary $x_{j+\frac{1}{2}}$ can be reconstructed either by the volume average $\bar{\mathbf{q}}_{j+1}$ from the right or by the volume average $\bar{\mathbf{q}}_j$ from the left

$$\begin{aligned}
\mathbf{q}^-_{j+\frac{1}{2}} &= \bar{\mathbf{q}}_j + \frac{\Delta x}{2}(\mathbf{q}_x)_j, \\
\mathbf{q}^+_{j+\frac{1}{2}} &= \bar{\mathbf{q}}_{j+1} - \frac{\Delta x}{2}(\mathbf{q}_x)_{j+1}.
\end{aligned} \tag{C.9}$$

Here $\mathbf{q}_x$ are the derivatives of the variables $\mathbf{q}(x,t)$ with respect to x. Numerically the slopes are calculated using a flux limiter by

$$(\mathbf{q}_x)_j = \mathrm{minmod}\left(\theta\frac{\bar{\mathbf{q}}_{j+1} - \bar{\mathbf{q}}_j}{\Delta x}, \frac{\bar{\mathbf{q}}_{j+1} - \bar{\mathbf{q}}_{j-1}}{2\Delta x}, \theta\frac{\bar{\mathbf{q}}_j - \bar{\mathbf{q}}_{j-1}}{\Delta x}\right), \quad \theta \in [1,2], \quad \text{(C.10)}$$

where the minmod function is defined as

$$\mathrm{minmod}(c_1, c_2, \ldots) = \begin{cases} \min(c_1, c_2, \ldots) & \text{if } c_i > 0 \ \forall i \\ \max(c_1, c_2, \ldots) & \text{if } c_i < 0 \ \forall i \\ 0 & \text{otherwise} \end{cases} \tag{C.11}$$

The use of the flux limiter is to avoid any possible large oscillatory behavior in the reconstructions. The value of θ is usually chosen close to 1. For the general situation when $a^+_{j+\frac{1}{2}} \neq -a^-_{j+1/2}$, the semi-discrete form of the central-upwind scheme can be found in [150]. The semi-discrete form of the central-upwind scheme Eq. (C.7) converts the original partial differential equations Eq. (C.1) to ordinary differential equations (ODE). To solve equations Eq. (C.7), one needs an ODE solver. We use the second-order strong stability preserving Runge-Kutta method. For an ordinary differential equation $dq/dt = L(q)$ the two steps are

$$
\begin{aligned}
q^{(1)} &= q(t_n) + \Delta t \, L(q(t_n)), \\
q(t_{n+1}) &= \frac{1}{2}q(t_n) + \frac{1}{2}q^{(1)} + \frac{1}{2}\Delta t \, L(q^{(1)}).
\end{aligned}
\tag{C.12}
$$

In solving hydrodynamic equations in the Milne coordinates, source terms show up so that the general equations are actually balance laws

$$
\mathbf{q}_t + \mathbf{f}(\mathbf{q})_x = \mathbf{S}(\mathbf{q}, t).
\tag{C.13}
$$

In dissipative hydrodynamics, the source terms contain spatial derivatives $\mathbf{q}_x$ and time derivatives of other coupled variables $\mathbf{q}_t$; see Eq. (4.5) for the explicit expressions of the 1+1D diffusive hydrodynamic equations. In principle, one has to redefine the independent variables so that the time derivatives of these redefined variables only appear on the left-hand side of the balance laws. In practice, this is difficult to achieve if not impossible. Instead, what MUSIC does is to assume the initial time derivatives in the source terms are zero at t_0 and advances the volume average to the next time step using the central-upwind scheme. After the first time step, time derivatives are explicitly calculated in the source terms using the finite-difference method. This should be a good numerical approximation as long as the time step is small and the overall evolution time is long.

In summary, the central-upwind scheme is ideally suited for perfect fluid hydrodynamics. For dissipative hydrodynamics, the central-upwind scheme is modified. Its validity has not been proven mathematically, while numerically it works well.

Appendix D

1+1D Diffusive Hydrodynamics in the Central-Upwind Scheme

The 1+1D diffusive hydrodynamic equations in Eqs. (4.5) is written in the form of balance laws. Equations (C.13) are

$$
\begin{aligned}
\partial_\tau q_1 + \partial_\eta f_1 &= S_1, \\
\partial_\tau q_2 + \partial_\eta f_2 &= S_2, \\
\partial_\tau q_3 + \partial_\eta f_3 &= S_3, \\
\partial_\tau q_4 + \partial_\eta f_4 &= S_4.
\end{aligned}
\tag{D.1}
$$

with

$$
\begin{aligned}
f_1 &= q_2/\tau, \qquad f_2 = \frac{(q_2)^2}{\tau(q_1 + \tau P)} + P, \\
f_3 &= \frac{q_2 q_3}{\tau(q_1 + \tau P)}, \quad f_4 = \frac{q_2 q_4}{\tau(q_1 + \tau P)}.
\end{aligned}
\tag{D.2}
$$

Here the pressure $P = P(\varepsilon, n_B)$ is an implicit function of q_1, q_2, q_3 but is independent of q_4 via the relations

$$\varepsilon = \frac{q_1}{\tau} - \frac{(q_2)^2}{\tau(q_1 + \tau P)}, \quad n_B = \frac{q_3}{\tau(q_1 + \tau P)} \sqrt{(q_1 + \tau P)^2 - (q_2)^2}. \tag{D.3}$$

The source terms are

$$\begin{aligned} S_1 &= -f_2, & S_2 &= -f_1, \\ S_3 &= S_B, & S_4 &= S_V. \end{aligned} \tag{D.4}$$

Explicit analytic expressions for S_3 and S_4 in terms of q_1, q_2, q_3, q_4 and their derivatives are difficult to obtain. They are calculated numerically using Eqs. (4.6).

To implement the central-upwind scheme, one has to obtain the one-sided local wave propagation speed at each cell interface. This comes from the eigenvalues of the Jacobian $A_{ij} = \partial f_i / \partial q_j$. From $\det(\mathbf{A} - \lambda \mathbf{I}) = 0$, one gets

$$\left(\frac{\partial f_4}{\partial q_4} - \lambda \right) \begin{vmatrix} -\lambda & \frac{\partial f_1}{\partial q_2} & 0 \\ \frac{\partial f_2}{\partial q_1} & \frac{\partial f_2}{\partial q_2} - \lambda & \frac{\partial f_2}{\partial q_3} \\ \frac{\partial f_3}{\partial q_1} & \frac{\partial f_3}{\partial q_2} & \frac{\partial f_3}{\partial q_3} - \lambda \end{vmatrix} = 0. \tag{D.5}$$

Two of the solutions are degenerate. They are u^η / u^τ. Another two solutions are

$$\lambda_\pm = \frac{u^\eta u^\tau (1 - v_s^2) \pm v_s/\tau}{(u^\tau)^2 - (\tau u^\eta)^2 v_s^2}, \tag{D.6}$$

with v_s^2 the speed of sound squared

$$v_s^2 = \partial_\varepsilon P + \frac{n_B}{\varepsilon + P} \partial_{n_B} P. \tag{D.7}$$

The speed of sound v_s is positive while the longitudinal velocity u^η can be either positive or negative depending on the projectile side or the target side after the collision. Therefore, the largest local propagation speed at the cell interface is

$$\lambda_{\mathbf{max}} = \frac{|u^\eta u^\tau (1 - v_s^2)| + v_s/\tau}{(u^\tau)^2 - (\tau u^\eta)^2 v_s^2}, \tag{D.8}$$

Finally, it is worth noting that, from the definition of q_1, q_2, q_3, q_4

$$q_1 = \tau T^{\tau\tau} = (\varepsilon + P)u^\tau u^\tau \tau - \tau P,$$

$$q_2 = \tau^2 T^{\tau\eta} = (\varepsilon + P)u^\tau u^\eta \tau^2,$$

$$q_3 = \tau J^\tau = n_B u^\tau \tau,$$

$$q_4 = \tau V^\eta,$$

$$(D.9)$$

the dimensions of q_1, q_2 are the same and equal to the energy cube $[E]^3$, q_3 has the dimension of $[E]^2$ and q_4 has the dimension of $[E]^3$.

Appendix E

Thermodynamic Relations

In numerical calculations using the crossover equation of state, especially in calculating the speed of sound and in inferring the temperature and baryon chemical potential given the energy density and baryon number density, thermodynamic relations that are constantly used are listed in this appendix. For a thermodynamic system whose equation of state is given as $P = P(T, \mu_B)$, the independent thermodynamic variables are the temperature T and the baryon chemical potential μ_B. All other thermodynamic quantities are functions of T and μ_B. The second law of thermodynamics and the Gibbs-Duhem equation are

$$d\varepsilon = Tds + \mu_B dn_B, \tag{E.1}$$

$$dP = sdT + n_B d\mu_B, \tag{E.2}$$

and

$$\varepsilon + P = Ts + \mu_B n_B. \tag{E.3}$$

From the equation of state $P = P(T, \mu_B)$ we can identify the entropy density s and baryon density n_B

$$s = \left(\frac{\partial P}{\partial T}\right)_{\mu_B}, \qquad n_B = \left(\frac{\partial P}{\partial \mu_B}\right)_T. \tag{E.4}$$

Additionally, the energy density becomes

$$\varepsilon = -P + Ts + \mu_B n_B. \tag{E.5}$$

Given the equation of state $P = P(T, \mu_B)$, the entropy density, the baryon density and the energy density can be readily computed by taking first order derivatives of P with respect to T and μ_B. The differential forms of various thermodynamic quantities can be expressed

$$\begin{aligned} ds &= \left(\frac{\partial s}{\partial T}\right)_{\mu_B} dT + \left(\frac{\partial s}{\partial \mu_B}\right)_T d\mu_B \\ &= \left(\frac{\partial^2 P}{\partial T^2}\right) dT + \left(\frac{\partial^2 P}{\partial T \partial \mu_B}\right) d\mu_B. \end{aligned} \tag{E.6}$$

Since by default the pressure is a function of T and μ_B, when taking derivatives with respect to T or μ_B, the other variable is held fixed. Without any ambiguities, we omit the labels for variables that are fixed in the derivatives. Also, we will use the following symbols for simplicity to represent the derivatives that constantly appear

$$\chi_{TT} = \left(\frac{\partial^2 P}{\partial T^2}\right), \quad \chi_{T\mu} = \left(\frac{\partial^2 P}{\partial T \partial \mu_B}\right), \quad \chi_{\mu\mu} = \left(\frac{\partial^2 P}{\partial \mu_B^2}\right). \tag{E.7}$$

Therefore, we have the expressions

$$ds = \chi_{TT} dT + \chi_{T\mu} d\mu_B, \tag{E.8}$$

$$dn = \chi_{T\mu} dT + \chi_{\mu\mu} d\mu_B, \tag{E.9}$$

$$d\varepsilon = (T\chi_{TT} + \mu_B\chi_{T\mu})\,dT + (T\chi_{T\mu} + \mu_B\chi_{\mu\mu})\,d\mu_B, \tag{E.10}$$

$$d\sigma = \left(-\frac{s}{n_B^2}\chi_{T\mu} + \frac{1}{n_B}\chi_{TT}\right)dT + \left(-\frac{s}{n_B^2}\chi_{\mu\mu} + \frac{1}{n_B}\chi_{T\mu}\right)d\mu_B. \tag{E.11}$$

Here $\sigma = s/n$ is the entropy per baryon. The strategy of computing the speed of sound at fixed σ,

$$v_\sigma^2 = \left(\frac{\partial P}{\partial\varepsilon}\right)_\sigma \tag{E.12}$$

is the following. Starting with

$$dP = \left(\frac{\partial P}{\partial\varepsilon}\right)_\sigma d\varepsilon + \left(\frac{\partial P}{\partial\sigma}\right)_\varepsilon d\sigma. \tag{E.13}$$

and recalling that $dP = sdT + n_B d\mu_B$, we express dT and $d\mu_B$ in terms of $d\varepsilon$ and $d\sigma$ from Eqs. (E.10) and (E.11)

$$
\begin{aligned}
dT &= \frac{(-s\chi_{\mu\mu} + n_B\chi_{T\mu})d\varepsilon - n_B^2(T\chi_{T\mu} + \mu_B\chi_{\mu\mu})d\sigma}{(\varepsilon + P)(\chi_{T\mu}^2 - \chi_{TT}\chi_{\mu\mu})}, \\
d\mu_B &= -\frac{(-s\chi_{T\mu} + n_B\chi_{TT})d\varepsilon - n_B^2(T\chi_{TT} + \mu_B\chi_{T\mu})d\sigma}{(\varepsilon + P)(\chi_{T\mu}^2 - \chi_{TT}\chi_{\mu\mu})}.
\end{aligned}
\tag{E.14}
$$

Substitute Eqs. (E.14) into Eq. (E.2) and compare with Eq. (E.12). One obtains the speed of sound

$$v_\sigma^2 = \frac{n_B^2\chi_{TT} - 2sn_B\chi_{T\mu} + s^2\chi_{\mu\mu}}{(\varepsilon + P)(\chi_{TT}\chi_{\mu\mu} - \chi_{T\mu}^2)}. \tag{E.15}$$

which is in direct relation with the second order derivatives of the equation of state $P = P(T, \mu_B)$ with respect to T and μ_B.

Appendix F

Two-Body Decays to Proton

In this appendix, the baryons that are included in the hadronic resonance gas model in calculating the crossover equation of state in [101] are analyzed. Specifically, we focus on the $N(xxxx)$ resonances, the Δ baryons and $\Delta(xxxx)$ resonances, the Λ baryon and $\Lambda(xxxx)$ resonances and the Σ baryons and $\Sigma(xxxx)$ resonances. All the possible two-body decays from these baryons that contribute to the production of the proton will be considered. Their branching ratios are calculated using isospin analysis.

- $N(xxxx)$ **Resonances**

  The nucleonic resonances $N(xxxx)$ decay to the nucleon via the most common two-body decay channel

  $$N(xxxx) \longrightarrow N\pi \qquad\qquad (\text{F.1})$$

  The branching ratios of this process for all the nucleonic resonances are listed in the Particle Data Group (PDG) book [1]. But these are the branching ratios for decays to the nucleon rather than to the proton. Isospin analysis

has to be carried out to figure out the branching ratio for the decay to proton given the branching ratio for the decay to nucleon. The resonance particle $N(xxxx)$ has isospin $I = 1/2$ and it has two different charge states $N^+(xxxx)$ and $N^0(xxxx)$. The nucleon N also has isospin $I = 1/2$ and two charge states $N^+ \equiv p$ and $N^0 \equiv n$. The pion however has isospin $I = 1$ and the three charge states π^+, π^0 and π^- have $I_3 = +1, 0, -1$, respectively. Therefore, the two-body decay (F.1) actually consists of four different decay processes

$$
\begin{aligned}
&(a)\ N^+(xxxx) \longrightarrow N^+ + \pi^0\,,\\
&(b)\ N^+(xxxx) \longrightarrow N^0 + \pi^+\,,\\
&(c)\ N^0(xxxx) \longrightarrow N^+ + \pi^-\,,\\
&(d)\ N^0(xxxx) \longrightarrow N^0 + \pi^0\,.
\end{aligned}
\tag{F.2}
$$

Among them only (a) and (c) contribute to the production of proton. To know the branching ratios of (a) and (c), the ratios of the decay widths between the four processes are needed. Assuming the isospin is conserved in the decay, which is true for decays via the strong interaction, isospin analysis follows

$$
\begin{aligned}
&(a)\ \left|\frac{1}{2}\frac{1}{2}\right\rangle \longrightarrow \left|\frac{1}{2}\frac{1}{2}\right\rangle |10\rangle = \sqrt{\frac{2}{3}}\left|\frac{3}{2}\frac{1}{2}\right\rangle - \sqrt{\frac{1}{3}}\left|\frac{1}{2}\frac{1}{2}\right\rangle,\\
&(b)\ \left|\frac{1}{2}\frac{1}{2}\right\rangle \longrightarrow \left|\frac{1}{2}-\frac{1}{2}\right\rangle |11\rangle = \sqrt{\frac{1}{3}}\left|\frac{3}{2}\frac{1}{2}\right\rangle + \sqrt{\frac{2}{3}}\left|\frac{1}{2}\frac{1}{2}\right\rangle,\\
&(c)\ \left|\frac{1}{2}-\frac{1}{2}\right\rangle \longrightarrow \left|\frac{1}{2}\frac{1}{2}\right\rangle |1-1\rangle = \sqrt{\frac{1}{3}}\left|\frac{3}{2}-\frac{1}{2}\right\rangle - \sqrt{\frac{2}{3}}\left|\frac{1}{2}-\frac{1}{2}\right\rangle,\\
&(d)\ \left|\frac{1}{2}-\frac{1}{2}\right\rangle \longrightarrow \left|\frac{1}{2}-\frac{1}{2}\right\rangle |10\rangle = \sqrt{\frac{2}{3}}\left|\frac{3}{2}-\frac{1}{2}\right\rangle + \sqrt{\frac{1}{3}}\left|\frac{1}{2}-\frac{1}{2}\right\rangle.
\end{aligned}
\tag{F.3}
$$

Here we used the Clebsch-Gordan coefficients. Let the decay amplitude for an isospin $I = 1/2$ decay process be $\mathcal{M}_{1/2}$, then the decay amplitudes of the four processes are $\mathcal{M}_a = \sqrt{\frac{1}{3}}\mathcal{M}_{1/2}$, $\mathcal{M}_b = \sqrt{\frac{2}{3}}\mathcal{M}_{1/2}$, $\mathcal{M}_c = \sqrt{\frac{2}{3}}\mathcal{M}_{1/2}$ and $\mathcal{M}_d = \sqrt{\frac{1}{3}}\mathcal{M}_{1/2}$. The decay width is proportional to the square of the decay amplitude $\Gamma \sim |\mathcal{M}|^2$. Therefore the ratios of the decay widths between the four processes are $\Gamma_a : \Gamma_b : \Gamma_c : \Gamma_d = 1 : 2 : 2 : 1$. It is worth noting that in the isospin analysis, we have ignored the minor mass differences between N^+ and N^0, as well as the mass difference among π^+, π^- and π^0. In conclusion, the branching ratio for the production of proton via $N(xxxx) \to N\pi$ is only $1/2$ of the value listed in the PDG book.

The second kind of two-body decays of the $N(xxxx)$ that contributes to the production of proton are

$$N(xxxx) \longrightarrow N\eta,$$
$$N(xxxx) \longrightarrow N\omega, \tag{F.4}$$
$$N(xxxx) \longrightarrow N\eta',$$

where the mesons η, ω, η' have isospin $I = 0$ and each of the decay consists of two different decay processes. For example, the decays that involves the η meson

$$(a)\ N^+(xxxx) \longrightarrow N^+ + \eta,$$
$$(b)\ N^0(xxxx) \longleftarrow N^0 + \eta. \tag{F.5}$$

The ratio of the decay widths between the two processes is $\Gamma_a : \Gamma_b = 1 : 1$. Consequently, only $1/2$ of the branching ratio listed in the PDG book

contributes to the production of the proton. The same conclusion applies to the ω meson and the η' meson.

- $\Delta(xxxx)$ **Resonances**

  The $\Delta(xxxx)$ resonances have isospin $I = 3/2$ and there are four charge states $\Delta^{++}(xxxx), \Delta^{+}(xxxx), \Delta^{0}(xxxx)$ and $\Delta^{-}(xxxx)$. The $\Delta(xxxx)$ resonances decay to the proton via the two-body decay channel

$$\Delta(xxxx) \longrightarrow N\pi \tag{F.6}$$

  which consists of six different decay processes

$$
\begin{aligned}
&(a)\, \Delta^{++}(xxxx) \longrightarrow N^{+} + \pi^{+}, \\
&(b)\, \Delta^{+}(xxxx) \longrightarrow N^{+} + \pi^{0}, \\
&(c)\, \Delta^{+}(xxxx) \longrightarrow N^{0} + \pi^{+}, \\
&(d)\, \Delta^{0}(xxxx) \longrightarrow N^{+} + \pi^{-}, \\
&(e)\, \Delta^{0}(xxxx) \longrightarrow N^{0} + \pi^{0}, \\
&(f)\, \Delta^{-}(xxxx) \longrightarrow N^{0} + \pi^{-}.
\end{aligned}
\tag{F.7}
$$

  After performing a similar isospin analysis, the decay width ratios are $\Gamma_a : \Gamma_b : \Gamma_c : \Gamma_d : \Gamma_e : \Gamma_f = 3 : 2 : 1 : 1 : 2 : 3$. Only the (a), (b), (d) decay processes contribute to the production of proton. The branching ratio for the production of proton from the $\Delta(xxxx)$ two-body decays should be $1/2$ of the branching ratio listed in the PDG book.

- Λ **and** $\Lambda(xxxx)$ **Resonances**

  The Λ particle and the $\Lambda(xxxx)$ resonances have isospin $I = 0$ and carry no electric charges. They carry a new quantum number other than the baryon

number, the strangeness. The Λ particle decays to the proton through the channel

$$\Lambda \longrightarrow p\pi^-. \tag{F.8}$$

This is a weak decay process as the strangeness is not conserved. Its branching ratio is listed in the PDG book. No isospin analysis is needed. The $\Lambda(xxxx)$ resonances contribute to the production of proton via the two-body decays

$$\Lambda(xxxx) \longrightarrow N\bar{K} \tag{F.9}$$

and

$$\Lambda(xxxx) \longrightarrow N\bar{K}^*(892). \tag{F.10}$$

The isospin analyses are the same and we only present the analysis for the first channel. It has two different decay processes

$$\begin{aligned} &(a)\, \Lambda(xxxx) \longrightarrow N^+ + (\bar{K})^- = N^+ + K^-, \\ &(b)\, \Lambda(xxxx) \longrightarrow N^0 + (\bar{K})^0 = N^0 + \bar{K}^0. \end{aligned} \tag{F.11}$$

These are decays via the strong interaction and the isospin analysis applies. The ratio of the decay width is $\Gamma_a : \Gamma_b = 1 : 1$. Only the decay channel (a) contributes to the production of proton. The branching ratio for the production of proton from the $\Lambda(xxxx)$ two-body decays should be $1/2$ of the branching ratio listed in the PDG book.

- **Σ particle and $\Sigma(xxxx)$ resonances**

  The Σ particle and the $\Sigma(xxxx)$ resonances have isospin $I = 1$. Among the three charge states $\Sigma^+, \Sigma^0, \Sigma^-$. Only Σ^+ contribute to the production of

proton through the two-body decay

$$\Sigma^+ \longrightarrow p\pi^0 \tag{F.12}$$

Its branching ratio is listed in the PDG book. The $\Sigma(xxxx)$ resonances contribute to the proton production via the two-body decay

$$\Sigma(xxxx) \longrightarrow N\bar{K} \tag{F.13}$$

which consists of four different decay processes

$$\begin{aligned} &(a)\,\Sigma^+(xxxx) \longrightarrow N^+ + \bar{K}^0, \\ &(b)\,\Sigma^0(xxxx) \longrightarrow N^+ + K^-, \\ &(c)\,\Sigma^0(xxxx) \longrightarrow N^0 + \bar{K}^0, \\ &(d)\,\Sigma^-(xxxx) \longrightarrow N^0 + K^-. \end{aligned} \tag{F.14}$$

These processes are mediated by the strong interaction and the isospin analysis still applies. The ratios of the decay widths are $\Gamma_a : \Gamma_b : \Gamma_c : \Gamma_d = 2 : 1 : 1 : 2$. Only the (a), (b) processes contribute to the production of proton. The branching ratio for the production of proton from $\Sigma(xxxx)$ two-body decays should be 1/2 of the branching ratio listed in the PDG book.